

Thèse pour obtenir le grade de docteur de
L'Ecole Nationale Supérieure de Chimie de Montpellier

En Chimie et Physico-chimie des Matériaux

École doctorale Sciences Chimiques Balard
Unité de recherche UMR 5635 IEM

Design of new Polymer-Derived Ceramic based electrodes for Hydrogen Evolution Reaction

Présentée par **Quentin HANNIET**
le 1^{er} décembre 2021

Sous la direction du **Pr. Philippe MIELE**
Et du **Dr. Chrystelle SALAMEH**

Devant le jury composé de

Mr Gurpreet SINGH	<i>Professeur des universités</i> Kansas State University, USA	Rapporteur
Mr Farid AKHTAR	<i>Professeur des universités</i> Luleå University of Technology, Sweden	Rapporteur
Mme Christel GERVAIS	<i>Professeur des universités</i> Sorbonne universités	Présidente du jury
Mr Benoit CHARLOT	<i>Directeur de recherche</i> Institut d'électronique et des systèmes (IES)	Examineur
Mme Valérie KELLER	<i>Directrice de recherche</i> Université de Strasbourg	Examinatrice
Mr Philippe MIELE	<i>Professeur des universités</i> Ecole nationale supérieure de chimie de Montpellier (ENSCM)	Directeur de thèse
Mme Chrystelle SALAMEH	<i>Maître de conférences</i> Ecole nationale supérieure de chimie de Montpellier (ENSCM)	Co-encadrante



TABLE OF CONTENTS

TABLE OF CONTENTS.....	ii
ACKNOWLEDGMENT.....	iv
DEFINITION.....	viii
GENERAL INTRODUCTION.....	1
1 State-of-the-art review	9
1.1 Introduction to ceramic materials: from conventional ceramics to “Polymer-Derived Ceramics “route.....	9
1.2 Electrocatalysis for dihydrogen production.....	35
1.3 Microfluidic and MEMS devices <i>via</i> soft and photo-lithography	50
1.4 Conclusion on state of the art review.....	64
1.5 Bibliography.....	68
2 Materials and methods	93
2.1 Reagents and materials	95
2.2 Preparation and characterization of PDC/rGO composites	96
2.3 Preparation of micropatterns based on Si(B)CN ceramic <i>via</i> soft-lithography	105
2.4 Photolithography of preceramic polymer	109
2.5 Bibliography :	113
3 Polymer-derived ceramics/reduced graphene oxide composite systems as active catalysts towards the hydrogen evolution reaction (HER).....	118
3.1 Introduction and state of the art reminder.....	118
3.2 Chemical characterization of the material.....	119
3.3 Electrocatalytic performances	132
3.4 Bibliography.....	144
4 Microfabrication of PDC based materials <i>via</i> soft-lithography in for the purpose of micro-electrolyser applications.....	153

4.1	Introduction and brief state-of-the-art review.....	153
4.2	Characterization of the synthesized photoresists.....	153
4.3	Micropattern fabrication from pure polymer.....	162
4.4	Introduction of fillers	166
4.5	Electrocatalytic performance.....	195
4.6	Chapter conclusion.....	208
4.7	Bibliography.....	209
5	Synthesis and characterization of novel preceramic photoresists for photolithography	218
5.1	Introduction and reminder of state of the art.....	218
5.2	Original photoresist synthesis	218
5.3	Photolithographic preparation of ceramic micropatterns.....	235
5.4	Chapter conclusions.....	255
5.5	Bibliography.....	256
6	Conclusions and perspectives	261
6.1	Results summary.....	261
6.2	Perspectives	264

ACKNOWLEDGMENT

Before starting the description of my Phd in this manuscript, I want to thank all the people I was able to meet at the European Membrane Institute (IEM). All the staff and students gave me a warm welcome, which greatly contributed to my development and my enthusiasm for my research.

My first thoughts are for to my supervisor Dr. Chrystelle Salameh and my thesis director Prof. Philippe Miele who gave me the chance to join their research team and work on this fascinating subject. Their support, encouragement, trust and advice were essential to the success of this thesis. I especially want to thank Philippe for his attempt to pass on part of his great experience and his taste for science. Chrystelle, thank you also for the opportunities you gave me, the wealth of knowledge you taught me and for the great freedom you gave me to explore different lines of research. I wish you lot of success in the next studies that you will carry out with your future students, many papers in *Nature* and *Science* and a successful career! Full of happiness also in your private life and once again congratulations for your little Jonas who is the cutest Franco-Lebanese I have ever seen!

I would then like to thank Damien Voiry and his team with whom we shared the laboratory, the equipment and the research work since we were able to publish a joint work, which has a particular value for me since it, was my first article in a scientific journal. The harmony with Damien's students has always been possible thanks to a great team spirit so special thanks to Kun Qi, Yang Zhang, Wensen Wang, Ji li, Huali Wu and Jiefeng Liu. I do not forget to thank Ghenwa El Chawich, Joelle Hayek, Bonito Karamoko and Marius N'Gatta, the other Chrystelle students with whom I spent 3 pleasant years made of solidarity, joyful moments, scientific spirit and collaboration. I am among the first to finish my thesis, I wish you good luck in finishing yours, you will get there!

This research would never have been possible without the help of the *Institute of Electronics and Systems (IES)* and of Benoit Charlot in particular who brought us his mastery of microfabrication processes and numerous equipment specific to this discipline. Without his help and their advice, we would not have been able to transpose this know-how to *IEM* and our research topics. This Phd wouldn't have been possible either without Eddy Petit (FT-IR,

NMR, Raman), Nathalie Masquelez (TGA-DSC), Arie Van Der Lee (XRD), Didier Cot (SEM, microscopy), Bertrand Rebière (EDX), Abdeslam El Manssouri (Hg Porosimetry), Christel Gervais (Solid-state NMR), Igor Iatsunskyi (HRTEM) and Valerie Flaud (XPS), all responsible for characterization techniques that were essential to the outcome of our research. A big thank you also to all the *IEM* PhD students with whom I shared all the hardships and joys inherent to a Phd. This feeling of not being alone to encounter a lot of problems that we have experienced collectively, in particular this sudden period of confinement or the misadventures related to the writing of the manuscript has really been a lifeline!

Finally, I must thank Prof. Gurpreet Singh, Prof. Farid Akthar, Prof. Christel Gervais, Dr. Benoit Charlot and Dr. Valérie Keller who agreed to be rapporteur and examiner for this thesis. I hope that reading this manuscript will not be too strenuous and that they can find inspiration for their own research.

Finally, I reserve a loving thought for my other half, Lucie Figuières, for her dedication and support despite my periods of doubts and bad humor linked to the stress that has sometimes gone through me during these 3 years. Thank you for the trust, thank you for supporting me, thank you for changing my mind, thank you, thank you, thank you! I hope that someday I can return the same attention to her and provide her with the same support when she needs it in her own endeavors. Thank you also to my family, my parents without whom I would never have reached this level of study, thank you for their sacrifices, their education and their immense generosity. I am overflowing with gratitude!

"First of all, science is not: it is done. The savant of one day is only the ignorant of the next."

Elisée Reclus

DEFINITION

AFM : Atomic force microscopy

AlN : Aluminium nitride

BDMB : 2-Benzyl-2-dimethylamino-1-(4-morpholinophenyl)-butanone-1 (Irgacure 369)

BDMS : Borane dimethyl sulfide

BN : Boron nitride

CG : Coal gasification

CV : Cyclic voltammetry

CVD : Chemical vapor deposition

C_{dl} : Double layer capacitance

DOSY : Diffusion ordered spectroscopy

EELS : Electron energy loss spectroscopy

ECSA : Electrochemical active surface area

FTIR : Fourier Transform Infra-Red

GO : Graphene oxide

HER : Hydrogen evolution reaction

HRNM : High resolution numerical microscopic

IEA : Isocyanate ethyl acrylate

IEM : Isocyanate ethyl methacrylate

MEMS : Micro electro-mechanical system

MoS₂ : Molybdenum disulfide

MoSi₂ : Molybdenum disilicide

NMR : Nuclear Magnetic Resonance

O-SiBCN : Oxidized Silicon-boro-carbo-nitride

O-SiCN : Oxidized Silicon -carbo-nitride

O-SiC : Oxidized Silicon-carbide

PECVD : Plasma-Enhanced Chemical Vapor Deposition

PDCs : Polymer-derived ceramics

PDMS : Polydimethylsiloxane

PVD : Physical vapor deposition

PVZ : Polyvinylsilazane

PBVZ : Boron modified polyvinylsilazane

rGO : Reduced graphene oxide

RHE : Reversible hydrogen electrode

SEM : Scanning electron microscopy

SiBCN : Silicon-boro-carbo-nitride

SiCN : Silicon carbo nitride

SiC : Silicon carbide

Si₃N₄ : Silicon nitride

SMR : Steam methane reforming

TEM : Transmission electron microscopy

TGA : Thermogravimetric analysis

THF : Tetrahydrofuran

TMDs : Transition metal dichalcogenides

WGS : Water-gas shift

XRD : X-ray diffraction

XPS : X-ray photoelectron spectroscopy

GENERAL INTRODUCTION

GENERAL INTRODUCTION

Our modern world has been built on a constantly increasing energy consumption for at least two centuries. During these years, the exploitation of fossil fuels has been the most direct and economical way to ensure a living environment to millions of people. However in order to meet the climate goals, a profound energy transition is required.

The scientific community, among others, has concentrated its efforts on the development of substitutes to the greenhouse gas emitting resources that are coal, oil and natural gas. Solutions are already being implemented since renewable energies (wind, solar, hydraulic, geothermal...) are becoming increasingly popular. However, while changing the whole energy production system, we also need to think about new ways to store, transport and convert this decarbonized or low carbon energy. Although these energy sources have many advantages, they have the disadvantage of producing energy intermittently and not on demand. Indeed, wind turbines do not turn when there is no wind and photovoltaic panels are inactive during the night.

Hydrogen is a promising solution for storing and converting energy. Nowadays, 95% of hydrogen comes from steam reforming of methane and coal gasification methods that cannot be incorporated into the energetic transition process. Thanks to fuel cell technology, dihydrogen can be converted into electricity, to power an electric motor for example, while emitting only water as by-product. Such technology is attracting many automotive manufacturers for the hydrogen car. We can also imagine the reverse operation of a fuel cell, i.e. producing hydrogen with a surplus of electricity coming from photovoltaic or wind power *via* electrolysis. In fact, 70% of the Earth's surface is covered with water which makes it an attractive feedstock that can be recycled back indefinitely into nature. Compared to other available processes, water electrolysis provides efficient and cost-effective production of pure hydrogen. However, to lower the energy needed for creating hydrogen from water expensive noble-metal-based electrocatalysts are usually employed.

The efforts of researchers have therefore been focused on the design of catalysts based on inexpensive materials to replace noble metals. The strategy to build such noble-metal-free catalysts consists in combining transition metals with non-metals elements. A bottom-up

strategy can be very interesting to build precise electronic structure with required catalytic properties. In this context, the “Polymer-Derived Ceramics” (PDCs) route offers unique opportunities for fine control at atomic scale of ceramics and tailoring “on-demand” their properties. In this manuscript we describe how PDC materials combined with 2D materials i.e. graphene and dichalcogenides may be implemented in energy conversion devices based on water-splitting procedure.

Furthermore, since several decades, the interest of microstructured materials is constantly growing in the scientific and industrial fields. The example of microelectronics is striking, as witnessed by Moore's law, edicted in the 60's, which predicted a doubling of the numbers of transistors on microprocessors each two years. This law has been confirmed over the years and has been translated into reality by the development of increasingly advanced and low-cost microfabrication techniques such as soft-lithography, photolithography, micro-stereolithography and many others. The constant search for innovation in this field has led to a diversification of potential applications related to microstructuring and led to the integration of new materials in these processes. Ceramics have been gradually incorporated into micro-devices to improve their thermal, mechanical and chemical properties especially in harsh environments. The aforementioned PDCs route particularly fits with soft-lithography and photolithography pathways for microstructuration since they are both based on the micro-shaping of polymer materials. The integration of ceramics in Micro Electro Mechanical System (MEMS) *via* precursors built at molecular level opens great perspectives for new applications in electrochemistry.

Both miniaturization and PDCs represent a potential breakthrough for the electrochemical field in particular for battery electrodes, capacitors and dihydrogen production via water-splitting. Moreover, due to the energy crisis inherent to our century, the research in this area is crucial if we want to reduce our global energy consumption. On one hand, miniaturization is a part of the solution since it allows to reduce the consumption of materials and to produce large number of micro-systems at once. On the other hand, the preparation of low cost and tuned ceramic based catalysts *via* the precursor route represent an interesting alternative to scarce materials essential in electrochemistry such as noble metals.

This PhD project is funded by the Graduate School “Ecole Nationale Supérieure de Chimie de Montpellier” and partially by the CNRS Cellule Energie exploratory project “CeraMicroPac”.

The manuscript is divided into 5 chapters. The first chapter consists in a state of the art of all the disciplines concerned in this thesis: i) Polymer-Derived Ceramics (PDCs) route, ii) Electrocatalytic water splitting, iii) Microfabrication techniques. Chapter 1 highlights the relation between these 3 parts as the main objective of this PhD work is to develop electrodes and microelectrodes for the hydrogen evolution reaction (HER).

The second chapter presents the experimental part of this work. A large number of the materials that we had to handle during the experiments are sensitive to air and moisture. They were thus handled and stored under inert conditions as will be described in this chapter. The methods for synthesizing ceramic precursors and preparing microstructured samples as well as the characterization protocols will finally be detailed.

In a third chapter, all the results and discussions on the elaboration of PDC/graphene-based composites as electrocatalysts for Hydrogen Evolution Reaction (HER) will be presented. The correlation between the (micro)structure of the materials and their electrocatalytic performance is evaluated. We successfully prepared ultrathin Si-C based ceramics supported on electrically conducting 2D reduced graphene oxide nanosheets (rGO) varying the nature and the composition of the ceramic with the inclusion of nitrogen, boron and oxygen. Our results suggest that the O-SiBCN/rGO based composites display the strongest activity with lowest onset potential and largest current densities thanks to a synergetic effect from the intrinsic activity of O-Si-B-C-N and the high porosity and electrical conductivity of rGO support. The activity is further improved upon oxygen doping, yielding thus ultra-stable O-SiBCN/rGO electrodes. Furthermore, we suggest a systematic approach for producing highly porous and mechanically resistant PDC/rGO free-standing electrodes for HER reaction.

A related approach to the development of efficient and economical catalysts is to miniaturize the energy conversion systems. A considerable impact of the use of the micrometer scale is the enhancement of the efficiency and economic viability of the

electrolyser device. Indeed, the downscaling of characteristic dimensions (channel width, distance between electrodes) in the device offers better flow control, enhances heat and mass transfer, boosts the surface-to-volume ratio and consumes less material. Therefore, we explore in chapters 4 and 5 two manufacturing methods for PDC based micro-electrodes: soft-lithography and photolithography. The fourth chapter is dedicated to elaborate proof-of-concept micro-objects based on PDC materials with micro-electrolyser perspective applications. Soft-lithography methods were combined with the PDCs route to propose a simple protocol for ceramic micro-patterning. We develop a strategy based on fillers utilization whether passive or active. Fillers aim to limit the cracks formation during pyrolysis. In addition to this role, active fillers will add new properties to the ceramic. A precise description of Si(B)CN micropatterns with passive and active fillers (Al_2O_3 and MoSi_2 or MoS_2 respectively) is conducted in this section with a detailed geometrical/topographical study and complete chemical characterization.

Finally, the fifth chapter develops the results and discussions associated with the microstructuration of PDC based materials *via* photolithography. SiCN and SiBCN precursors were chemically modified with acrylate and methacrylate groups in order to integrate photoresist properties. Thanks to a careful optimization of such synthetic preceramic photoresists and of the photolithographic process parameters, we succeeded in manufacturing crack-free ceramic micro-objects with faithful geometrical reproducibility.

A general conclusion closes this manuscript by recapitulating the different strategies (bottom-up and top-down) we used to fabricate PDC and 2D materials based composites as electrodes and microelectrodes for HER. Perspectives related to the use of as-prepared ceramic based microelectrodes in an actual microelectrolyzer are highlighted at the end.

Chapter I : State-of-the-art

1	State-of-the-art review	9
1.1	Introduction to ceramic materials: from conventional ceramics to “Polymer-Derived Ceramics” route	9
1.1.1	Ceramic processes	11
1.1.1.1	Conventional ceramics	11
1.1.1.2	Focus on non-oxide ceramics	13
1.1.1.3	Chemical precursor route for ceramics preparation.....	14
1.1.2	“Polymer derived ceramics” route	16
1.1.2.1	History and general methodology.....	16
1.1.2.2	Focus on SiCN and SiBCN systems.....	24
1.1.2.3	Filler strategy	29
1.1.3	PDCs applications for energy.....	32
1.1.3.1	Hydrogen storage and generation	33
1.1.3.2	Battery electrodes	34
1.1.3.3	Hydrogen production via electrocatalysis	35
1.2	Electrocatalysis for dihydrogen production.....	35
1.2.1	Current dihydrogen production	36
1.2.1.1	Steam Methane Reforming (SMR)	37
1.2.1.2	Coal Gasification (CG)	38
1.2.2	Importance of electrocatalysts.....	41
1.2.2.1	Hydrogen Evolution Reaction (HER) principle	42
1.2.2.2	Practices for reporting electrocatalytic performances	43
1.2.2.3	Noble metal catalyst-Platinum	44
1.2.2.4	Noble-metal-free catalysts	45
1.2.3	Miniaturization of microdevices for HER applications.....	47
1.3	Microfluidic and MEMS devices <i>via</i> soft and photo-lithography	50
1.3.1	Interest of microfluidics in general	50
1.3.2	Principle of soft and photo-lithography	52
1.3.2.1	PDMS based microdevices	52

1.3.2.2	Soft-lithography processes for micromolding	53
1.3.3	Photolithography for direct micro-patterning.....	56
1.3.4	Specific case of ceramic MEMS <i>via</i> PDC route	59
1.3.4.1	Theory and interest	59
1.3.4.2	Examples from literature.....	60
1.4	Conclusion on state of the art review.....	64
1.4.1	Ceramic, MEMS and electrochemistry	64
1.4.2	Introduction to works developed in this study	67
1.5	Bibliography.....	68

1 State-of-the-art review

The purpose of this state-of-the-art is to introduce all the disciplines involved and used in this thesis. First, an overview on ceramics and a focus on the specificity of “Polymer-Derived ceramic” (PDC) materials and their applications are developed. Second, the issue around the hydrogen generation and its place in the carbon-free energy production are discussed with a focus on the water-splitting process and its specific challenges. Third, a development devoted to soft and photolithography as microfabrication techniques will be the subject of a synthesis.

1.1 Introduction to ceramic materials: from conventional ceramics to “Polymer-Derived Ceramics” route

The term “ceramic” designates a very specific category of materials, it comes from "keramos" in Greek translatable to "potter's earth or clay". Indeed, this definition refers to a past reality designating objects such as vase, jar and vessel produced by arts and crafts of that period [1]. In spite of everything, such definition has crossed the times. For example, for the general public, the term ceramic still refers to objects made from clay or terracotta including earthenware, stoneware, porcelain, etc...What about the definition of this term among the scientific field? Well the question is not that easy to decide and debates are still going on around these semantic questions. MIT (Massachusetts Institute of Technology) has defined ceramics as "iono-covalent solids", in other words, would be ceramic all non-organic and non-metallic solids [2]. However, this definition is problematic since cements, glasses, rocks would then be considered as ceramics while in scientific circles clear distinctions are made between these types of materials.

Another way to define ceramics would be to describe them by their manufacturing process. Indeed, there is a so-called "ceramic" process consisting in several steps: i) starting from an inorganic powder ii) dispersing it in a solvent (conventionally water) to make a colloidal suspension or a paste (a slip) iii) shaping the suspension or paste (by molding for example) iv) drying and debinding steps to remove the solvent and v) densification of the object by a heat treatment called sintering which consists in welding the grains together to obtain the final ceramic part. The final material usually consists in a fragile, refractory, insulating, and

polycrystalline solid. By this definition, glasses, cements, and rocks are no longer arranged with ceramics since their manufacturing process differs from that described above (shaping by fusion for glasses and heat treatment before shaping for cements). The definition *via* the description of the process was valid for all ceramic materials prepared until the beginning of the 20th century. In fact, in the 1950s new processes were developed in order to prepare ceramics from chemical precursors. This new generation of ceramics from precursors has greatly changed the use of such materials in industry and technology. Sometimes referred as "precursor-derived ceramics", this new generation of ceramics has enabled the development of thin films, coatings, membranes, MEMS (Micro Electro Mechanical Systems) and many others.

Nowadays, one of the definitions of "ceramics" would undoubtedly be to describe these materials by their properties and no longer by their method of preparation. The ceramics would then group together inorganic, non-metallic materials with a brittle behavior, refractory, without glass transition temperature and generally obtained after a final heat treatment at high temperature.

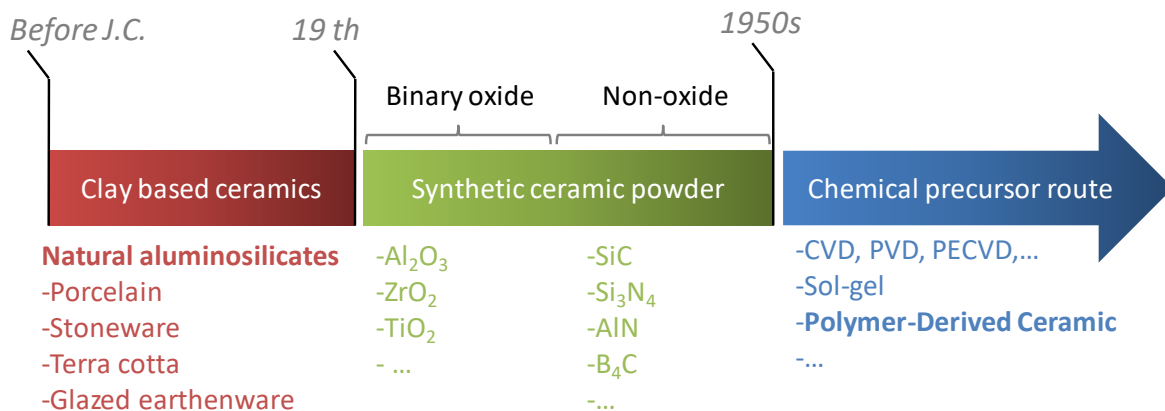


Figure 1-1: Chronology of ceramic materials elaboration

Figure 1-1 provides a timeline associated with the history of ceramic materials preparation. Archaeologists have discovered many ceramic parts made well before J.C. (Jesus Christ) [3][4]. This first generation of ceramics is based on the shaping of raw inorganic powders such as natural clay and begins with the preparation of terracotta pieces, it has led to the mastery of porcelain and earthenware [2]. In the middle of the 19th century, a second

generation of ceramics began to emerge. No longer based on natural materials but synthetic powders, this second generation of ceramics made it possible to develop, binary oxides such as alumina (Al_2O_3) or zirconia (ZrO_2). For example, the development of the Delville process in 1860[5] consisted in synthesizing Al_2O_3 powder from chemical treatment of natural bauxite mineral. With the mastery of the preparation of silicon carbide SiC ceramics in 1891 (creation of the Carborundum company, first SiC producer) [6] a new sub-category of so-called non-oxide ceramics has emerged and has led to the industrial production of silicon nitride Si_3N_4 , aluminum nitride AlN or boron carbide B_4C today widely used in the industry. Non-oxide ceramics sometimes refer to a category called “technical ceramics” due to their specific properties (semi-conduction of the SiC for example) and their applications in high technology industry. The third and latest generation of ceramics originates from the 1950s allowing the synthesis of hard ceramic materials from molecular precursors [7]. For example, Titanium carbide TiC coating prepared in 1950 by chemical vapor deposition (CVD) from Titanium tetrachloride TiCl_4 and methane CH_4 after Pollard and Woodward works [9] is one of the milestones marking the emergence of this latest generation of ceramics. Based on this work, processes such as sol-gel, hydrothermal syntheses and “Polymer-Derived Ceramics” (PDCs) were intensively studied and developed [10][11]. These processes have made it possible to develop “bottom up” strategies allowing the functionalization of materials at the molecular scale to deliver structures and microstructures tailored for specific applications.

1.1.1 Ceramic processes

1.1.1.1 Conventional ceramics

Even if its principle has been enacted centuries ago, the “conventional ceramic” process is still widely used today either in arts and crafts or high-tech industry. Figure 1-2 gives an illustration of the process steps: inorganic powder is dispersed in a solvent, generally water to form a colloidal suspension; the slurry is traditionally shaped by mold casting and partially dried to form a so called green part strong enough to be handled; a first heat treatment is sometimes carried out at relatively low temperature to remove last traces of moisture and/or organic compounds, it results in a fragile and porous part named brown

part; final step is the densification of the porous part *via* high temperature thermal treatment called sintering [12].

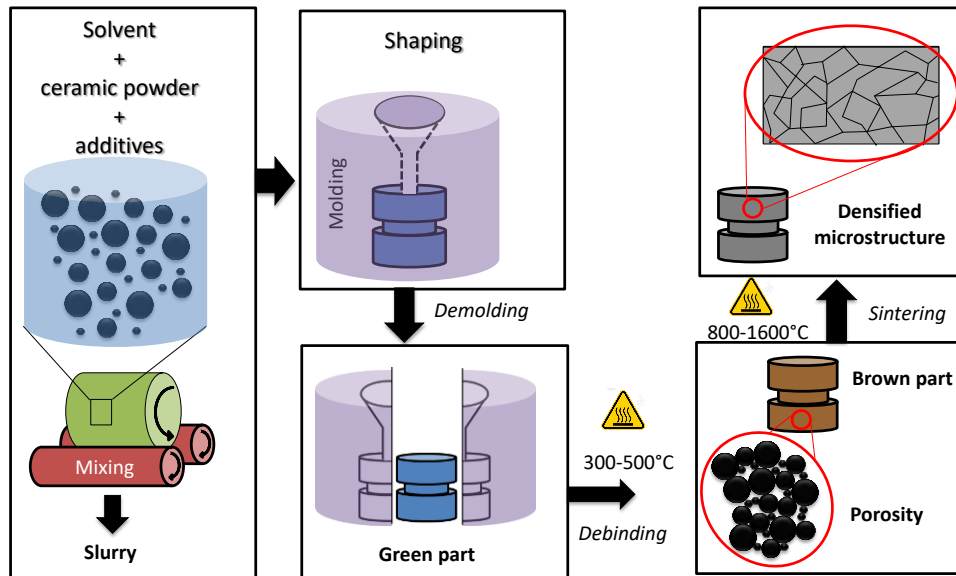


Figure 1-2: Conventional ceramic process

Despite years of experiences and studies, each step of the process is still an industrial challenge and requires rigor and precision [13]. Ceramics being brittle materials, their fracture toughness is directly linked to the number, shape and size of the defects contained in the final part. A poor powder dispersion, a badly mastered molding and drying step, an inhomogeneous porosity or an incomplete densification may be source of defects formation. The dispersion and the stabilization in the initial colloidal suspension to control its rheology can be assisted with the addition of dispersants, surfactants and plasticizers. The rheology must be optimized in agreement with the shaping method used to ensure a proper grain stacking as well as elimination of bubbles and agglomerates. The different heat treatment implemented in the process (drying, debinding and sintering) may also be source of defect formation and must thus be optimized. For example, a very rapid drying can conduct to mud cracks formation leading to fracture of the final part.

A constant innovation towards the performances of functional ceramics has led to the industrialization of high-tech materials. For example, non-oxide ceramics are technical ceramics given their specific properties and they will be the subject of the next section.

1.1.1.2 Focus on non-oxide ceramics

The growing interest of non-oxide ceramics in the high-tech industry since the 1950-60s is due to their exceptional thermal, mechanical, optical, and electronic properties. Nevertheless, their fabrication process is very specific especially because of their high sintering temperature and the requirement of a non-oxidizing atmosphere [14]. Thus, due to their cost of fabrication each step of the ceramic process has to be carefully optimized:

First, non-oxide ceramic powders are most of the time synthetic powders and must be very fine to favor sintering step. Because of the small grain size, specific surface area of the powder is very high which makes the powder difficult to disperse and stabilize in solvents. The use of dispersants and additives to optimize rheology is thus inevitable.

During the process of drying, the solvent in the green parts must be removed without damaging the components. In the case of non-oxide ceramics, considerable drying stresses can occur due to the small pores (caused by small grain size). Too fast or uneven drying leads to cracking or deformation. The local drying rates are strongly dependent on the relative humidity (solvent concentration), the temperature and the flow rate of the drying atmosphere. It is thus necessary to use drying devices that can be used to weigh samples under controlled atmosphere, temperature and gas flow during drying.

In the debinding process, the organic additives to the ceramic green bodies, such as binders, plasticizers or dispersants, are generally removed thermally. The organic additives are pyrolyzed or - in an oxygen-containing atmosphere - burnt out. However, the use of oxygen is only possible to a very limited extent, as otherwise oxidation of the non-oxide ceramics occurs. If the binder is vaporized too fast, the released gases cannot be transported quickly enough through the pore channels to the component surface. The resulting overpressure in the pore channels can also lead to component damage. There are other undesirable phenomena which may occur during debinding, e.g. the absorption of low temperature gases by colder green bodies in continuous furnaces or the segregation of the liquid binder in the pore channels. Similar to drying, it is important to find the fastest yet safest temperature profile where the debinding can be carried out without producing defects. The flow velocity and the composition of the furnace gases can be varied in many cases.

At the sintering step, densification with a defined residual porosity has to be achieved. The structure should be defect-free and homogeneous, and the component must not deform. The high costs associated with the final processing of non-oxide ceramics require production as close to net-shape as possible. This means, the sintering shrinkage has to be included in the dimensioning of the green bodies. Deviations from the desired geometry can occur during sintering due to an uneven distribution of the porosity in the green body or because of the influence of friction, gravitation and temperature differences during the heat treatment.

During the densification process, thermodynamic driving forces can lead to phase separation or inhomogeneous sintering even though the initial green body was homogeneous. At the end of the densification step, increased grain growth occurs, which tends to degrade the quality of the sintering and then the mechanical properties of the ceramic part. Other phenomena that must be controlled during sintering are gas-phase processes that are caused by reactions of the sintered material with the furnace atmosphere or by gas release. Finally, to reduce the efforts required for densifying non-oxide ceramics, sintering additives (mostly oxides) are used. Carbothermic reduction between those oxides and carbon derived from pyrolysis or impurities in the furnace atmosphere, can cause defects within the final microstructure [15].

As described above, fabricating non-oxide ceramics is extremely complex. Each step is critical and can lead to poor quality or broken final part if it is not perfectly mastered. Such complexity causes inevitable high cost of such high-tech ceramics. In this perspective, “easier” ways to produce ceramics and more specifically non-oxide ceramics have emerged in the 50-60s, the next section is dedicated to a brief overview of these processes.

1.1.1.3 Chemical precursor route for ceramics preparation

Besides the conventional ceramic process, more modern processes such as the sol-gel route, thin film processes (CVD: chemical vapor deposition or PECVD: Plasma-enhanced CVD), the PDCs route (Polymer Derived Ceramics), hydrothermal synthesis, atomic layer deposition (ALD) and others have led to materials with “typical” ceramic properties but sometimes with specific microstructures. Most of the time these new routes are based on the

conversion of a chemical precursor into a ceramic material thanks to a contribution of energy (for example a thermal treatment at low temperature). Figure 1-3 displays some examples of these modern processes conducting to precursor-derived ceramic materials.

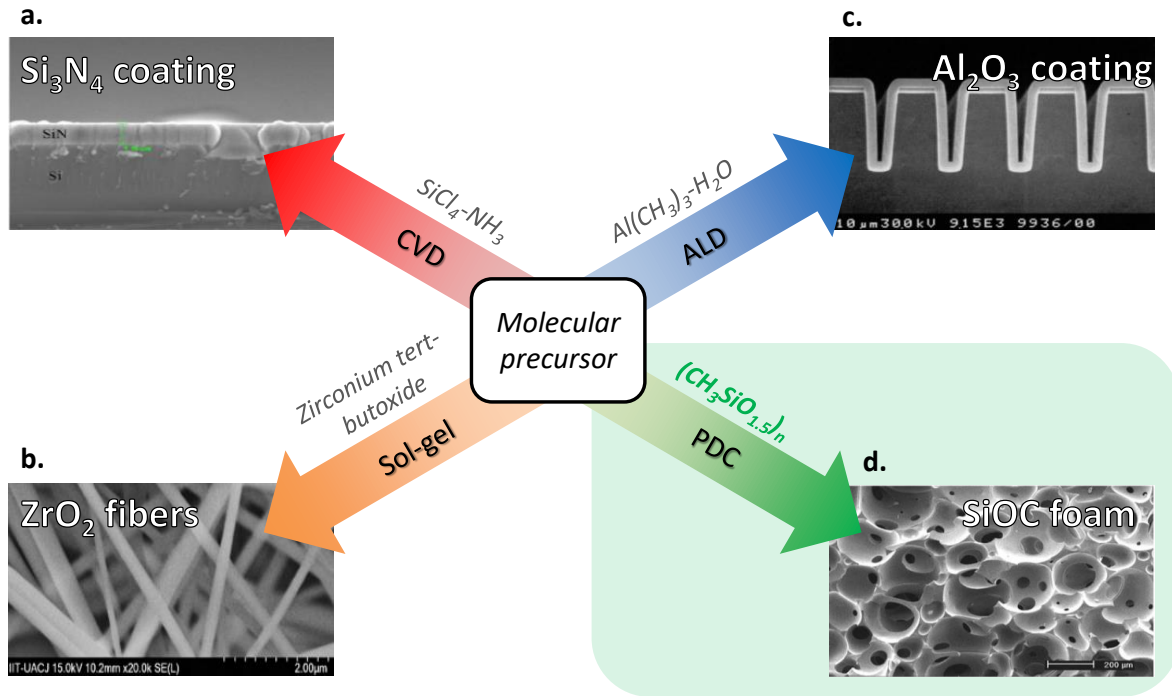


Figure 1-3: Chemical precursor routes for ceramic materials. a) Silicon nitride coating prepared via CVD and from silicon tetrachloride and ammonia [16] b) Zirconia fibers via sol-gel route and from zirconium tert-butoxide [17] c) Alumina coatings prepared via ALD and from trimethylaluminum and water precursor [18] and d) SiOC foam elaborated via PDC route and from polysiloxane [19].

One example of Figure 1-3.a. shows a Si₃N₄ coating deposited on a silicon wafer *via* CVD technique. The coating is derived from combination of gaseous silicon tetrachloride (SiCl₄) and ammonia (NH₃) [16]. The sol-gel example in Figure 1-3.b. shows ZrO₂ fibers derived from zirconium tert-butoxide *via* electrospinning and low temperature conversion [17]. From trimethylaluminum (Al(CH₃)₃) precursor combined with H₂O it is possible to prepare high quality Al₂O₃ coating as displayed in Figure 1-3.c. [18]. Finally, the SiOC ceramic foam in Figure 1-3.d. was obtained from pyrolysis of polymethylsiloxane polymer [19]. The microstructures of such materials are radically different from the one obtained with the conventional ceramic process, no micrometric grains are observable, very fine microstructuration and specific fibers or macroporous shapes are generated. In this thesis, we have favored the PDCs route because of the easy processability and molecular design

ability of preceramic polymers. The following section explores in detail the advantages, the subtleties and the history of the PDCs approach.

1.1.2 "Polymer derived ceramics" route

1.1.2.1 History and general methodology

We have seen in the previous sections that PDC materials are part of a new generation of ceramics that established itself in the 1950s [20]. The beginning of PDC materials science is generally attributed to the work of Verbeek and Yajima in 1973 and 1978 [21][22] who were respectively the first to synthesize Si_3N_4 , SiOC and SiC fibers from inorganic polymers. This discipline nevertheless has its source in the work of Fritz, Ainger and Popper[23][24][25] who discovered the precursor's properties of silane, siloxane and silazane molecules. In 1956, Fritz *et al.* obtained non-oxide C-Si-C ceramics by pyrolyzing silane species [23]. The work of Ainger and Herbert [24] which followed, founded a solid basis for establishing the science of PDCs as it is displayed in the timeline in Figure 1-4 (based on Colombo and Riedel's book [26]). The decade that followed Yajima's work on the preparation of SiC fiber from polycarbosilane [21] was devoted to the synthesis of new inorganic preceramic polymers of conventional or novel ceramics such as AlN [27], SiBCN [28][29][30], Si-Fe-CN [31], BN [32], Polysilylcarbodiimide derived SiCN [33]... During these years of breakthroughs, the laws governing the behavior of PDCs were established and served to optimized ceramic performances, processability or intrinsic properties. Between the end of the 90s and the 2000s, PDC process engineering then emerged allowing the use of these preceramic polymers in industry. The study of the characteristic microstructures of preceramic polymers and their modeling have led to a more detailed understanding of the behavior of these materials with respect to high temperatures, mechanical stresses and their electronic properties [34][35][39]. The preparation of large-scale commercial preceramic polymers started in the early 2000s with companies like Kion, Clariant and Starfire [26][36] with industrial fabrication of polyvinylsilazane (PVZ), perhydropolysilazane (PHPS) and allylhydridopolycarbosilane (AHPCS), respectively. These materials could then start to be utilized in industrial applications consisting, for example, of surface treatment and SiC fibers elaboration.

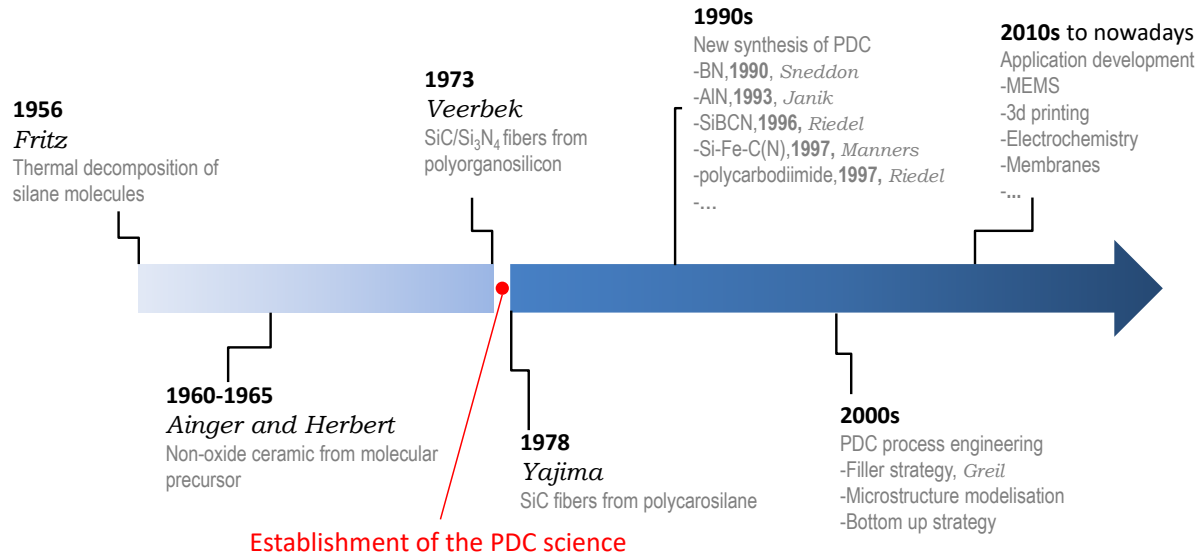


Figure 1-4: Chronology of “Polymer-derived Ceramics” progress [26]

Greil's work between 1995 and 2000 was decisive in overcoming one of the weak points of this process, namely the strong shrinkage occurring during heat treatment [37][38][39]. Greil's advances have consisted in mixing additives with the preceramic polymer in order to reduce or even suppress shrinkage and thus allow the manufacture of large “bulk” parts. Between the late 2000s and today, the amount of research and industrial work has grown almost steadily to develop applications for these materials in a wide variety of fields. In a non-exhaustive way, PDCs could be used in several fields such as membranes [40] and battery electrodes [43] and they can be obtained by un-conventional fabrication techniques such as 3D printing [41] and microfabrication [42]. This work is part of this dynamic and focuses on the investigation of the electrocatalytic properties of such materials. The next sections will be devoted to a more detailed explanation of the subtleties of the PDCs approach, the difference between the preceramic polymers used to date, the shaping techniques mastered in this discipline and the specificity of the final microstructures obtained.

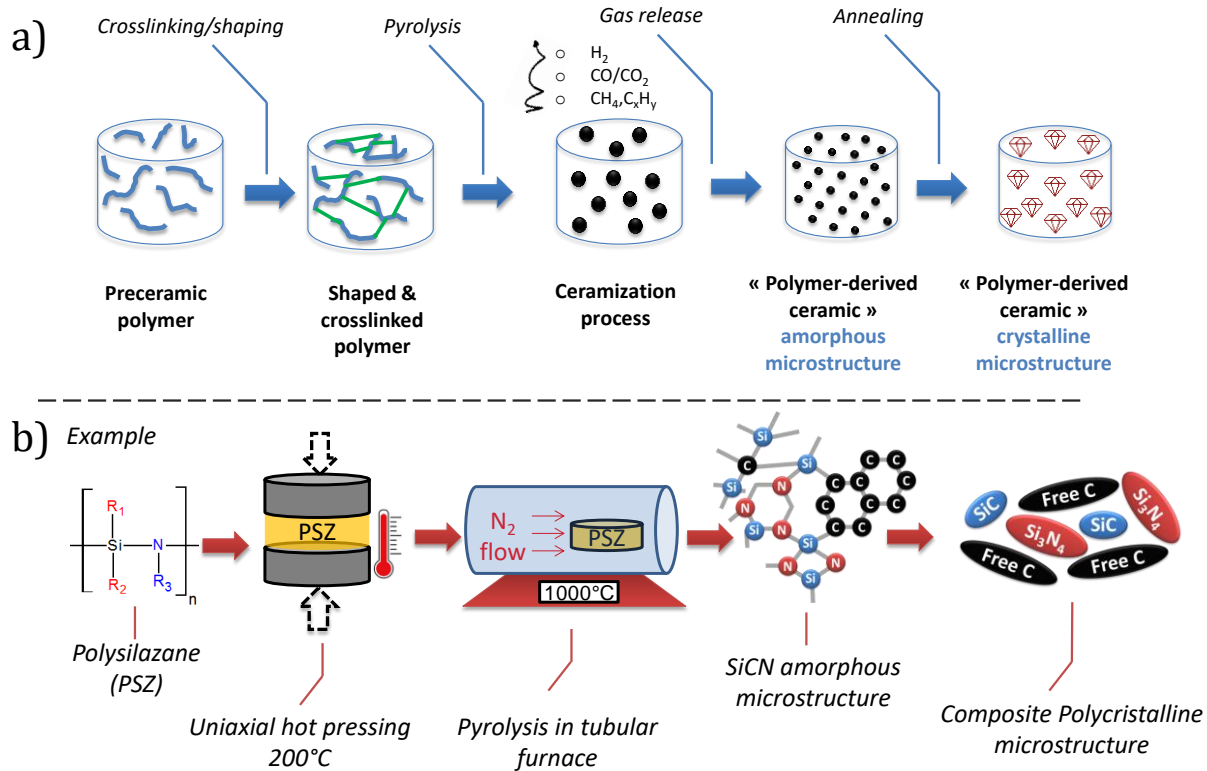


Figure 1-5: Description of the PDCs route (adapted from [34][35]).

Figure 1-5.a. provides a schematic description of the PDCs process. The preceramic polymer is first shaped using one of various shaping techniques compatible with the process. This is followed by a crosslinking step, usually a heat treatment, simultaneous or subsequent to the shaping process or can be assisted by a crosslinking agent. The green part is then transferred in a furnace to be pyrolyzed and converted into ceramic generally between 800 and 1100°C and under a controlled atmosphere (inert, oxidizing or reducing). This treatment is accompanied by a release of gaseous species (CH_4 , H_2 , C_xH_y , NH_3 ...) and a significant shrinkage (30-40 vol%). As a result of this treatment, the obtained material hardly contains any more hydrogen and consists of a hard solid with an amorphous microstructure. To obtain a crystalline microstructure, it is necessary to perform annealing at higher temperatures ranging from 1500 to 2000 °C depending on the nature of the ceramic concerned. Figure 1-5.b. illustrates an example of a PDCs process implemented with a polysilazane precursor of SiCN ceramic. Polysilazane is simultaneously cross-linked and shaped as pellet *via* uniaxial warm pressing at around 200°C. The pressed polymer is then transferred in a tubular furnace and converted into SiCN ceramic after a pyrolysis at

1000°C under nitrogen to avoid oxidation. The resulting microstructure consists in an amorphous phase containing SiC, Si₃N₄ and C nanodomains as represented in Figure 1-5.b. After an annealing treatment at >1500°C the amorphous phase transforms into a polycrystalline structure composed of SiC, Si₃N₄ grains in a carbon network.

1.1.2.1.1 Preceramic polymers

According to Colombo's review published in 2010 [34] one of the important branches of PDC materials is silicon based compounds. There are at least four major families among these silicon-based polymers, polycarbosilanes, polysilazanes, polysiloxanes and polyborosilanes with hybrid variants such as polyborosilazane (see details in Figure 1-6). By changing the functional groups R_x on the silicon atoms, thermal and chemical stability, solubility of the polymer, as well as electronic, optical, and rheological properties can be modified and adjusted. Usually, hydrogen, aliphatic or aromatic organic side groups R_x are attached on the silicon atoms. A precise selection of the functional groups can also conduct to specific compositions with high carbon contents or introduction of heterogeneous atoms.

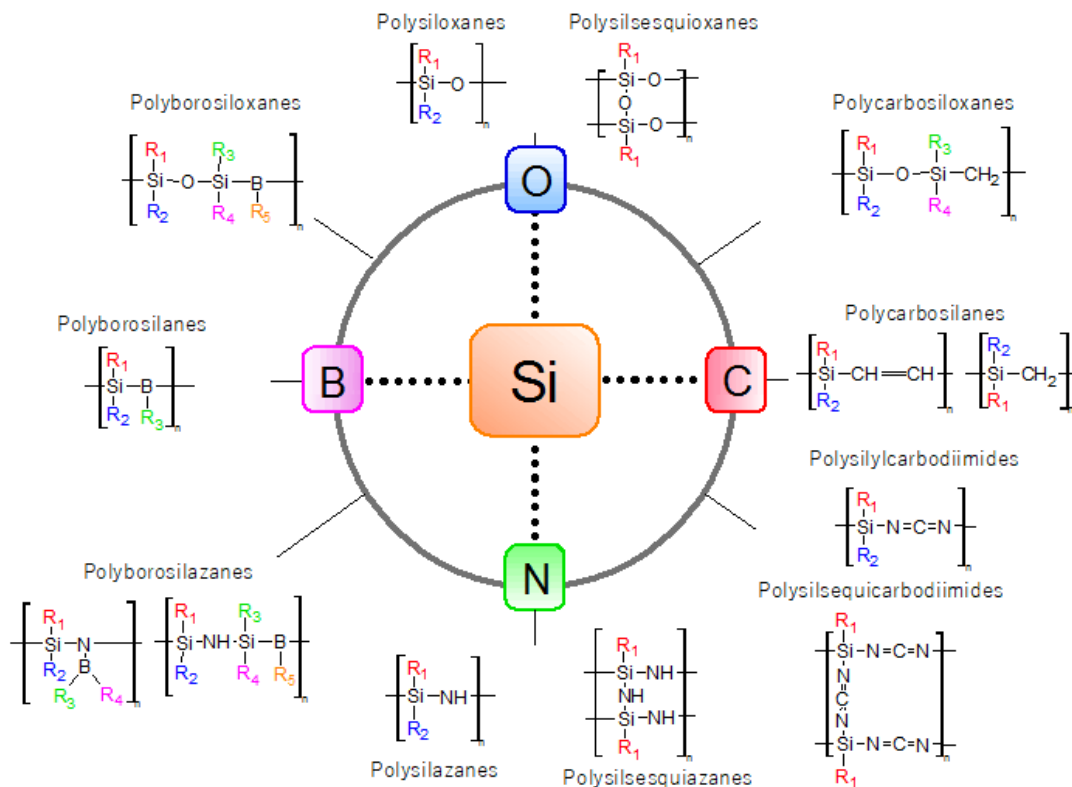


Figure 1-6: Overview of silicon based preceramic polymers (adapted from [34])

Figure 1-7 provides a brief description of the synthesis method of the most wide spreads silicon based pre-ceramic polymers. Conventionally, all of these preceramic polymers result from a polymerization of dichlorosilane precursors. Polycarbosilanes are synthesized by polycondensation of the monomer and by increasing the temperature. After the Kumada rearrangement, a C-Si-C backbone with alkane or alkyl branches is obtained. For polysilazanes, this is polymerization by ammonolysis or aminolysis between ammonia or amine and the dichlorosilane monomer [34]. This synthesis route nevertheless leads to by-products formation that must be removed in order to obtain highly pure polymers. On the other hand, polysilylcarbodiimides are another class of nitrogen-based preceramic polymers synthesized from silylcarbodiimide. Both polysilazanes and polysilylcarbodiimides conduct to SiCN ceramics but with different microstructures:

- on one hand a single amorphous SiC_xN_y phase with mixed bonds is obtained from polysilazane
- on the other hand 3 phases $x\text{SiC} + y\text{Si}_3\text{N}_4 + z\text{C}$ microstructures without mixed bonds are derived from the polysilylcarbodiimides polymers [34]

Polysiloxanes can be synthesized *via* several routes. The chloro(organo)silanes reaction with water conduct to polymerization in -Si-O-Si- backbone but polysiloxane can also be formed *via* the polycondensation of linear silane, silylcarbodiimide or silazanes.

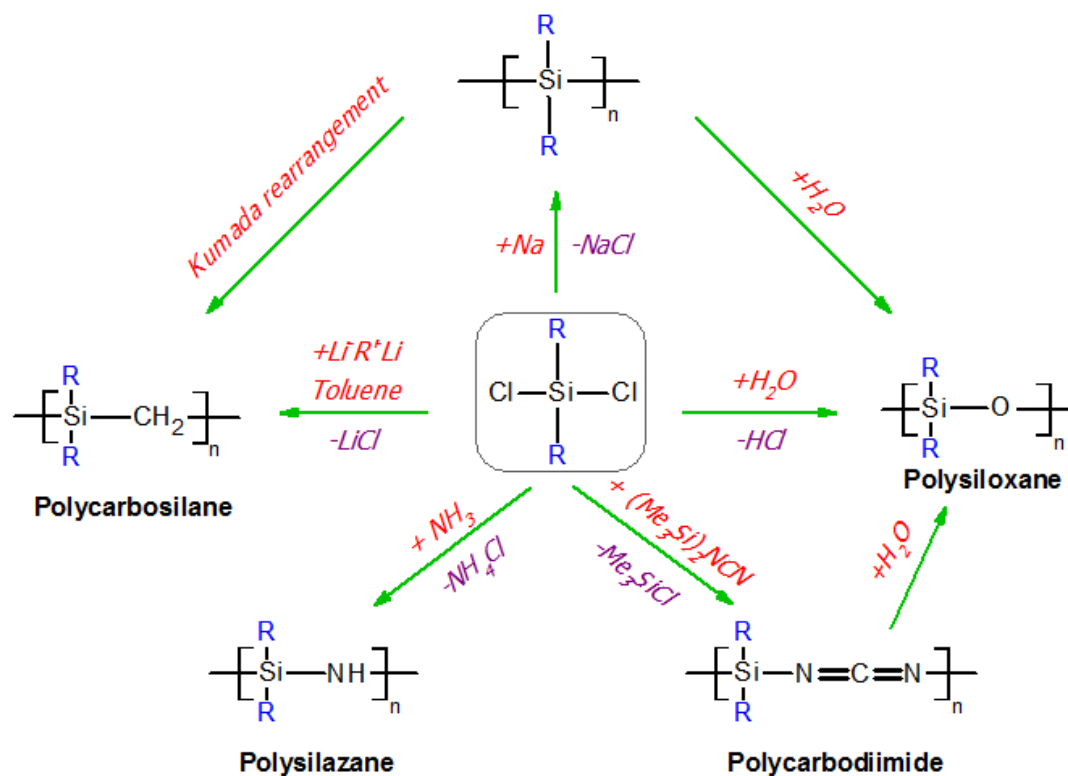


Figure 1-7: Synthesis ways for pre-ceramic polymers from dichlorosilane monomers (adapted from [34])

Once these polymers have been synthesized, they can then be cross-linked and shaped according to the PDCs process as described in Figure 1-5. The initial precursor must have properties compatible with the selected shaping technique but it can be chemically modified in order to fit with the specificity of some methods. Those details will be discussed in the next part.

1.1.2.1.2 Shaping

When the preceramic precursor is polymeric, almost all plastic shaping techniques are compatible. The literature reports the use of various conventional techniques in the PDCs process: tape casting [44][45], coating [46], fibers[47][48], casting [51][52], warm isostatic [53][54] and uniaxial pressing [55][56], injection molding [57][58] and recently 3D printing [41][49][50]. One of the advantage of the PDCs route versus traditional ceramic elaboration process lies in the possibilities of machining before the ceramization while avoiding problems of tool wear, brittle fractures, and “handle with care” precautions. The finishing

steps are therefore less critical in the PDCs process. Figure 1-8 gives a non-exhaustive list of examples of PDCs compatible shaping techniques.

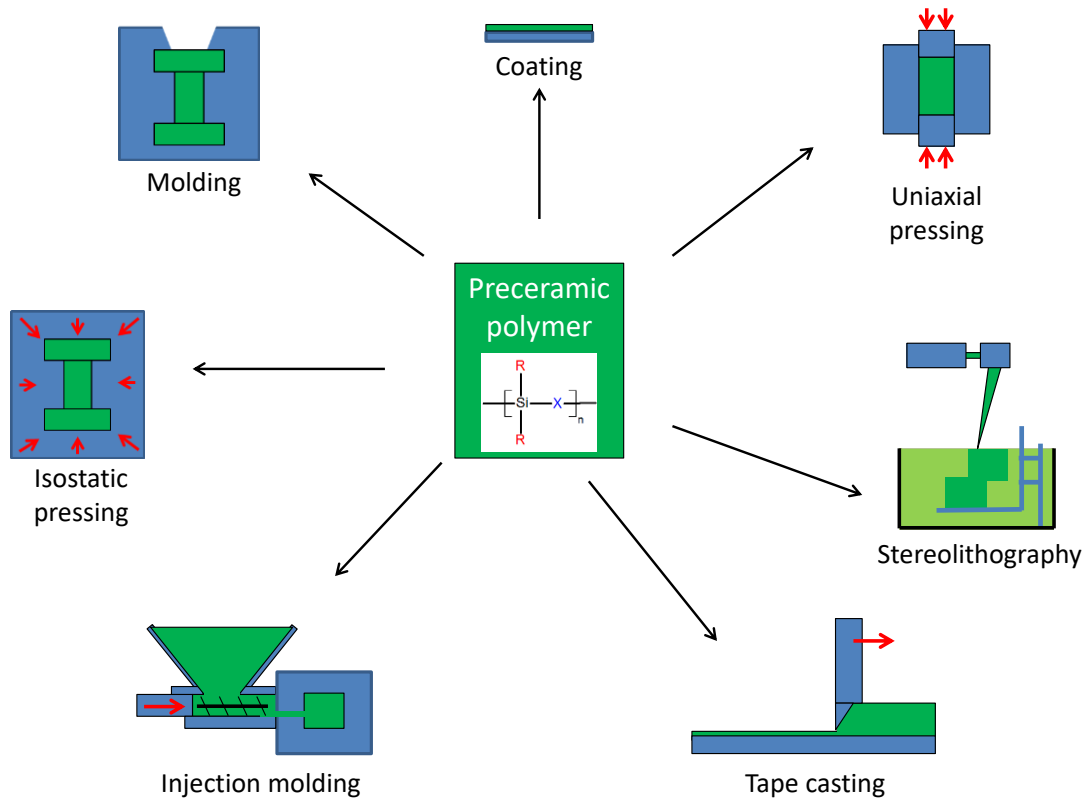


Figure 1-8: Examples of shaping techniques compatible with the PDCs route.

The viscosity, the solubility, the photosensitivity, the fusibility and many other properties concerned by the shaping processes are adjustable by chemical modification of the preceramic polymer. For example, Sneddon *et al.*[59] successfully modified polyborazylene (BN precursor) with dialkylamine to shift its crosslinking temperature to higher values and gives hot-melt properties to the polymer. Modified polyborazylene were then implemented in a hot-spinning process and conducts to 30 μm diameter BN fibers after pyrolysis. It is possible to enhance photosensitivity of preceramic polymers to make them compatible with photolithographic and stereolithographic processes. Gyak *et al.*[49] work demonstrates how grafting photosensitive methacrylate units on a polyvinylsilazane backbone gives the polymer photocurable properties. 3D SiCN/SiO₂ micro-parts were then manufactured from modified polysilazane *via* micro-stereolithography followed by subsequent thermolysis [60]. According to theses few examples, the great adaptability of the PDCs route makes it

possible to use almost any imaginable shaping technique as long as the preceramic polymer is designed for the concerned technique.

Besides those forming techniques, the “polymer infiltration and pyrolysis (PIP)” (also called impregnation) method particularly fits with PDCs process and is almost considered specific to it [48][61]. It is the fabrication method of choice for ceramic matrix composites [62][63][64]. The liquid preceramic polymer is infiltrated in a porous preform (for example a porous ceramic fiber or a graphene foam) by capillarity, it may be assisted by vacuum or pressure increasing. Infiltrated preform is then pyrolysed and turned into a porous composite. The infiltration and pyrolysis steps can be repeated several times to achieve the desired porosity. Such method offers good control of the matrix composition, allows net shape part manufacturing and reinforces preform thanks to a relatively low temperature treatment. It is nevertheless a time consuming method due to the multiple re-infiltration steps required to try to fill all the porosity of the preform.

1.1.2.1.3 Pyrolysis

The polymer-to-ceramic transformation (illustrated in Figure 1-9) occurs through 3 distinctive stages. A first weight loss at low temperature consisting in the decomposition of small oligomers accompanied by the release of gaseous species (CH_4 , H_2 and other volatile compounds [65]). Then around 300-400 °C the polymer begins to further decompose and to lose most of the hydrogen contained in its structure. The result is an amorphous microstructure forming a network of Si and C interconnected with a small amount of residual hydrogen. By further increasing the annealing temperature, the residual hydrogen ends up being completely evacuated and the microstructure is rearranged in the crystalline phase [34][35][37][38][39][46]. The conversion described above is illustrated in Figure 1-9 by the simple example of polycarbosilane (SiC preceramic polymer) where three keys microstructures are shown:

- The polymeric structure of the initial precursor
- The amorphous structure after polymer thermal decomposition and beginning of dehydrogenation
- The crystalline structure after carbothermal reduction at high temperature

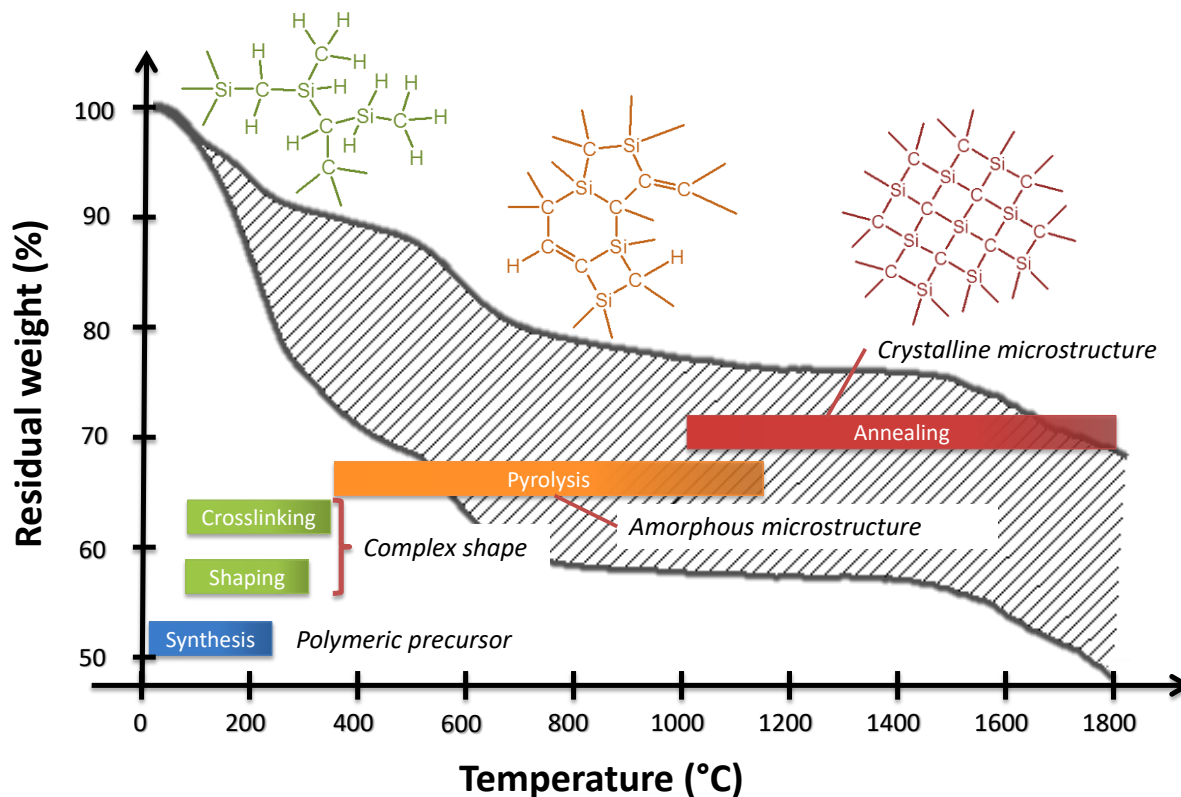


Figure 1-9: Polymer-to-ceramic conversion via thermal treatment under argon (adapted from [37][46]).

Up to now, we delivered the main steps of the PDCs process. In the following part, a more detailed description of SiCN and SiBCN ceramics (systems studied and used in this work) will be carried out.

1.1.2.2 Focus on SiCN and SiBCN systems

Silicon carbonitride is a polysilazane preceramic polymer composed of -Si-N-Si- chains. These nitrogenous silicon chains are often functionalized with ethyl, vinyl, phenyl or simple hydrogen groups. The first work on silazanes dates from the 19th century [66][67] but only resulted in syntheses of cyclic polysilazanes in the 1960s [68][69]. Verbeek's work [22] on the introduction of nitrogen into Si-C systems was decisive. Such polymers are now prepared in industry and commercialized by Merck *via* their durazane line [70].

It was a few decades later that the first attempts to synthesize more complex PDC materials in quaternary systems had their first successes [71]. The idea was to add a fourth element onto the Si-C-N system to improve thermal resistance (introduction of boron) and

resistance to oxidation (introduction of aluminum). The first pre-SiBCN polymer consisted in combining a BN precursor (borazine) with -N-Si-N- chains [72][73][74].

1.1.2.2.1 Preceramic polymer synthesis

The common synthesis method accepted by the literature for polysilazanes was mentioned in Figure 1-7. It consists in ammonolysis or aminolysis described with more details in Figure 1-10.a. and equation (1). The synthesis of such a polymer could be quickly transferred to an industrial scale since it offers many possibilities of variants and a cost 10 times lower than that of polycarbosilanes [71][75][76]. Regarding the synthesis of pre-SiBCN polymer, two major routes can be considered:

- The monomeric route, illustrated in equation (2)-Figure 1-10.b, which consists in introducing boron in the monomer and polymerization by ammonolysis or aminolysis. [71][75]
- The polymeric route, illustrated in equation (3)-Figure 1-10.c, where boron is introduced thanks to reaction between a borated species and a group attached to the polymer backbone (vinyl for example). [71][75]

Obviously, going from a ternary system to a quaternary system influences the final microstructure and therefore the properties of the ceramic. The next section is devoted to the specificity of the SiCN and SiBCN microstructure derived from polysilazane and boron modified polysilazane, respectively.

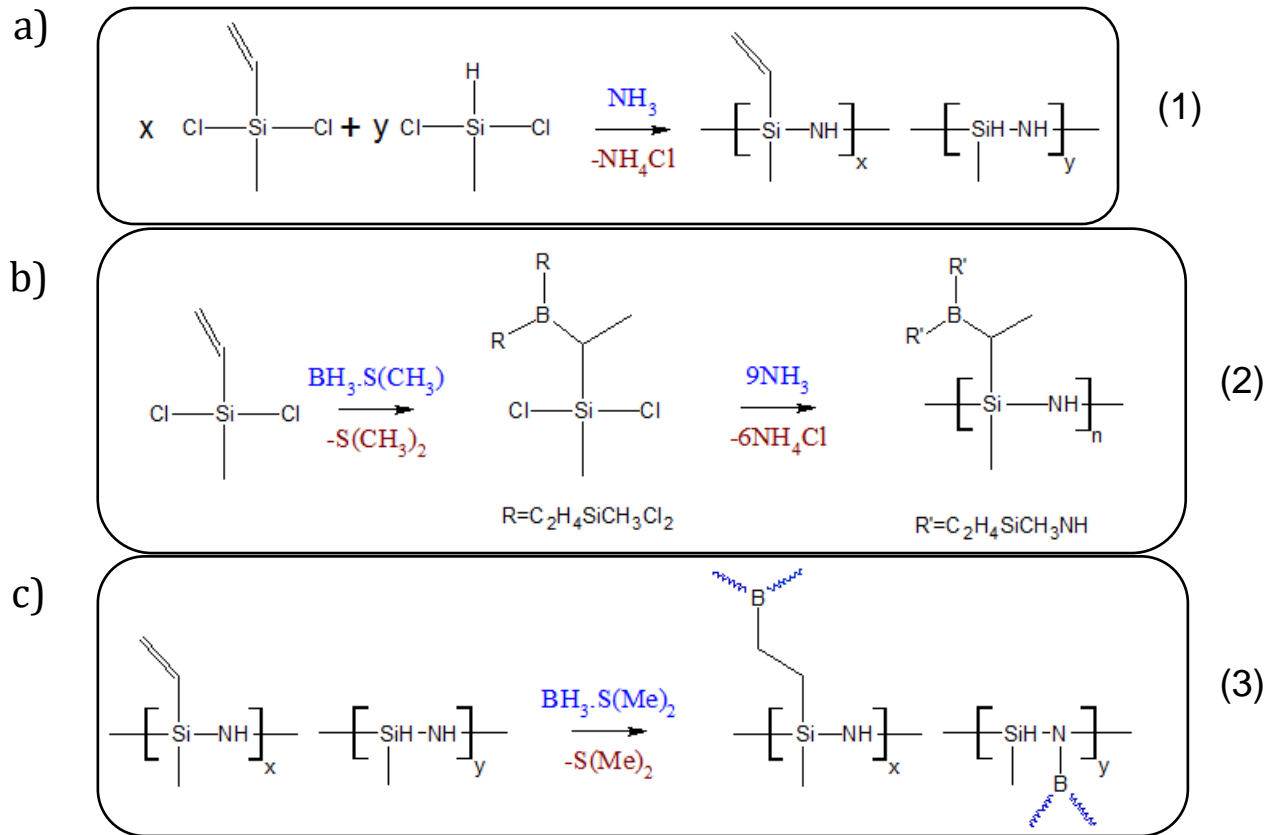


Figure 1-10: Synthesis of (a) polysilazane and polyborosilazane via (b) monomeric route and (c) polymeric route

1.1.2.2.2 Final microstructure

The type of the preceramic polymer used influences the final microstructure of the ceramic prepared by the PDCs route. The microstructure of SiCN consists in an amorphous and interconnected network of nanodomains of SiC, Si₃N₄ and free carbon as illustrated in Figure 1-11.a. [77]. After pyrolysis at 1000 °C, the amorphous SiBCN ceramic is generally composed of four distinct phases: SiC-Si₃N₄-BN and free carbon, but too localized in space to be considered as polycrystalline (Figure 1-11.b.) [78].

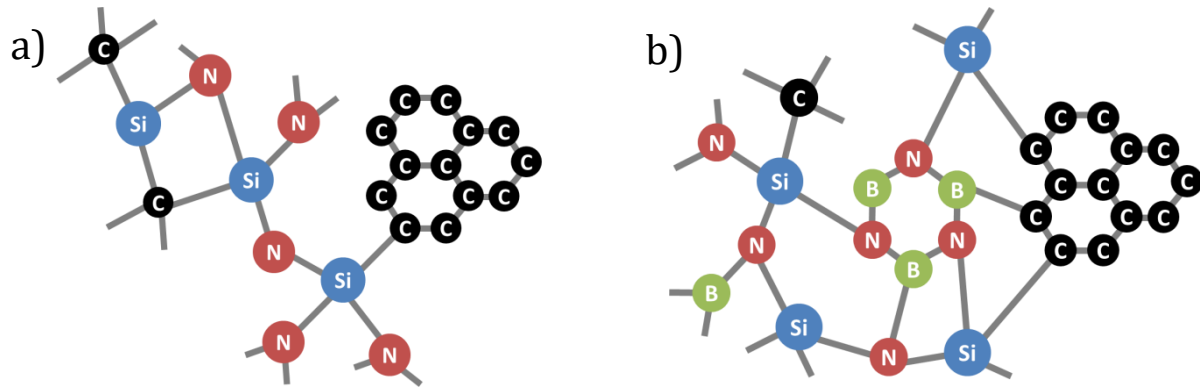


Figure 1-11: Representation of (a) SiCN amorphous microstructure derived from polysilazane [77] and (b) SiBCN amorphous microstructure derived from poly(boro)silazane [78].

By increasing the temperature, the segregation of the $\text{SiC}_x\text{N}_{4-x}$ phases takes place to form $\text{SiC}/\text{Si}_3\text{N}_4$. Aldinger's work [79] has enabled us to understand the evolution of these different phases and their roles in the thermal properties of materials. According to their studies, the microstructure can rearrange into nanograins of Si_3N_4 and SiC separated by a turbostratic $\text{BN}(\text{C})$ boundary (see Figure 1-12.a.). This re-arrangement at high temperature of microstructure is very likely the reason of the very high thermal stability of SiBCN [80]. The turbostratic $\text{BN}(\text{C})$ barrier limits nitrogen diffusion between the nanodomains. By keeping the nitrogen trapped in the Si_3N_4 grains, the partial pressure of N_2 in them tends to increase. The degradation reaction of Si_3N_4 into SiC will then take place at a higher temperature if the pressure of N_2 increases as it is suggested by the diagram in Figure 1-12.b. [79][81]. In addition, in this microstructure configuration, the free carbon is connected to BN and is therefore less reactive since it is located at the grain boundary [79][81]. The structural phenomena that occur in high temperature SiBCN ceramics are still poorly understood and not fully elucidated. The quantity of boron introduced and the nature of the initial polymer plays a decisive role in the stability of the phases involved and can promote the formation of certain bonds and structural units leading to particular properties. Mastering the synthesis therefore seems to be a decisive step in optimizing the thermal performance of SiBCN materials.

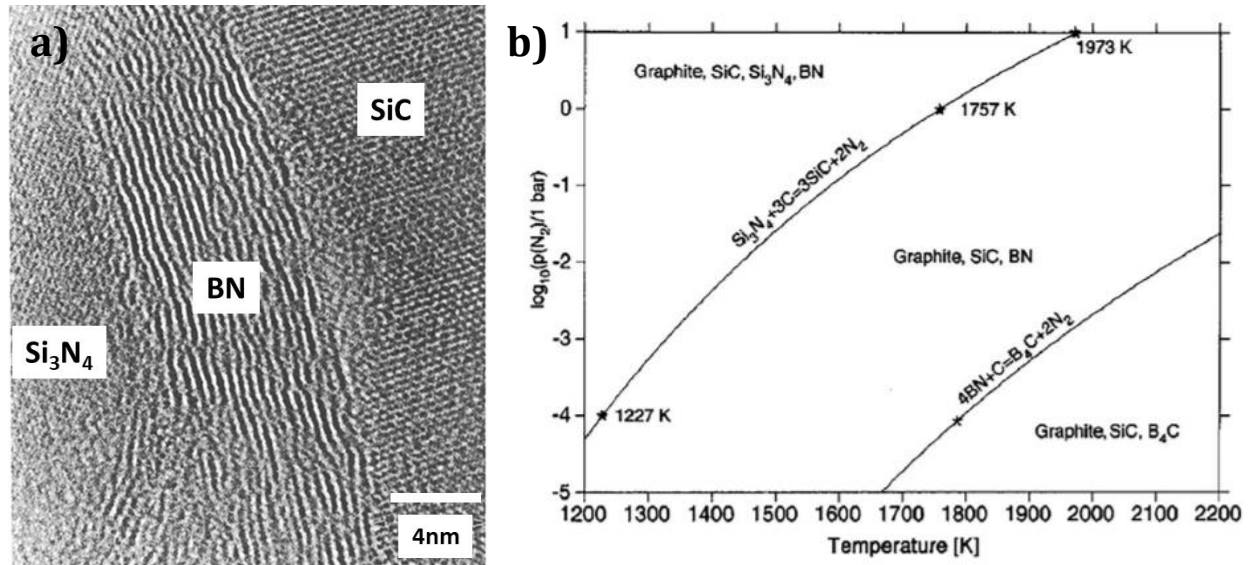


Figure 1-12: (a) TEM pictures of SiBCN (Aldinger work's) and (b) silicon nitride/carbon phase evolution with temperature and nitrogen pressure [79][81]

In the case of SiCN, the amorphous phase is generally preserved up to 1400-1450°C. For higher annealing temperature, the material is changed in a polycrystalline Si₃N₄/SiC micro/nano-composite[35]. SiCN decomposition is generally associated with the high temperature carboreduction reaction between silicon nitride nanodomains and free carbon $Si_3N_4 + 3C \rightarrow 3SiC + 2N_2$ which takes place between 1400 and 1500°C under inert atmosphere depending on the chemistry of the initial preceramic polymer. As an element of comparison, pure crystalline Si₃N₄ decomposes at 1400°C. Due to the specific microstructure described above, SiBCN ceramics can resist to temperatures up to 2000°C [80] before decomposition. Crystallization temperature of SiBCN is also pushed back to >1600°C for high boron contents. SiCN and SiBCN materials exhibit also state-of-the-art oxidation resistance similar to CVD silicon nitride and silicon carbide thin films. As suggested by Butchereit work's [82][83] SiBCN materials can resist to oxidation up to 1500°C. The oxygen based SiOC PDCs exhibit lower resistance to high temperature with decomposition under argon reaching 1350°C and crystallization occurring at 1300°C [84][85][34]. Moreover, the creep resistance of Si(B)CN reaches 1550°C versus 1300°C for SiOC ceramics.

According to the discussion developed in this section, the introduction of a third or a fourth element is a profitable strategy to obtain a significant improvement in the intrinsic

properties of the ceramic. Unfortunately, this is sometimes not sufficient to overcome some inherent difficulties related to the PDCs process itself. Therefore, solutions based on the use of additives called “fillers” were developed as we will try to present in the following part.

1.1.2.3 Filler strategy

As previously mentioned, one of the main weakness in the PDCs process lies in the large shrinkage occurring during cross-linking and pyrolysis. Strong deformation, poor dimension resolution, cracking and micro-cracking are difficulties generated by this approach. The filler strategy, widely documented between the end of the 90s and the beginning of the 2000s by Greil *et al.* [37][38][39] consists in mixing the polymer with powdery additives. The material shrinkage fraction is decreased according to the filler volume effect. Two main categories of fillers are commonly used to reduce the shrinkage:

- Inert fillers consist in decreasing the shrinkage of the green-body when the polymer matrix is filled with inert additives
- Actives fillers play the same role of inert fillers but involve in addition chemical reaction leading to formation of expansive phase compensating the shrinkage of the polymer. The *in-situ* phase formation comes from reaction with the pyrolysis atmosphere or the gaseous species released during the polymer decomposition.

1.1.2.3.1 Towards a near-net-shape strategy

Fillers of various nature (polymeric, metallic, ceramic) and shape/dimension (nano- or microsized powders, platelets, nanotubes, nanofibers, chopped, or long fibers) can be added to a preceramic polymer before shaping. Fillers can serve multiple purposes and have several effects. Figure 1-13 sums up the effects of inert, actives and sacrificial fillers on the final PDC part. First of all, inert fillers which do not react at all, at any stage, with the preceramic polymer, conducts to composites made of fillers occlusions dispersed in the PDC matrix. For examples, SiO₂, Al₂O₃, SiC, Si₃N₄ and others are sometimes used as inert fillers but with this strategy the shrinkage or the formation of porosity are never totally recovered. In this case, they mainly serve the purpose of reducing the shrinkage of the component upon ceramization and eliminate the presence of macrodefects (cracks or large pores), by providing means of escape for the gases generated during pyrolysis.

The active fillers, mainly metallic or intermetallic powder, can react with the gaseous products generated from polymer-to-ceramic conversion or with the heating gas. They generally lead to carbide, nitride or silicide expansive phase formation that compensates the shrinkage. This approach of using volume-expanding fillers in PDCs is called active-filler-controlled pyrolysis (AFCOP). Considering changes in mass and volume of preceramic polymer and filler, it is possible to estimate the filler loading leading to dense PDCs with zero shrinkage during ceramization process. By carefully choosing the active filler loading, the polymer and filler nature, the pyrolysis temperature and atmosphere, it is possible to establish a near-net-shape strategy documented in Greil *et al.* works [37][38][39]. The most common active fillers are materials based on Si, Al, and B, transition metals from groups 4 to 6 of the periodic table and their respective silicides and borides. For example, CrSi_2 , MoSi_2 , TiSi_2 , ZrSi_2 , Ti, W, V and others are known active fillers but their efficiency depends on their compatibility with the selected preceramic polymer and pyrolysis atmosphere. For example, the combination of Ti powder and polysilsesquioxane in an AFCOP treatment can lead to SiOC/TiC or SiOC/TiN composites according to the pyrolysis atmosphere selected. [86]

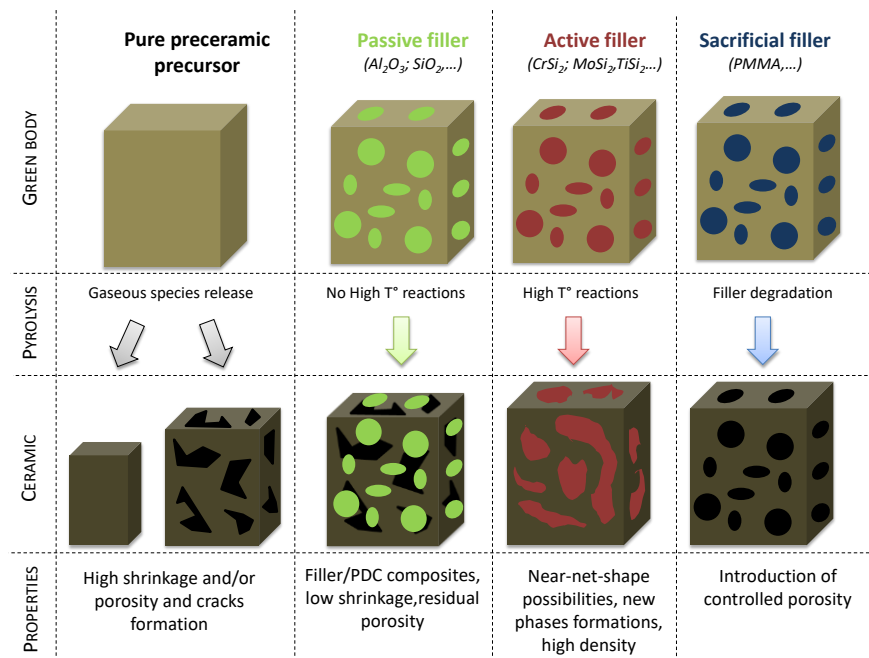


Figure 1-13: Description of the filler types and their influence on the final microstructure (adapted from [46])

Other kinds of fillers can be used to conduct to other specific ceramics like meltable or sacrificial fillers [46]. Meltable fillers mainly consist in glass powder which soften or melt during the thermal treatment in order to seal porosity and densify the final ceramic. The obtained solid is then very resistant to corrosion and oxidation. Hydride fillers with meltable and active properties can also be used to avoid strong deformation. On the other hand, the sacrificial fillers, besides reducing shrinkage, aim to generate porosity within the material. They can be organic compounds (i.e. Polystyrene [87] or PMMA [88] microspheres) or inorganic (i.e. SiO₂ [87][89]) mixed with preceramic polymers, shaped, cross-linked and finally removed *via* thermal decomposition or chemical dissolution. The porosity shape, size and volume are directly linked with the nature of the sacrificial filler used.

1.1.2.3.2 Towards functionalization

In addition to their utilization in the PDCs process, the fillers are often used to functionalize the final ceramic. By introducing new phases in the PDCs matrix thanks to passive or active filler, the properties of the composite will be dependent on the filler nature and quantity.

For example, in the case of passive fillers, by introducing TiO₂ fillers in SiOC matrix for coating applications, Tavares *et al.* [90] were able to obtain activation of photocatalytic properties of the treated surface. Another possible functionalization of coating properties were performed by Barroso *et al.* [91][92]. They used high loads of yttria-stabilized zirconia and a polysilazane as ceramic binder to obtain low thermal conductivity and high coefficient of thermal expansion coatings, characteristic properties of the selected filler. The thermo-mechanical properties of coatings or bulk parts are also adjustable thanks to the filler strategy, for example: by using glassy fillers, meltability behavior is added to the composite; by introducing porosity thanks to sacrificial fillers, effective material stiffness and Young's modulus can be reduced.

The improvement of electronic conduction of PDC based materials were also explored with the filler strategy. In 2001, Greil's *et al* [93] works on Mo-Si-O-C composites prepared from polysiloxane/MoSi₂ mixing showed a resistance below 10⁻³ Ω.cm which explores interesting electronic properties of such composites. More recent works related to SiOC/Ti composites

for *in-vitro* pacemaker electrodes applications reports conductivity close to 10 S.cm⁻¹ and cytocompatibility [94].

The filler strategy is a key solution for resolving processability problems in PDCs route (shrinkage, crack formation) and adjust properties of the final ceramic based composites.

1.1.2.3.3 Limits

For any type of filler, achieving a good dispersion of the filler particles in the suspension is very important to insure a uniform distribution of the fillers in the final ceramic part, improving strength and surface quality. The particle agglomeration in the suspensions is also a barrier to perform an adequate shaping, especially in the case of coating preparation. To achieve a good dispersion the use of suitable dispersing agents and/or adequate methods for dispersion, such as ultra-sonication, ball-milling and mechanical stirring, is generally inevitable [46]. The homogeneous dispersion must nevertheless be carried out in accordance with the cross-linkable nature of the preceramic polymers. Highly energetic methods, such as ultra-sonication and ball milling, may cause a premature cross-linking of the polymers. The safest method in some cases is to first disperse the particles in a solvent and then add the preceramic polymer. The particle size must be taken into consideration as it has an important effect on dispersion. Most of the time the fillers used have very small sizes (5 μm to 30 nm) in order to allow the manufacture of micro-objects (one of the advantages of the PDCs process), which makes dispersion even more challenging due to tendency of fine particles to agglomerate.

1.1.3 PDCs applications for energy

Since the 1970s, the risks linked to the environmental and energy crisis are known, it is therefore urgent to start the energy transition towards a more renewable and clean model. Replacing fossil fuels with low-carbon or even carbon-free energies such as wind or solar power involves energy storage solutions given the discontinuous operation of renewable energies. PDC materials have their role to play in this field and particularly in the hydrogen and battery sector. Those applications and the works already published in those fields will be discussed in the following sections.

1.1.3.1 Hydrogen storage and generation

The fuel cell technology for electricity generation from dihydrogen molecules is a key field for a carbon-free energy sector. The proton exchange membrane fuel cells (PEMFC) are particularly attractive for transports and mobility applications because of their ability to work at relatively low temperature (60 to 90°C) [95][96]. PEMFC are divided in 3 components: a fuel-cell stack, a hydrogen generator and a hybrid power management system. One of the challenges to overcome in order to move to a more widespread use is to control the hydrogen release powering the fuel cell. Boron and nitrogen based materials are a potential hydrogen carrier for such applications and are widely studied since early 2000s [97]. Those materials can store and release hydrogen “on demand”, their stability is optimal on long periods of storage, they are non-flammable, non-toxic and their density in hydrogen elements is very high.

Polymer-Derived Ceramics containing nitrogen and/or boron elements have a potential role to play in two distinct ways :

- BN PDCs can be used as catalysts supports for hydrogen released from sodium borohydride (NaBH_4) during its hydrolysis, alkaline solution of NaBH_4 being used as liquid phase hydrogen carriers.
- Amminoborane (AB) is also a hydrogen carrier able to release pure hydrogen *via* thermolysis. AB can be stored in a porous/aerogel made of PDC materials and releasing dihydrogen at moderate temperatures and with a lower emission of by products such as ammonia or borazine.

The interest of PDCs for the first pathways lies in their high chemical and thermal resistance. The NaBH_4 hydrolysis (4) occurs in severe conditions because of the strong exothermal nature of the reaction and the releasing of sodium borate which is a strong base.



The use of Si_3N_4 and SiAlCN ceramic materials derived from preceramic polymers and elaborated with ordered mesoporosity as a Pt catalyst support [98][99] allowed the stable generation of hydrogen for 2h at 80°C (hydrogen generation rate of 13.54 and 5.67 L.min⁻¹

$1.\text{g}_{\text{Pt}}^{-1}$ for Si_3N_4 and SiAlCN , respectively [99]) . The performances of such catalyst supports were directly linked to its high surface area and porosity volumes, parameters easily tunable thanks to the PDCs process.

Concerning the second pathway, the most effective strategy, developed in Gutowska works [100][101], is the nanoconfinement of AB in mesoporous materials structured in nanoscaffolds. Numerous materials has been reported for this application [102][103][104][105][106][107] such as MOF, zeolites, silica hollowspheres and nanotubes. Nevertheless, carboneous or oxide nano-scaffolds are usually unstable when filled with amminoborane at room temperature. Boron nitride (BN) materials, which can be produced and nanostructured *via* the PDCs route [108][112][113][114][115] has been used to confine amminoborane. BN shaped as nanopolyherons with hollow cores and mesoporous shells were able to liberate pure H_2 between 40 and 80°C, the only by-products detected (i.e. NH_3) is formed at temperature $> 80^\circ\text{C}$. Considering the effective regenerability of AB, the composite material represents a safe and practical hydrogen storage material which opens the way to a very broad set of non-oxide materials including ceramics and nanocomposites using single-source molecules.

1.1.3.2 *Battery electrodes*

According to Singh's team work on batteries, [43] silicon based PDCs have great potential as battery electrodes, especially in the case of LiB (Lithium-ion battery) technology. LiB cells consist in a system using dissimilarity of electrodes materials undergoing oxidation-reduction reactions. The energy storage is possible thanks to its ability to accept and release Li^+ ions in its microstructure over several charge and discharge cycles. In theory, silicon-based nanostructures have capacity exceeding 4000 mAhg^{-1} , an order of magnitude higher than commercial graphite anodes. Such materials are therefore very studied for this type of application but are in practice subject to large volume expansion ($> 400\%$). It can lead to the total destruction of the electrode making them incompatible with large-scale marketing [43].

The recognized thermodynamic and chemical stability of PDC materials make them viable candidates for anode LiB applications. Their high mechanical strength, tunable porosity and

electronic properties are other assets which conduct to a great interest of the scientific community in this new generation of ceramics.

Experimental studies have shown that PDC based materials are able to reversibly store lithium between 0 and 3 V with coulombic efficiency over from 99%, capacity around 900 mAhg⁻¹, great processing flexibility and a thermodynamically stable amorphous microstructure [43][109][110][111]. Strong progresses must be done to reduce their first cycle loss and voltage hysteresis in order to make PDCs innovative electrodes for LiB cells. According to literature [43], those problems are solvable by altering initial polymer chemistry (and thus final materials) structure, increasing surface area and improving electronic conductivity in the material.

Thanks to the amorphous structure made of free carbon and O-Si-C bonds in tetrahedral structure, SiOC ceramics are the most promising PDC candidates for anode electrodes in LiB cells [116]. Current approaches to enhance performances of this material consist in introducing porosity (for example through aerogels structures) and in introducing conductive fillers to overcome the insulating nature of the ceramics.

1.1.3.3 Hydrogen production via electrocatalysis

PDC materials have been widely used as catalyst supports associated with all kind of reactions [117][118][119][120]. More recently, a few studies on their potential applications in electrocatalysis for water splitting have been published. For example, Feng works on Mo_{3+2x}Si₃C_{0.6}/SiC/C [121][122] and W₂C/SiC [123] as nanocomposite cathodes with catalytic activities for water splitting has shown the potential of PDCs in this field and to our knowledge that was the only work investigating SiC PDCs for HER. One of the main goal of this thesis is to evaluate the performances of other complex PDC materials and in different conditions in this very new research field. Therefore, an overview on water-splitting catalysis and all the tremendous efforts performed these last decades will be developed and summarized in the next sections.

1.2 Electrocatalysis for dihydrogen production

In the context of the environmental crisis that humanity is experiencing today, the hydrogen vector has many advantages making it an ideal fuel to replace current

hydrocarbons and reduce CO₂ emissions. Its combustion is carbon-free and generates about three times more energy than gasoline at constant weight [124][125]. Hydrogen is one of the most abundant elements on earth in the form of water or hydrocarbon. However, there are still many obstacles to overcome for using hydrogen on a larger scale. One of the important steps to achieve, concerns the carbon-free production of dihydrogen at a lower cost. The H₂ molecule hardly exists naturally on earth apart from a few submarine deposits, but it is very difficult to access. Therefore, it must be generated either from hydrocarbons or from water.

1.2.1 Current dihydrogen production

Figure 1-14 describes the three main production methods currently available for the production of H₂: i) methane steam reforming, ii) coal gasification and iii) water-splitting [127]. Water splitting represents one of the most promising ways since it allows the production of H₂ from water and electricity and does not directly release greenhouse gases. Steam reforming and gasification use methane and coal as raw materials, respectively, and release significant amounts of CO₂. The latter are the most used processes to date, representing 95% of world production versus only 5% for water splitting (figure 2021 (France hydrogène) [126]). Some alternative pathways as photoelectrochemical water-splitting and methane pyrolysis are currently studied for a clean and efficient production of dihydrogen but no industrial solutions are yet proposed for those processes.

The problematic around the production of hydrogen could be well summed up by a statement by Guy Maisonnier in 2021 (economist engineer at IFPEN): *“Today, 95% of hydrogen is produced from hydrocarbons (petroleum, natural gas and coal), which is the cheapest solution. However, this process is, except for methane pyrolysis, emitter of CO₂, greenhouse gas. To produce low-carbon hydrogen, three options are therefore available to manufacturers: capture the CO₂ emitted during production by transformation of fossil fuels, then transport it to store it geologically, pyrolyze methane and separate the carbon in solid form and finally, to produce it via the electrolysis of water, the electrolysis being operated from low carbon electricity supplied by nuclear, wind or solar energy. The stake remains for this last option, however, the cost of this mode of production, more expensive to date than that*

of reforming natural gas, even taking into account the additional cost associated with CO₂ capture." [125]

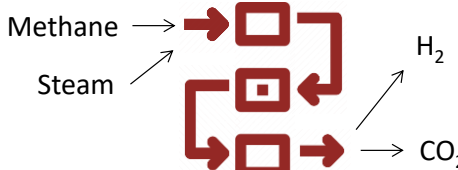
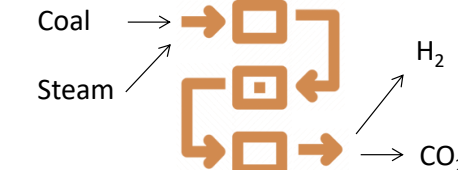
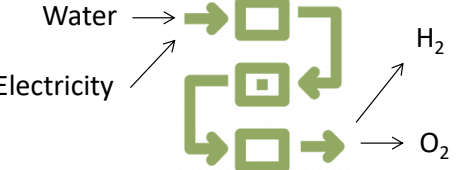
TECHNOLOGY	PROCESS	REACTION_INVOLVED
Steam methane reforming (SMR)		$\text{CH}_4 + 2\text{H}_2\text{O} \rightarrow 4\text{H}_2 + \text{CO}_2$
Coal gasification (GC)		$\text{C} + 2\text{H}_2\text{O} \rightarrow 2\text{H}_2 + \text{CO}_2$
Water splitting (WS)		$2\text{H}_2\text{O} \rightarrow 2\text{H}_2 + \text{O}_2$

Figure 1-14: Current process for dihydrogen production (adapted from[127])

The following sections will be devoted to a detailed description of the processes presented above with an in-depth discussion on water-splitting since it represents one of the most promising process for the production of a decarbonized H₂ and it is the main application behind our work

1.2.1.1 Steam Methane Reforming (SMR)

Steam methane reforming is a mature industrial process to harvest H₂ from a methane source (e.g., natural gas) under high-temperature steam (700–1000 °C) with a pressure range of 3–25 bar [128]. Figure 1-15 presents the configuration and a picture of an active plant for H₂ production *via* SMR [131][129]. Besides H₂, carbon monoxide (CO), and a relatively small amount of carbon dioxide (CO₂) are also obtained from SMR, which was developed to manufacture syngas (H₂ and CO) traditionally. When coupled with a water–gas shift (WGS) reaction, the co-product CO from SMR could further react with steam to result in one extra H₂ and CO₂ as final products [130].

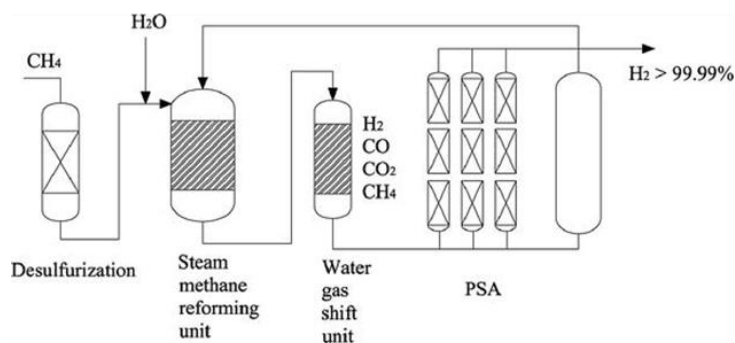


Figure 1-15: Steam methane reforming plant [131][129]

SMR still suffers from several disadvantages caused by the reactant properties and reaction thermodynamics: High-energy consumption, high production cost, harsh reaction conditions, low reaction efficiency, and low process stability [128]. Specifically the disadvantages are mainly reflected in three aspects: Firstly, methane is very stable, and thus hard to activate. Due to the highly endothermic nature ($\Delta H^\circ = 206 \text{ kJ/mol}$), SMR requires extra energy and designed instruments to proceed the reaction at high temperature and pressure, which also introduces mass transfer and heat transfer issues. Secondly, the design of catalysts still needs improvement. On one hand, noble metal catalysts (e.g., Ru, Rh) display high SMR activities with good stability. However, the cost and availability of noble metals limit their application [128]. Thirdly, SMR coproduces CO_2 , especially when coupled with a WGS for H_2 production (9–14 kg CO_2/kgH_2). The CO_2 has a strong greenhouse effect and its handling further increases the cost of the SMR process.

1.2.1.2 Coal Gasification (CG)

The coal gasification process produces syngas (a mixture of CO, H_2 , and other constituents), which can be used for the generation of electricity or for the production of liquid hydrocarbon fuels, natural gas surrogates, and valuable chemical products as dihydrogen. Although CO_2 is also generated during the process, advanced coal gasification methods include solutions for carbon capture with lower costs than in conventional coal-fired power plants. It is expected that carbon sequestration will become a commercial technology, mandatory in newly constructed power plants.

Meanwhile, there is an alternative method, denoted underground coal gasification (UCG) [132], in which injection and production wells are drilled from the surface and linked together in a coal seam (see description in Figure 1-16). Once the wells are linked, air or oxygen is injected, and the coal is ignited in a controlled way. Water present in the coal seam or in the surrounding rocks flows into the cavity formed by the combustion and is used in the gasification process. The produced gases (primarily H_2 , CO , CH_4 , and CO_2) flow to the Earth's surface through one or more production wells. The UCG process has several advantages over surface coal gasification, especially the possibility to use cavities formed as a result of the process for CO_2 sequestration. Nevertheless, CO_2 sequestration is still under study and does not present the entire guarantee for a fast utilization in big industries.

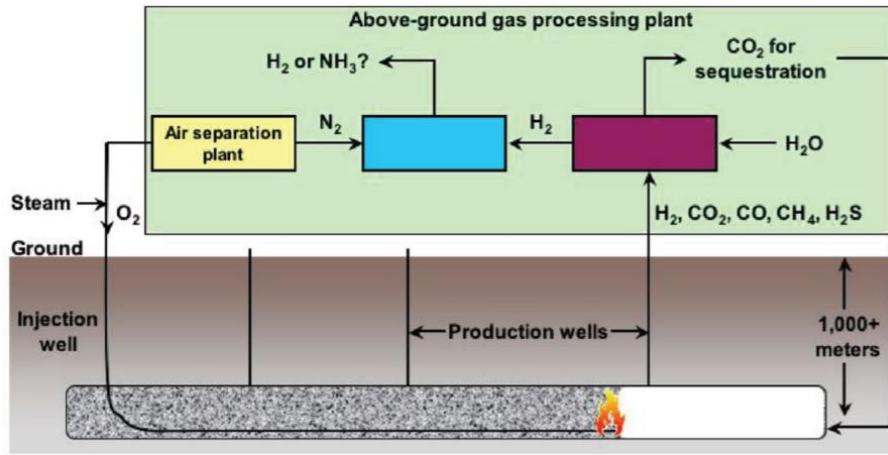
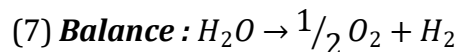
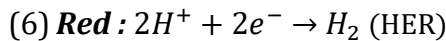
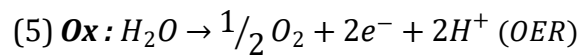


Figure 1-16: Underground coal gasification principle [132].

1.2.1.3 Water splitting principle

As discussed above, the water splitting process involves converting water and electricity into hydrogen. If the electricity is carbon-free, we obtain clean hydrogen without the use of fossil gas. The operating principle of such a process is described in Figure 1-17. The device is composed of an anode and a cathode being the site of the oxidation and reduction reactions, respectively, as described below:



HER stands for hydrogen evolution reaction, it corresponds to the reaction happening at the cathode and conducting to H_2 production. OER stands for oxygen evolution reaction, it is associated with water oxidation happening at the anode.

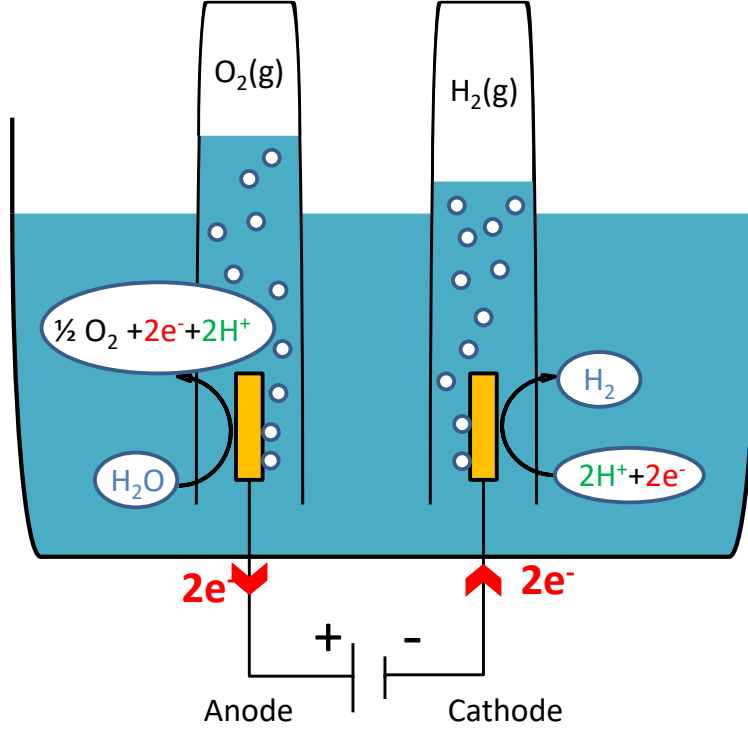


Figure 1-17: Schematic description of an electrochemical water-splitting system.

Based on standard state thermodynamic data, for equation (7) we have:

$$\Delta_r H^\circ = 285,8 \text{ kJ/mol} ; \Delta_r S^\circ = 163 \text{ kJ/mol} ; \Delta_r G^\circ = 237,2 \text{ kJ/mol}$$

Thermodynamic considerations make it possible to notice that the dissociation of water requires an external energy corresponding to the enthalpy of dissociation of water $\Delta_r H^\circ = 286 \text{ kJ/mol}$. Moreover, since $\Delta_r G^\circ > 0$ the reaction is not spontaneous, this is why electrolysis and the supply of energy *via* electricity are necessary. This dissociation requires an electrical energy $\Delta_r G$ and a thermal energy $T\Delta_r S$. We therefore have:

$$\Delta_r H = \Delta_r G + T\Delta_r S \quad (8)$$

The thermodynamic voltage and the thermoneutral voltage can be calculated respectively from $\Delta_r G$ and $\Delta_r H$. The thermodynamic voltage only takes into account the electrical

energy to be supplied while the thermoneutral voltage takes into account the totality of the energy necessary [133]. Under standard conditions:

$$E^{\circ}_{Thermodynamic} = \frac{\Delta_r G^{\circ}}{2F} \approx 1.23V \quad (9)$$

$$E^{\circ}_{Thermoneutral} = \frac{\Delta_r H^{\circ}}{2F} \approx 1.48V \quad (10)$$

In fact, the voltage to be applied is higher than the thermodynamic potential value to achieve electrochemical water splitting. The excess potential (also known as overpotential, η) is mainly used to overcome the intrinsic activation barriers present on both anode (η_a) and cathode (η_c), as well as some other resistances (η_{other}), such as solution resistance and contact resistance. Thus, the practical operational voltage (E_{op}) for water splitting can be described as [127]:

$$E_{op} = 1.23 + \eta_a + \eta_c + \eta_{other} \quad (11)$$

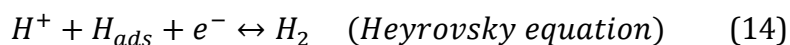
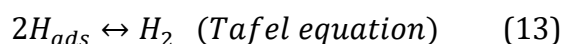
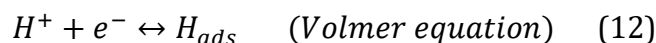
For industrial cells, the usual voltage values are of the order of 1.6 to 2.1V, i.e. electrolysis efficiency between 59 and 77%. For large-scale electrolyzers the power consumption is generally in the order of 4 to 6 kWh/Nm³ instead of 2.94 kWh/Nm³ in theory. The water-splitting process therefore has a cost closely related to that of electricity, which is generally more expensive when produced from wind or solar technology than from fossil fuel or nuclear resources. With the price of gas in 2014 being well below that of electricity, water splitting is currently a more expensive producing method than VRM or CG. [134]

1.2.2 Importance of electrocatalysts

As implied in the previous section, the keys of cost reduction of water-splitting lay in either reduction of electricity cost and/or the reduction of electricity consumption of electrolyzers. Thanks to efficient electrocatalysts for HER and OER it is possible to decrease η_a and η_c overpotentials and then enhance electrolyzers yields, those catalysts are called HEC and OEC for HER and OER catalysis, respectively. The elaboration of efficient and low-cost electrocatalysts is an important research field either for HER or for OER. Nevertheless, in this work, the studies were focused on HEC.

1.2.2.1 Hydrogen Evolution Reaction (HER) principle

The mechanism of electrocatalysis associated to HER are divided in two steps: First protons are adsorbed at the catalyst surface and then the formation of dihydrogen takes place *via* recombination of the adsorbed protons. The key of an efficient catalysis lies in the electronic and thermodynamics interaction between the protons in solution and the catalysts surface. According to the Sabatier principle [135][136], the heterogeneous catalysis is optimal when the adsorption of reactive species is “just right”, if the interaction is too weak the binding between reactive and catalyst will fail, if it's too strong the product won't dissociate from the surface. In the case of the HER mechanism the adsorption corresponds to the Volmer step illustrated by equation (12) below. The dissociation leading to H₂ release happens according to two different pathways, either by combination of two adsorbed protons (see Tafel equation (13)) or by combination of an adsorbed proton and a proton in solution (see Heyrovsky equation (14)) [137].



In thermodynamic language, the optimum of Sabatier principle is translatable as a standard Gibbs free energy of proton adsorption $\Delta G^\circ(H_{ads})$ close to zero. The volcano plot (see Figure 1-18) is a visual illustration of the Sabatier principle, it represents the overpotential against $\Delta G^\circ(H_{ads})$ associated to the electrocatalyst [137]. The best catalysts are found at the top of the volcano plot, on the left of the curve, the proton adsorption is too high and it is too low on the right.

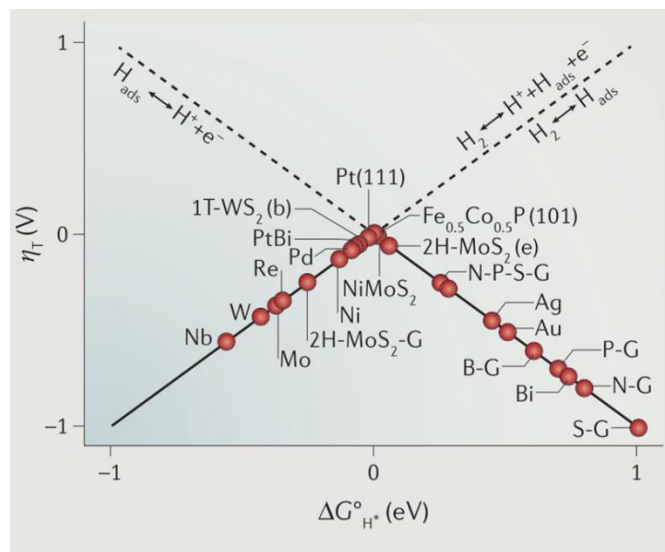


Figure 1-18: Volcano plot-Sabatier principle associated with different efficient catalysts for HER [137]

Data of the different catalysts presented in the volcano plot show the great efficiency of Platinum towards HER catalysis [139]. TMDs such as MoS_2 and WS_2 are also well placed [140] and represent a potential low-cost alternative to expensive noble metal such as Pt. Finally, the recent breakthroughs on low dimensional materials such as doped graphene are also reported (B-G, P-G, N-G, and S-G) [137]. Mainly made of carbon, their cost is potentially compatible with widespread utilization but their performance is still below Pt. The next sections are dedicated to the specificities of the different electrocatalysts mentioned above.

1.2.2.2 Practices for reporting electrocatalytic performances

The conventional procedure for evaluating performances of electrocatalysts is based on the usage of three-electrode set-up and cyclic voltammetry as described in Figure 1-19. It consists in three electrodes named working electrode (WE), reference electrode (REF) and counter electrode (CE) immersed in an electrolyte (Figure 1-19.a.). A potential V is applied between the WE and REF and tends to bring required electrical energy for Red-Ox reactions to take place which leads to an electron circulation. The electron circulation results in the measurement of an electric current i between WE and CE thanks to a potentiostat. For an efficient electrocatalyst deposited on WE, Red-Ox reactions will start at low potential leading to an increasing absolute value of i . Polarization curves are obtained by plotting i against V , we can extract the overpotential η_c as shown on Figure 1-19.b [138]. The

reactions mechanisms at the catalyst surface may be identified thanks to Tafel slopes which are obtained by plotting the overpotential against the logarithm of current density.

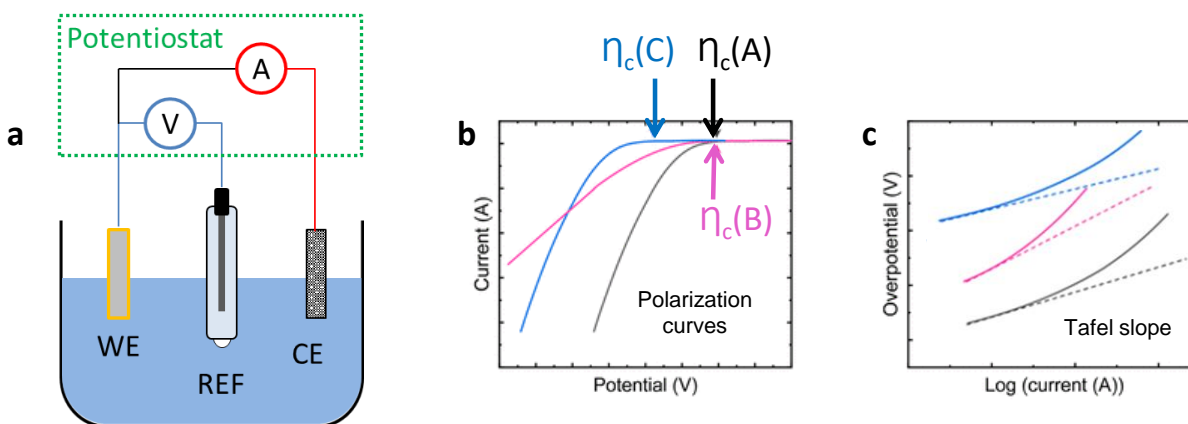


Figure 1-19 : a) three electrodes set up representation; b) Polarization curves; c) Tafel slopes [138].

A crucial parameter when evaluating the electrocatalyst performance is the specific surface area of the working electrode since it is directly proportional to the current measured during electrode sweep. Therefore, a precise estimation of the active surface area (**ECSA**) is important to be able to compare intrinsic performance of the tested material [138]. **ECSA** is measured in non-Faradaic region, i.e. in potential range where no charge transfer reactions occurs (typically, the low values of potential in general). The electrode cycling at different scan rates (ν) conducts to a linear evolution of non-Faradaic current (i) against ν with a slope equal to the electrical double-layer capacitance ($C_{dl} = i/\nu$). Roughness factor is then assessed by normalizing C_{dl} electrode with the double layer capacitance of a flat surface ($ECSA = C_{dl}/C_{dlref}$). To properly compare cyclic voltammetry data with literature we can normalize the current density j by **ECSA** value and obtain $j_{ECSA} = j/ECSA$.

1.2.2.3 Noble metal catalyst-Platinum

A famous category of electrocatalysts is noble metal based materials which today remain the most efficient HER catalysts. Platinum is considered as benchmark electrocatalyst (either for HER or OER) thanks to its very low overpotential (overpotential close to 50mV and Tafel slope $\sim 30\text{mV/dec}$ [139][141]). Its properties are well known since the early 19th century and discoveries of Sir Humphry Davy on the phenomenon of heterogeneous catalysis [142]. Nevertheless, the use of Pt on an industrial scale is hampered because of

the enormous cost caused by its very low abundance in the Earth's crust. Platinum has also stability limitations, as its performance decreases with time due to fouling, leaching or poisoning phenomena [139]. Other noble metal based electrocatalysts exist, for example Ruthenium or Iridium [139], but face the same scarcity and stability problems. Nevertheless, progress was made those last years to limit the magnitude of these two main disadvantages.

Miniaturization of catalysis electrodes has been an efficient way to decrease the amount of metal required for water-splitting while maintaining optimal performance. It has been achieved thanks to:

- Preparation of thin films, nanoparticles, single atoms structures anchored on conductive carbon based matrix
- Elaboration of alloy between costless transition metal and noble metals
- Interface engineering strategies to counteract stability problems

Several steps still need to be considered before an utilization at large scale water splitting even if promising studies are being conducted. Due to the scarcity and prohibitive cost of noble metals, researchers got interested in the development of low cost noble-metal-free electrocatalysts. The whys and wherefores of the noble-metal-free electrocatalysts are presented in the following section.

1.2.2.4 Noble-metal-free catalysts

According to Zou review [127], the preparation of low-cost electrocatalysts is based on the combination of transition metals (Fe, Co, Ni, Cu, Mo and W) with non-metals elements (like B, C, N, P, S and Se). Figure 1-20 gives a non-exhaustive list of efficient electrocatalysts built with this strategy and sorted according to different categories:

- The transition metal dichalcogenides (TMDs) based on the combination of transition metals and sulfur or selenium
- Metal phosphides based on combination of transition metals and phosphorus
- Metal carbides and nitrides based on combination of one or several transition metals with carbon and or nitrogen

- Heteroatom-doped nanocarbons consist in introducing defects in low dimension carbon based materials, generally without HER activity (for example, carbon nanotubes or graphene). Defects are created by introducing heteroatoms in carbon microstructure which acts as active sites for the catalysis
- Photoelectrocatalysts, which consist in a specific water splitting strategy based on using both solar energy and electricity to dissociate the H_2O molecule. The photocatalysis wasn't studied in this work. For more information please refer to the different review articles mentioned in the literature [143][144][145][146].

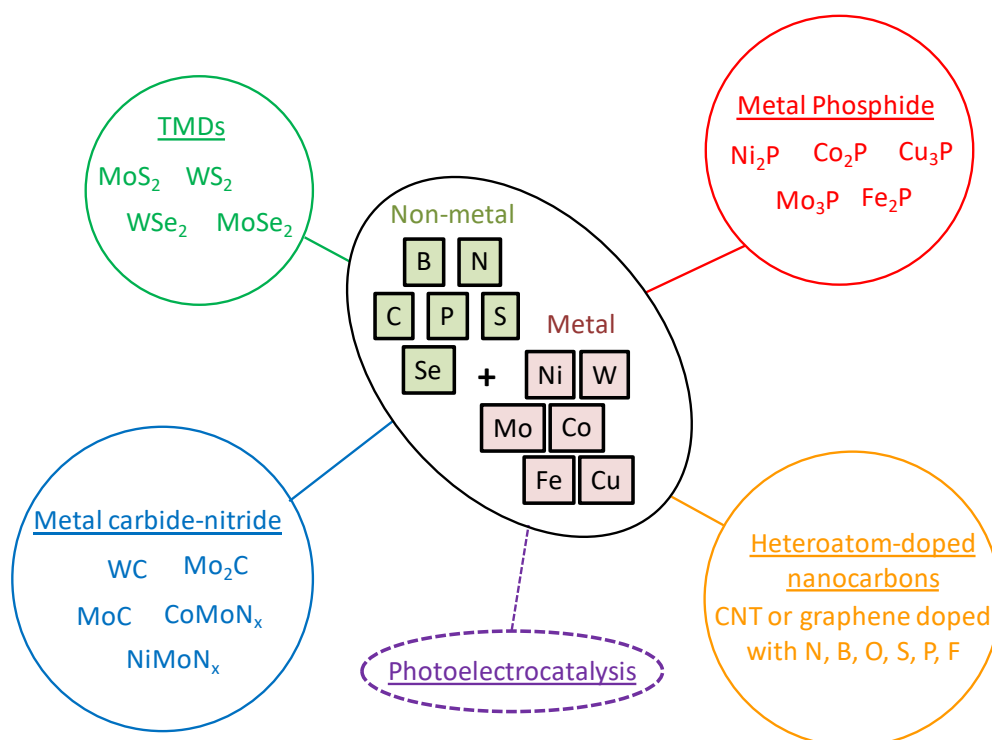


Figure 1-20: Non exhaustive list of noble-metal-free electrocatalysts.

One of the most promising noble-metal-free electrocatalyst is MoS_2 . Thanks to theoretical works of Himmerman *et al.*[147] on Mo-edge structure showing that the free energy of bonding was close to that of Pt, the research on this material as an electrocatalyst for HER was relaunched after their abandonment in 1970s [148]. TMDs exist in several crystalline phase with specific electronic configuration influencing their properties. The trigonal prismatic (2H) and octahedral (1T) are the two common structural phases associated with TMDs materials. In the case of the 2H phase, the stacking order of three atomic plane consists in ABA scheme in which chalcogen atoms occupy the same position in the different

atomic planes. On the other hand, the 1T phase consists in an ABC stacking with non-equivalent A and C planes. Because of its layered structure, the material shows a tendency to form nano-sheet like crystal thanks to exfoliation operation [149]. Bulk MoS₂, is generally crystallized in stable 2H phase but after exfoliation, the material phase transforms to metastable 1T phase. Interestingly, Jin's and Chhowalla's groups demonstrated the better performances of 1T against 2H caused by the higher electronic conductivity and the increase of active sites for 1T, respectively [127][150].

Low dimensions materials include 0D nanoparticles, 1D nanotubes and 2D nanosheets. At such nanometric scale, quantum confinement on the electronic density of state can modify the electronic structure of the material which conducts to considerable difference between bulk and low dimension materials properties. In this perspective, by working with low dimension materials it is, in theory, possible to tune the catalytic properties that are largely determined by the electronic structure. The optimization of catalytic properties is possible thanks to the design of heterostructures either through assembly of low dimension materials units (0D+1D, 0D+2D, 1D+2D and 2D+2D) or through introduction of defects in a low dimension materials nanostructure [137]. For example, the doping of graphene nanosheets with heteroatoms such as N, O, B and/or P can conduct to HER active sites formation. What makes these materials very promising is the possibility of precisely adjust their electronic structures and therefore their properties. We can imagine developing catalyst materials that are both very active but also very selective for the production of H₂. They also represent a very inexpensive alternative to current reference materials. In theory, the overpotential and Tafel slopes associated with these low-dimensional materials are close to ideal values, however, their current density remains below that of platinum and other noble metals. The present trend to improve current density is to increase the density of active sites by enhancing the surface area of the electrode.

1.2.3 Miniaturization of microdevices for HER applications

In the past few years, a growing interest on miniaturized electrolyzers for dihydrogen production has emerged as demonstrated in the review article of Modestino *et al.* published in 2016[151] (and other work [152]). In terms of materials saving and maximization of surface interaction, moving to a micrometric scale is an effective strategy to counter the

limits of electrocatalysis presented in the previous sections. The global interest on going at low-scale by elaborating microdevices is well known since the emergence of the microfluidic discipline. It allows greater control over the flow, increase rate of heat and mass transfer and favors phenomenon dictated by surface interaction. An overview of the advantages of fluid flow in microchannels will be developed in the next sections.

In addition, by using the microfluidic technology specific water splitting problems can be solved. This can be shown by considering a simple electrolyser model: We consider two surfaces of infinite and parallel electrodes separated by a distance d , an electric potential V is applied between the electrodes. An electrolyte flow is applied in the space between the electrodes with a surface flow Q and an uniform electronic conductivity σ , for simplicity this flow is assumed to be Newtonian (parabolic). Because of the tension between the two electrodes, electrochemical reaction takes place at the electrode surface at a rate imposed by the current density j . For a considered chemical transformation (in our case the water splitting), the thermodynamic equilibrium potential is named E° . Finally, if we suppose no mass transport limitations at the electrodes surfaces and we neglect the volume fraction of products in the electrolyte the only factors that depend on d are the ionic and fluidic resistances.

The power losses occurring due to ionic resistance P_{ion} for a reactor length L is given by equation (16) below:

$$P_{ion} = \frac{j^2 d L}{\sigma} \quad (16)$$

The power losses due to fluidic resistances, P_{fluid} depend on the fluid viscosity μ . It is expressed according to equation (17):

$$P_{fluid} = \frac{12\mu Q^2 L}{d^3} \quad (17)$$

On the other hand, the potential energy stored in the considered products $P_{storage}$ is:

$$P_{storage} = j E^\circ \quad (18)$$

The efficiency of such system is:

$$\eta = \frac{P_{storage}}{P_{storage} + P_{ion} + P_{fluid}} \quad (19)$$

The optimal distance d_{opt} conducting to a maximal efficiency of the device is:

$$d_{opt} = \left(\frac{36\mu\sigma Q^2}{j^2} \right)^{1/4} \quad (20)$$

Expressed as a function of the fluid velocity v

$$d_{opt} = \sqrt{36\mu\sigma} \frac{v}{j} \quad (21)$$

For typical aqueous electrolytes, the viscosity and conductivity are in the order of $10^{-3} \text{ Kg.m}^{-1}\text{s}^{-1}$ and 10^{-1} S.m^{-1} , respectively. According to the common fluid velocity employed in microfluidic and the practical current densities in water splitting it can be demonstrated that d_{opt} values are below 500 μm . Such small inter-electrode distances are possible in a miniaturized water splitting device.

In addition to the dimensional optimization demonstrated above, microfluidic device can lead to other specific advantages. Increases in power density due to the low amount of electrolytes can be obtained. In addition, fluidic forces could be used to direct species to the desired device locations with precision, reducing losses due to mixing of reactants or products. The performances enhancement offered by miniaturization of water splitting device has motivated several groups to publish studies on this topic.

In 2013, Modestino group has demonstrated the elaboration of the first microfluidic electrolyser providing 100 mA/cm^2 current density at 2.5 V [153]. They also proposed an improved device in 2015 working under vapor feeds and without membranes leading to 300 mA/cm^2 current density at 2.5 V [154]. Nevertheless, the electrodes employed in these devices were all based on Pt electrodes and until today, no other electrocatalysts has been tested at micrometric scale.

1.3 Microfluidic and MEMS devices *via* soft and photo-lithography

In this section, we will develop the principles and interests of the disciplines of microfluidics and lithography techniques. In a first sub-section (1.3.1), the subtleties and advantages of microfluidics will be mentioned. The techniques employed for the fabrication of those microfluidic systems, namely soft and photolithography, will be described in a second (1.3.2) and a third sub-section (1.3.3). Finally, in the fourth sub-section (1.3.4) a review on the PDC materials shaped through those micropatterning techniques will be presented.

1.3.1 Interest of microfluidics in general

Microfluidics are present in humans and in nature, the circulation of fluids in blood capillaries, in the veins of a tree leaf or the weaving of a spider web are good examples of fluid management on a microscopic scale. Microfluidics are the science of flows at the microscopic scale but it is also a technology that is already found in many applications of everyday life and research (e-reader, inkjet printer, laboratories on chip) [155][156]. Lab-on-a-Chip consists of holding the equivalent of several cutting-edge research devices over a few square centimeters. Why such systems would have interesting properties thanks to their size? One way to answer this question is to look at the laws of scale. Establish a scale law is to say in a very general way how a physical quantity varies according to the size of the system considered. For example for an object of size L , the area varies like the size squared L^2 and its volume varies like the size cubed L^3 , by representing on a graph the size, the area and the cube (see Figure 1-21). For $L > 1$ we have $L < L^2 < L^3$ but for $L < 1$ the order is reversed and we have $L > L^2 > L^3$. In other words, for macroscopic objects, volume phenomena are predominant over surface phenomena but this is reversed at the microscopic scale.

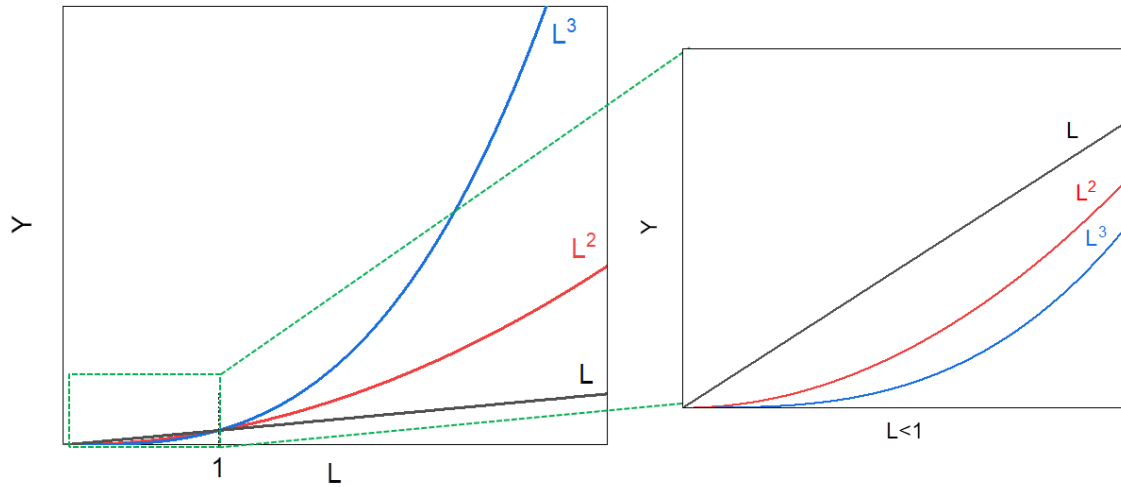


Figure 1-21: Low scale advantage for microfluidics [155]

When objects interact with each other, the interaction occurs either through their surface or through their volume and it produces very different results. For example, for a cube and a disc of the same volume and weight, when deposited on the surface of a water basin, one could sink and the other float since in one case there will be predominance of surface interactions and in the other case is the volume that predominates. At microscopic scale, surface interactions predominate which gives rise to several counter-intuitive situations on macroscopic scale. Surface and volume are not the only physical quantities to behave differently at the micro and macroscopic scale, for example, the forces of surface tension vary as the size of the object in question while the forces of gravity are proportional to mass and volume. On a microscopic scale, surface tension forces dominate the forces of gravity, giving rise to phenomena such as capillarity or the ability of some insects to walk on water.

The exploration of the micrometric world and its specific phenomena is a discipline widely studied today, especially since, the micro-lithography techniques made it possible to design objects from micrometric to nanometric size. The following part is therefore devoted to a more detailed description of these top-down lithography techniques.

1.3.2 Principle of soft and photo-lithography

1.3.2.1 PDMS based microdevices

Soft-lithography is based on the use of elastomeric stamp with patterns on its surface and structures with feature sizes from 30 nm to 100 μm . This strategy is a low cost and effective method based on self-assembly and replica molding for the manufacture of micro and nanostructures. The benchmarking elastomer used in soft-lithography is the polydimethylsiloxane (PDMS). The low-cost, transparence, viscoelasticity, hydrophobic surface, biocompatibility, facility in molding and compatibility with glass and silicon wafer conduct to a large utilization of the PDMS in industry and research fields [157][158].

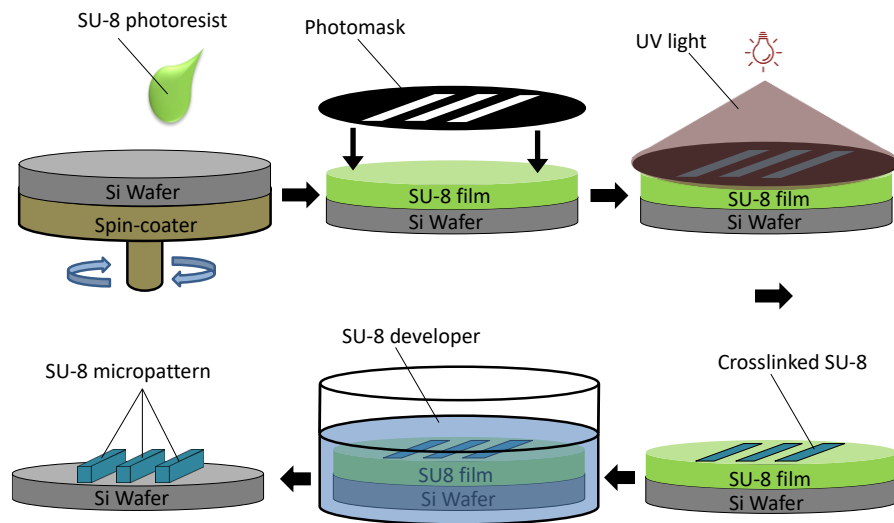


Figure 1-22: Manufacture of SU-8 masters by photolithography

The preparation of structured PDMS mold is performed by micromolding of masters prepared by photolithography. The preparation of these masters is described in Figure 1-22. From a Computer-Aided-Design (CAD) file, representing the pattern to be reproduced, a photomask is manufactured. A positive photoresist (usually SU-8 resist that consists in a viscous epoxy monomer crosslinkable under UV light) is spin-coated on a silicon wafer. The photomask is applied on the spin-coated film and thanks to the irradiation of UV light, the drawn pattern in the photomask is reproduced on the photoresist. Thanks to the action of a developer, the un-irradiated resist is dissolved which shows the shape of the masters. Those masters consist in hard polymer micro-objects in relief on a silicon wafer. The PDMS mold structuration is carried out by pouring the viscous liquid on those masters (see Figure

1-23). The gas bubble trapped in the liquid are removed under vacuum chamber, the mold is then cross-linked by thermal treatment at low temperature. After its solidification, the mold can be detached from the masters and consists in an elastic soft solid with hydrophobic surface.

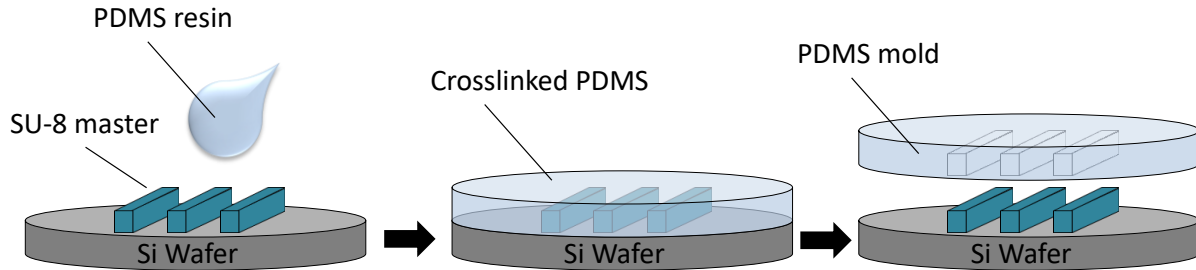


Figure 1-23: PDMS mold preparation by means of SU-8 masters

In practice, micro-objects and micro-channels structuring the stamp can be clogged or altered by the presence of small dusts. Those manipulations are generally carried out in clean-room environments to obtain best quality PDMS molds and SU-8 masters.

The manufactured PDMS mold is generally directly used as microfluidic device but it can also serve for a number of soft-lithographic techniques for fabricating high-quality microstructures and nanostructures based on alternative materials. A detailed description of these techniques is developed in the next section.

1.3.2.2 Soft-lithography processes for micromolding

The strength of soft-lithography lies in replicating rather than fabricating the master, the ability to deform the elastomeric stamp or mold gives it unique capabilities even in fabricating master patterns. Soft-lithography techniques require remarkably low investment and are easy to implement [156][158][159][160]: They are not subject to the limitations set by optical diffraction and optical transparency (the edge definition is set, in principle, by Van der Waals interactions and, in practice, by the properties of the materials involved), and they provide alternative routes to structures that are smaller than 100 nm without the need for advanced lithographic techniques. They also offer access to new types of surfaces, optical structures, sensors, prototype devices, and systems that could be difficult to fabricate by photolithography (details in section 1.3.3). The reference material

for mold preparation is the polydimethylsiloxane (PDMS) which demonstrates remarkable properties for soft-lithography: The low interfacial free energy (~ 21.6 dyn/cm) and the good stability of PDMS prevent any sticking or reaction of the patterned molecules or polymers with the surface. PDMS is thermally curable and has a good thermal stability (close to 200°C under air). Molds are reusable up to 50 times and their mechanical (deformable) and optical (transparent for $>300\text{nm}$ light) properties are preserved in time. Finally, the interfacial properties of PDMS can be changed readily either by modifying the prepolymers or by treating the surface with plasma. The subsequent formation of siloxane gives appropriate interfacial interactions with materials that themselves have a wide range of interfacial free energies.

The exceptional properties of this elastomer are commonly exploited in various soft-lithography techniques. Figure 1-24 explains the principle of such patterning techniques (extracted from Martin and Aksay-Shulz review [161][162]):

- In micro transfer molding (μTM) [163], a precursor is deposited into the hollow relief of the patterned PDMS mold. The excess of precursor is removed and the stamp is then brought into contact with the substrate. The lower interfacial energy of the PDMS relative to the substrate allows the patterned material to remain on the surface as the stamp is peeled away. The material is then ready for heat treatment.
- Micromolding in capillaries (MIMIC) [164] is a single step procedure using capillarity to aspire the precursor in the PDMS mold cavities. The mold must be brought in contact and stick to the substrate to form a microchannel networks and is cut to expose the entrance of the channels. After solidification of the precursor *via* drying or crosslinking, the mold is removed.
- With embossing method [165], a layer of precursor is deposited onto the substrate and then patterned by applying pressure on the mold. After, precursor solidification by heat treatment for example, the mold is peeled off revealing the patterned structure
- With micro contact printing (μCP) [166], the surface of the substrate is first modified before the deposition of a precursor. Micro-patterned PDMS is used to transfer a self-assembled monolayer (SAM) pattern onto the substrate to selectively modify the

surface. The SAM is prepared thanks to weak interactions, which allow the organization of molecules spontaneously into a thermodynamically stable structure. The molecules used to prepare SAM consist of ligands of the form $Y(CH_2)_nX$ where Y is designed to link with the substrate surface and X is tailored to change SAM surface properties (hydrophilicity for example). Once the SAM is transferred to the substrate, a precursor layer is deposited *via* spin-coating for example. A low temperature heat treatment (100-400°C) allows crosslinking leading to densification of the film. When the precursor is deposited on the SAM, the adhesion is of low quality, which leads to cracks while the material directly in contact with the substrate remains attached.

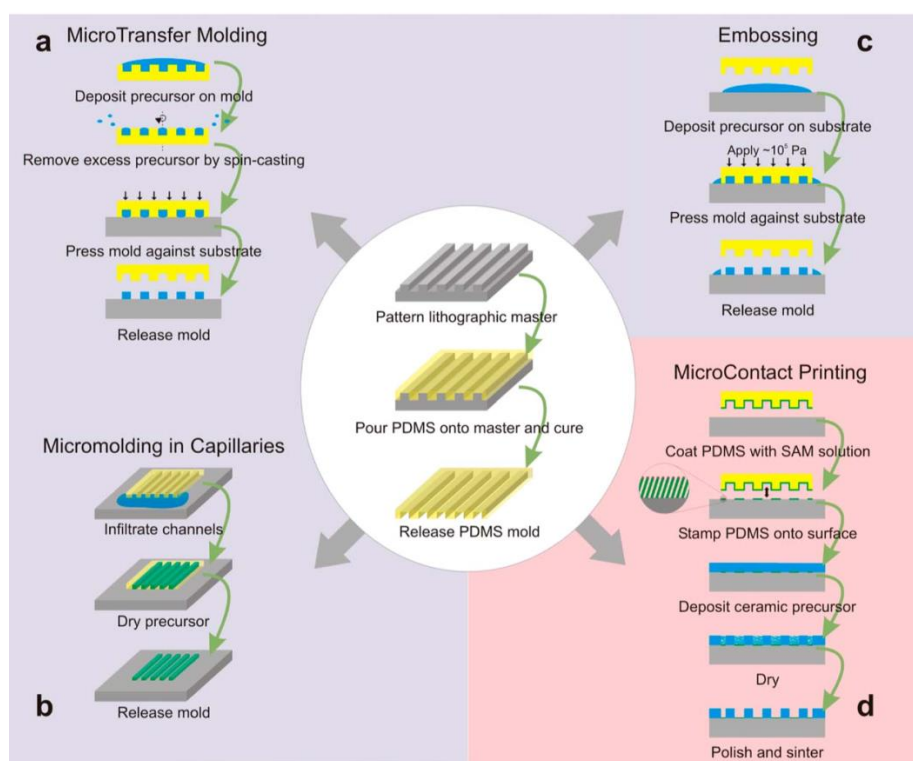


Figure 1-24: Schematic illustration of PDMS mold preparation and different soft lithography techniques: a) MicroTransfer molding (μ TM); b) Micromolding in Capillaries (MiMiC); c) Embossing; d) MicroContact Printing (μ CP) [161]

Soft-lithography techniques are inexpensive and easy to implement for the microstructuring of polymer materials. There are, however, several limitations inherent in this type of method leading to significant manufacturing defects on microstructured patterns:

- First, during crosslinking, PDMS undergoes a small shrinkage (about 1%) which can lead to poor reproduction of the dimensions of the initial masters. In addition, by contact with certain solvents, it may be deformed (toluene, hexane) or even dissolved (THF).
- Second, the elasticity and thermal expansion of PDMS make it difficult to achieve high precision in recording over a large area and may limit the utility of soft-lithography in multilayer fabrication and/or nanofabrication.
- Finally, because of these plastic and elastic properties, shapes with high aspect ratio are difficult to manufacture. The aspect ratio is the ratio between the width of an object and its depth or height. For a ratio that is too high, the shape of the PDMS mold may deform very easily when in contact with the substrate or the polymer. When it is too low, the mold may collapse and the reliefs of the mold are then blocked. According to the literature, PDMS gives suitable results for aspect ratios between 0.2 and 20.

The photolithography is generally an alternative to soft-lithography for direct patterning of microstructures. It has been mentioned in the previous part (see 1.3.2.1) for the SU-8 masters' preparation. It is generally preferred to soft-lithography because it leads to processes with less manufacturing step. However, several conditions must be respected to be able to implement such technique. The most important being that the shaped material must have photocurable properties. The next section is dedicated to photolithography subtleties.

1.3.3 Photolithography for direct micro-patterning

Photolithography is based on the photopolymerization principle consisting in initiating polymerization under light irradiation. It is widely used today for the fabrication of electronic microcomponents since the first Intel microprocessor was manufactured *via* photolithography in 1971 [167][168]. The principle of this technique has already been described in Figure 1-22 of the section 1.3.2.1 with SU-8 example for preparation of masters for PDMS molding. SU-8 photoresist can be replaced by one of the many photosensitive resins available to obtain micropatterns with tuned properties.

On the contrary of SU-8 resist, most of the photopolymerizations are usually performed *via* free-radical initiation. The latter implies the assistance of additives able to absorb light energy and convert it into chemical energy leading to the formation of intermediate reactive species (free-radicals) [169][170]. Those additives are commonly called photoinitiators and most of them react to UV light irradiation. A widespread kind of photoinitiators is Norrish type I which is characterized by cleavage reaction of ketone based species into two radical fragments [171][172]. UV-light irradiation leads to a homolytic bond cleavage and generation of two highly reactive radical species. These radicals then initiate the polymerization. Type I photoinitiator is irreversibly incorporated into the polymer matrix. An example of Norrish type I initiator (the Tert-butyl(4-methylphenyl)ketone) and its conversion in free radical are presented in Figure 1-25 in the equation (22). The reactive intermediate may in turn react with a monomer, here an acrylate species (example of Figure 1-25) to initiate polymerization. Once the polymerization launched, propagation and termination occur, which results in a linear, planar or tridimensional network where the UV-exposed medium is cross-linked and solidified.

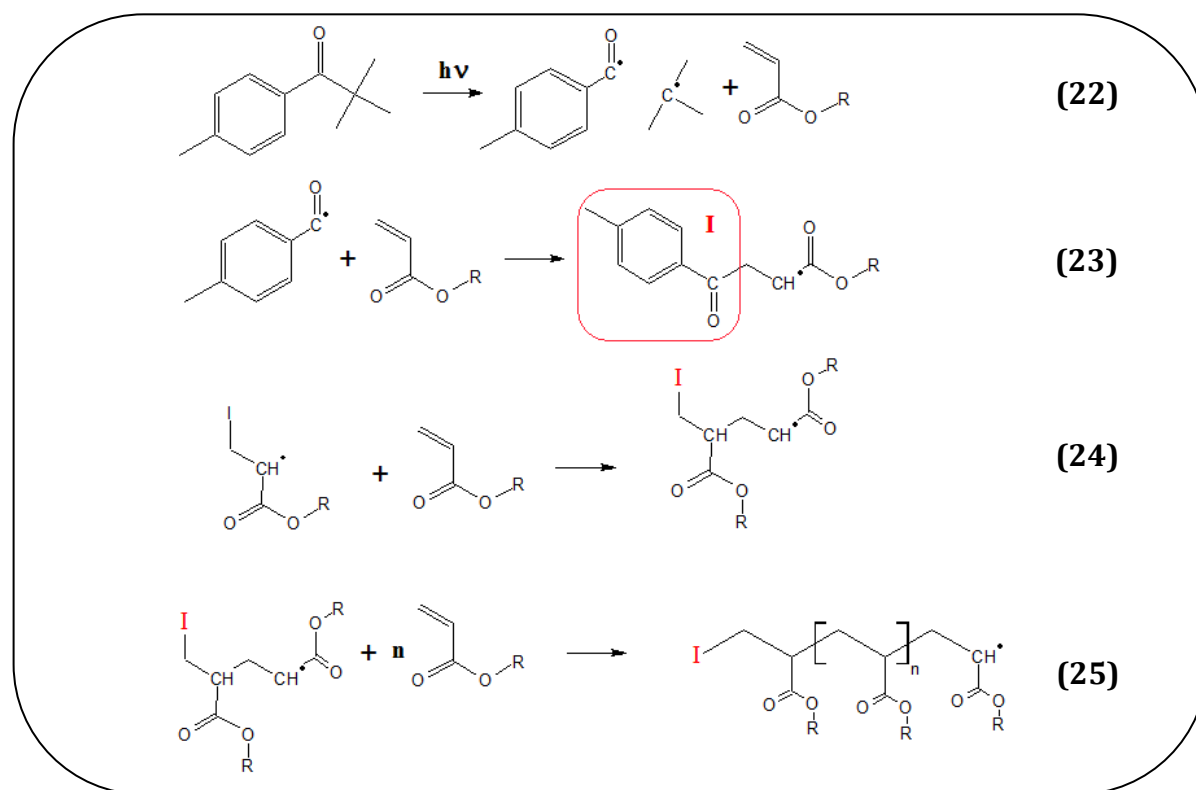


Figure 1-25: Free radical photopolymerization

Radical photoinitiators are added at a relatively low weight percent to a low molecular resin to obtain light-curing formulations. The most widespread resins compatible with free radical photopolymerization are acrylate and methacrylate species (as shown in [173][174]) because of their high reactivity and their facile functionalization. Acrylic compounds are by far the monomers of choice for UV curing systems. Their rapid rate conversion compared to other monomer (acrylate>methacrylate>vinyl>allyl) and the wide range of chemical structures (mono, di, tri, or tetra-functional) justify their wide utilization [169][173]. On the other hand, methacrylate based photoresists demonstrate higher mechanical and thermal properties than acrylates. They are sometimes preferred for applications requiring higher hardness and stiffness and/or in harsh environment (for example as dental resins) [173][174]. After the three classic step of polymerization (initiation, propagation and termination), the final cross-linked polyacrylates or polymethacrylates are insoluble in organic solvents and normally exhibit a high glass transition and notable resistance to thermal treatments.

A successful photolithographic patterning depends on many parameters: light exposition time, concentration and type of photoinitiator, wavelength of the irradiating light etc. For a selected monomer/PI couple and at fixed concentration and wavelength, the optimal resolution and contrast of the desired pattern are obtained for an exposition dose named “dose to size” E_s . E_s value corresponds to the dose necessary to print patterns at the size provided by the mask if this dose is greater, the resin is overexposed and on the contrary, when the dose is too low the resin is underexposed. The difference in dose compared to the normal dose causes a surplus or a lack of radicals in the resin conducting to sur-polymerization or under-polymerization [167].

Today, most of the commercial photoresists consist in cheap organic polymers and only have a transitory role in microfabrication processes. In other words, they are used for shaping silicon or oxide circuits but they are not kept in the final device. The prospect of using photosensitive resins convertible into a functional material for a MEMS or microfluidic devices represents a considerable advantage. It would reduce the number of steps inherent to current microfabrication processes (less development steps, etching, etc.). It is within this context that the use of preceramic polymers was imagined. Preceramic resins are well suited for soft and photolithography and they can then be converted into insulating or semiconducting materials performing a function in the printed circuit. This specific case of PDC materials in the context of MEMS is discussed in more detail in the next part.

1.3.4 Specific case of ceramic MEMS *via* PDC route

1.3.4.1 Theory and interest

Since the 90s, development of MEMS fabrications conducts to the mastery of silicon and/or polymer based devices. Still, material choice has great effects on MEMS properties. The opportunity to integrate ceramic materials in micro-devices is interesting due to their recognized properties such as chemical inertness, high thermal and mechanical resistance, biocompatibility etc. The direct shaping of sintered ceramics *via* mechanical methods like Si micromachining is critical because of the hardness of the material. On the other hand, shaping micro-parts at green state before sintering is a technical challenge since it requires

dispersion of very fine powder and is subject to strong shrinkage leading to poor accuracy in device dimension. Thanks to their polymer nature, preceramic polymers are easily integrated in a micro-fabrication process (soft-lithography, photolithography). Their tunable properties at molecular level are also an advantage in order to adapt electronic, optic or chemical properties to the intended application. The next sections present some examples of preceramic polymers employed in a lithography process to prepare PDCs based micro-objects.

1.3.4.2 Examples from literature

The processing of PDC materials *via* lithographic techniques started in the early 2000s and was studied with precision. Figure 1-26 illustrates some examples of micro-objects and micro-patterns manufactured thanks to different soft-lithography and photolithography methods (see part 1.3.2). The advances performed in this area are gathered in the Martin, Aksay and Schulz reviews previously mentioned [161][162].

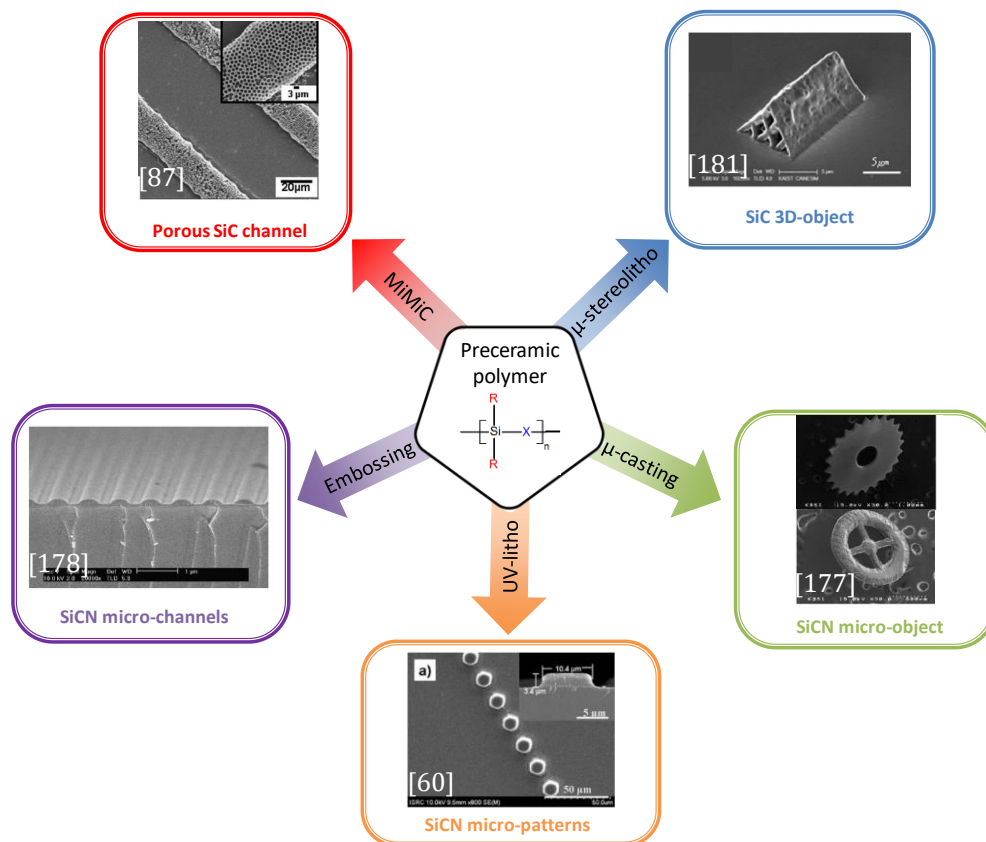


Figure 1-26: Some examples of PDC micro-pattern prepared by soft and photo-lithography method [87]

[181][178][177][60]

Early works of Freimuth *et al.* in 1996, conduct to the elaboration of PVZ micro-objects *via* LiGA method (from the German Lithographie, Galvanoformung, and Abformung process) [176]. Those polymeric micro-patterns were converted into SiCN ceramics after an ultra-slow thermal cycle taking place over 6 to 9 days. Based on Freimuth studies, Yang and Whiteside's article published in 2001 [177] demonstrates the feasibility of freestanding SiBCN micro-parts and honeycomb micropatterns *via* μ TM and MIMIC method. At this stage, the compatibility between modern soft-lithography method and PDCs process was proved. Kim's group attempted the preparation of more complex structures in 2006 [87] when they reported the fabrication of porous SiC microchannels *via* MiMiC method, porosity being generated thanks to SiO₂ sacrificial microspheres dissolved by HF solution after the polymer pyrolysis. Thanks to microcasting route, Chung *et al* [178], were able to prepare SiCN micro-objects with hardness around 10 GPa. The embossing shaping of polysilazane made by Lee *et al.* in 2008 has led to sub-micrometric thick SiCN micro-channels with hardness over 12GPa after pyrolysis at 1000°C [179].

Direct patterning *via* photolithography and micro-stereolithography were also explored by Kim's group through chemical modification of preceramic polymers. Ingeniously, photosensitive functions such as methacrylate were grafted to polymers and implemented as photoresists in the microfabrication process. Two approaches for methacrylation have been reported in the literature, i) *via* allyl bromide addition or ii) *via* isocyanate addition :

- One route to graft photosensitive functions on preceramic polymers backbone is to use bromine based additives such as Methyl-2-(bromo-methyl)acrylate and Ethyl-4-bromocrotonate as described in Li's works [180][181]. The synthesis consists in a reaction between nucleophilic amines group of polysilazane with allyl bromide in the acrylated additives. After elimination of solid HBr by-products and residual solvent, a functional preceramic negative photoresist is obtained. Such acrylation of pre-SiCN polymers significantly improve the photo-sensibility, UV-curing taking less than 1 min against 20 min for non-modified PVZ.

- The other synthesis route for photosensitive preceramic polymers preparation was developed in Anh Pham works in 2006 [60]. Bromine based additives were replaced by 2-isocyanatoethyl methacrylate species. Nucleophilic amine groups in the initial polymer were then subjected to addition reaction with isocyanate species. Sensitive methacrylate groups are linked to polymer chains *via* an urea function. Such synthesis is simpler and cheaper, no steps of solid by-products elimination is necessary and the reaction can occur at room temperature.

Kim's group privileged the second route. Acrylated polysilazane *via* isocyanate addition was crosslinked under two-photon and UV-lithography process. Anh Pham *et al* in 2006 combined a pre-SiCN photoresist with two-photon photoinitiator to manufacture SiCN/SiO₂ 3D-microlattice composites [60]. SiCN micropatterns shown in Figure 1-26 were obtained *via* UV-lithography of an acrylated polysilazane. On the other hand, SiC micro-objects were designed by two-photons micro-stereolithography in Park *et al.* [182] work published in 2009. Since the preliminary works carried out until 2010s, research efforts have focused on the improvement of the preceramic polymer photosensitivity and the elaboration of new applications of PDC materials in MEMS field. Bifunctionnal additives such as 1,1-Bis(acryloyloxymethyl) ethyl isocyanate were also employed in Li *et al.* works in 2015 [183] to confer UV-sensitivity properties to the polysilazane and obtain SiCN micro-objects. In this case, the grafted groups contain two acrylates functions versus one methacrylate when 2-isocyanatoethyl methacrylate is preferred. Latest work of Kim's group concerned the elaboration of a SiCN microbot, biocompatible and magnetically activable prepared *via* the two-photon micro-stereolithography. Such inert and hard microbot allows to consider biomedical applications such as *in vivo* cells delivery for injured tissues reparation [49].

A literature review on stereolithography applications of PDCs materials was done for this work. Indeed, stereolithography technology implies a photo-polymerization step, it is then very close to previously described photolithography process. Several pathways have been explored for the preparation of PDC parts *via* 3D printing., Table 1.1. gives a non-exhaustive list of studies on such application.

The most direct and easy method to manufacture PDC parts *via* stereolithography is to mix the preceramic polymer with a commercial acrylic resin. Under the action of the UV light, the acrylic resin is crosslinked and contains the preceramic polymer in its own matrix. During the pyrolysis, the acrylic resin decomposes and leaves a 3D ceramic object. Such a strategy has been studied in Wang *et al.* and Li *et al.* publications, for the preparation of SiCN and SiBCN parts (3D lattice and honeycomb structure). Nevertheless, with this pathway the shrinkage occurring during the heat treatment is very high, acrylic resin being entirely decomposed. The mixing of acrylic resin and preceramic polymers has then important disadvantages, this is why subtler approaches have been explored. In Colombo and Schmidt work [187], functional acrylic or epoxy groups of commercial pre-SiOC polymers were integrate in a stereolithographic process based on DLP and radical photopolymerization. They achieved the preparation of SiOC 3D lattice with manageable shrinkage, acrylic or epoxy units acting as photosensitive groups.

In several other studies, preceramic polymers were chemically modified by grafting photosensitive units on their backbone. For example, Zanchetta *et al.* [188] were able to introduce acrylate groups thanks to modification of commercial polysiloxane (Silres MK) with acrylated siloxane *via* hydrolysis and condensation. They were the first to succeed in the manufacturing of highly resolved DLP printed SiOC dense 3D lattice. Similarly, Gyak *et al.* [49] were able to prepare bulk 3D printed SiCN micro-reactors from methacrylate modified commercial polyvinylsilazane. Thanks to the specificity of the PDCs route, multiple modifications are possible at molecular scale to obtain a wide selection of ceramic materials. Therefore, the results of Fu *et al.* [189] document a procedure for fabrication 3D printing of metal-doped SiOC ceramic parts. Their strategy consisted in synthesizing a pre-Si-Zr-Ti-O-C photoresin from siloxane, zirconium and titanium propoxide.

Table 1-1 Literature examples of 3D printed PDC parts via stereolithography

Material	Technique	Photopolymerization route	Shape	Reference
<i>SiBCN/wSi₃N₄</i>	DLP	Acrylate and methacrylate (radical photoinitiator)	Honeycomb	<i>Li et al.[184]</i>
<i>SiBCN</i>	DLP	Acrylate and methacrylate (radical photoinitiator)	3D lattice	<i>Li et al.[185]</i>
<i>SiCN</i>	DLP	Acrylate and methacrylate (radical photoinitiator)	Honeycomb-3D lattice	<i>Wang et al.[186]</i>
<i>SiOC</i>	DLP	Acrylic or epoxy (radical photoinitiator)	3D lattice	<i>Schmidt and Colombo et al.[187]</i>
<i>SiOC</i>	DLP	Acrylate and methacrylate (radical photoinitiator)	3D lattice	<i>Zanchetta et al. [188]</i>
<i>SiCN-SiO₂</i>	DLP	Acrylate and methacrylate (radical photoinitiator)	Micro-reactor	<i>Gyak et al.[49]</i>
<i>Si-(Zr-Ti)-OC</i>	DLP	Acrylate and methacrylate (radical photoinitiator)	3D lattice	<i>Fu et al. [189]</i>
<i>SiOC(S)-SiCN(S)-SiC(S)</i>	DLP	Thiol-vinyl + radical photoinitiator	3D lattice	<i>Wang et al. [50]</i>
<i>SiOC(S)</i>	SPPW	Thiol-vinyl + radical photoinitiator	Cellular architecture	<i>Eckel et al. [41]</i>

To avoid the introduction of acrylate or methacrylate in the polymer backbone, thiol-vinyl photo-polymerization has emerged as an alternative. Wang *et al.* [50] experimented such pathway with SiC, SiCN and SiOC precursors containing vinyl groups combined with hexanedithiol and a compatible photo-initiator. Similarly, Eckel *et al.* [41] were able to prepare 3D lattice, honeycomb and other cellular architecture in SiOC(S) from a mixture of (mercaptopropyl) methylsiloxane and vinylmethoxysiloxane. The “thiol-vinyl route” is more direct than the grafting of “photosensitive unit” method as no synthesis step is required before the stereolithography process, however residual sulfur based impurities are found in the final PDC microstructure.

1.4 Conclusion on state of the art review

1.4.1 Ceramic, MEMS and electrochemistry

In this literature review, we explored diverse disciplines related to the work of this thesis. In a first part, the specificities of the “Polymer-Derived ceramics” route and the characteristics of the resulting materials were presented. We have seen how these materials fit into a “new generation” of ceramics made from molecular and polymeric

preceramic precursors. The specific amorphous microstructure of PDCs impart them unique properties such as high thermal and chemical stability sometimes superior to conventional ceramics. One of the strengths of this approach lies in the possibility of adjusting the properties of the initial preceramic polymer and the final material by incorporating new elements or chemical functions in the system at the atomic scale. The applications of PDC materials began to multiply in the 2000s and they are already used to prepare protective coatings, fibers and ceramic matrix composites. In recent years, they were the subject of studies demonstrating their compatibility with modern shaping techniques (3D printing, soft/photolithography, etc.). The use of PDCs in energy storage and production applications has revealed promising results both as a battery electrode, in the chemical storage of hydrogen or as an electrocatalyst for HER. In our work, we were interested in investigating Si-C-N and Si-B-C-N systems for the production of H_2 by water-splitting.

The second part of the introduction was therefore devoted to questions concerning the production of H_2 and more particularly related to the specificities of the water-splitting technique. The techniques currently implemented for industrial generation of dihydrogen (namely steam reforming of methane and coal gasification) release CO_2 and are based on the exploitation of fossil energy (methane-coal). The most promising alternative to these processes is water-splitting, which consists in synthesizing dihydrogen from water and electricity and directly emits only oxygen (thus compatible with sustainable energy production). To move to an industrial scale, several barriers must be overcome in order to improve the efficiency of this process, reduce its cost and therefore encourage broader use. Reducing the cost of this technique will require the use of stable and less expensive catalysts capable of replacing the rare and expensive benchmark catalyst platinum. Noble-metal-free catalysts have been successfully developed over the last few years, which leave hope for the development of inexpensive and abundant materials. Recent studies have shown that PDC-based catalysts may have a role to play in the development of these catalysts. Another strategy that might lead to significant efficiency enhancement of water-splitting devices consists in reducing the electrolyser scale. Studies demonstrated that optimal distance between electrolyser electrodes is in the order of a few tens of microns.

The manufacturing of water splitting devices with such small dimensions involves micro-fabrication methods such as soft and photolithography. In our work, those techniques were employed for the elaboration of PDCs based micro-objects as a proof of concept for preparing ultimately PDC micro-electrodes.

The third part of the state-of-the-art review was then dedicated to the fabrication techniques developed for the elaboration of MEMS and microfluidic devices. The miniaturization implies great interest in general for many reasons: it conducts to materials and resources economy; it allows designing devices with large specific surface areas. The soft-lithography is a cheap and simple microfabrication technique based on the use of micropatterned PDMS molds. Soft-lithography techniques are available in different sub-categories such as MIMIC, embossing, micro-transfer molding or micro-contact printing. Each sub-category has its own specificities, advantages and restraints. Despite non-negligible interests, soft-lithography techniques are subject to limitations inherent in the PDMS material: its accuracy is limited due to the plasticity and elasticity of the mold itself, the forms of strong or weak aspect ratios are difficult to print for the same reasons. On the other hand, photolithography is an alternative route for a more direct fabrication of micropatterns. Direct patterning *via* photolithography is based on the use of photocurable (or photodegradable) resins and therefore involves the use of photosensitive polymers and photoinitiators. Using a photomask, a film of photosensitive resin is selectively irradiated with light (usually UV) in order to draw a positive or negative version of the mask layout. Through a development step, the non-irradiated resin is dissolved in the case of a negative resin (and *vice-versa* for positive resists).

In the case of these two lithography routes, the shaped material is most of the time a crosslinkable polymer, which makes such techniques compatible with the PDCs route in theory. Indeed, since the end of the 90s, the development of PDC-based micro-objects has been experimented several times. The manufacturing of microparts, MEMS and microfluidic devices in SiCN, SiBCN, SiOC or SiC materials is spreading rapidly and has led to the beginnings of applications as sensors, actuators, insulators, micro-reactors ...

The purpose of this thesis was to couple three disciplines *i.e.* PDC materials, electrocatalysis for the hydrogen production and the microfabrication of MEMS and microfluidic devices. The ultimate goal is to develop a micro-water splitting device composed of PDCs based microelectrodes. The work carried out during this PhD was divided into three correlated chapters:

- Si-(B)-C-N ceramic/reduced graphene oxide composite systems as active catalysts towards the hydrogen evolution reaction (HER)
- Microfabrication of Si-(B)-C-N based micro-patterns *via* soft-lithography for eventual micro-electrolyser applications
- Synthesis and characterization of novel polysilazane and polyborosilazane photoresists implemented in photolithography process

1.4.2 Introduction to works developed in this study

In the first chapter, Si-C systems containing B, N and/or O were combined with 2D graphene in order to elaborate efficient electrocatalysts for HER. The rGO (reduced graphene oxide) foams were impregnated by AHPCS (commercial), Polyvinylsilazane (commercial) and boron-modified polyvinylsilazane (synthesized in the lab). After pyrolysis, Si(B)CN/rGO composites were tested in electrocatalysis to evaluate the influence of preceramic polymer nature, porosity, oxygen content and microstructure on the catalysts efficiency. For the first time such studies have shown the intrinsic HER activity of Si(B)CN ceramic and revealed a superior stability of such materials in comparison to state-of-the-art electrocatalysts. Thanks to its foamy monolithic shape, applications as freestanding electrodes with high surface area were also demonstrated. Through this study, the potential of PDCs for electrocatalysis, when combined with conducting substrates, was demonstrated.

In the second chapter, polyvinylsilazane (PVZ) and boron modified polyvinylsilazane (PBVZ) preceramic polymers were implemented in a soft-lithography strategy. Thanks to PDMS mold those preceramic polymers were shaped through the embossing pathway then pyrolyzed to achieve Si(B)CN based micro-objects. One major problem of the embossing technique is the formation of microcracks during the pyrolysis. Different ratios of boron

were introduced in the PVZ to enhance its ceramic yield. For the same reason, passive and active fillers such as Al_2O_3 , MoSi_2 and MoS_2 were employed to proceed a “near-net-shape” strategy. MoSi_2 and MoS_2 fillers were also selected for their intrinsic properties of electronic conduction and HER activity in the perspective of micro-object functionalization. This study has demonstrated the feasibility of SiCN and SiBCN based micropatterns fabrication *via* soft-lithography. Functionalization with MoS_2 and MoSi_2 fillers was intended to fabricate conducting catalytic micro-electrodes in the perspective of microfluidic electrolyser. The HER activity of the Si(B)CN- MoSi_2 - MoS_2 composites was then finally evaluated and optimized.

In the third chapter, PVZ and PBVZ preceramic polymers were chemically modified with grafting of acrylate and methacrylate units to provide photosensitive properties to these polymers. Photosensitive functions were grafted onto the polymer backbone *via* addition reactions of isocyanatoethyl acrylate and methacrylate on amines groups. As-synthesized photoresists were then implemented in photolithography process for UV patterning of PDC based micro-objects. Preceramic photoresists were fully characterized to prove the grafting of the photosensitive functions on the polymer backbone. To manufacture the ceramic patterns with the most precise dimension, the “dose to size” E_s energy associated with each of the synthesized photoresists was finally evaluated.

The following section (Chapter 2 entitled "Materials and methods") is devoted to a detailed and illustrated description of the methods, chemicals and materials used for the experiments carried out during this PhD work.

1.5 Bibliography

[1] K. J. Klabunde, « The Prehistory & History of Ceramic Kilns: Ceramics and Civilization Volume VII By Proudence M. Rice », *Materials and Manufacturing Processes*, vol. 13, n° 4, p. 624-625, juill. 1998, doi: [10.1080/10426919808935285](https://doi.org/10.1080/10426919808935285).

[2] France culture: Céramique technique : innovation, recherche et développement <https://www.franceculture.fr/conferences/fondation-dentreprise-hermes/ceramique-technique-innovation-recherche-et-developpement>

[3] Y. V. Kuzmin, « Origin of Old World pottery as viewed from the early 2010s: when, where and why? », *World Archaeology*, vol. 45, no 4, p. 539-556, oct. 2013, doi: 10.1080/00438243.2013.821669.

[4] E. Boaretto et al., « Radiocarbon dating of charcoal and bone collagen associated with early pottery at Yuchanyan Cave, Hunan Province, China », *Proceedings of the National Academy of Sciences*, vol. 106, no 24, p. 9595-9600, juin 2009, doi: 10.1073/pnas.0900539106.

[5] G. A. Baudart (janvier 1955) « Histoire française de l'alumine », *Revue de l'aluminium*, no 217, page 35.

[6] <https://www.carbo.com/en-us/our-history>

[7] M. Jansen, « A new class of promising ceramics based on amorphous inorganic networks », *Current Opinion in Solid State and Materials Science*, vol. 2, n° 2, p. 150-157, avr. 1997, doi: [10.1016/S1359-0286\(97\)80059-9](https://doi.org/10.1016/S1359-0286(97)80059-9).

[8] R. Haubner, « The history of hard CVD coatings for tool applications at the University of Technology Vienna », *International Journal of Refractory Metals and Hard Materials*, vol. 41, p. 22-34, nov. 2013, doi: [10.1016/j.jirmhm.2013.01.012](https://doi.org/10.1016/j.jirmhm.2013.01.012).

[9] F. H. Pollard et P. Woodward, « The stability and chemical reactivity of titanium nitride and titanium carbide », *Trans. Faraday Soc.*, vol. 46, p. 190, 1950, doi: [10.1039/tf9504600190](https://doi.org/10.1039/tf9504600190).

[10] K. J. Wynne et R. W. Rice, « Ceramics Via Polymer Pyrolysisdagger », *Annual Review of Materials Science*, vol. 14, n° 1, p. 297-334, août 1984, doi: [10.1146/annurev.ms.14.080184.001501](https://doi.org/10.1146/annurev.ms.14.080184.001501).

[11] R. Roy, « Ceramics by the Solution-Sol-Gel Route », *Science*, vol. 238, n° 4834, p. 1664-1669, déc. 1987, doi: [10.1126/science.238.4834.1664](https://doi.org/10.1126/science.238.4834.1664).

[12] A. G. King, *Ceramic technology and processing*. Norwich, N.Y: Noyes Publications, 2002.

[13] R. Janssen, S. Scheppokat, et N. Claussen, « Tailor-made ceramic-based components—Advantages by reactive processing and advanced shaping techniques », *Journal of the*

European Ceramic Society, vol. 28, n° 7, p. 1369-1379, janv. 2008, doi: 10.1016/j.jeurceramsoc.2007.12.022.

[14] A. Bellosi, « Design and Process of Non-Oxide Ceramics », in *Materials Science of Carbides, Nitrides and Borides*, Y. G. Gogotsi et R. A. Andrievski, Éd. Dordrecht: Springer Netherlands, 1999, p. 285-304. doi: [10.1007/978-94-011-4562-6_16](https://doi.org/10.1007/978-94-011-4562-6_16).

[15] https://www.htl-enertherm.eu/en/material_production/non-oxide_ceramics.html

[16] S. Shi *et al.*, « Fabricating processes of free-standing silicon nitride thin film for MEMS devices », in *2013 14th International Conference on Electronic Packaging Technology*, Dalian, China, août 2013, p. 23-26. doi: [10.1109/ICEPT.2013.6756412](https://doi.org/10.1109/ICEPT.2013.6756412).

[17] « Sol-Gel Ceramics for SEIRAS and SERS Substrates », *Crystals*, vol. 11, n° 4, p. 439, avr. 2021, doi: [10.3390/cryst11040439](https://doi.org/10.3390/cryst11040439).

[18] J. K. Sprenger, « Electron Enhanced Atomic Layer Deposition (Ee-Ald) for Room Temperature Growth of Gallium Nitride, Silicon, and Boron Nitride Films », *undefined*, 2018, Consulté le: oct. 21, 2021. [En ligne]. Disponible sur: [https://www.semanticscholar.org/paper/Electron-Enhanced-Atomic-Layer-Deposition-\(Ee-Ald\)-Sprenger/5dccda700e268d49183c46f505bb9f718b226b3c](https://www.semanticscholar.org/paper/Electron-Enhanced-Atomic-Layer-Deposition-(Ee-Ald)-Sprenger/5dccda700e268d49183c46f505bb9f718b226b3c)

[19] R. M. Rocha, E. A. B. Moura, A. H. A. Bressiani, et J. C. Bressiani, « SiOC ceramic foams synthesized from electron beam irradiated methylsilicone resin », *J Mater Sci*, vol. 43, n° 13, p. 4466-4474, juill. 2008, doi: [10.1007/s10853-008-2654-6](https://doi.org/10.1007/s10853-008-2654-6).

[20] D. Seyferth, « Dimethyldichlorosilane and the Direct Synthesis of Methylchlorosilanes. The Key to the Silicones Industry », *Organometallics*, vol. 20, n° 24, p. 4978-4992, nov. 2001, doi: [10.1021/om0109051](https://doi.org/10.1021/om0109051).

[21] S. Yajima, Y. Hasegawa, K. Okamura, et T. Matsuzawa, « Development of high tensile strength silicon carbide fibre using an organosilicon polymer precursor », *Nature*, vol. 273, n° 5663, p. 525-527, juin 1978, doi: [10.1038/273525a0](https://doi.org/10.1038/273525a0).

[22] W. Verbeek, « Production of shaped articles of homogeneous mixtures of silicon carbide and nitride », US3853567A, déc. 10, 1974 Consulté le: oct. 21, 2021. [En ligne]. Disponible sur: <https://patents.google.com/patent/US3853567A/en>

- [23] G. Fritz et B. Raabe, « Bildung siliciumorganischer Verbindungen. V. Die Thermische Zersetzung von $\text{Si}(\text{CH}_3)_4$ und $\text{Si}(\text{C}_2\text{H}_5)_4$ », *Z. Anorg. Allg. Chem.*, vol. 286, n° 3-4, p. 149-167, juill. 1956, doi: [10.1002/zaac.19562860307](https://doi.org/10.1002/zaac.19562860307).
- [24] W. Ainger, « 12F. and , “The Preparation of Phosphorus-Nitrogen Compounds as Non-Porous Solids”; pp. 168–82 in *Special Ceramics*, Edited by P. Popper. Academic press, New York, 1960. », p. 168-82, 1960.
- [25] « 13P. G. Chantrell and P. Popper, “Inorganic Polymers and Ceramics”; pp. 87–103 in *Special Ceramics*, Edited by P. Popper. Academic Press, New York, 1965. ».
- [26] P. Colombo, R. Riedel, G.D. Sorarù, H.-K. Kleebe (Eds.), *Polymer Derived Ceramics: from Nanostructure to Applications*, DEStech Publications Inc., Lancaster, PA (2010), pp. 1-12
- [27] Janik, J. F.; Paine, R. T., *Journal of organometallic chemistry* 1993, 449 (1), 39-44.
- [28] Sneddon, L.G.; Su, K.; Fazen, P.J.; Lynch, A.T.; Remsen, E.E.; Beck, J.S. Polymeric precursors to boron nitride ceramics. In *Inorganic and Organometallic Oligomers and Polymers*; Springer:Heidelberg, Germany, 1991; pp. 199–208.
- [29] Ralf Riedel, Joachim Bill, and Andreas Kienzle. Boron-modified Inorganic PolymersPrecursors for the Synthesis of Multicomponent Ceramics. *Applied Organometallic Chemistry*, 10(3-4) :241–256, 1996. 26
- [30] M Jansen, H-P Baldus, and O Wagner. Silicon Boron Nitride Ceramics and Precursor Compounds, Process of Producing Them and Their Application. Patent NumberEP 0502399, 1992. 26
- [31] G. R. Whittell et I. Manners, « Metallopolymers: New Multifunctional Materials », *Advanced Materials*, vol. 19, n° 21, p. 3439-3468, 2007, doi: [10.1002/adma.200702876](https://doi.org/10.1002/adma.200702876).
- [32] S. Bernard et P. Miele, « Polymer-Derived Boron Nitride: A Review on the Chemistry, Shaping and Ceramic Conversion of Borazine Derivatives », *Materials*, vol. 7, n° 11, p. 7436-7459, nov. 2014, doi: [10.3390/ma7117436](https://doi.org/10.3390/ma7117436).
- [33] A. O. Gabriel, R. Riedel, S. Storck, et W. F. Maier, « Synthesis and thermally induced ceramization of a non-oxidic poly(methylsilsesquicarbodi-imide) gel », *Applied*

Organometallic Chemistry, vol. 11, n° 10-11, p. 833-841, 1997, doi: [10.1002/\(SICI\)1099-0739\(199710/11\)11:10/11<833::AID-AOC643>3.0.CO;2-S](https://doi.org/10.1002/(SICI)1099-0739(199710/11)11:10/11<833::AID-AOC643>3.0.CO;2-S).

[34] P. Colombo, G. Mera, R. Riedel, et G. D. Sorarù, « Polymer-Derived Ceramics: 40 Years of Research and Innovation in Advanced Ceramics », *Journal of the American Ceramic Society*, vol. 93, n° 7, p. 1805-1837, juill. 2010, doi: [10.1111/j.1551-2916.2010.03876.x](https://doi.org/10.1111/j.1551-2916.2010.03876.x).

[35] R. Riedel, G. Mera, R. Hauser, et A. Klonczynski, « Silicon-Based Polymer-Derived Ceramics: Synthesis Properties and Applications-A Review », *Journal of the Ceramic Society of Japan*, vol. 114, n° 1330, p. 425-444, 2006, doi: [10.2109/jcersj.114.425](https://doi.org/10.2109/jcersj.114.425).

[36] <https://www.starfiresystems.com>

[37] P. Greil, « Active-Filler-Controlled Pyrolysis of Preceramic Polymers », *Journal of the American Ceramic Society*, vol. 78, n° 4, p. 835-848, avr. 1995, doi: [10.1111/j.1151-2916.1995.tb08404.x](https://doi.org/10.1111/j.1151-2916.1995.tb08404.x).

[38] P. Greil, « [38] Near Net Shape Manufacturing of Polymer Derived Ceramics », *Journal of the European Ceramic Society*, vol. 18, n° 13, p. 1905-1914, nov. 1998, doi: [10.1016/S0955-2219\(98\)00129-0](https://doi.org/10.1016/S0955-2219(98)00129-0).

[39] P. Greil, « Polymer Derived Engineering Ceramics », *Advanced Engineering Materials*, vol. 2, n° 6, p. 339-348, juin 2000, doi: [10.1002/1527-2648\(200006\)2:6<339::AID-ADEM339>3.0.CO;2-K](https://doi.org/10.1002/1527-2648(200006)2:6<339::AID-ADEM339>3.0.CO;2-K).

[40] Y. Jüttke *et al.*, « Polymer Derived Ceramic Membranes for Gas Separation », *Chemical Engineering Transactions*, vol. 32, p. 1891, janv. 2013, doi: [10.3303/CET1332316](https://doi.org/10.3303/CET1332316).

[41] Z. C. Eckel, C. Zhou, J. H. Martin, A. J. Jacobsen, W. B. Carter, et T. A. Schaedler, « Additive manufacturing of polymer-derived ceramics », *Science*, vol. 351, n° 6268, p. 58-62, janv. 2016, doi: [10.1126/science.aad2688](https://doi.org/10.1126/science.aad2688).

[42] N. R. Nagaiah, J. S. Kapat, L. An, et L. Chow, « Novel polymer derived ceramic-high temperature heat flux sensor for gas turbine environment », *J. Phys.: Conf. Ser.*, vol. 34, n° 1, p. 458, 2006, doi: [10.1088/1742-6596/34/1/075](https://doi.org/10.1088/1742-6596/34/1/075).

- [43] R. Bhandavat, Z. Pei, et G. Singh, « Polymer-derived ceramics as anode material for rechargeable Li-ion batteries: a review », *Nanomaterials and Energy*, vol. 1, n° 6, p. 324-337, nov. 2012, doi: [10.1680/nme.12.00030](https://doi.org/10.1680/nme.12.00030).
- [44] P. Cromme, M. Scheffler, et P. Greil, « Ceramic Tapes from Preceramic Polymers », *Advanced Engineering Materials*, vol. 4, n° 11, p. 873-877, nov. 2002, doi: [10.1002/1527-2648\(20021105\)4:11<873::AID-ADEM873>3.0.CO;2-G](https://doi.org/10.1002/1527-2648(20021105)4:11<873::AID-ADEM873>3.0.CO;2-G).
- [45] D. Hotza, R. K. Nishihora, R. A. F. Machado, P.-M. Geffroy, T. Chartier, et S. Bernard, « Tape casting of preceramic polymers toward advanced ceramics: A review », *International Journal of Ceramic Engineering & Science*, vol. 1, n° 1, p. 21-41, 2019, doi: [10.1002/ces2.10009](https://doi.org/10.1002/ces2.10009).
- [46] G. Barroso, Q. Li, R. K. Bordia, et G. Motz, « Polymeric and ceramic silicon-based coatings – a review », *J. Mater. Chem. A*, vol. 7, n° 5, p. 1936-1963, 2019, doi: [10.1039/C8TA09054H](https://doi.org/10.1039/C8TA09054H).
- [47] H. Ichikawa, « Polymer-Derived Ceramic Fibers », *Annual Review of Materials Research*, vol. 46, n° 1, p. 335-356, juill. 2016, doi: [10.1146/annurev-matsci-070115-032127](https://doi.org/10.1146/annurev-matsci-070115-032127).
- [48] R. Jones, A. Szveda, et D. Petrak, « Polymer derived ceramic matrix composites », *Composites Part A: Applied Science and Manufacturing*, vol. 30, n° 4, p. 569-575, avr. 1999, doi: [10.1016/S1359-835X\(98\)00151-1](https://doi.org/10.1016/S1359-835X(98)00151-1).
- [49] K.-W. Gyak *et al.*, « Magnetically Actuated SiCN-Based Ceramic Microrobot for Guided Cell Delivery », *Advanced Healthcare Materials*, vol. 8, n° 21, p. 1900739, nov. 2019, doi: [10.1002/adhm.201900739](https://doi.org/10.1002/adhm.201900739).
- [50] X. Wang, F. Schmidt, D. Hanaor, P. H. Kamm, S. Li, et A. Gurlo, « Additive manufacturing of ceramics from preceramic polymers: A versatile stereolithographic approach assisted by thiol-ene click chemistry », *Additive Manufacturing*, vol. 27, p. 80-90, mai 2019, doi: [10.1016/j.addma.2019.02.012](https://doi.org/10.1016/j.addma.2019.02.012).
- [51] X. Liu, Y.-L. Li, et F. Hou, « Fabrication of SiOC Ceramic Microparts and Patterned Structures from Polysiloxanes via Liquid Cast and Pyrolysis », *Journal of the American Ceramic Society*, vol. 92, n° 1, p. 49-53, 2009, doi: [10.1111/j.1551-2916.2008.02849.x](https://doi.org/10.1111/j.1551-2916.2008.02849.x).

- [52] B.-H. Yoon, E.-J. Lee, H.-E. Kim, et Y.-H. Koh, « Highly Aligned Porous Silicon Carbide Ceramics by Freezing Polycarbosilane/Camphene Solution », *J American Ceramic Society*, vol. 90, n° 6, p. 1753-1759, juin 2007, doi: [10.1111/j.1551-2916.2007.01703.x](https://doi.org/10.1111/j.1551-2916.2007.01703.x).
- [53] E. Breval, M. Hammond, et C. G. Pantano, « Nanostructural Characterization of Silicon Oxycarbide Glasses and Glass-Ceramics », *Journal of the American Ceramic Society*, vol. 77, n° 11, p. 3012-3018, 1994, doi: [10.1111/j.1151-2916.1994.tb04538.x](https://doi.org/10.1111/j.1151-2916.1994.tb04538.x).
- [54] S. Ishihara, H. Gu, J. Bill, F. Aldinger, et F. Wakai, « Densification of Precursor-Derived Si-C-N Ceramics by High-Pressure Hot Isostatic Pressing », *Journal of the American Ceramic Society*, vol. 85, n° 7, p. 1706-1712, déc. 2004, doi: [10.1111/j.1151-2916.2002.tb00339.x](https://doi.org/10.1111/j.1151-2916.2002.tb00339.x).
- [55] R. Haug, M. Weinmann, J. Bill, et F. Aldinger, « Plastic forming of preceramic polymers », *Journal of the European Ceramic Society*, vol. 19, n° 1, p. 1-6, janv. 1999, doi: [10.1016/S0955-2219\(98\)00167-8](https://doi.org/10.1016/S0955-2219(98)00167-8).
- [56] D. Galusek, J. Sedláček, et R. Riedel, « Al₂O₃-SiC composites prepared by warm pressing and sintering of an organosilicon polymer-coated alumina powder », *Journal of the European Ceramic Society*, vol. 27, n° 6, p. 2385-2392, janv. 2007, doi: [10.1016/j.jeurceramsoc.2006.09.007](https://doi.org/10.1016/j.jeurceramsoc.2006.09.007).
- [57] T. Zhang, J. R. G. Evans, et J. Woodthorpe, « Injection moulding of silicon carbide using an organic vehicle based on a preceramic polymer », *Journal of the European Ceramic Society*, vol. 15, n° 8, p. 729-734, janv. 1995, doi: [10.1016/0955-2219\(95\)00049-Z](https://doi.org/10.1016/0955-2219(95)00049-Z).
- [58] S. Walter, D. Suttor, T. Erny, B. Hahn, et P. Greil, « Injection moulding of polysiloxane/filler mixtures for oxycarbide ceramic composites », *Journal of the European Ceramic Society*, vol. 16, n° 4, p. 387-393, janv. 1996, doi: [10.1016/0955-2219\(95\)00120-4](https://doi.org/10.1016/0955-2219(95)00120-4).
- [59] T. Wideman, E. E. Remsen, E. Cortez, V. L. Chlanda, et L. G. Sneddon, « Amine-Modified Polyborazylens: Second-Generation Precursors to Boron Nitride », *Chem. Mater.*, vol. 10, n° 1, p. 412-421, janv. 1998, doi: [10.1021/cm970572r](https://doi.org/10.1021/cm970572r).
- [60] T. A. Pham, D.-P. Kim, T.-W. Lim, S.-H. Park, D.-Y. Yang, et K.-S. Lee, « Three-Dimensional SiCN Ceramic Microstructures via Nano-Stereolithography of Inorganic Polymer

Photoresists », *Advanced Functional Materials*, vol. 16, n° 9, p. 1235-1241, juin 2006, doi: [10.1002/adfm.200600009](https://doi.org/10.1002/adfm.200600009).

[61] Y. Zhu, Z. Huang, S. Dong, M. Yuan, et D. Jiang, « Manufacturing 2D carbon-fiber-reinforced SiC matrix composites by slurry infiltration and PIP process », *Ceramics International*, vol. 34, n° 5, p. 1201-1205, juill. 2008, doi: [10.1016/j.ceramint.2007.02.014](https://doi.org/10.1016/j.ceramint.2007.02.014).

[62] Z. Ren, C. Gervais, et G. Singh, « Preparation and structure of SiOCN fibres derived from cyclic silazane/poly-acrylic acid hybrid precursor », *R. Soc. open sci.*, vol. 6, n° 10, p. 190690, oct. 2019, doi: [10.1098/rsos.190690](https://doi.org/10.1098/rsos.190690).

[63] M. R. O'Masta, E. Stonkevitch, K. A. Porter, P. P. Bui, Z. C. Eckel, et T. A. Schaedler, « Additive manufacturing of polymer-derived ceramic matrix composites », *J Am Ceram Soc*, vol. 103, n° 12, p. 6712-6723, déc. 2020, doi: [10.1111/jace.17275](https://doi.org/10.1111/jace.17275).

[64] Z. Ren et G. Singh, « Nonoxide polymer-derived CMCs for “super” turbines », *American Ceramic Society bulletin*, vol. 98, n° 3, avr. 2019, Consulté le: oct. 21, 2021. [En ligne]. Disponible sur: <https://par.nsf.gov/biblio/10108196-nonoxide-polymer-derived-cmcs-super-turbines>

[65] M. S. Bazarjani, M. M. Müller, H.-J. Kleebe, C. Fasel, R. Riedel, et A. Gurlo, « In situ formation of tungsten oxycarbide, tungsten carbide and tungsten nitride nanoparticles in micro- and mesoporous polymer-derived ceramics », *J. Mater. Chem. A*, vol. 2, n° 27, p. 10454, 2014, doi: [10.1039/c4ta01509f](https://doi.org/10.1039/c4ta01509f).

[66] R. C. Osthoff et S. W. Kantor, « Hexamethylcyclotrisilazane and Octamethylcyclotetrasilazane », *Inorganic Syntheses*, vol. 5, p. 61, 1957.

[67] S. D. Brewer et C. P. Haber, « Alkylsilazanes¹ and Some Related Compounds », *Journal of the American Chemical Society*, vol. 70, no 11, p. 3888–3891, 1948.

[68] E. G. Rochow, « Polymeric methylsilazanes », *Pure and Applied Chemistry*, vol. 13, no 1-2, p. 247–262, 1966.

[69] W. Fink, « Silicium-stickstoff-heterocyclen », *Angewandte Chemie*, vol. 78, no 17, p. 803–819, 1966.

[70] <https://www.merckgroup.com/en/brands/pm/durazane/durazane-product-finder.html>

[71] A. Viard *et al.*, « Polymer Derived Si-B-C-N Ceramics: 30 Years of Research », *Adv. Eng. Mater.*, vol. 20, n° 10, p. 1800360, oct. 2018, doi: [10.1002/adem.201800360](https://doi.org/10.1002/adem.201800360).

[72] L. G. Sneddon, K. Su, P. J. Fazen, A. T. Lynch, E. E. Remsen, et J. S. Beck, « Polymeric Precursors to Boron Nitride Ceramics », in *Inorganic and Organometallic Oligomers and Polymers*, Dordrecht, 1991, p. 199-208. doi: [10.1007/978-94-011-3214-5_15](https://doi.org/10.1007/978-94-011-3214-5_15).

[73] K. Su, E. E. Remsen, G. A. Zank, et L. G. Sneddon, « Synthesis, characterization, and ceramic conversion reactions of borazine-modified hydridopolysilazanes: new polymeric precursors to silicon nitride carbide boride (SiNCB) ceramic composites », *Chemistry of Materials*, vol. 5, n° 4, p. 547-556, avr. 1993, doi: [10.1021/cm00028a024](https://doi.org/10.1021/cm00028a024).

[74] D. Seyferth et H. Plenio, « Borasilazane Polymeric Precursors for Borosilicon Nitride », *Journal of the American Ceramic Society*, vol. 73, n° 7, p. 2131-2133, 1990, doi: [10.1111/j.1151-2916.1990.tb05286.x](https://doi.org/10.1111/j.1151-2916.1990.tb05286.x).

[75] Structure, élaboration, propriétés et modification de surface de fibres creuses non-oxydées à partir de polymères pré-céramiques pour des applications membranaires, Antoine Viard, 2016

[76] A. Viard *et al.*, « Molecular Chemistry and Engineering of Boron-Modified Polyorganosilazanes as New Processable and Functional SiBCN Precursors », *Chemistry – A European Journal*, vol. 23, n° 38, p. 9076-9090, 2017, doi: [10.1002/chem.201700623](https://doi.org/10.1002/chem.201700623).

[77] E. Barrios et L. Zhai, « A review of the evolution of the nanostructure of SiCN and SiOC polymer derived ceramics and the impact on mechanical properties », *Mol. Syst. Des. Eng.*, vol. 5, n° 10, p. 1606-1641, déc. 2020, doi: [10.1039/D0ME00123F](https://doi.org/10.1039/D0ME00123F).

[78] X. Ji, S. Wang, C. Shao, et H. Wang, « High-Temperature Corrosion Behavior of SiBCN Fibers for Aerospace Applications », *ACS Appl. Mater. Interfaces*, vol. 10, n° 23, p. 19712-19720, juin 2018, doi: [10.1021/acsami.8b04497](https://doi.org/10.1021/acsami.8b04497).

- [79] A. Jalowiecki, J. Bill, F. Aldinger, et J. Mayer, « Interface characterization of nanosized B-doped Si₃N₄/SiC ceramics », *Composites Part A: Applied Science and Manufacturing*, vol. 27, n° 9, p. 717-721, janv. 1996, doi: [10.1016/1359-835X\(96\)00004-8](https://doi.org/10.1016/1359-835X(96)00004-8).
- [80] R. Riedel, A. Kienzle, W. Dressler, L. Ruwisch, J. Bill, et F. Aldinger, « A silicoboron carbonitride ceramic stable to 2,000°C », *Nature*, vol. 382, n° 6594, p. 796-798, août 1996, doi: [10.1038/382796a0](https://doi.org/10.1038/382796a0).
- [81] M. Christ, A. Zimmermann, A. Zern, M. Weinmann, et F. Aldinger, « High temperature deformation behavior of crystallized precursor-derived Si-B-C-N ceramics », *Journal of Materials Science*, vol. 36, n° 24, p. 5767-5772, déc. 2001, doi: [10.1023/A:1012991618775](https://doi.org/10.1023/A:1012991618775).
- [82] E. Butchereit, K. G. Nickel, et A. Müller, « Precursor-Derived Si-B-C-N Ceramics: Oxidation Kinetics », *Journal of the American Ceramic Society*, vol. 84, n° 10, p. 2184-2188, déc. 2004, doi: [10.1111/j.1151-2916.2001.tb00985.x](https://doi.org/10.1111/j.1151-2916.2001.tb00985.x).
- [83] E. Butchereit et K. G. Nickel, « Oxidation Behavior of Precursor Derived Ceramics in the System Si-(B)-C-N », *KEM*, vol. 175-176, p. 69-78, oct. 1999, doi: [10.4028/www.scientific.net/KEM.175-176.69](https://doi.org/10.4028/www.scientific.net/KEM.175-176.69).
- [84] H.-J. Kleebe et Y. D. Blum, « SiOC ceramic with high excess free carbon », *Journal of the European Ceramic Society*, vol. 28, n° 5, p. 1037-1042, janv. 2008, doi: [10.1016/j.jeurceramsoc.2007.09.024](https://doi.org/10.1016/j.jeurceramsoc.2007.09.024).
- [85] K. Lu, D. Erb, et M. Liu, « Thermal stability and electrical conductivity of carbon-enriched silicon oxycarbide », *J. Mater. Chem. C*, vol. 4, n° 9, p. 1829-1837, 2016, doi: [10.1039/C6TC00069J](https://doi.org/10.1039/C6TC00069J).
- [86] M. Seibold et P. Greil, « Thermodynamics and microstructural development of ceramic composite formation by active filler-controlled pyrolysis (AFCOP) », 1993, doi: [10.1016/0955-2219\(93\)90041-O](https://doi.org/10.1016/0955-2219(93)90041-O).
- [87] Q. D. Nghiem, A. Asthana, I.-K. Sung, et D.-Pyo. Kim, « Fabrication of porous SiC-based ceramic microchannels via pyrolysis of templated preceramic polymers », *J. Mater. Res.*, vol. 21, n° 6, p. 1543-1549, juin 2006, doi: [10.1557/jmr.2006.0192](https://doi.org/10.1557/jmr.2006.0192).

- [88] P. Colombo, E. Bernardo, et L. Biasetto, « Novel Microcellular Ceramics from a Silicone Resin », *Journal of the American Ceramic Society*, vol. 87, n° 1, p. 152-154, janv. 2004, doi: [10.1111/j.1551-2916.2004.00152.x](https://doi.org/10.1111/j.1551-2916.2004.00152.x).
- [89] H. Wang, S. Zheng, X. Li, et D. Kim, « Preparation of three-dimensional ordered macroporous SiCN ceramic using sacrificing template method », *Microporous and Mesoporous Materials*, vol. 80, n° 1-3, p. 357-362, mai 2005, doi: [10.1016/j.micromeso.2005.01.014](https://doi.org/10.1016/j.micromeso.2005.01.014).
- [90] M. T. S. Tavares *et al.*, « TiO₂/PDMS nanocomposites for use on self-cleaning surfaces », *Surface and Coatings Technology*, vol. 239, p. 16-19, janv. 2014, doi: [10.1016/j.surfcoat.2013.11.009](https://doi.org/10.1016/j.surfcoat.2013.11.009).
- [91] G. Barroso, *Thermal barrier coating by polymer-derived ceramic technique for application in exhaust systems*. Göttingen: Cuvillier Verlag, 2018. Consulté le: oct. 21, 2021. [En ligne]. Disponible sur: <https://public.ebookcentral.proquest.com/choice/publicfullrecord.aspx?p=5510385>
- [92] G. S. Barroso, W. Krenkel, et G. Motz, « Low thermal conductivity coating system for application up to 1000°C by simple PDC processing with active and passive fillers », *Journal of the European Ceramic Society*, vol. 35, n° 12, p. 3339-3348, oct. 2015, doi: [10.1016/j.jeurceramsoc.2015.02.006](https://doi.org/10.1016/j.jeurceramsoc.2015.02.006).
- [93] J. Cordelair et P. Greil, « Electrical Characterization of Polymethylsiloxane/MoSi₂-Derived Composite Ceramics », *Journal of the American Ceramic Society*, vol. 84, n° 10, p. 2256-2259, 2001, doi: [10.1111/j.1151-2916.2001.tb00998.x](https://doi.org/10.1111/j.1151-2916.2001.tb00998.x).
- [94] P. Vallachira Warriam Sasikumar *et al.*, « In Vitro Cytocompatibility Assessment of Ti-Modified, Silicon-oxycarbide-Based, Polymer-Derived, Ceramic-Implantable Electrodes under Pacing Conditions », *ACS Appl. Mater. Interfaces*, vol. 12, n° 15, p. 17244-17253, avr. 2020, doi: [10.1021/acsami.0c01465](https://doi.org/10.1021/acsami.0c01465).
- [95] https://media.xpair.com/auxidev/nB42a_PilesComb.pdf

- [96] Afhypac, T. Alleau, Conversion direct de l'hydrogène en électricité : Les piles de type PEM, form 5.2.2, Jan. 2017, Reviewed Mar. 2020 http://www.afhypac.org/documents/tout-savoir/fiche_5.2.2_pemfc_rev.oct2014_ta.pdf
- [97] T. Umegaki, J.-M. Yan, X.-B. Zhang, H. Shioyama, N. Kuriyama, et Q. Xu, « Boron- and nitrogen-based chemical hydrogen storage materials », *International Journal of Hydrogen Energy*, vol. 34, n° 5, p. 2303-2311, mars 2009, doi: [10.1016/j.ijhydene.2009.01.002](https://doi.org/10.1016/j.ijhydene.2009.01.002).
- [98] O. Majoulet *et al.*, « Preparation, Characterization, and Surface Modification of Periodic Mesoporous Silicon–Aluminum–Carbon–Nitrogen Frameworks », *Chem. Mater.*, vol. 25, n° 20, p. 3957-3970, oct. 2013, doi: [10.1021/cm401605a](https://doi.org/10.1021/cm401605a).
- [99] C. Salameh, A. Bruma, S. Malo, U. B. Demirci, P. Miele, et S. Bernard, « Monodisperse platinum nanoparticles supported on highly ordered mesoporous silicon nitride nanoblocks: superior catalytic activity for hydrogen generation from sodium borohydride », *RSC Adv.*, vol. 5, n° 72, p. 58943-58951, 2015, doi: [10.1039/C5RA05901A](https://doi.org/10.1039/C5RA05901A).
- [100] A. Gutowska *et al.*, « Nanoscaffold Mediates Hydrogen Release and the Reactivity of Ammonia Borane », *Angewandte Chemie International Edition*, vol. 44, n° 23, p. 3578-3582, 2005, doi: [10.1002/anie.200462602](https://doi.org/10.1002/anie.200462602).
- [101] P. E. de Jongh et P. Adelhelm, « Nanosizing and Nanoconfinement: New Strategies Towards Meeting Hydrogen Storage Goals », *ChemSusChem*, vol. 3, n° 12, p. 1332-1348, 2010, doi: [10.1002/cssc.201000248](https://doi.org/10.1002/cssc.201000248).
- [102] L. Li *et al.*, « Lithium-Catalyzed Dehydrogenation of Ammonia Borane within Mesoporous Carbon Framework for Chemical Hydrogen Storage », *Advanced Functional Materials*, vol. 19, n° 2, p. 265-271, 2009, doi: [10.1002/adfm.200801111](https://doi.org/10.1002/adfm.200801111).
- [103] S. F. Li, Y. H. Guo, W. W. Sun, D. L. Sun, et X. B. Yu, « Platinum nanoparticle functionalized CNTs as nanoscaffolds and catalysts to enhance the dehydrogenation of ammonia-borane », *J. Phys. Chem. C*, vol. 114, n° 49, p. 21885-21890, déc. 2010, doi: [10.1021/jp1091152](https://doi.org/10.1021/jp1091152).

- [104] J. Zhao *et al.*, « A soft hydrogen storage material: poly(methyl acrylate)-confined ammonia borane with controllable dehydrogenation. », *Advanced materials*, 2010, doi: [10.1002/adma.200902174](https://doi.org/10.1002/adma.200902174).
- [105] S. Gadipelli, J. Ford, W. Zhou, H. Wu, T. J. Udovic, et T. Yildirim, « Nanoconfinement and Catalytic Dehydrogenation of Ammonia Borane by Magnesium-Metal–Organic-Framework-74 », *Chemistry – A European Journal*, vol. 17, n° 22, p. 6043-6047, 2011, doi: [10.1002/chem.201100090](https://doi.org/10.1002/chem.201100090).
- [106] G. Srinivas, W. Travis, J. Ford, H. Wu, Z.-X. Guo, et T. Yildirim, « Nanoconfined ammonia borane in a flexible metal–organic framework Fe–MIL-53: clean hydrogen release with fast kinetics », *J. Mater. Chem. A*, vol. 1, n° 13, p. 4167-4172, mars 2013, doi: [10.1039/C3TA00037K](https://doi.org/10.1039/C3TA00037K).
- [107] T. Zhang *et al.*, « Silica hollow nanospheres as new nanoscaffold materials to enhance hydrogen releasing from ammonia borane », *Phys. Chem. Chem. Phys.*, vol. 13, n° 41, p. 18592-18599, oct. 2011, doi: [10.1039/C1CP22657F](https://doi.org/10.1039/C1CP22657F).
- [108] J. G. Alauzun *et al.*, « Novel monolith-type boron nitride hierarchical foams obtained through integrative chemistry », *J. Mater. Chem.*, vol. 21, n° 36, p. 14025-14030, août 2011, doi: [10.1039/C1JM12751A](https://doi.org/10.1039/C1JM12751A).
- [109] J. Shen, D. Ahn, et R. Raj, « C-rate performance of silicon oxycarbide anodes for Li+ batteries enhanced by carbon nanotubes », *Journal of Power Sources*, vol. 196, n° 5, p. 2875-2878, mars 2011, doi: [10.1016/j.jpowsour.2010.11.009](https://doi.org/10.1016/j.jpowsour.2010.11.009).
- [110] M. Graczyk-Zajac, L. Toma, C. Fasel, et R. Riedel, « Carbon-rich SiOC anodes for lithium-ion batteries: Part I. Influence of material UV-pre-treatment on high power properties », *Solid State Ionics*, vol. 225, p. 522-526, oct. 2012, doi: [10.1016/j.ssi.2011.12.007](https://doi.org/10.1016/j.ssi.2011.12.007).
- [111] J. Shen et R. Raj, « Silicon-oxycarbide based thin film anodes for lithium ion batteries », *Journal of Power Sources*, vol. 196, n° 14, p. 5945-5950, juill. 2011, doi: [10.1016/j.jpowsour.2011.02.091](https://doi.org/10.1016/j.jpowsour.2011.02.091).

- [112] S. Bernard et P. Miele, « Nanostructured and architected boron nitride from boron, nitrogen and hydrogen-containing molecular and polymeric precursors », *Materials Today*, vol. 17, n° 9, p. 443-450, nov. 2014, doi: [10.1016/j.mattod.2014.07.006](https://doi.org/10.1016/j.mattod.2014.07.006).
- [113] S. Schlienger *et al.*, « Micro-, Mesoporous Boron Nitride-Based Materials Templated from Zeolites », *Chemistry of Materials*, vol. 24, p. 88, janv. 2012, doi: [10.1021/cm201938h](https://doi.org/10.1021/cm201938h).
- [114] S. Bernard *et al.*, « High-yield synthesis of hollow boron nitride nano-polyhedrons », *J. Mater. Chem.*, vol. 21, n° 24, p. 8694-8699, juin 2011, doi: [10.1039/C1JM10774G](https://doi.org/10.1039/C1JM10774G).
- [115] V. Salles *et al.*, « Design of highly dense boron nitride by the combination of spray pyrolysis of borazine and additive free sintering of derived ultrafine powders », *Chemistry of Materials*, vol. 21, n° 13, p. 2920-2929, 2009, doi: [10.1021/cm900641s](https://doi.org/10.1021/cm900641s).
- [116] M. A. Abass, A. A. Syed, C. Gervais, et G. Singh, « Synthesis and electrochemical performance of a polymer-derived silicon oxycarbide/boron nitride nanotube composite », *RSC Adv.*, vol. 7, n° 35, p. 21576-21584, 2017, doi: [10.1039/C7RA01545C](https://doi.org/10.1039/C7RA01545C).
- [117] L. Meng, X. Zhang, Y. Tang, K. Su, et J. Kong, « Hierarchically porous silicon-carbon-nitrogen hybrid materials towards highly efficient and selective adsorption of organic dyes », *Sci Rep*, vol. 5, n° 1, p. 7910, juill. 2015, doi: [10.1038/srep07910](https://doi.org/10.1038/srep07910).
- [118] Y. Feng, S. Lai, L. Yang, R. Riedel, et Z. Yu, « Polymer-derived porous Bi₂WO₆/SiC(O) ceramic nanocomposites with high photodegradation efficiency towards Rhodamine B », *Ceramics International*, vol. 44, n° 7, p. 8562-8569, mai 2018, doi: [10.1016/j.ceramint.2018.02.061](https://doi.org/10.1016/j.ceramint.2018.02.061).
- [119] M. Hojamberdiev *et al.*, « Template-free synthesis of polymer-derived mesoporous SiOC/TiO₂ and SiOC/N-doped TiO₂ ceramic composites for application in the removal of organic dyes from contaminated water », *Applied Catalysis B: Environmental*, vol. 115-116, p. 303-313, avr. 2012, doi: [10.1016/j.apcatb.2011.12.036](https://doi.org/10.1016/j.apcatb.2011.12.036).
- [120] M. Hojamberdiev, R. M. Prasad, K. Morita, M. A. Schiavon, et R. Riedel, « Polymer-derived mesoporous SiOC/ZnO nanocomposite for the purification of water contaminated with organic dyes », *Microporous and Mesoporous Materials*, vol. 151, p. 330-338, mars 2012, doi: [10.1016/j.micromeso.2011.10.015](https://doi.org/10.1016/j.micromeso.2011.10.015).

[121] Y. Feng *et al.*, « Nowotny phase $\text{Mo}_{3+2x}\text{Si}_3\text{C}_{0.6}$ dispersed in a porous SiC/C matrix: A novel catalyst for hydrogen evolution reaction », *J Am Ceram Soc*, vol. 103, n° 1, p. 508-519, janv. 2020, doi: [10.1111/jace.16731](https://doi.org/10.1111/jace.16731).

[122] S. Abinaya, P. Moni, V. Parthiban, A. K. Sahu, et M. Wilhelm, « Metal Silicide Nanosphere Decorated Carbon-Rich Polymer-Derived Ceramics: Bifunctional Electrocatalysts towards Oxygen and their Application in Anion Exchange Membrane Fuel Cells », *ChemElectroChem*, vol. 6, n° 13, p. 3268-3278, juill. 2019, doi: [10.1002/celc.201900475](https://doi.org/10.1002/celc.201900475).

[123] Z. Yu, K. Mao, et Y. Feng, « Single-source-precursor synthesis of porous W-containing SiC-based nanocomposites as hydrogen evolution reaction electrocatalysts », *J Adv Ceram*, août 2021, doi: [10.1007/s40145-021-0508-8](https://doi.org/10.1007/s40145-021-0508-8).

[124] Hydrogène énergie : définition, production, application, enjeux, sécurité (2011). En ligne : <https://www.connaissancedesenergies.org/fiche-pedagogique/hydrogene-energie>, consulté le 23 juillet 2021.

[125] Tout savoir sur l'hydrogène (2021). In : IFPEN. En ligne : <https://www.ifpenergiesnouvelles.fr/enjeux-et-prospective/decryptages/energies-renouvelables/tout-savoir-lhydrogene>, consulté le 23 juillet 2021.

[126] L'hydrogène en France, les chiffres clés, France hydrogène, 2021, <http://www.afhypac.org/documents/documentation/publications/FHInfographie%20Hydrog%C3%A8ne-FR%20-%20mars%202021.pdf>

[127] X. Zou et Y. Zhang, « Noble metal-free hydrogen evolution catalysts for water splitting », *Chem. Soc. Rev.*, vol. 44, n° 15, p. 5148-5180, 2015, doi: [10.1039/C4CS00448E](https://doi.org/10.1039/C4CS00448E).

[128] L. Chen, Z. Qi, S. Zhang, J. Su, et G. A. Somorjai, « Catalytic Hydrogen Production from Methane: A Review on Recent Progress and Prospect », *Catalysts*, vol. 10, n° 8, p. 858, août 2020, doi: [10.3390/catal10080858](https://doi.org/10.3390/catal10080858).

[129] Q. Wang, « Hydrogen Production », in *Handbook of Climate Change Mitigation*, W.-Y. Chen, J. Seiner, T. Suzuki, et M. Lackner, Éd. New York, NY: Springer US, 2012, p. 1091-1130. doi: [10.1007/978-1-4419-7991-9_29](https://doi.org/10.1007/978-1-4419-7991-9_29).

[130] S. Martin *et al.*, *Progress Update on the Allam Cycle: Commercialization of NET Power and the NET Power Demonstration Facility*. 2018.

[131] https://www.engineering-airliquide.com/sites/activity_eandc/files/styles/retina_cover_page/public/2019/11/06/steam-methane-reforming-plant-germany-800-625.jpg?itok=w0R34Pm6

[132] E. Shafirovich et A. Varma, « Underground Coal Gasification: A Brief Review of Current Status », *Ind. Eng. Chem. Res.*, vol. 48, n° 17, p. 7865-7875, sept. 2009, doi: [10.1021/ie801569r](https://doi.org/10.1021/ie801569r).

[133] B. Guenot, « Étude de matériaux catalytiques pour la conversion électrochimique de l'énergie », Theses, Univ. Montpellier, 2017. Consulté le: oct. 21, 2021. [En ligne]. Disponible sur: <https://hal.umontpellier.fr/tel-01684435>

[134] Afhypac, Th.A. Production d'hydrogène par électrolyse de l'eau , form 3.2.1, Jan.2017 <https://www.afhypac.org/documents/tout-savoir/Fiche%203.2.1%20-%20Electrolyse%20de%20l%27eau%20revjanv2017%20ThA.pdf>

[135] P. Sabatier, « Hydrogénations et déshydrogénations par catalyse », *Ber. Dtsch. Chem. Ges.*, vol. 44, n° 3, p. 1984-2001, juill. 1911, doi: [10.1002/cber.19110440303](https://doi.org/10.1002/cber.19110440303).

[136] R. Parsons, « The rate of electrolytic hydrogen evolution and the heat of adsorption of hydrogen », *Trans. Faraday Soc.*, vol. 54, p. 1053, 1958, doi: [10.1039/tf9585401053](https://doi.org/10.1039/tf9585401053).

[137] D. Voiry, H. S. Shin, K. P. Loh, et M. Chhowalla, « Low-dimensional catalysts for hydrogen evolution and CO₂ reduction », *Nat Rev Chem*, vol. 2, n° 1, p. 0105, janv. 2018, doi: [10.1038/s41570-017-0105](https://doi.org/10.1038/s41570-017-0105).

[138] D. Voiry et al., « Best Practices for Reporting Electrocatalytic Performance of Nanomaterials », *ACS Nano*, vol. 12, n° 10, p. 9635-9638, oct. 2018, doi: [10.1021/acsnano.8b07700](https://doi.org/10.1021/acsnano.8b07700).

[139] C. Li et J.-B. Baek, « Recent Advances in Noble Metal (Pt, Ru, and Ir)-Based Electrocatalysts for Efficient Hydrogen Evolution Reaction », *ACS Omega*, vol. 5, n° 1, p. 31-40, janv. 2020, doi: [10.1021/acsomega.9b03550](https://doi.org/10.1021/acsomega.9b03550).

- [140] Q. Fu *et al.*, « 2D Transition Metal Dichalcogenides: Design, Modulation, and Challenges in Electrocatalysis », *Adv. Mater.*, vol. 33, n° 6, p. 1907818, févr. 2021, doi: [10.1002/adma.201907818](https://doi.org/10.1002/adma.201907818).
- [141] N. Cheng *et al.*, « Platinum single-atom and cluster catalysis of the hydrogen evolution reaction », *Nat Commun*, vol. 7, n° 1, p. 13638, déc. 2016, doi: [10.1038/ncomms13638](https://doi.org/10.1038/ncomms13638).
- [142] Matthey, Johnson (2021) "Sir Humphry Davy on Platinum." In : Johnson Matthey Technology Review. En ligne : <https://www.technology.matthey.com/article/23/1/29-31/>, consulté le 23 juillet 2021.
- [143] J. Corredor, M. J. Rivero, C. M. Rangel, F. Gloaguen, et I. Ortiz, « Comprehensive review and future perspectives on the photocatalytic hydrogen production », *J. Chem. Technol. Biotechnol.*, vol. 94, n° 10, p. 3049-3063, oct. 2019, doi: [10.1002/jctb.6123](https://doi.org/10.1002/jctb.6123).
- [144] Z. Li, X. Meng, et Z. Zhang, « Recent development on MoS₂-based photocatalysis: A review », *Journal of Photochemistry and Photobiology C: Photochemistry Reviews*, vol. 35, p. 39-55, juin 2018, doi: [10.1016/j.jphotochemrev.2017.12.002](https://doi.org/10.1016/j.jphotochemrev.2017.12.002).
- [145] H. H. Do *et al.*, « Recent progress in TiO₂-based photocatalysts for hydrogen evolution reaction: A review », *Arabian Journal of Chemistry*, vol. 13, n° 2, p. 3653-3671, févr. 2020, doi: [10.1016/j.arabjc.2019.12.012](https://doi.org/10.1016/j.arabjc.2019.12.012).
- [146] M. Z. Rahman, M. G. Kibria, et C. B. Mullins, « Metal-free photocatalysts for hydrogen evolution », *Chem. Soc. Rev.*, vol. 49, n° 6, p. 1887-1931, 2020, doi: [10.1039/C9CS00313D](https://doi.org/10.1039/C9CS00313D).
- [147] B. Hinnemann *et al.*, « Biomimetic Hydrogen Evolution: MoS₂ Nanoparticles as Catalyst for Hydrogen Evolution », *J. Am. Chem. Soc.*, vol. 127, n° 15, p. 5308-5309, avr. 2005, doi: [10.1021/ja0504690](https://doi.org/10.1021/ja0504690).
- [148] H. Tributsch et J. C. Bennett, « Electrochemistry and photochemistry of MoS₂ layer crystals. I », *Journal of Electroanalytical Chemistry and Interfacial Electrochemistry*, vol. 81, n° 1, p. 97-111, août 1977, doi: [10.1016/S0022-0728\(77\)80363-X](https://doi.org/10.1016/S0022-0728(77)80363-X).
- [149] Q. Fu *et al.*, « 2D Transition Metal Dichalcogenides: Design, Modulation, and Challenges in Electrocatalysis », *Adv. Mater.*, vol. 33, n° 6, p. 1907818, févr. 2021, doi: [10.1002/adma.201907818](https://doi.org/10.1002/adma.201907818).

- [150] S. Manzeli, D. Ovchinnikov, D. Pasquier, O. V. Yazyev, et A. Kis, « 2D transition metal dichalcogenides », *Nat Rev Mater*, vol. 2, n° 8, p. 17033, août 2017, doi: [10.1038/natrevmats.2017.33](https://doi.org/10.1038/natrevmats.2017.33).
- [151] M. A. Modestino, D. Fernandez Rivas, S. M. H. Hashemi, J. G. E. Gardeniers, et D. Psaltis, « The potential for microfluidics in electrochemical energy systems », *Energy Environ. Sci.*, vol. 9, n° 11, p. 3381-3391, 2016, doi: [10.1039/C6EE01884J](https://doi.org/10.1039/C6EE01884J).
- [152] M. E. Oruc, A. V. Desai, R. G. Nuzzo, et P. J. A. Kenis, « Design, fabrication, and characterization of a proposed microchannel water electrolyser », *Journal of Power Sources*, vol. 307, p. 122-128, mars 2016, doi: [10.1016/j.jpowsour.2015.12.062](https://doi.org/10.1016/j.jpowsour.2015.12.062).
- [153] M. A. Modestino, C. A. Diaz-Botia, S. Haussener, R. Gomez-Sjoberg, J. W. Ager, et R. A. Segalman, « Integrated microfluidic test-bed for energy conversion devices », *Phys. Chem. Chem. Phys.*, vol. 15, n° 19, p. 7050, 2013, doi: [10.1039/c3cp51302e](https://doi.org/10.1039/c3cp51302e).
- [154] M. A. Modestino, M. Dumortier, S. M. Hosseini Hashemi, S. Haussener, C. Moser, et D. Psaltis, « Vapor-fed microfluidic hydrogen generator », *Lab Chip*, vol. 15, n° 10, p. 2287-2296, 2015, doi: [10.1039/C5LC00259A](https://doi.org/10.1039/C5LC00259A).
- [155] Le projet lutetium, <https://www.lutetium.paris/fr/>,
- [156] P. Gravesen, J. Branebjerg, et O. S. Jensen, « Microfluidics-a review », *J. Micromech. Microeng.*, vol. 3, n° 4, p. 168-182, déc. 1993, doi: [10.1088/0960-1317/3/4/002](https://doi.org/10.1088/0960-1317/3/4/002).
- [157] J. C. McDonald *et al.*, « Fabrication of microfluidic systems in poly(dimethylsiloxane) », *Electrophoresis*, vol. 21, n° 1, p. 27-40, janv. 2000, doi: [10.1002/\(SICI\)1522-2683\(20000101\)21:1<27::AID-ELPS27>3.0.CO;2-C](https://doi.org/10.1002/(SICI)1522-2683(20000101)21:1<27::AID-ELPS27>3.0.CO;2-C).
- [158] Y. Xia et G. M. Whitesides, « SOFT LITHOGRAPHY », *Annu. Rev. Mater. Sci.*, vol. 28, n° 1, p. 153-184, août 1998, doi: [10.1146/annurev.matsci.28.1.153](https://doi.org/10.1146/annurev.matsci.28.1.153).
- [159] J. A. Rogers et R. G. Nuzzo, « Recent progress in soft lithography », *Materials Today*, vol. 8, n° 2, p. 50-56, févr. 2005, doi: [10.1016/S1369-7021\(05\)00702-9](https://doi.org/10.1016/S1369-7021(05)00702-9).
- [160] D. Qin, Y. Xia, et G. M. Whitesides, « Soft lithography for micro- and nanoscale patterning », *Nat Protoc*, vol. 5, n° 3, p. 491-502, mars 2010, doi: [10.1038/nprot.2009.234](https://doi.org/10.1038/nprot.2009.234).

- [161] C. R. Martin et I. A. Aksay, « Submicrometer-Scale Patterning of Ceramic Thin Films », *Journal of Electroceramics*, vol. 12, n° 1/2, p. 53-68, janv. 2004, doi: [10.1023/B:JECR.0000034001.15359.98](https://doi.org/10.1023/B:JECR.0000034001.15359.98).
- [162] M. Schulz, « Polymer derived ceramics in MEMS/NEMS – a review on production processes and application », *Advances in Applied Ceramics*, vol. 108, n° 8, p. 454-460, nov. 2009, doi: [10.1179/174367609X422171](https://doi.org/10.1179/174367609X422171).
- [163] C.-Y. Chang, S.-Y. Yang, L.-S. Huang, et T.-M. Jeng, « A novel method for rapid fabrication of microlens arrays using micro-transfer molding with soft mold », *J. Micromech. Microeng.*, vol. 16, n° 5, p. 999-1005, mai 2006, doi: [10.1088/0960-1317/16/5/017](https://doi.org/10.1088/0960-1317/16/5/017).
- [164] W. S. Beh, I. T. Kim, D. Qin, Y. Xia, et G. M. Whitesides, « Formation of Patterned Microstructures of Conducting Polymers by Soft Lithography, and Applications in Microelectronic Device Fabrication », *Adv. Mater.*, vol. 11, n° 12, p. 1038-1041, août 1999, doi: [10.1002/\(SICI\)1521-4095\(199908\)11:12<1038::AID-ADMA1038>3.0.CO;2-L](https://doi.org/10.1002/(SICI)1521-4095(199908)11:12<1038::AID-ADMA1038>3.0.CO;2-L).
- [165] M. H. Lee, M. D. Huntington, W. Zhou, J.-C. Yang, et T. W. Odom, « Programmable Soft Lithography: Solvent-Assisted Nanoscale Embossing », *Nano Lett.*, vol. 11, n° 2, p. 311-315, févr. 2011, doi: [10.1021/nl102206x](https://doi.org/10.1021/nl102206x).
- [166] M.-S. Kim *et al.*, « Preparation of fluoropolymer structures for orthogonal processing of diverse material by Micro-Contact Printing », *Microelectronic Engineering*, vol. 123, p. 33-37, juill. 2014, doi: [10.1016/j.mee.2014.05.013](https://doi.org/10.1016/j.mee.2014.05.013).
- [167] Etude des résines à amplification chimique 193nm de tonalité positive ou négative pour une application microélectronique sub65nm, (2017) Micheal May
- [168] C. G. Willson, R. R. Dammel, et A. Reiser, « Photoresist materials: a historical perspective », Santa Clara, CA, USA, juill. 1997, p. 38. doi: [10.1117/12.275921](https://doi.org/10.1117/12.275921).
- [169] M. Kaur et A. K. Srivastava, « PHOTOPOLYMERIZATION: A REVIEW », *Journal of Macromolecular Science, Part C: Polymer Reviews*, vol. 42, n° 4, p. 481-512, janv. 2002, doi: [10.1081/MC-120015988](https://doi.org/10.1081/MC-120015988).
- [170] J.-P. Fouassier et J. F. RABEK, *Radiation Curing in Polymer Science and Technology: Practical aspects and applications*, vol. 4. Springer Science & Business Media, 1993.

[171] R. G. W. Norrish et R. R. Smith, « CATALYSED POLYMERIZATION OF METHYL METHACRYLATE IN THE LIQUID PHASE », *Nature*, vol. 150, n° 3803, p. 336-337, sept. 1942, doi: [10.1038/150336a0](https://doi.org/10.1038/150336a0).

[172] C. E. Hoyle, « Photocurable Coatings », in *Radiation Curing of Polymeric Materials*, vol. 417, 0 vol., American Chemical Society, 1990, p. 1-16. doi: [10.1021/bk-1990-0417.ch001](https://doi.org/10.1021/bk-1990-0417.ch001).

[173] P. T. Weissman, « COMPARISON of PERFORMANCE of ACRYLATE and METHACRYLATE ALIPHATIC URETHANES », 2004. <https://www.semanticscholar.org/paper/COMPARISON-of-PERFORMANCE-of-ACRYLATE-and-ALIPHATIC-Weissman/23ee454dfd6745853adebc21b94a002e5747a5c4> (consulté le oct. 21, 2021).

[174] S. H. Dickens, J. W. Stansbury, K. M. Choi, et C. J. E. Floyd, « Photopolymerization Kinetics of Methacrylate Dental Resins », *Macromolecules*, vol. 36, n° 16, p. 6043-6053, août 2003, doi: [10.1021/ma021675k](https://doi.org/10.1021/ma021675k).

[175] L. R. Harriott, « Limits of lithography », *Proc. IEEE*, vol. 89, n° 3, p. 366-374, mars 2001, doi: [10.1109/5.915379](https://doi.org/10.1109/5.915379).

[176] H. Freimuth *et al.*, « Formation of Complex Ceramic Miniaturized Structures by Pyrolysis of Poly(vinylsilazane) », *J American Ceramic Society*, vol. 79, n° 6, p. 1457-1465, juin 1996, doi: [10.1111/j.1151-2916.1996.tb08750.x](https://doi.org/10.1111/j.1151-2916.1996.tb08750.x).

[177] H. Yang, P. Deschatelets, S. T. Brittain, et G. M. Whitesides, « Fabrication of High Performance Ceramic Microstructures from a Polymeric Precursor Using Soft Lithography », *Adv. Mater.*, vol. 13, n° 1, p. 54-58, janv. 2001, doi: [10.1002/1521-4095\(200101\)13:1<54::AID-ADMA54>3.0.CO;2-Y](https://doi.org/10.1002/1521-4095(200101)13:1<54::AID-ADMA54>3.0.CO;2-Y).

[178] G.-S. Chung, « Characteristics of SiCN microstructures for harsh environment and high-power MEMS applications », *Microelectronics Journal*, vol. 38, n° 8-9, p. 888-893, août 2007, doi: [10.1016/j.mejo.2007.07.078](https://doi.org/10.1016/j.mejo.2007.07.078).

[179] D.-H. Lee, K.-H. Park, L.-Y. Hong, et D.-P. Kim, « SiCN ceramic patterns fabricated by soft lithography techniques », *Sensors and Actuators A: Physical*, vol. 135, n° 2, p. 895-901, avr. 2007, doi: [10.1016/j.sna.2006.09.003](https://doi.org/10.1016/j.sna.2006.09.003).

- [180] Y.-H. Li, X.-D. Li, et D.-P. Kim, « Chemical development of preceramic polyvinylsilazane photoresist for ceramic patterning », *J Electroceram*, vol. 23, n° 2-4, p. 133-136, oct. 2009, doi: [10.1007/s10832-007-9331-z](https://doi.org/10.1007/s10832-007-9331-z).
- [181] Y.-H. Li, X.-D. Li, et D.-P. Kim, « Acrylation of polyvinylsilazane with allyl bromide for an UV photosensitive inorganic polymer », *Journal of Organometallic Chemistry*, vol. 692, n° 23, p. 5303-5306, nov. 2007, doi: [10.1016/j.jorganchem.2007.08.016](https://doi.org/10.1016/j.jorganchem.2007.08.016).
- [182] S. Park, D.-H. Lee, H.-I. Ryoo, T.-W. Lim, D.-Y. Yang, et D.-P. Kim, « Fabrication of three-dimensional SiC ceramic microstructures with near-zero shrinkage via dual crosslinking induced stereolithography », *Chem. Commun.*, n° 32, p. 4880, 2009, doi: [10.1039/b907923h](https://doi.org/10.1039/b907923h).
- [183] Y.-H. Li, K.-D. Ahn, et D.-P. Kim, « Synthesis and properties of UV curable polyvinylsilazane as a precursor for micro-structuring: UV CURABLE POLYVINYLSILAZANE AS A PRECURSOR FOR MICRO-STRUCTURING », *Polym. Adv. Technol.*, vol. 26, n° 3, p. 245-249, mars 2015, doi: [10.1002/pat.3448](https://doi.org/10.1002/pat.3448).
- [184] S. Li *et al.*, « Additive manufacturing of SiBCN/Si₃N₄ w composites from preceramic polymers by digital light processing », *RSC Adv.*, vol. 10, n° 10, p. 5681-5689, 2020, doi: [10.1039/C9RA09598E](https://doi.org/10.1039/C9RA09598E).
- [185] S. Li *et al.*, « The fabrication of SiBCN ceramic components from preceramic polymers by digital light processing (DLP) 3D printing technology », *Journal of the European Ceramic Society*, vol. 38, n° 14, p. 4597-4603, nov. 2018, doi: [10.1016/j.jeurceramsoc.2018.06.046](https://doi.org/10.1016/j.jeurceramsoc.2018.06.046).
- [186] M. Wang *et al.*, « Polymer-derived silicon nitride ceramics by digital light processing based additive manufacturing », *J Am Ceram Soc*, vol. 102, n° 9, p. 5117-5126, sept. 2019, doi: [10.1111/jace.16389](https://doi.org/10.1111/jace.16389).
- [187] J. Schmidt et P. Colombo, « Digital light processing of ceramic components from polysiloxanes », *Journal of the European Ceramic Society*, vol. 38, n° 1, p. 57-66, janv. 2018, doi: [10.1016/j.jeurceramsoc.2017.07.033](https://doi.org/10.1016/j.jeurceramsoc.2017.07.033).
- [188] E. Zanchetta *et al.*, « [185] Stereolithography of SiOC Ceramic Microcomponents », *Adv. Mater.*, vol. 28, n° 2, p. 370-376, janv. 2016, doi: [10.1002/adma.201503470](https://doi.org/10.1002/adma.201503470).

[189] Y. Fu, G. Xu, Z. Chen, C. liu, D. Wang, et C. Lao, « Multiple metals doped polymer-derived SiOC ceramics for 3D printing », *Ceramics International*, vol. 44, n° 10, p. 11030-11038, juill. 2018, doi: [10.1016/j.ceramint.2018.03.075](https://doi.org/10.1016/j.ceramint.2018.03.075).

Chapter II : Materials and methods

2	Materials and methods	93
2.1	Reagents and materials	95
2.2	Preparation and characterization of PDC/rGO composites	96
2.2.1	Boron-modified polyvinylsilazane synthesis and characterization.....	96
2.2.2	Graphene oxide preparation.....	99
2.2.3	rGO foam preparation.....	99
2.2.4	PDC/rGO composites preparation.....	100
2.2.5	Chemical and mechanical characterization of PDC/rGO composites	101
2.2.6	Evaluation of the electro-catalytic performance of the PDC/rGO material	102
2.2.6.1	Working electrode preparation.....	102
2.2.6.2	Electrocatalytic measurements	103
2.2.7	Free standing electrodes preparation.....	104
2.3	Preparation of micropatterns based on Si(B)CN ceramic <i>via</i> soft-lithography	105
2.3.1	Boron-modified polyvinylsilazane synthesis and characterization	105
2.3.2	Soft-lithography procedure	105
2.3.2.1	PDMS mold preparation.....	105
2.3.2.2	Micropattern preparation via embossing	106
2.3.2.3	Micropattern preparation via MiMiC/injection	107
2.3.3	Chemical and geometrical characterization of micropatterns	108
2.3.4	Electrocatalytic measurements on Si(B)CN/(MoS ₂ /MoSi ₂)	109
2.3.5	Pellets preparation and impedance spectroscopy measurement.....	109
2.4	Photolithography of preceramic polymer	109
2.4.1	Preceramic photoresist synthesis and characterization.....	109
2.4.2	Photolithography procedure	111
2.4.3	Surface characterization.....	113
2.4.4	Nanoindentation - microindentation.....	113

2.5	Bibliography :	113
-----	----------------------	-----

2 Materials and methods

Exposition of Silicon based non-oxide preceramic polymers to oxygen and moisture can conduct to hydrolysis of Si-H and/or Si-N-H groups to form Si-OH and Si-O-Si functions [1][2]. For the preparation of non-oxide ceramic, it is then necessary to work under inert atmosphere (Ar, N₂) or under vacuum. To do so, different tools have been employed. First of all, to conduct synthesis under inert atmosphere, vacuum/Ar Schlenk line and Schlenk glassware were employed. A description of such tools is available in Figure 2-1. Schlenk line operating under vacuum/Ar is a glass device composed of two tubes, one of the tubes is connected to a vacuum pump and the other one is connected to a source of pure Argon. Schlenk glassware is connectable thanks to pipe linked to one of the four stopcocks ports allowing the selection of either vacuum or inert gas. A P₂O₅ column and a “U shaped glass tube” between the Ar gas line and the Ar tube are used to further dehydrate argon and to visualize the passage of the gas, respectively. Vacuum pump is protected from eventual solvent vapors thanks to a liquid nitrogen trap (solvent vapor is condensed before entering the pump). Finally, an additional stopcock at the end of the Ar Tube is available to proceed argon sweep. Schlenk flask is a glassware equipped with a stopcock enabling the introduction or evacuation of gas through connection with Schlenk line.

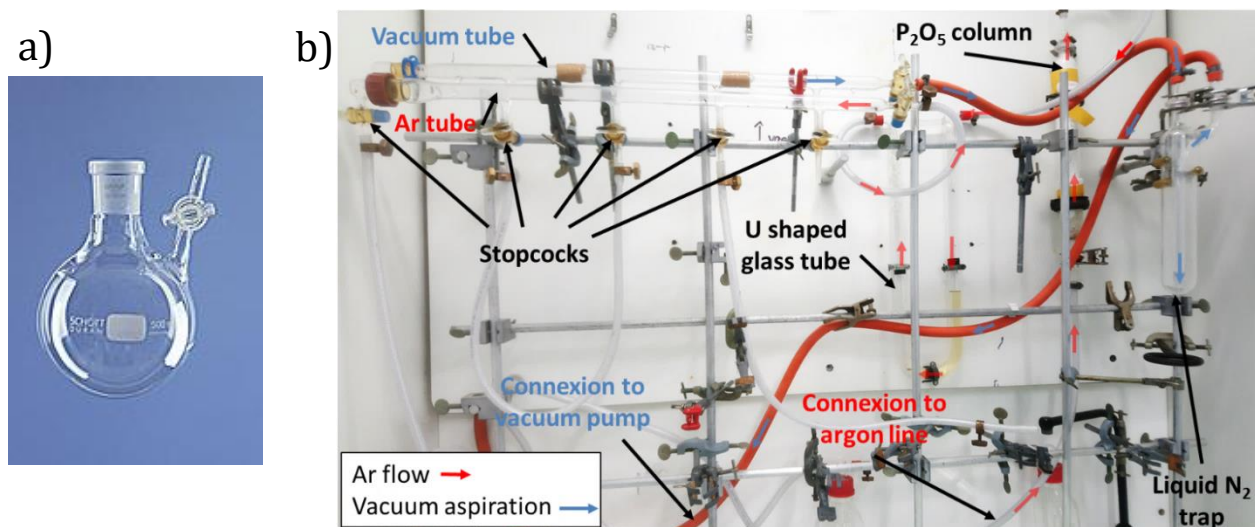


Figure 2-1: a) Schlenk flask and b) Vacuum/Ar lines description

The as-synthesized preceramic polymers were then handled in a glove-box MBraun-Labstar Eco (Figure 2-2). It is composed of two independent airlocks (a small and a big one). Introduction of product through the airlock is operated successive vacuum/argon cycles.



Figure 2-2: Glove box M-Braun working under Argon atmosphere

After synthesis, manipulation and shaping steps in the glove box, the samples are heat treated for their conversion from inorganic precursors to amorphous materials. The crosslinking and pyrolysis of the shaped green bodies are performed in a tubular furnace (Thermoconcept ROK 70/500/11) with controllable atmosphere (see Figure 2-3.a.). The quartz tube is connected to Ar and N₂ line to set a continuous gas flow evacuated through a bubbler at the furnace outlet. It is also possible to connect the oven enclosure to vacuum pump in order to evacuate the atmosphere and potential oxygen/moisture pollution.



Figure 2-3:a)Tubular furnace b) Graphite furnace (Gero, Model HTK8)

Annealing at higher temperatures ($>1000^{\circ}\text{C}$ and up to 1700°C) are carried out in a graphite furnace Gero, Model HTK8 under nitrogen or argon flow. In order to avoid any oxidation of the sample during the heat treatment the samples are introduced in the furnace under argon flow (in the case of the tubular furnace). Degassing under dynamic vacuum 30min is performed prior to the pyrolysis in order to evacuate any oxygen-polluted atmosphere.

2.1 Reagents and materials

Precursors of SiCN and SiC were respectively polyvinylsilazane (**PVZ**) purchased from Merck and AllylHydridoPolyCarboSilane (**AHPCS**) purchased from Starfire (Figure 2-4). Toluene (anhydrous 99.8%, Sigma Aldrich), borane dimethyl sulfide complex (**BDMS**, 2 M in toluene under argon, Alfa Aesar), Nafion (D-520 dispersion, 5%w/w in water and 1-propanol, Sigma Aldrich), isopropanol (100%, VWR chemical), potassium permanganate (KMnO_4 , 99.0%min., Alfa Aesar), hydrogen peroxide (H_2O_2 , ACS, 29–32% aqueous solution, Alfa Aesar) and sulfuric acid (H_2SO_4 , ACS reagent 95–98%, Sigma Aldrich) were used as received without further purification. To avoid any oxidation PVZ, AHPCS, BDMS and toluene were kept under argon atmosphere.

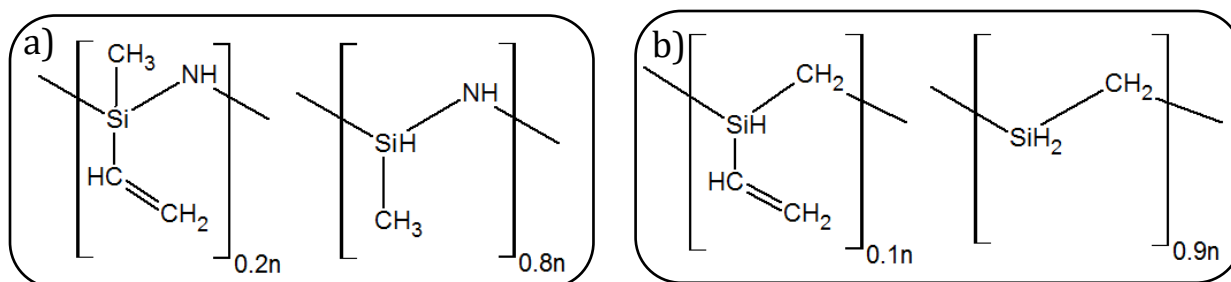


Figure 2-4: a)PVZ and b)AHPCS chemical structure

2.2 Preparation and characterization of PDC/rGO composites

This part describes the method employed for the preparation and the characterization of PDC/rGO composite (PDC= SiC, O-SiC, SiCN, O-SiCN, SiBCN, O-SiBCN; rGO=reduced graphene oxide) including the:

- Synthesis description of boron-modified polyvinylsilazane (PBVZ) and polycarbosilane (B-AHPCS) as SiBCN and SiBC precursors at a fixed Si/B ratio. AHPCS and PVZ are commercial polymers that were used as received
- Preparation of rGO foam *via* hydrothermal synthesis
- Impregnation of rGO foam with preceramic polymers
- Pyrolysis of impregnated foam to generate PDC/rGO composites
- Preparation of samples for chemical characterization of PDC/rGO composites
- Preparation of samples for electrocatalytic characterization of PDC/rGO composites
- Method of preparation of PDC/rGO free standing electrodes

2.2.1 Boron-modified polyvinylsilazane synthesis and characterization

All the glassware used is washed and dried at 70°C one day before the beginning of the synthesis. The synthesis assembly is composed of a 500 ml three-neck round-bottom flask (TNR flask), a dropping funnel and sealed by Schlenk stopcocks and PTFE vacuum grease. The assembly is kept 24h under dynamic vacuum to evacuate air and moisture before introduction of reagents. A schematic description is given in Figure 2-5. Typically, 5g of PVZ and 100 ml of toluene were added to the TNR flask under argon sweep and kept under stirring [3]. The quantity of BDMS was determined thanks to the Si/B ratio fixed at 3 for this

part of the study. This ratio of 3 was applied for a complete hydroboration and dehydrocoupling of vinyl and N-H groups in the PVZ [3]. Molecular mass of the commercial PVZ isn't communicated by the fabricant, calculation were then based on the molecular mass of one monomer of the polyvinylsilazane:

$$\text{Eq1: } M_{PVZ} = 0.2(M_{Si} + M_N + 3M_C + 7M_H) + 0.8(M_{Si} + M_N + M_C + 5M_H)$$

For 5g of PVZ and for a Si/B=3 the volume of BDMS solution (2M in toluene) introduced in the addition funnel is ~13 ml. TNR flask is then immersed in an ice bath to cool down the reaction medium. The BDMS solution is added dropwise under vigorous stirring, bubbles of dihydrogen are observed in the bubbler.

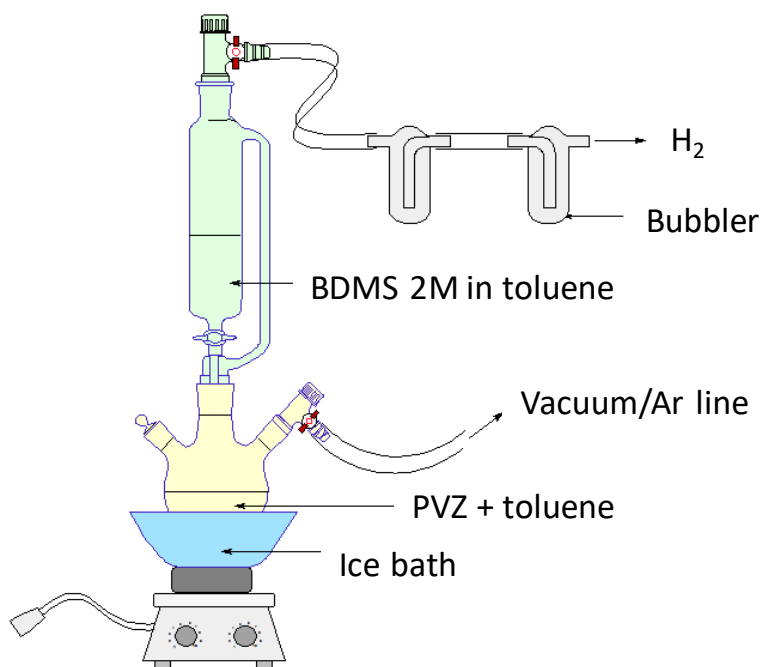


Figure 2-5: Schematic of experimental setup for synthesis of preceramic polymer for SiBCN ceramic

The mixture is left under stirring at room temperature for 3 days. The toluene is removed thanks to a distillation step described by the assembly scheme presented in Figure 2-6. A glass-like translucent-white solid polymer is obtained with a 81% yield.

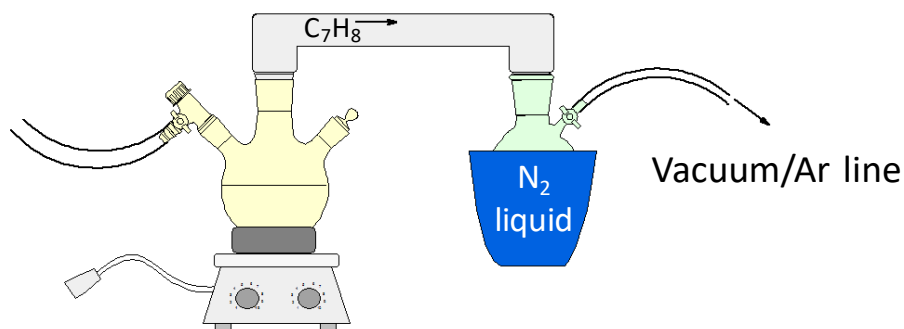


Figure 2-6: Solvent removal step during the synthesis of SiBCN precursor

The same procedure was applied for the synthesis of SiBC precursor with AHPCS as initial preceramic polymer and BDMS as borane complex. The same calculation method was adopted to determine the quantity of boron to add and fix the Si/B ratio at 30:

$$\text{Eq2: } M_{AHPCS} = 0.1(M_{Si} + 3M_C + 6M_H) + 0.9(M_{Si} + M_C + 4M_H)$$

Typically, for 5g of AHPCS, 1.71 ml of 2M in toluene BDMS is added.

The chemical structure of the preceramic polymers is investigated by Fourier Transform InfraRed (FT-IR) spectroscopy with a Nicolet iS50 Thermo scientific spectrometer. KBr (Sigma Aldrich) pellets with 2 wt% of precursor previously mixed and crushed in mortar are prepared by uniaxial pressing. The compaction step consists in pressing the mixed powder at 2 tons for 2 min with an Atlas™ Automatic (Auto) 8Ton hydraulic press. It is also characterized by solid-state NMR spectroscopy. Solid-state ^{13}C CP MAS and ^{29}Si MAS NMR were recorded on a Bruker Advance 300 spectrometer ($B_0 = 7.0\text{ T}$, $\nu_0 (^1\text{H}) = 300.29\text{ MHz}$, $\nu_0 (^{13}\text{C}) = 75.51\text{ MHz}$, $\nu_0 (^{29}\text{Si}) = 59.66\text{ MHz}$) using a 4 mm Bruker probe and spinning frequency of 10 kHz. While ^{11}B MAS spectra were recorded on a Bruker Advance 700 spectrometer ($B_0 = 16.4\text{ T}$, $\nu_0 (^{11}\text{B}) = 224.6\text{ MHz}$) using a 3.2 mm Bruker probe and spinning frequency of 20 kHz. ^{11}B spectra were acquired using a spin-echo θ - τ - 2θ pulse sequence with $\theta = 90^\circ$, to overcome problems related to the probe signal. The τ delay (50 μs) was synchronized with the spinning frequency. The chemical shift values were referenced to TMS for ^{13}C and ^{29}Si , and $\text{BF}_3\cdot\text{OEt}_2$ for ^{11}B . The NMR spectra were simulated with the DMFIT program.[7]

Investigations on the ceramic conversion of preceramic polymers were carried out by thermogravimetric analysis (TGA) on a TGA-STD Q600 thermal analysis device. The analysis were performed under atmospheric pressure from RT up to 1000 ° C with a heating rate of 5°C.min⁻¹ under nitrogen in the case of the preceramic polymers and under air for the PDC/rGO composites.

2.2.2 Graphene oxide preparation

Graphene oxide (GO) was synthesized thanks to a modified Hummers method [4] as described in Figure 2-7. In a typical synthesis, 1g of graphite (powder 59) is introduced in a beaker containing 25ml of concentrated sulfuric acid (H₂SO₄). To oxidize the graphite, 3g of potassium permanganate (KMnO₄) is carefully added to the mixture and left under stirring for 10 days. Deionized water is then slowly added, followed by 5 ml of hydrogen peroxide (H₂O₂) to reduce remaining KMnO₄. GO is finally washed thanks to deionized water and several cycles of centrifugation at 3000 rpm were done until a neutral pH is achieved. A light brown low concentration aqueous GO solution is obtained.

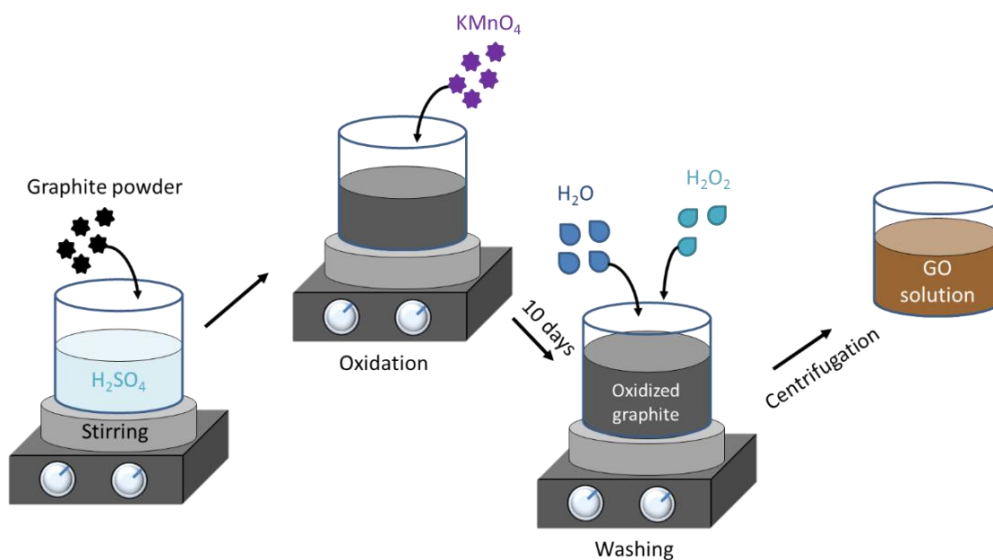


Figure 2-7: Synthesis of graphene oxide according to modified Hummers method

2.2.3 rGO foam preparation

Graphene oxide foam was prepared *via* hydrothermal synthesis [5] as described in Figure 2-8. 10ml of GO solution (at a 1.5 mg/ml concentration) are poured in an autoclave reactor

(Parr Instrument Company, Teflon reactor). The sealed autoclave is then heated at 180°C for 12h. The as-formed wet gel is placed in freezer for one night and consequently freeze-dried (Labonco Freezone 4.5; 0.05 mBar as freeze-drier).

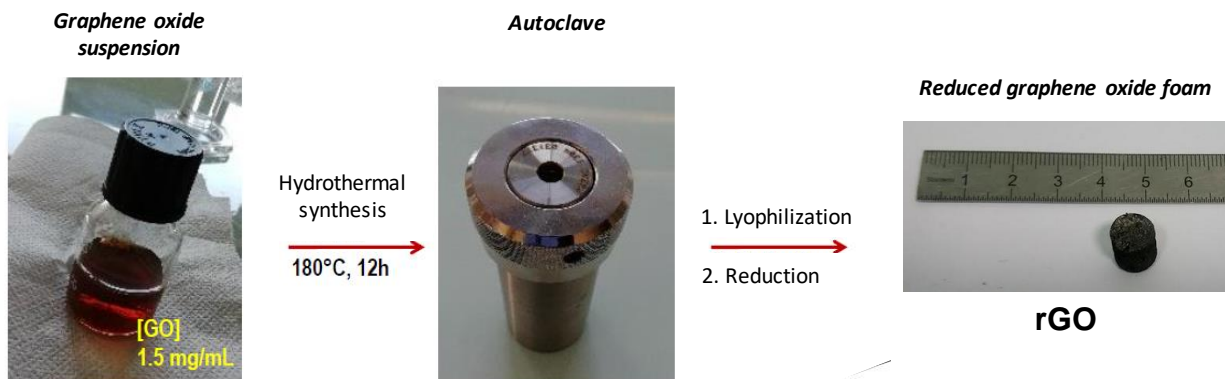


Figure 2-8: Hydrothermal synthesis of rGO foam

The GO foam obtained is then reduced by thermal treatment under Ar/H₂ atmosphere (200 scc/min) at 900°C for 2h in a tubular furnace and generated graphene-like reduced graphene oxide foams noted rGO.

2.2.4 PDC/rGO composites preparation

The preparation of PDC/rGO composites consists in an impregnation of the rGO foam by a solution of preceramic polymer dissolved in toluene. This method is described in Figure 2-9. The rGO foam is first kept under dynamic vacuum in a Schlenk flask for 24h to evacuate air and moisture from small pores in the foam. Under static vacuum, the preceramic polymer/toluene solution is introduced through a septum plug with a syringe to totally immerse the rGO foam in solution for 24h. After the impregnation step, the Schlenk flask is filled with argon. A washing step (with toluene (4x 10ml)) is needed to remove the excess of preceramic polymer solution. Finally, a drying step (under dynamic vacuum for 12h) is necessary to remove the residual traces of solvent in the foam.

The impregnated foam is finally extracted from the Schlenk flask under argon atmosphere in a glove box and placed in alumina crucible. The transformation of the polymer in the foam into ceramic is carried out by pyrolysis in a tubular furnace under nitrogen atmosphere at 1000°C for 2h. A subsequent annealing treatment of the PDC/rGO

composites was made in a graphite furnace under nitrogen atmosphere to study the structural evolution of the composite.

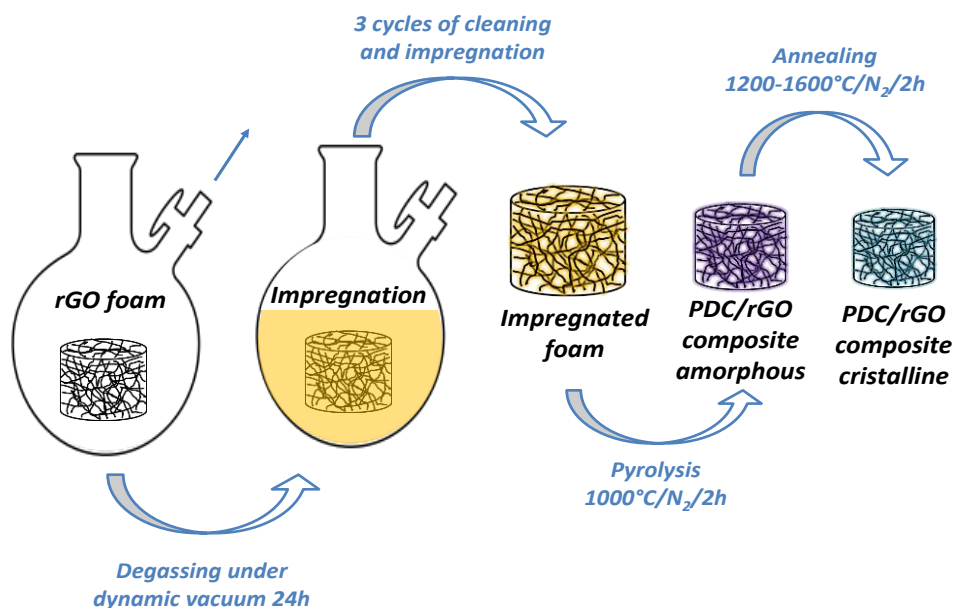


Figure 2-9: Impregnation method for preparation of PDC/rGO composites

Composites with various PDC contents were prepared by varying the ratio between the polymer and the solvent in the impregnating solution. Polymer/solvent ratios varying from 0.2:99.8 to 10:90 were tested. The nature and composition of the preceramic polymer was also investigated: PVZ, PBVZ, AHPCS and B-AHPCS were the different preceramic polymers used in this study.

2.2.5 Chemical and mechanical characterization of PDC/rGO composites

Scanning Electron Microscopy (SEM) (Hitachi S4800, operating with an acceleration voltage between 0.1 kV and 30 kV) and Transmission Electron Microscopy (TEM) measurements (JEOL ARM 200F operating at 200 eV, equipped with an energy dispersive X-Ray spectroscopy—EDX and an energy electron loss spectroscopy—EELS) were used to investigate the morphology and microstructure of the composites. Energy dispersive X-ray spectroscopy (Detector: Oxford Instruments X-Max^N SDD; Microscopy: Zeiss EVO HD15) and X-ray photoelectron spectroscopy XPS (ESCALAB 250, ThermoElectron equipped with an Al K α line 1486.6 eV as monochromatic excitation source with a 400- μ m spot size) were

used to analyze the chemical composition of the ceramics and composites. The samples for XPS were prepared on a silicon wafer coated with gold.

Raman spectroscopy (LABRAM 1B) and X-ray diffraction (Philips X'pert PRO X-ray diffraction system operating at 20 mA and 40 kV from 10 to 90° with a step size of 0.0167, using a $K\alpha_1$ of copper as source) were used to study the evolution of the structure of PDCs with the temperature.

The electrical conductivity was measured by using a two-probe method with silver as contact metal. Compression measurements were carried out on the rGO foam and on the O-SiBCN/rGO composite using a LLOYD 01/LF compression device equipped with a 50 N capacity force sensor. The porosity of the foams was characterized by mercury intrusion porosimetry using a Micrometrics Autopore IV 9500 penetrometer.

2.2.6 Evaluation of the electro-catalytic performance of the PDC/rGO material

2.2.6.1 Working electrode preparation

Sample preparation for electrocatalytic measurements is described in Figure 2-10a. A mixture composed of 62,5 vol% of water, 25 vol% of isopropanol and 12,5 vol% of 5wt% nafion solution (WIN solution) is previously prepared. PDC/rGO composite is gently crushed in a mortar and dispersed in the WIN solution with a concentration of 5mg/ml. The solution is then sonicated for 5min. 10 μ l of the as-prepared “ink” is drop casted on a glassy carbon electrode. The ink is left for drying at room temperature for 1h, a picture of such typical drop casted PDC/rGO electrode is presented in Figure 2-10b.

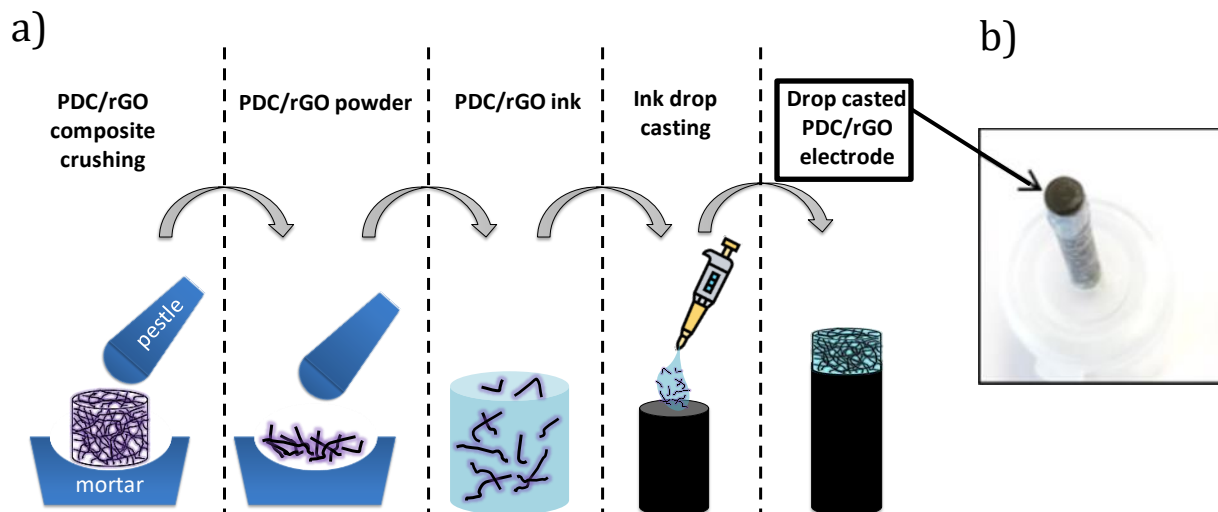
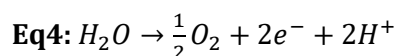
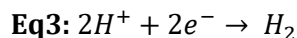


Figure 2-10: a) Sample preparation for electrocatalytic test of PDC/rGO composites b) Picture of a drop casted PDC/rGO electrode

2.2.6.2 Electrocatalytic measurements

Evaluation of the electrocatalytic performance is performed thanks to the traditional three-electrode setup connected to a VSP500 potentiostat from Biologic. A description of the setup is presented in Figure 2-11. The $\text{Hg}_2\text{Cl}_2/\text{Hg}$ electrode and graphite rod (Alfa Aesar) were used as reference (REF) and counter electrode (CE), respectively, and immersed in $0.5 \text{ mol.L}^{-1} \text{ H}_2\text{SO}_4$ electrolyte. The working electrode (WE) previously prepared (see 2.2.6.1) is also immersed in the electrolyte solution and a potential (V) is applied between REF and WE. The application of this potential leads to the activation of water electrolysis reactions taking place on the surface of the WE and CE. The semi-equation of the involved electrochemical reactions is mentioned in Figure 2-11. The reduction (Eq3) and oxidation (Eq4) reactions occurring at the WE and CE conduct respectively to the production of dihydrogen and dioxygen.



The electron flow created by those reactions RedOx is translated by a current I measured between WE and CE. The intensity of this current I versus the potential V gives indications on the quantity of H_2 created from the Eq3 and thus on the performances of the electrocatalyst.

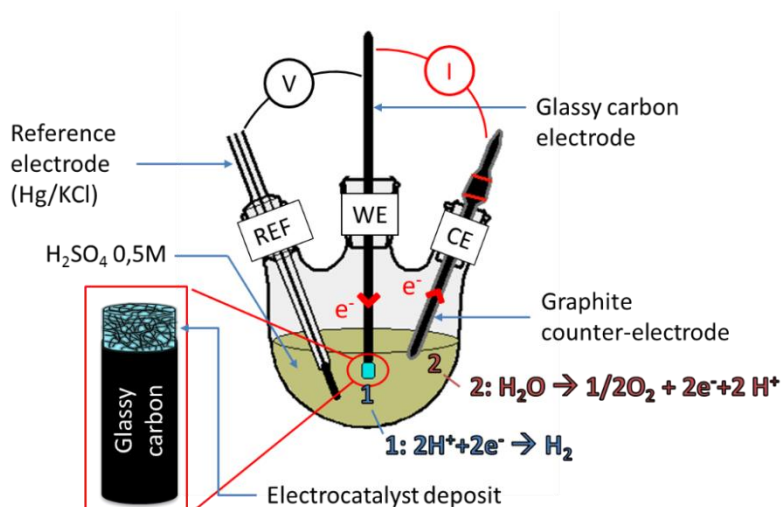


Figure 2-11: Three electrode setup for electrochemical characterization of electrocatalysts

Applied potential was corrected to the reversible hydrogen electrode (RHE). The double-layer charge capacitance (C_{dl}) evaluated by cycling the electrocatalyst at increasing steps from 5 mV s^{-1} up to 250 mV s^{-1} between 241 and 91 mV vs. RHE. An estimation of the C_{dl} was operated thanks to the calculus of the slope of the anodic and cathodic current densities at 166mV vs. RHE. All potentials presented were corrected for iR losses unless specifically noted.

2.2.7 Free standing electrodes preparation

The preparation of free standing electrodes follow the method described in section 2.2.3 but the volume of GO solution introduced in the autoclave reactor is higher (30 ml in the case of free-standing electrode versus 10 ml for classical rGO foam). The resulting GO foam is presented in Figure 2-12 and presents significantly larger dimensions.

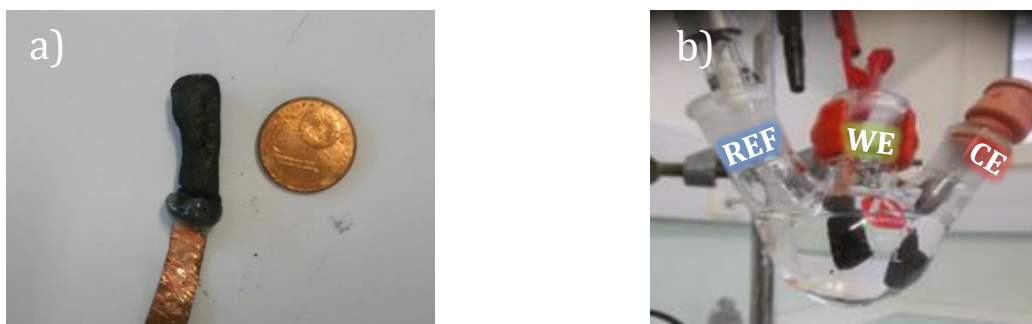


Figure 2-12: a) large PDC/rGO composite with copper foil connection b) Free standing PDC/rGO electrodes

After reduction, impregnation and pyrolysis of the composites, as-obtained free standing PDC/rGO electrode is directly used as a WE in the three-electrode setup described in section 2.2.6.2.

2.3 Preparation of micropatterns based on Si(B)CN ceramic *via* soft-lithography

2.3.1 Boron-modified polyvinylsilazane synthesis and characterization

The synthesis method of SiBCN precursor with Si/B ratio of 17 and 30 is identical to that presented in section 2.3.1. The only variation with the synthesis of Si/B ratio is the quantity of BDMS solution introduce in the reaction medium. The ratio of 17 corresponds to a complete hydroboration of vinyl groups (with almost no dehydrocoupling of N-H). We increase the ratio to 30 to decrease the crosslinking rate in PBVZ to obtain more fluid polymer. Typically, for 5g of PVZ 2.3 and 1.3 ml of BDMS is added *via* dropping funnel for Si/B= 17 and 30, respectively.

The description of the equipment used for FT-IR and solid-state NMR spectroscopy and TGA analysis is already presented in section 2.3.1. Nevertheless, some precursors were characterized with ^1H , ^{13}C , ^{11}B and ^{29}Si liquid-state NMR spectroscopy. Studied chemicals were dissolved in deuterated THF and analyzed with a Bruker AM 300 spectrometer operating at 300 MHz.

2.3.2 Soft-lithography procedure

2.3.2.1 PDMS mold preparation

A PDMS mixture composed of curing agent and elastomeric base is prepared according to a ratio 10:90. The preparation of PDMS molds consists in pouring the viscous PDMS preparation (Sylgard184, Dow-Corning) on SU-8 master. Briefly, a master mold was made with SU-8 photoresist on a 3inch silicon wafer using photolithography process. A layer of SU-8 2015 (25 μm high) was spin-coated (1500 rpm) on wafer, then baked, exposed and developed. The obtained SU-8 masters and their Computer Aided Design (CAD) layout are displayed in Figure 2-13.

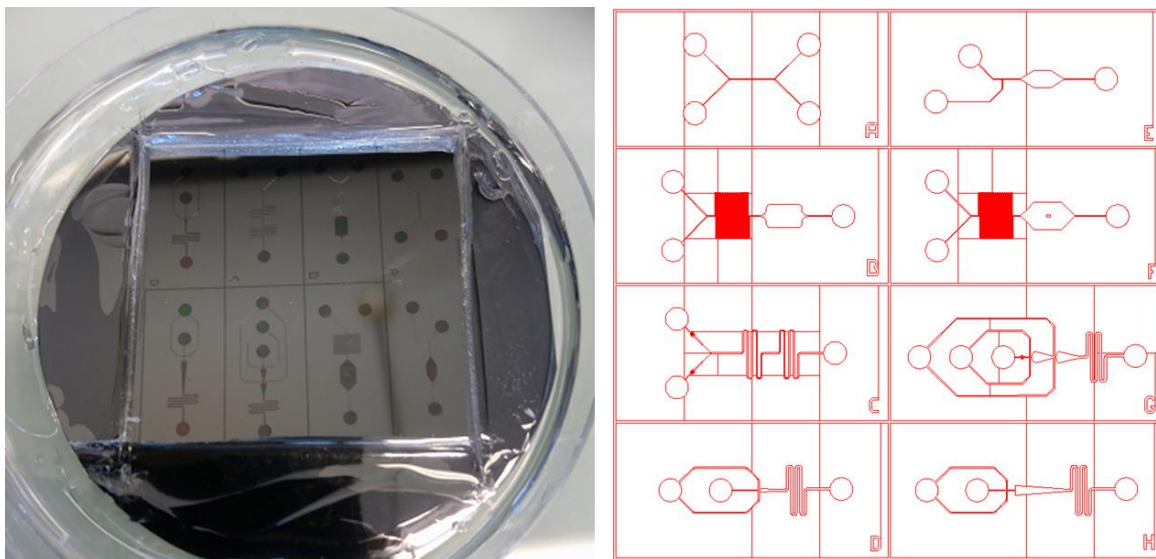


Figure 2-13: SU-8 master used for PDMS mold preparation (left) and CAD drawing associated (right)

After PDMS pouring, eventual air bubbles trapped in the viscous liquid are removed by degassing the preparation during 30 min in a vacuum chamber. Degassed PDMS is then transferred in an oven at 70°C and for 12h. PDMS molds are cut with a cutter and detached from the wafer out for individual utilization.

2.3.2.2 Micropattern preparation via embossing

The scheme presented in Figure 2-14 describes the embossing technique employed for the preparation of PDC based micropatterns. Silicium wafer were previously washed by 2 min sonication in acetone followed by 2 min in ethanol. The last small dust and residual solvent were removed by compressed air blow.

Mixture of preceramic polymer and fillers (with polymer:fillers ratio ranging from 10:90 to 50:50) are prepared under argon atmosphere in a glove box. Different fillers are tested: MoS₂ (Nanografi, 1-3µm), MoSi₂ (Sigma Aldrich, 1-3µm) and Al₂O₃ (CHI instrument, 30-50nm). The as-prepared suspensions are intensively mixed and homogenized with a speedmixer (1600 rpm for 2 min). Few droplets of the fillers-containing preceramic suspensions are deposited on silicon wafer and PDMS mold is applied with a small pressure. The assembly is then transferred in a tubular furnace for crosslinking the polymer at 130°C for 10h under N₂ (heating and cooling rate at 1°C/min). After the thermal treatment, samples are reintroduced in a glove box for PDMS mold removal. The pyrolysis

step is finally carried under nitrogen at 1000°C for 2h with a heating rate of 1°C/min and cooling rate 2°C/min.

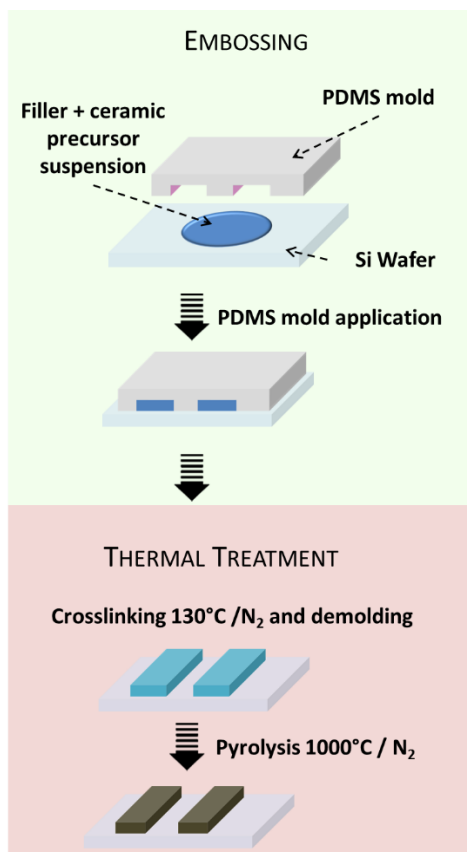


Figure 2-14: Embossing technique for preparing PDC/filler micro-patterns

2.3.2.3 Micropattern preparation via MiMiC/injection

Figure 2-15 describes the method employed to perform micro-patterns *via* MIMIC technique. Previously prepared PDMS mold is disposed on a clean silicon wafer. A “homemade” device manufactured from a petrish dish maintains the PDMS plated on the surface (see Figure 2-15.right). Inset for capillary tube are drilled in the mold to connect micro-channels with a syringe filled with precursor solution. The liquid is carefully introduced in the channel by using a syringe pump.

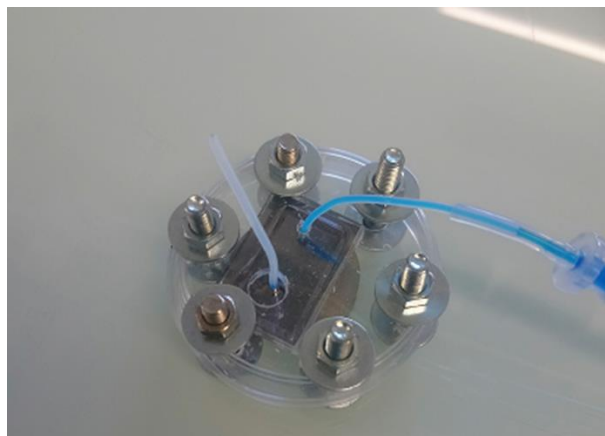
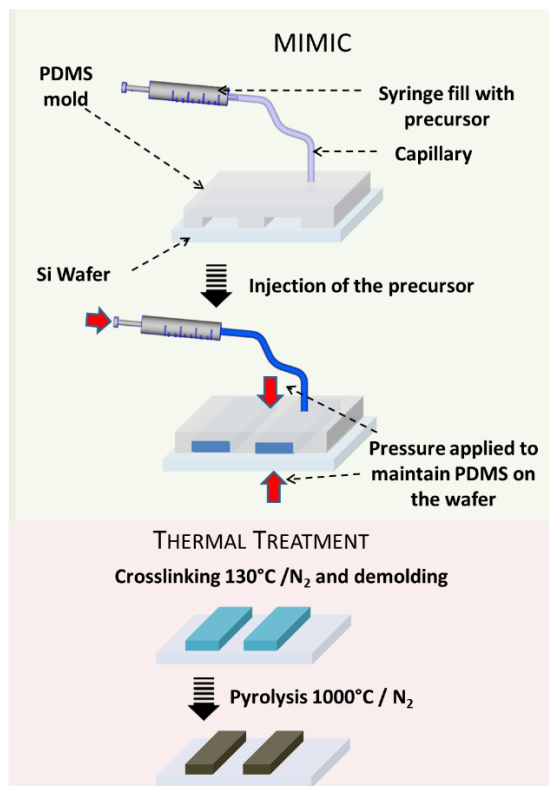


Figure 2-15: MiMiC injection technique for preparing PDC/filler micro-patterns (left: schematic principle, right: camera picture)

While maintaining the pressure on the wafer, the assembly is transferred in a furnace for pre-crosslinking at 70°C for 1h under N₂ flow. After this pre-treatment, the holding pressure is removed and crosslinking of the MIMIC shaped precursor is performed at 200°C for 1h under N₂ atmosphere. PDMS mold is then removed in a glove box atmosphere and subsequent pyrolysis of the micro-patterns assured the polymer-to-ceramic transformation.

2.3.3 Chemical and geometrical characterization of micropatterns

The morphology of the as-prepared samples is investigated with SEM and High Resolution Numerical Microscopy. SEM observations are carried out on Pt metalized samples and observed with Hitachi S4800 SEM. High resolution pictures are produced thanks to a Keyence VHX-7000 microscope. Depth from Defocus (DFD) technology integrated in the Keyence microscope allowed topography and profilometry reproduction of the PDCs based micropatterns.

Elemental composition of the samples is also investigated by EDX analysis thanks to a Zeiss EVO HD1R analyzer and Oxford instruments X-Max SDD sensor.

2.3.4 Electrocatalytic measurements on Si(B)CN/(MoS₂/MoSi₂)

Suspensions of MoSi₂ and/or MoS₂ in PVZ or PBVZ polymers were prepared thanks to Speedmixer, DAC 150.1 FV (1600 rpm for 2 min) and consecutively pyrolysed at 1000°C/2h under nitrogen. The material obtained was crushed in a mortar and dispersed (5mg/ml) in a mixture composed of 62,5 vol% of water, 25 vol% of isopropanol and 12,5 vol% of 5wt% nafion (WIN solution). After 5 min of sonication, 10µl of the as-prepared “ink” is drop casted on a glassy carbon electrode. The ink is left for drying at room temperature for 1h and used as a working electrode in a three-electrode set up for electrocatalytic measurements (see description in 2.2.6.2).

2.3.5 Pellets preparation and dielectric spectroscopy measurement

The electronic characterization of the materials prepared in this thesis was carried out on small pellets and by dielectric spectroscopy. The prepared pellets consists in composites with SiCN matrix and fillers (MoS₂ or MoSi₂). In a first step, a PVZ precursor suspension loaded with 40wt% of filler and 3wt% Dicumyl peroxide was cross-linked in tubular furnace at 200°C for 2h under nitrogen atmosphere. The resulting solid was then crushed in a mortar and warm-pressed with Atlas™ Automatic (Auto) 8Ton and at 250°C, for 40min under 3 tons of pressure. The formed pellet was then placed in tubular furnace for pyrolysis under nitrogen at 1000°C/2h. Dielectric spectroscopy (from 1 mHz to 100 kHz) was then carried out with a Novo-control spectrum analyzer

2.4 Photolithography of preceramic polymer

2.4.1 Preceramic photoresist synthesis and characterization

The synthesis of photosensitive preceramic polymers consists in grafting photosensitive functions (acrylate or methacrylate) on the polymer backbone. The assembly used for this synthesis is presented in Figure 2-16. In a typical reaction, 5g of precursor PVZ (or PBVZ) is introduced in a TNR flask and dissolved in 100ml of toluene. IEM (or IEA) additive is then added dropwise to the reaction medium [6]. The quantity of introduced IEM (or IEA) ranged from 5 to 20 wt% of IEM (or IEA) versus PVZ (or PBVZ) preceramic polymers.

Reaction is left under stirring at RT for 24h and the solvent is removed from the reaction medium by distillation step described in section 2.2.1. The final product consists in a translucent viscous liquid or a solid depending on the crosslinking degree i.e. quantity of introduced boron and/or photosensitive additives.

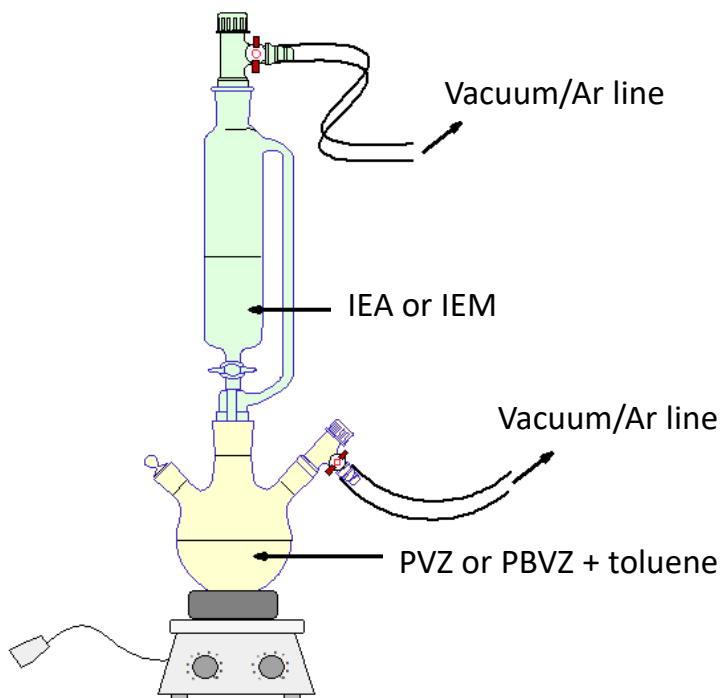


Figure 2-16: Assembly description for the synthesis of photosensitive precursor

The photosensitive preceramic polymers were characterized by FT-IR, solid-state NMR, liquid state NMR spectroscopy and TGA analysis with the same method and equipment presented in sections 2.2.1 and 2.3.1. Chemical characterization was completed with diffusion-ordered NMR spectroscopy (DOSY) performed with Bruker Avance III 600 spectrometer operating at 600 MHz and equipped with a probe Prodigy TCI. DOSY data set is typically acquired using a pulsed field gradient spin echo or stimulated echo (PFGSE or PFGSTE) pulse sequence. Informations on diffusion is obtained by recording spectra with different field gradient pulse amplitudes. A diffusion coefficient for each signal can normally be obtained by fitting the signal attenuation to the equation Eq5 for unrestricted diffusion.

$$\text{Eq5 : } \rho = \exp[-D(\gamma g \delta)^2 \left(\Delta - \frac{\delta}{3}\right)]$$

where ρ is the attenuation factor, D is the diffusion coefficient, γ is the magnetogyric ratio, g is the gradient strength, Δ is the corrected diffusion time and δ is the gradient pulse width.

The evaluation of the photosensitivity of the synthesized polymers was investigated by UV-vis spectroscopy. UV absorbance spectra were obtained with a JASCO V-570 spectrometer on 200-450 nm wavelength range. Analysed products were dissolved in THF with concentration of 0.5mg/ml and placed in quartz cells.

2.4.2 Photolithography procedure

To prepare PDC micropatterns by photolithography, photosensitive preceramic polymers are dissolved in toluene with a concentration of 50mg/ml. 2-Benzyl-2-dimethylamino-1-(4-morpholinophenyl)-butanone-1 (BDMB, ABCR chemical) is used as photo-initiator and is dissolved in the previously prepared polymer/toluene solution. BDMB ratios varying from 1 to 5wt% in the polymer/toluene solution were tested.

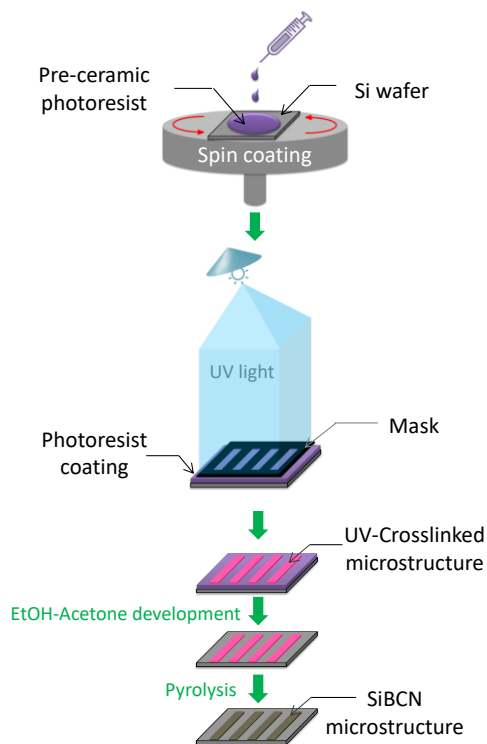


Figure 2-17: Description of the photolithographic process for preparing ceramic micro-patterns

The full description of the photolithographic method for the preparation of PDC micro-patterns is presented in Figure 2-17. To prepare a film of preceramic photoresist, a silicon

wafer is introduced in a spin-coater and covered with few droplets of photoresist solution. The spin-coating cycle consists in a first step of 30s with a speed rotation of 1000 rpm. During this first step 0.5 ml of additional photoresist solution is added dropwise to fully cover the silicon wafer. Second step of 10s at 2000 rpm is then applied to dry the film by evacuating the toluene contained in the film.

A mask is placed on the as-prepared photoresist film and exposed to UV light with a UVP B-100AP/R lamp. The exposed films are then developed in ethanol to dissolve un-exposed resist and rinsed with acetone to remove residues. Silicon wafer was subject to a thermal treatment at 1000°C for 2h (heating rate of 1°C/min and cooling rate of 2°C/min).

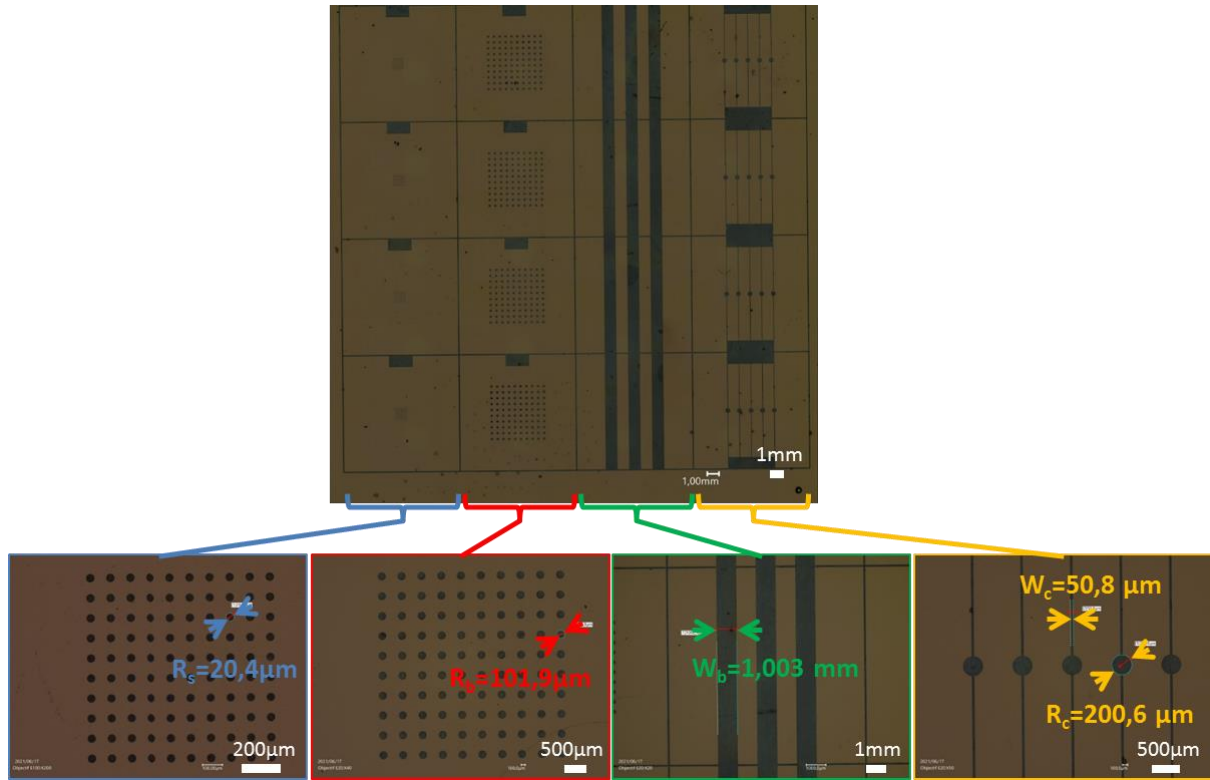


Figure 2-18: Optical microscopy and dimensions of the photomask layout

High resolution numerical microscopy observations and measurements of the UV-mask used in this study are presented in Figure 2-18. UV-mask consists in four different simple patterns disposed in column and replicated on four lines. The four drawn patterns consist in small dots with radius R_s , big dots with radius R_b , big channels with W_b width and small

channels with W_c width and R_c radius. The dimensions associated with each of this pattern are displayed in Figure 2-18

2.4.3 Surface characterization

The SEM and high resolution numerical microscopy observation are carried out with the same method and apparel described in part 2.3.3. Moreover, the profilometric and topographic investigation of the samples are carried out with a Veeco Dektak 150 profiler (Veeco, Plainview, NY, USA) and a Nano-observer (CSInstrument) atomic force microscope (AFM) in tapping mode. Silicon cantelivers (PPP-NCH, Nanosensors) with tip radius of ~ 5 nm with a resonance frequency of about 235 kHz were used.

2.4.4 Nanoindentation - microindentation

Nanoindentation experiments are performed using CSM Instruments Open Platforms. Indentations are conducted using a Berkovitch indenter (pyramidal tip). Indentation sites are selected by optic microscopy (x500). The load range is from 10 μ N to 500 μ N (resolution 0.1 μ N and 0.1nm) for the ultra nanoindentation platform and from 100 μ N to 8 mN (resolution 0.1mN and 0.3nm) for the microindentation platform.

The force required to indent the material is monitored as a function of the penetration depth. The elastic modulus of the samples can be derived from the load-displacement loading/unloading curves. The data are analyzed with the most extensively used method proposed by Oliver and Pharr [8].

2.5 Bibliography :

- [1] <https://www.paint.org/coatingstech-magazine/articles/polysilazanes-binders-that-make-a-difference-to-surfaces/>
- [2] Okamura, T., Kanda, T., Sakurai, I., Barnickel, B.B., and Aoki, H., "Perhydropolysilazane, composition containing same, and method for forming silica film using same," United States Patent No. US9793109B2 (2014).
- [3] A. Viard *et al.*, « Molecular Chemistry and Engineering of Boron-Modified Polyorganosilazanes as New Processable and Functional SiBCN Precursors », *Chemistry – A European Journal*, vol. 23, n° 38, p. 9076-9090, 2017, doi: [10.1002/chem.201700623](https://doi.org/10.1002/chem.201700623).

[4] W. S. Hummers et R. E. Offeman, « Preparation of Graphitic Oxide », 1958, doi: [10.1021/JA01539A017](https://doi.org/10.1021/JA01539A017).

[5] Y.-C. Shi *et al.*, « One-step hydrothermal synthesis of three-dimensional nitrogen-doped reduced graphene oxide hydrogels anchored PtPd alloyed nanoparticles for ethylene glycol oxidation and hydrogen evolution reactions », *Electrochimica Acta*, vol. 293, p. 504-513, janv. 2019, doi: [10.1016/j.electacta.2018.10.068](https://doi.org/10.1016/j.electacta.2018.10.068).

[6] T. Anh Pham, P. Kim, M. Kwak, K. Y Suh, et D. Kim, « Inorganic Polymer Photoresist for Direct Ceramic Patterning by Photolithography », *Chemical communications (Cambridge, England)*, vol. 39, p. 4021-3, nov. 2007, doi: [10.1039/b708480c](https://doi.org/10.1039/b708480c).

[7] D. Massiot *et al.*, « Modelling one- and two-dimensional solid-state NMR spectra », *Magnetic Resonance in Chemistry*, vol. 40, n° 1, p. 70-76, 2002, doi: [10.1002/mrc.984](https://doi.org/10.1002/mrc.984).

[8] Oliver, W.C. and Pharr, G.M. "An Improved Technique for Determining Hardness and Elastic Moduli using Load and Displacement Sensing Indentation Experiments" *Journal of Materials Research*, 7, 1564-1583, 1992, doi: [10.1557/JMR.1992.1564](https://doi.org/10.1557/JMR.1992.1564)

***Chapter III : Polymer-derived
ceramics/reduced graphene oxide
composite systems as active catalysts
towards the hydrogen evolution reaction
(HER)***

3	Polymer-derived ceramics/reduced graphene oxide composite systems as active catalysts towards the hydrogen evolution reaction (HER).....	118
3.1	Introduction and state of the art reminder.....	118
3.2	Chemical characterization of the material.....	119
3.2.1	Preceramic polymer characterization.....	119
3.2.2	PDC/rGO composite characterization.....	123
3.2.2.1	Microscopy observation	123
3.2.2.2	PDC/rGO composite nano and microstructure	127
3.3	Electrocatalytic performances.....	132
3.3.1	Influence of chemical composition on performance	132
3.3.1.1	ECSA (Electrochemical active surface area) estimation	132
3.3.1.2	Polarization curves and Tafel slopes	134
3.3.2	Influence of microstructure on performances.....	137
3.3.3	Influence of porosity/active surface.....	138
3.3.4	Stability investigation.....	139
3.3.4.1	Stability curves	139
3.3.4.2	Comparison with the literature	140
3.3.5	Free standing electrodes	141
3.3.5.1	Polarization curves	141
3.3.5.2	Mechanical performances of composites	142
3.3.6	Conclusion/perspectives.....	143
3.4	Bibliography.....	144

3 Polymer-derived ceramics/reduced graphene oxide composite systems as active catalysts towards the hydrogen evolution reaction (HER)

3.1 Introduction and state of the art reminder

In chapter 1 dedicated to the literature review, we put forward the importance of electrocatalysts materials for Hydrogen Evolution Reaction (HER). We hypothesized that PDCs could play a significant role for the design of low-cost, stable and HER active catalysts. Indeed, the PDCs route offers an atomic scale control of the ceramic microstructure and leads to functionalized materials for specific applications. Combining PDCs with 2D materials seemed to us a promising composite since for example graphene doped with heteroatoms may develop catalysts properties for HER. This is why, our study focus on (O)-Si-(B)-C-(N) PDC impregnated in reduced graphene oxide (rGO) foams.

The main objective of the work in this section was to design and study PDC/rGO based electrocatalysts for HER to evaluate their performances in comparison with state of the art catalysts. Several PDC systems were considered i.e. SiC, SiCN, and SiBCN before and after doping with oxygen. To fulfill this purpose we elaborate a protocol for the preparation of PDC/rGO composite with tuned microstructure. By varying the composition of preceramic polymers, the porosity and the crystallinity in such composites, we were able to identify key parameters in the materials microstructure conducting to optimized performances.

The present chapter is divided in three sections. Firstly, the chemical characterization of the SiBCN precursor synthesized for this work is presented and compared with commercial SiCN precursor properties. Secondly, the microstructure of a whole range of O, N, B, C and Si based ceramics incorporated into rGO matrix was carefully elucidated according to their elemental composition and their preparation approach. Thirdly, the performances of those composites as electrocatalysts for HER was measured and correlated with their tuned microstructure.

3.2 Chemical characterization of the material

3.2.1 Preceramic polymer characterization

The chemical structure and the composition were first investigated for two preceramic polymers: **PVZ** (polyvinylsilazane) and **PBVZ** (boron-modified polyvinylsilazane) used as precursors of SiCN and SiBCN, respectively. We prepared **PBVZ** polymer by reacting **PVZ** with **BDMS** (borane dimethylsulfide complex) as a hydroboration agent [1] (see section 2.2.1.). The Si/B ratio in **PBVZ** polymer was fixed at 3 to induce a complete hydroboration and dehydrocoupling of the vinyl and N-H groups of PVZ, respectively, thus conducting to the formation of B-C and B-N bonds. With the **BDMS** action, B-N bonds formation also occurs *via* dehydrocoupling reactions with N-H groups. FT-IR spectra are presented in Figure 3-1. The spectrum of **PVZ** precursor displays the conventional absorption bands of the chemical functions of organosilazane with notably N-H bonds at 3382 cm^{-1} coupled to the vibration of Si-N at 1170 cm^{-1} [2][3]. For **PBVZ**, intensities of the signals attributed to the vinyl groups decrease in comparison with **PVZ** suggesting thus that a hydroboration reaction occurred. Simultaneously, the increase of the signal around 1325 cm^{-1} confirms the emergence of B-N bonds *via* dehydrocoupling reactions. The intensity of the peak of N-H bonds at 3382 cm^{-1} decreases significantly after the incorporation of boron.

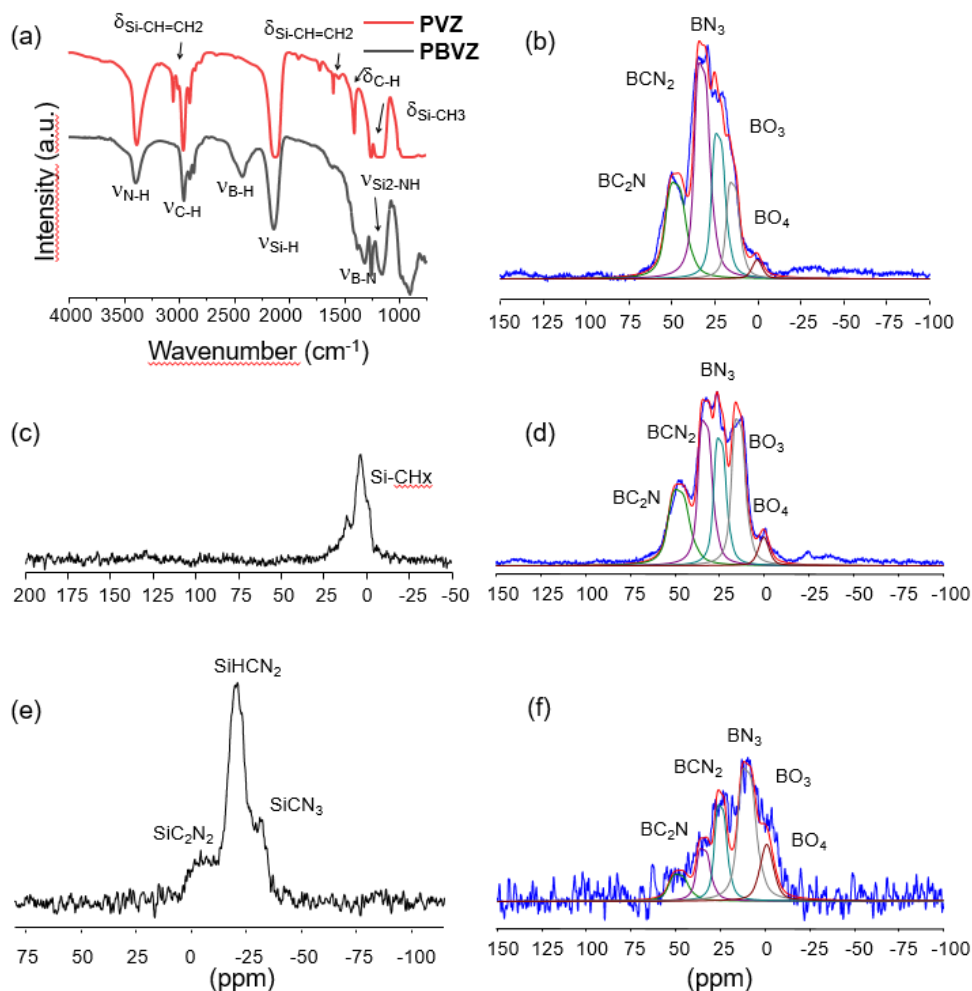


Figure 3-1: (a) FTIR spectra of PVZ and PBVZ preceramic polymers. ¹¹B MAS NMR spectra of (b) PBVZ, (d) O-PBVZ polymers and (f) O-PBVZ/rGO composite. (c) ¹³C CP MAS NMR spectrum of PBVZ polymer and (e) ²⁹Si MAS NMR spectrum of PBVZ polymer.

The chemical structure of **PBVZ** was more precisely described thanks to solid-state NMR analysis for identifying the local environment around boron, carbon and silicon atoms. The solid-state NMR spectra of ¹¹B, ¹³C and ²⁹Si recorded for **PBVZ** are shown in Figure 3-1b,c and e, respectively. Because of the heterogeneity in the local chemical environment of the boron nuclei and the presence of quadrupolar interactions, the ¹¹B MAS NMR spectra display an important complexity. The presence of tri-coordinated boron atoms is however clearly observed. BC_2N , BCN_2 and BN_3 signals (or also BN_2H since B-H unit is observed by FTIR) can be detected in the broad peak appearing at $\delta_{\text{iso}} \sim 55$ ppm, 40 ppm and 30 ppm respectively in agreement with the literature [1]. According to these results, dehydrocoupling and hydroboration reactions resulting in the formation B–N and B–C

bonds, respectively, are confirmed. The presence of negligible amount of oxygen is also detected by the presence of BO_3 and BO_4 environments at $\delta_{\text{iso}} \sim 15$ ppm, and 0 ppm respectively.

The ^{13}C CP MAS NMR spectrum associated with **PBVZ** shown in Figure 3-1.c. displays a signal centered around 10 ppm in the aliphatic region that can be attributed to the superposition of SiCH_3 (~ 2 ppm), $\text{SiCH}_2\text{CH}_2\text{-B}$ (~ 6 ppm), $\text{SiCHCH}_3\text{-B}$ (~ 11 ppm) and $\text{SiCH}_2\text{CH}_2\text{-B}$ (~ 16 ppm). Again, the presence of these signals is another strong confirmation of the hydroboration reaction in perfect agreement with the FT-IR results. Finally, the ^{29}Si MAS spectrum of the polymer in Figure 3-1.e. displays a relatively complex distribution of $\text{SiN}_x\text{C}_{4-x}$ environments with the obvious presence of $\text{H-SiN}_2\text{-CH}_3$ units centered around -20 ppm [4]. The two other peaks observed around -5 ppm and -30 ppm are attributed to SiC_2N_2 and SiCN_3 respectively.

According to recent publications, heteroatom such as oxygen can play beneficial role in HER electrocatalysis [5][6]. Oxygen-rich **PBVZ** (**O-PBVZ**) was then prepared by exposing the preceramic polymer in air for 48 h to allow the diffusion of oxygen within the polymer and its reaction with the excess of B-H units. The modification of the environments of C, Si and B atoms by oxygen introduction was explored using NMR. The results are displayed in Figure 3-1.d. (^{11}B MAS NMR) and Figure 3-2 ((a) ^{29}Si MAS and (b) ^{13}C CP MAS NMR). The partial oxidation of **PBVZ** is confirmed by the increase of the BO_3 and BO_4 signals in the **O-PBVZ** compared to those in **PBVZ**. Oxidation of the SiN_x species into $\text{SiN}_x\text{C}_y\text{O}_z$ can be identified at -80 ppm as depicted in the ^{29}Si MAS NMR spectrum (Figure 3-2.a). On the other hand, the ^{13}C CP MAS NMR spectrum of **O-PBVZ** (Figure 3-2.b) present no distinction with that of **PBVZ** previously discussed. Finally, ^{11}B MAS NMR analysis of the **O-SiBCN/rGO** composite (Figure 3-1.f.) was carried out. The conductivity of rGO and/or the possible presence of free radicals conduct to poor signal-to-noise ratio compared to **PBVZ** and **O-PBVZ** NMR signals. Nevertheless, careful examination of the ^{11}B spectrum reveals that the signatures of the boron environment in the composite match those from the **PBVZ** preceramic polymer. **O-PBVZ/rGO** composite exhibits the same environments with nonetheless a higher proportion of BO_3 and BO_4 environments compared to BC_2N , BCN_2 and BN_3 confirming that mixing rGO and PDCs does not alter the chemical structure of the

ceramic in the composite. Based on those results, no doping by nitrogen or boron of the graphene support has been revealed since no changes in the chemical environment of boron atoms was noticed between pure **O-PBVZ** signals and O-SiBCN/rGO composite signals.

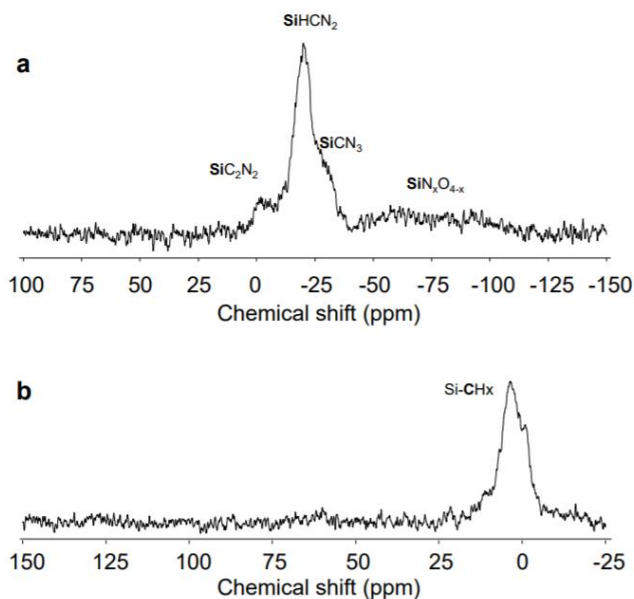


Figure 3-2: (a) ^{29}Si MAS and (b) ^{13}C CP MAS NMR spectra of **O-PBVZ.**

To evaluate the polymer-to-ceramic conversion thermogravimetric analyses (TGA) were performed on the different synthesized polymers. TGA curves display the weight loss of **PVZ**, **PBVZ** and **O-PBVZ** when increasing the temperature up to 1000 °C under nitrogen (Figure 3-3). Results show that the addition of boron significantly increases the ceramic yield of the polymer from 60 to 78% for **PVZ** and **PBVZ** respectively. Remarkably, the addition of oxygen does not drastically affect the weight loss of the **PBVZ** and the ceramic yield is maintained as high as 77%.

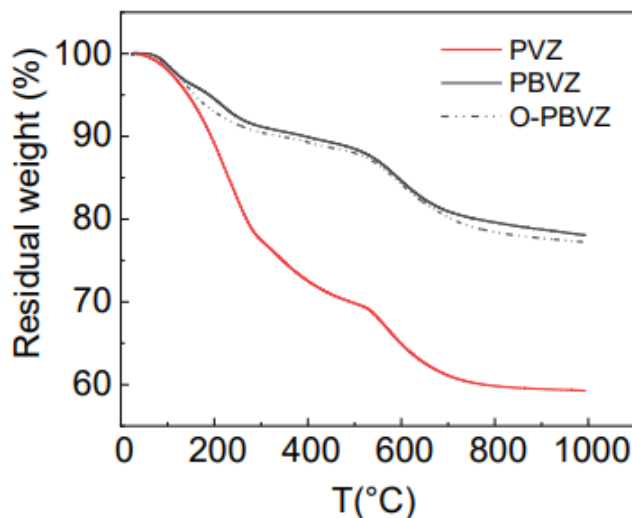


Figure 3-3: TGA curves of PVZ, PBVZ and O-PBVZ up to 1000°C under N_2 (heating rate $5^\circ\text{C}\cdot\text{min}^{-1}$).

The polymer-to-ceramic transformation occurs through several distinctive stages, in particular, two weight losses are predominant: the first one from room temperature up to 300°C (~ 3 wt.% for **PBVZ**) and the second one from 300 up to 1000°C (~ 19 wt.% for **PBVZ**). They are associated to the decomposition of organic components accompanied by the release of gaseous compounds such as H_2 , CH_4 , C_xH_y , NH_3 and other volatile species.

According to the results and discussions developed in this section, we can confirm the synthesis of SiBCN precursor consisting of silazane backbone (Si-NH, Si-H, Si-CH₃, ...) and B-C; B-N branches revealed thanks to FT-IR and NMR investigations. Such composition leads to a significant increase of the ceramic yield as confirmed by TGA. Such preceramic polymers were implemented in the fabrication method of PDC/rGO composites (see section 2.2.4). The characterization of those composites is developed in the next section.

3.2.2 PDC/rGO composite characterization

3.2.2.1 Microscopy observation

Porous structure of rGO, O-SiBCN/rGO and O-SiCN/rGO composites was studied using SEM and TEM. Figure 3-4.a shows the low-magnification SEM images of rGO and O-SiBCN/rGO composite with a 1:1 and 2:1 mass ratio R. The observation of the rGO foam reveals its highly porous structure while the images of O-SiBCN/rGO composites show the reduction of the porosity with the increase of the ceramic/graphene ratio. Similar observations are

made with O-SiCN/rGO composites showing a porosity decreasing with R increasing. The increase of the ceramic ratio in the composite leads to the progressive filling of the pores of the rGO scaffold. For R close to 1 the porous structure of the foam is not altered as suggested by the mercury intrusion porosimetry measurement showing 93% and 97% of porosity for O-SiBCN/rGO (R=1) and rGO alone, respectively. In order to further confirm the presence of O-SiBCN ceramics on the rGO nanosheets, TEM and EELS observations were carried out on the composite (Figure 3-5).

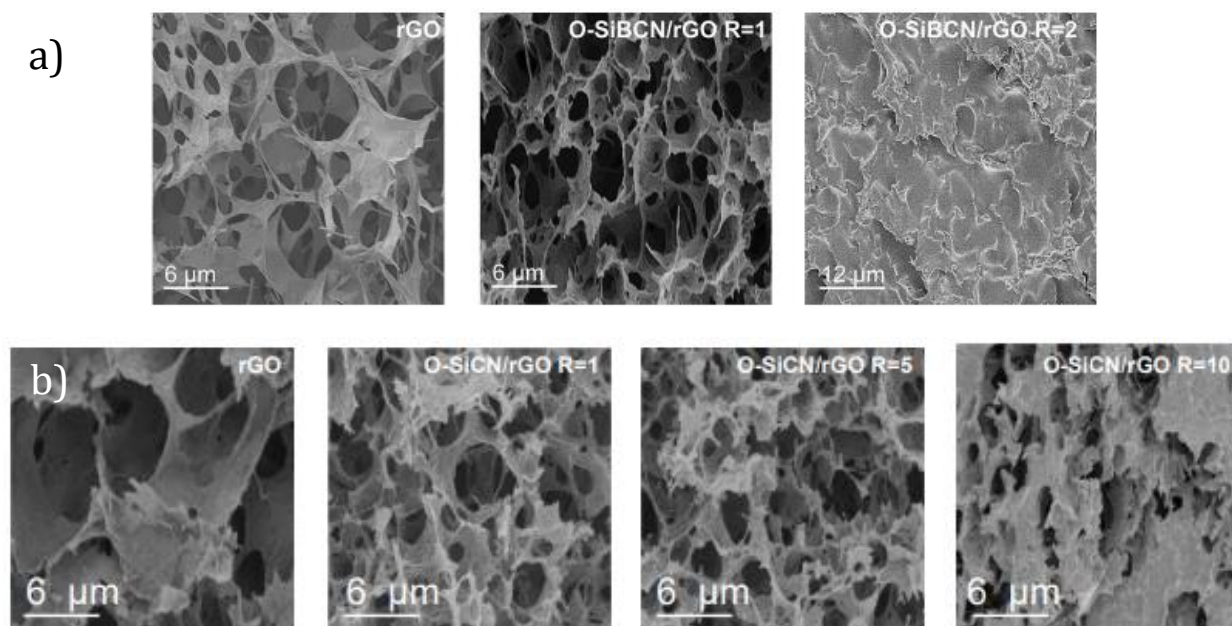


Figure 3-4: High-magnification SEM images of rGO foam, a) O-SiBCN/rGO and b) O-SiCN/rGO composites with a PDC/rGO ratio from 1 to 10..

The two-dimensional nature in the composite is identified from the TEM images and attributed to rGO nanosheets. High-resolution TEM (HRTEM) images reveal that the wall of the foam consists of 4–8 rGO layers with sizes ranging from 50 to few hundred nanometers (Figure 3-5.a.). The measured interplanar distance (d_{002}) for rGO is estimated to ~ 3.85 Å—a value close to interlayer distance of stacked graphene nanosheets of 3.43 Å reported in the literature [7]. Thanks to EELS investigations in Figure 3-5.b, we observed that rGO is coated by O-SiBCN. EELS mapping clearly demonstrates that the ceramic is composed of Si, B, C and N elements homogeneously distributed in the sample. The diffraction pattern suggests a rather disordered structure of the composites as expected from the turbostatic

stacking of the graphene nanosheets and the amorphous nature of the ceramic (Inset Figure 3-5.a).

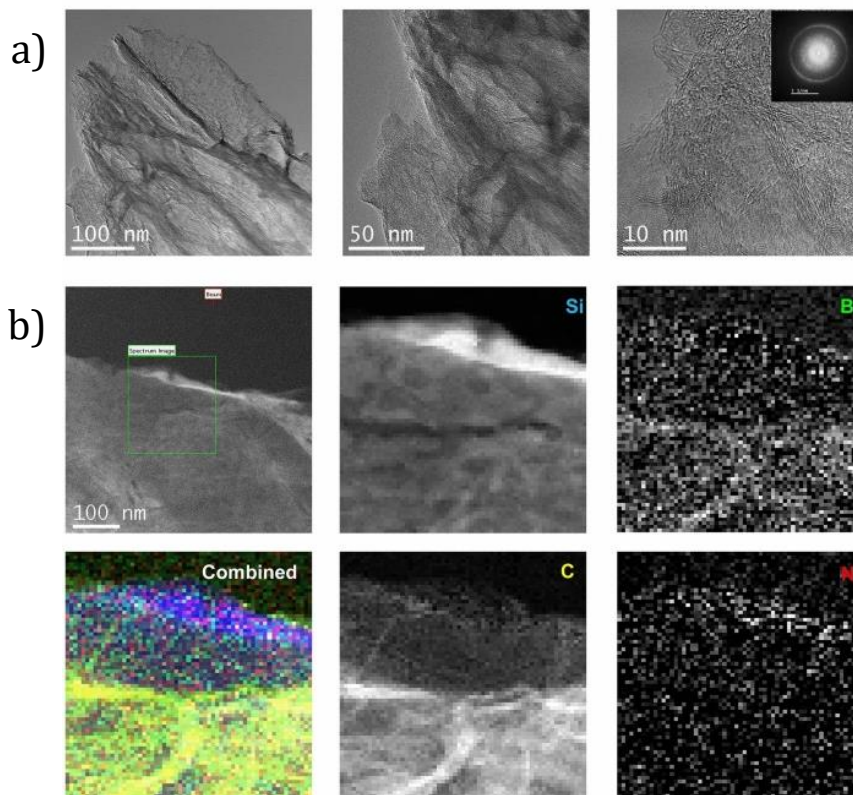


Figure 3-5: a) TEM images of O-SiBCN/rGO ($R_{O-SiBCN/rGO} = 1$). (b) TEM images and the corresponding EELS chemical maps of O-SiBCN/rGO ($R_{O-SiBCN/rGO} = 1$) (Silicon (blue), Boron (green), Carbon (yellow), Nitrogen (red)).

O-SiCN/rGO (derived from **PVZ**/rGO sample) and O-SiC/rGO (derived from **AHPCS**/rGO sample) composites with a 1:1 ratio were also observed with TEM/EELS as displayed in Figure 3-6.a and b, respectively. The presence of silicon carbide (from Si edge) and graphitic carbon (C edge) with small contents of amorphous carbon is detected from the EELS spectra.

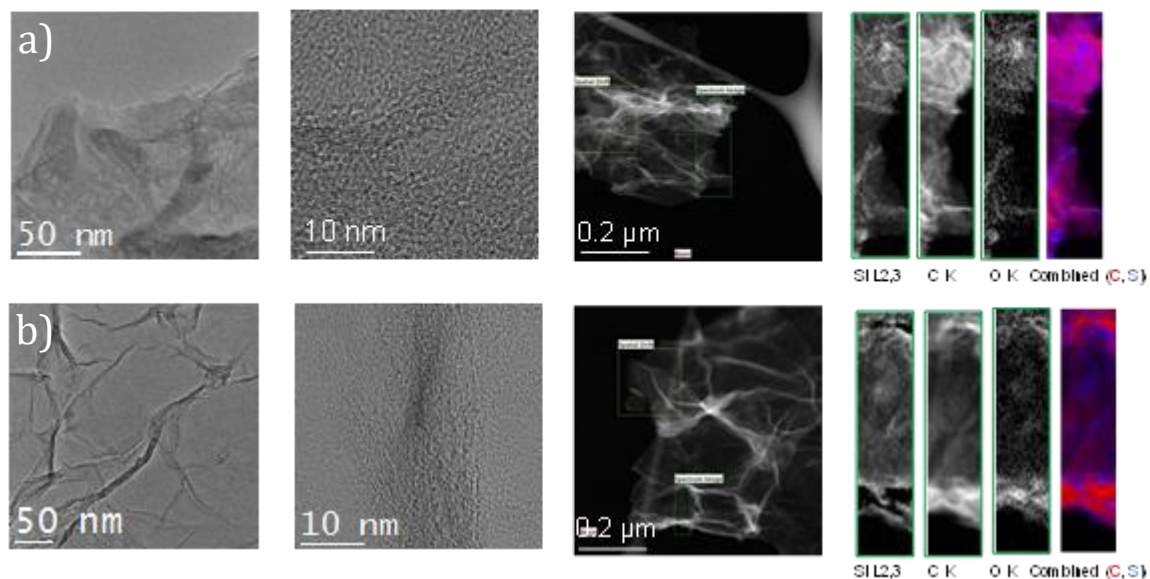


Figure 3-6: EELS with chemical maps for respectively (a) O-SiCN/rGO and (b) O-SiC/rGO composites with a 1:1 ratio.

Finally, EDX mapping shown in Figure 3-7 is an additional confirmation of the O-SiBCN/rGO composite structure. The porous aspect is obvious while the presence of boron, nitrogen and silicon is once again confirmed and suggests the successful infiltration of the preceramic polymer in the foam porosity.

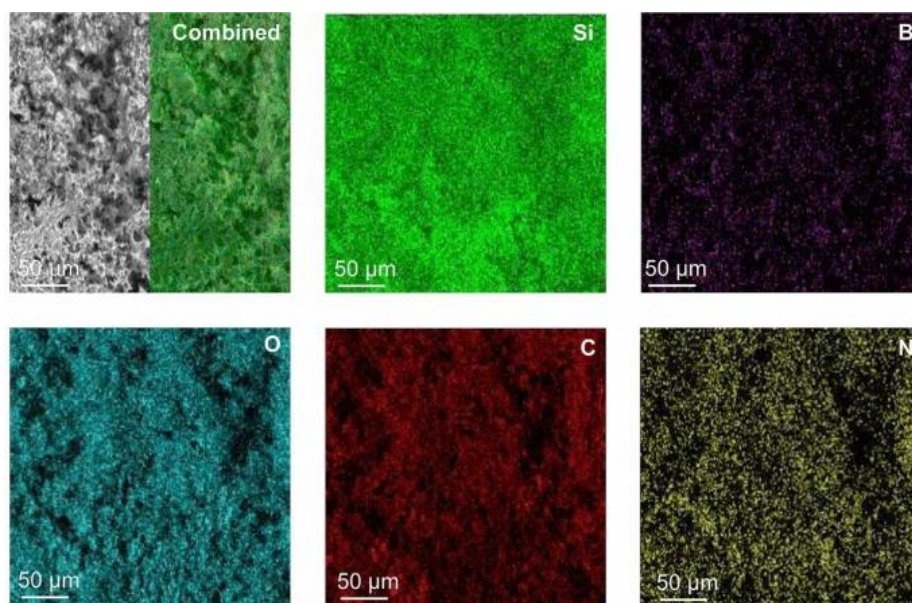


Figure 3-7: Low-magnification SEM image of O-SiBCN/rGO (top left panel) and the corresponding elemental maps.

Thanks to this global microscopy study of the prepared composites several conclusions can be drawn:

- The introduction of ceramic in the rGO pores foams conduct to porosity decrease but for low ceramic/graphene ratio ~ 1 the porous structure is globally conserved
- The graphene nanosheets are still observable after the infiltration and pyrolysis steps
- The ceramic presence after pyrolysis is confirmed by EDX and EELS mapping while Si, B and N elements are detected in the composite

The next section is dedicated to a closer investigation of the material microstructure after the pyrolysis *via* Raman spectroscopy, XRD and XPS, the influence of temperature and polymer composition.

3.2.2.2 PDC/rGO composite nano and microstructure

Using XRD and Raman spectroscopy techniques, we have attempted to elucidate the microstructure of PDCs and PDC/rGO composites. Both O-SiBCN and O-SiCN ceramics progressively crystallize at temperatures higher than 1200 °C as shown by the rise of the peaks at 35.7° (111), 60.3° (220) and 71.25° (311) corresponding to the formation of nanosized β -SiC crystals (Figure 3-8.a-b). The peaks growth is more intense in the case of O-SiCN than for O-SiBCN, boron being an inhibitor of early crystallization (see section 1.1.2.2.2). The incapacity of Si_3N_4 to react with free carbon *via* the carboreduction reaction: $\text{Si}_3\text{N}_4 + 3\text{C} \rightarrow \text{SiC} + 2\text{N}_2$ primarily induces the crystallization into β - Si_3N_4 as confirmed by the peaks detected at 26.5°, 33.7° and 36.1° [8]. Of note, the presence of oxygen has no deleterious effect on the amorphous behavior [8]. It may suggest that the selected ceramics SiBCN and O-SiBCN share similar microstructural framework. According to Raman spectra presented in Figure 3-8.c-d the increase of crystallinity in the composites is also confirmed by the strengthening of Raman peaks from rGO graphitic domains. The position of the G band of O-SiBCN/rGO pyrolyzed between 1000 °C and 1600 °C continuously blue-shifts from 1587.5 to 1579.7 cm^{-1} due to the transition from amorphous disordered carbon to graphitic domains in agreement with the increase of the 2D band [9].

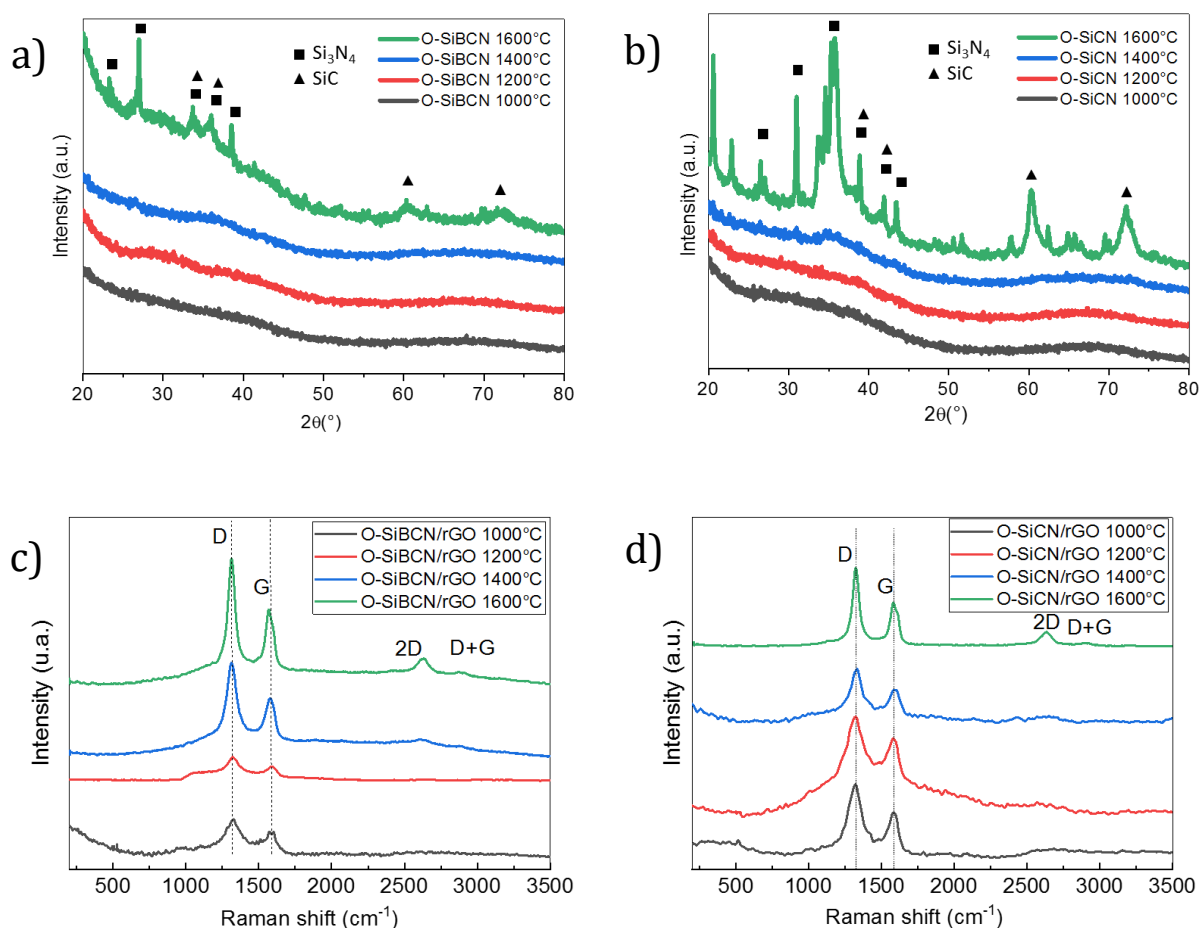


Figure 3-8: (a, b) X-Ray diffractograms of O-SiBCN ceramics and O-SiCN ceramics at different temperatures. (c, d) Corresponding Raman spectra of O-SiBCN/rGO and O-SiCN/rGO composites.

X-ray photoelectron spectroscopy (XPS) was then conducted to investigate the chemical composition of O-SiBCN and O-SiCN based composites pyrolyzed at 1000 °C (Figure 3-9.a and .b). The survey spectra of the composites confirm again the presence of all the elements from the ceramics: Si, B, C, N and O, while no metal impurities can be detected (samples are deposited on a gold-coated substrate which, explains the detection of gold in the survey). High-resolution spectra of O-SiBCN ceramic is presented in Figure 3-10. C1s region was deconvoluted in three distinct components at 283.2, 284.8 and 286.2eV attributed to C-Si, C-C and C-O, respectively. The B1s and N1s signals contain components characteristic of B-C, B-N and N-B at 190.6, 192.2 and 399.1eV, respectively, which are relevant to the B-N and B-C bonds detected in the precursor by NMR analysis. Signals at 101.2, 102.0, and 397.8 eV correspond to Si-C, Si-N and N-Si derived from the polysilazane.

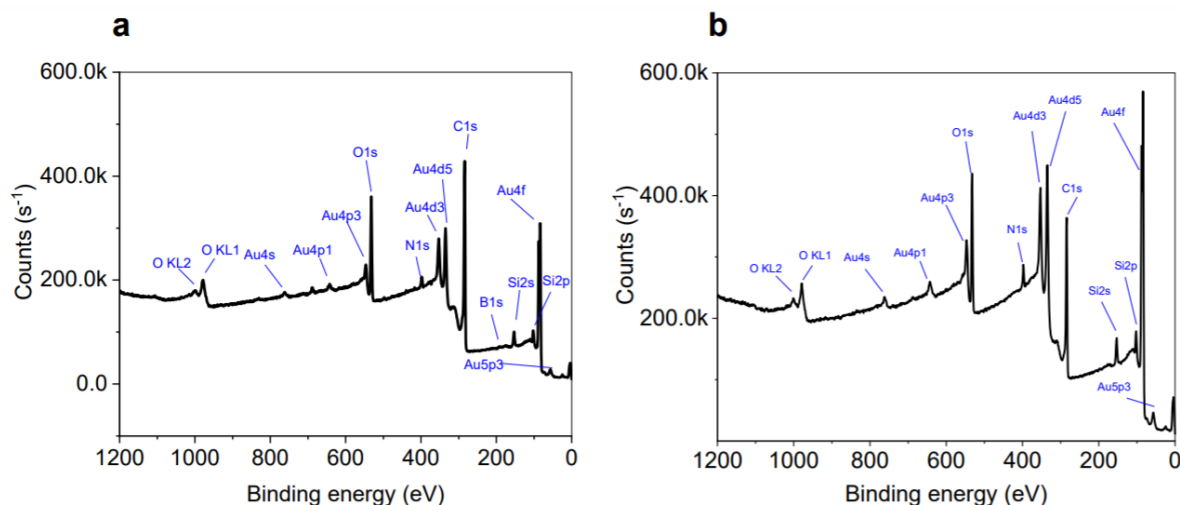


Figure 3-9: XPS survey spectra of (a) O-SiBCN/rGO and (b) O-SiCN/rGO composites.

In comparison, XPS signals associated with O-SiBCN/rGO and O-SiCN/rGO composites are gathered in Figure 3-11. The intense peak at 284.4 eV is attributed to C=C bonds from sp^2 carbons in rGO. Remaining C-O and C=O bonds detected at 285.2 and 286 eV respectively come from the incomplete reduction of the GO foams during the reduction step [10]. Si-O, Si-N, N-SiO_x and N-Si peaks at 103.4 eV, 102.2 eV, 398.4 eV and 397.8 eV respectively confirm the existence of the SiN_xO_y phase in the microstructure of the composite [11][12]. B1s and N1s regions can be deconvoluted with peaks at 190.7 eV, 192.3 eV and 193.4 eV from B-C, B-N and B-O respectively and N-B at 399.1 eV in agreement with the formation of the BN_xO_y phase [13][14]. Remarkably, the value of Si/B ratio is estimated to 3—fully consistent with the expected Si/B ratio for O-SiBCN. This hints that no reaction occurred between the polymer and the rGO during the impregnation and the ceramization process, strongly supporting the observations of NMR.

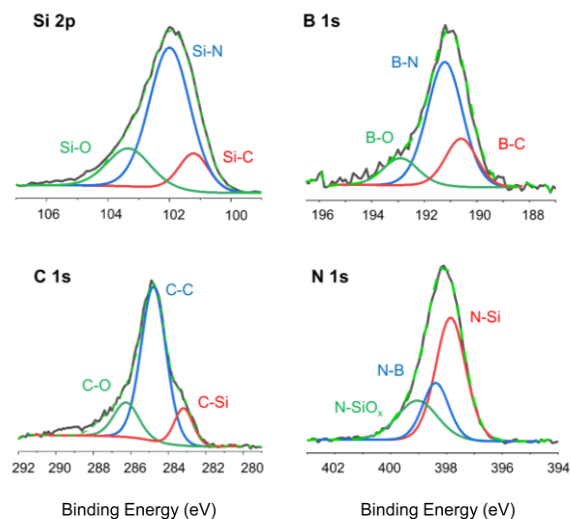


Figure 3-10: XPS spectra of the N1s, C1s, B1s, Si2p regions of O-SiBCN

The formation of SiCN ceramic in O-SiCN/rGO composites was also confirmed from the XPS analyses. Si-C, Si-N, and Si-O bonds are detected at 101.4, 102.4 and 103.7 eV respectively from the Si2p region, while the peaks of N-SiO_x, N-Si, Si-N and Si-C are identified at 399.6, 398, 102.3 and 99.3 eV. [11][12][15][16]

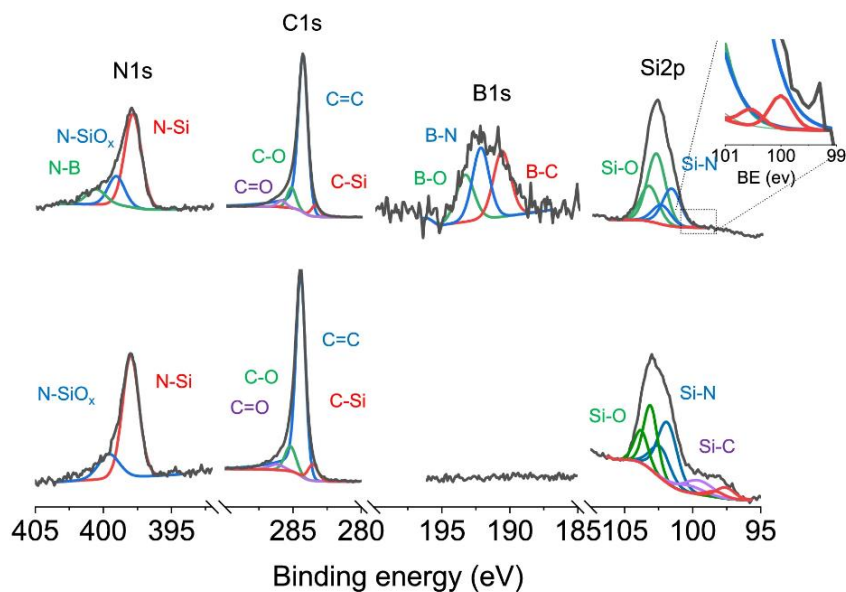


Figure 3-11: XPS spectra of N1s, C1s, B1s, Si2p regions of O-SiBCN/rGO (top) and O-SiCN/rGO (bottom)

To give a final proof of the presence of the ceramic in the composite, we performed TGA of the sample under air atmosphere (Figure 3-12). The weight loss at 1000 °C reaches 63% for O-SiBCN/rGO composites compared to 100% and 0.5% for rGO and O-SiBCN respectively. The weight loss for the composite is attributed to the integral combustion of rGO leaving the O-SiBCN ceramic as confirmed by our EDX analyses. Overall, TGA and XPS confirm the presence of the ceramics within the different PDC/rGO composites.

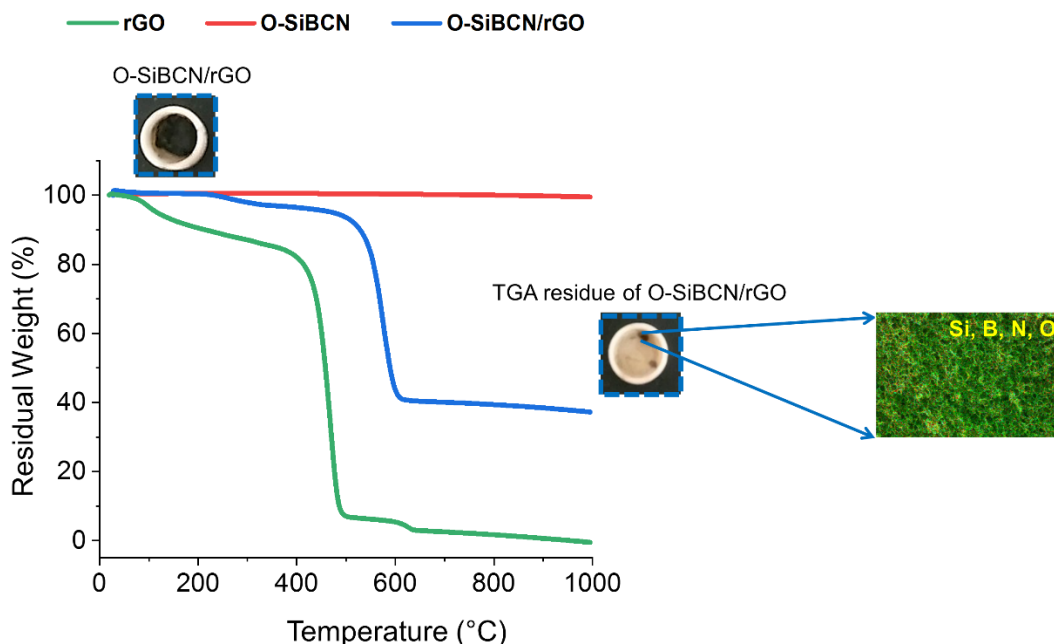


Figure 3-12: TGA of the rGO foam, O-SiBCN ceramic, O-SiBCN/rGO composite under air up to 1000 °C

According to the discussion developed in this section, the microstructure of PDC/rGO composites has been unveiled. Thanks to XRD investigation, the amorphous nature of SiCN and SiBCN ceramics pyrolyzed below 1200°C and their crystallization at higher temperature have been confirmed. More specifically, Raman spectroscopy shows the crystallization of the carbon phase with the annealing temperature increasing from 1000 to 1600°C (see Figure 3-8). The observation of XPS signals gathered from bulk SiCN and SiBCN samples unveiled Si-C, Si-N, C-C characteristics bonds of polysilazane-derived ceramics. On the other hand, SiBCN ceramic differs from SiCN with the detection of B-N and B-C bonds introduced at the synthesis step and conserved after heat treatment. Furthermore, XPS investigation performed on PDC/rGO composites confirms the presence of both graphene nanosheets and Si(B)CN, suggesting that no reaction between the precursor and the

reduced graphene oxide occurs during heat treatment. Finally, the presence of the ceramic in the composite was clearly proven thanks to TGA under air conducting to decomposition.

3.3 Electrocatalytic performances

In this section, the performances of all PDC/rGO composites are evaluated using a potentiostat and a three electrodes set-up as described in section 2.2.6.2. The influence of the porosity, the chemical composition, the ceramic/graphene oxide ratio and the microstructure of the samples will be presented.

3.3.1 Influence of chemical composition on performance

The electrocatalytic performance of pristine ceramics and rGO-based composites was investigated towards the evolution of hydrogen in an acidic solution ($0.5 \text{ mol.L}^{-1} \text{ H}_2\text{SO}_4$). HER activity from the glassy carbon was also measured to confirm that no activity arises from the electrode support. When this is not specified, the results presented are associated with samples with ceramic/graphene ratio equal to 1.

3.3.1.1 ECSA (*Electrochemical active surface area*) estimation

Figure 3-13 gathers several Cyclic Voltammograms (CVs) associated with rGO, SiC/rGO, O-SiC/rGO, SiCN/rGO, O-SiCN/rGO, SiBCN/rGO and O-SiBCN/rGO. By collecting CVs data in the region of 0-0.15V at different scan rates (from 5 to 250 mV/s) the current response is only due to charging of the double layer (see section 1.2.2.2). The double layer capacitance (C_{dl}) has been calculated from the slope of linear fit of current at 0.075V against scan rate. The C_{dl} slopes associated with the different composites are displayed in Figure 3-14, it varies from 420 mV/dec for O-SiBCN/rGO to 301mV/dec for O/SiCN/rGO. Interestingly the composite electrodes display larger C_{dl} than pristine rGO (420 vs. 316 $\mu\text{F.cm}^{-2}$). This is attributed to the mechanical reinforcement of rGO by the ceramics. Indeed, the graphene nanosheets are roughened by the ceramics which prevents the porous structure from collapsing.

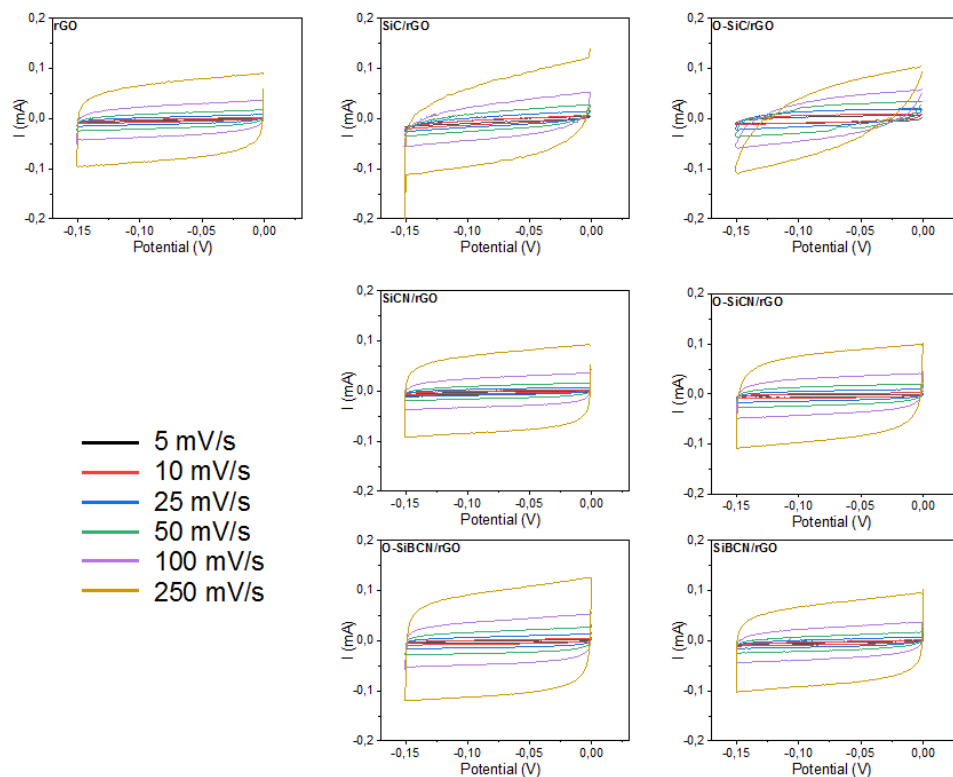


Figure 3-13: Cyclic voltammetry curves for rGO, SiC/rGO, O-SiC/rGO, SiCN/rGO, O-SiCN/rGO, SiBCN/rGO and O-SiBCN/rGO composites. (Ceramic/graphene mass ratio $R=1$)

From the collected C_{dl} values, we estimated the electrochemical active surface area (ECSA). The ECSA was calculated assuming an ideal capacitance of 0.015 mF cm^{-2} [17] for a flat surface of graphene—it is worth noting that the contribution of the ceramic can be neglected due to its insulating nature (see Figure 3-16). All the composites exhibit larger C_{dl} compared to the glassy carbon support revealing the porosity of the electrode in agreement with our SEM observations (see Figure 3-14). The porous network combined with the high electric conductivity of the rGO scaffold provides (i) accessibility to more active sites and (ii) efficient transport pathways of the electrons to the active sites. Among all the different PDC/rGO composites, O-SiBCN/rGO exhibits the largest C_{dl} and therefore the largest ECSA of 28 cm^{-2} .

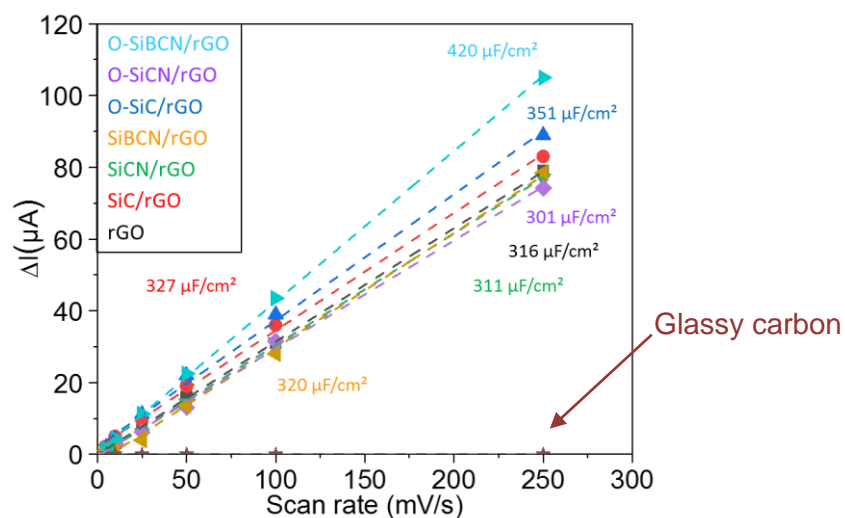


Figure 3-14: Estimation of the double layer capacitance (C_{dl}) for the different electrodes.

3.3.1.2 Polarization curves and Tafel slopes

The polarization curves from the different composite catalysts i.e. SiC/rGO, O-SiC/rGO, SiCN/rGO, O-SiCN/rGO, SiBCN/rGO and O-SiBCN/rGO are presented in Figure 3-15.a. The HER activity is clearly improved in the case of the PDC/rGO compared to glassy carbon and rGO alone—ruling out any possible activity from impurities present in rGO or the conducting support.

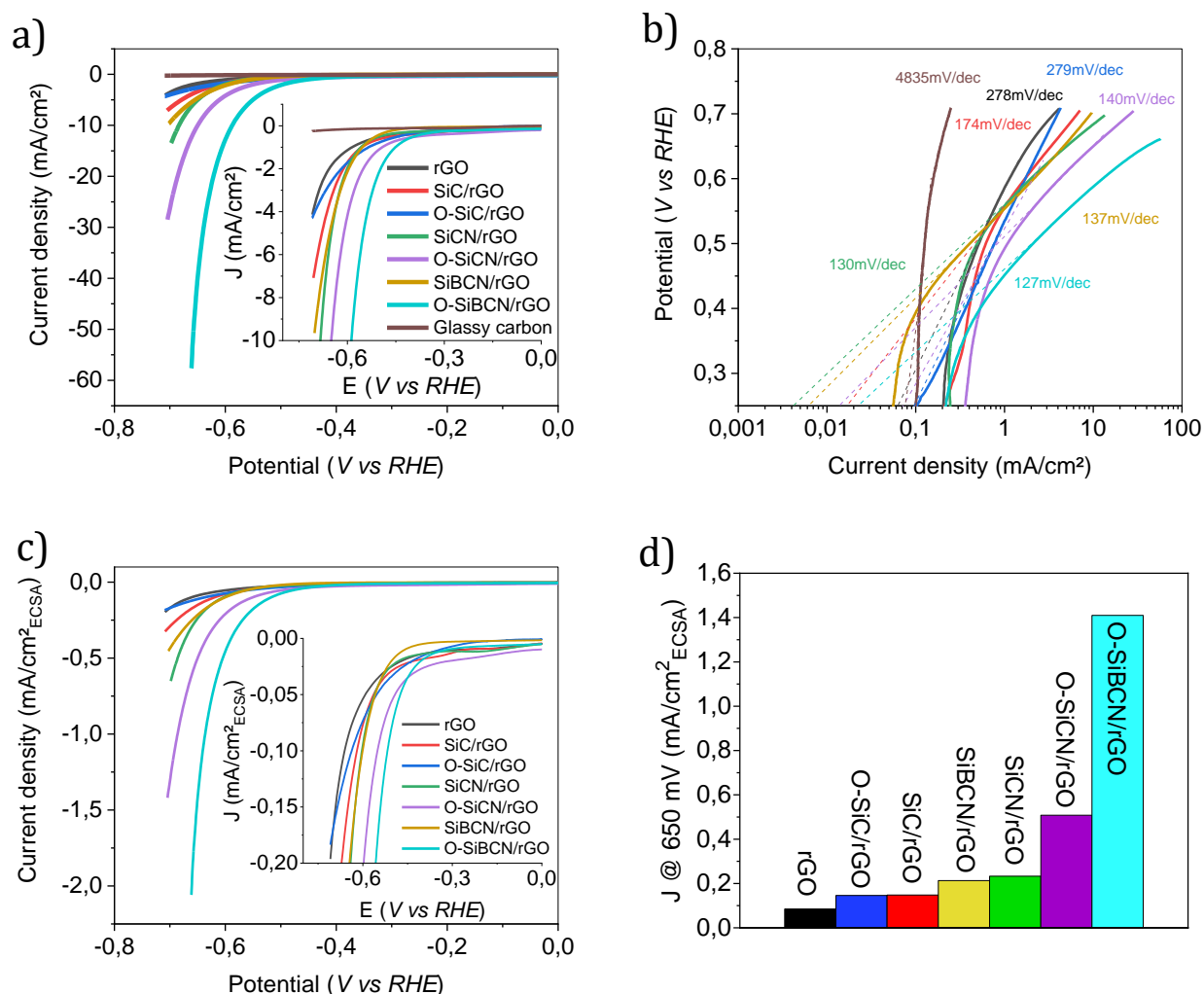


Figure 3-15: (a, b) Polarization curves and Tafel slopes of rGO, SiC/rGO, O-SiC/rGO, SiCN/rGO, O-SiCN/rGO, SiBCN/rGO and O-SiBCN/rGO catalysts. (c) Corresponding ECSA-normalized polarization curves and (d) Histograms displaying the ECSA-normalized current density (J) at $\eta = 650$ mV for the different catalysts.

Remarkably O-SiBCN/rGO showed the best performance among the different PDC/rGO electrodes with an onset potential of -340 mV vs. RHE and a current density as high as 60 mA.cm⁻² at an overpotential of $\eta = 660$ mV. O-SiBCN/rGO also exhibits the lowest Tafel slope at 127 mV dec⁻¹ suggesting faster kinetics and the overpotential at 10 mA cm⁻² reaches 590 mV (Figure 3-15.b). For comparison, overpotentials of $\eta = 51$ mV and $\eta = 20$ mV for driving a current of 10 mA cm⁻² have been measured using Pt-based alloyed catalysts such as Pt-Pd supported on graphene oxide and Pt-Ni-Co [18][19], respectively. As for noble metal-free catalysts such as phosphides, overpotentials of 130–200 mV are requested to produce a current of 10 mA cm⁻² [20] ; comparable to that of MoS₂ deposited

on graphene [21]. It has been shown that a Tafel slope value of 120 mV dec^{-1} corresponds to a kinetically limiting stage attributed to the hydrogen adsorption: Volmer step, $\text{H}^+ + \text{e}^- \rightarrow \text{H}^*$ [22]. In the case of O-SiBCN/rGO, the value of 127 mV dec^{-1} suggests that the reaction on the catalyst surface proceeds *via* the Volmer-Heyrovsky mechanism with the Volmer step being the rate-determining step (RDS). To obtain a fair comparison of the electrodes and avoid any contribution from the porosity of the different composites, we normalized the geometrical current density to the ECSA (Figure 3-15.c). We estimated the ECSA-normalized current density at an overpotential of $\eta = 650 \text{ mV}$ to compare the different composites and the performances follow the trend: $\text{rGO} < \text{O-SiC/rGO} \approx \text{SiC/rGO} < \text{SiBCN/rGO} \approx \text{SiCN/rGO} < \text{O-SiCN/rGO} < \text{O-SiBCN/rGO}$ (Figure 3-15.d.).

Based on the electrochemical measurements and the physic-chemical characterization of the composite, we speculate that the active sites in the composite O-SiBCN/rGO are likely to be located around BN_3 , BC_xN_y nanodomains of the ceramic. This calls for additional investigation notably using first principle calculations that are however beyond the scope of this thesis.

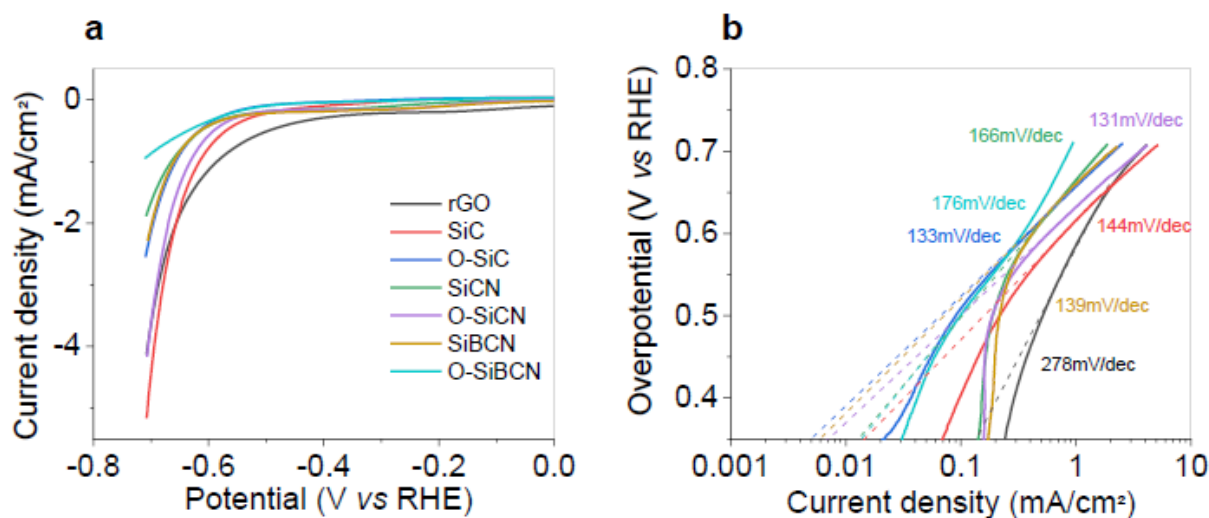


Figure 3-16: (a) Polarization curves and (b) Tafel slopes of rGO, SiC, O-SiC, SiCN, O-SiCN, SiBCN, O-SiBCN catalysts.

Moreover, to examine the role of rGO on the catalytic performance, we assess the electrochemical behavior of the ceramics alone (Figure 3-16). We can see that the ceramics display poor HER activity demonstrating that rGO allows activating the PDCs *via* a

synergistic effect as previously described for supported semiconducting materials [21]. The decrease in Tafel values for the composites compared to their ceramic counterparts emphasizes the role of rGO as a conductive support.

3.3.2 Influence of microstructure on performances

To get further understanding of the nature of the active sites of the O-SiBCN ceramics, the effect of the crystallinity of the ceramics on the electrocatalytic activity of O-SiBCN/rGO and O-SiCN/rGO by annealing the composites at increasing temperatures (Figure 3-17.a-b). Overall our results point out the importance of the amorphous ceramics—notably O-SiBCN—on the electrocatalytic activity towards the production of hydrogen. Indeed, as the investigations of the microstructure presented in the part 3.2.2 suggests, the materials tends to shift from amorphous to crystalline nature for annealing temperature $> 1200^{\circ}\text{C}$.

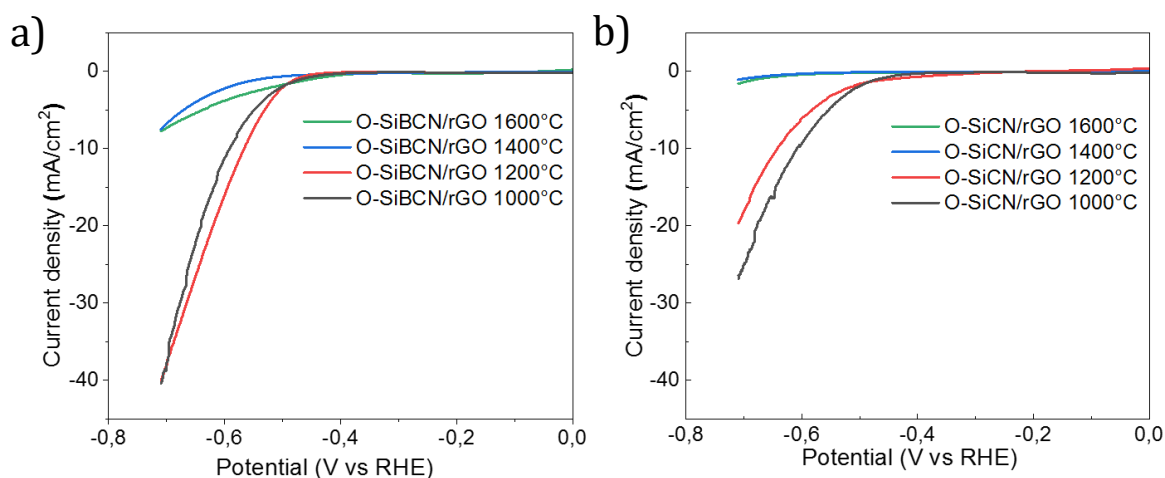


Figure 3-17: Polarization curves of O-SiBCN/rGO (a) and O-SiCN/rGO (b) composites at different temperatures.

Other amorphous catalysts such as metal chalcogenides, metal alloys, metal phosphides have already demonstrated larger catalytic activity relative to their crystalline counterparts [23][24][25]. Both O-SiBCN and O-SiCN catalysts remain active after annealing at temperatures up to 1200°C but then lose most of the activity at 1400°C and above.

The HER activity decreasing with the annealing temperature was attributed to the crystallization of the carbon phase in the ceramic. It also proves the intrinsic HER activity of the amorphous microstructure of the PDC materials.

3.3.3 Influence of porosity/active surface

The previous results were collected with a ceramic: graphene ratio fixed at 1. This ratio was chosen according to the measurements carried out on samples with ratio varying from 0.2 to 1 and presented in Figure 3-18. The polarization curves associated with O-SiBCN/rGO and O-SiCN/rGO show the highest current density and the lowest overpotential for R=1.

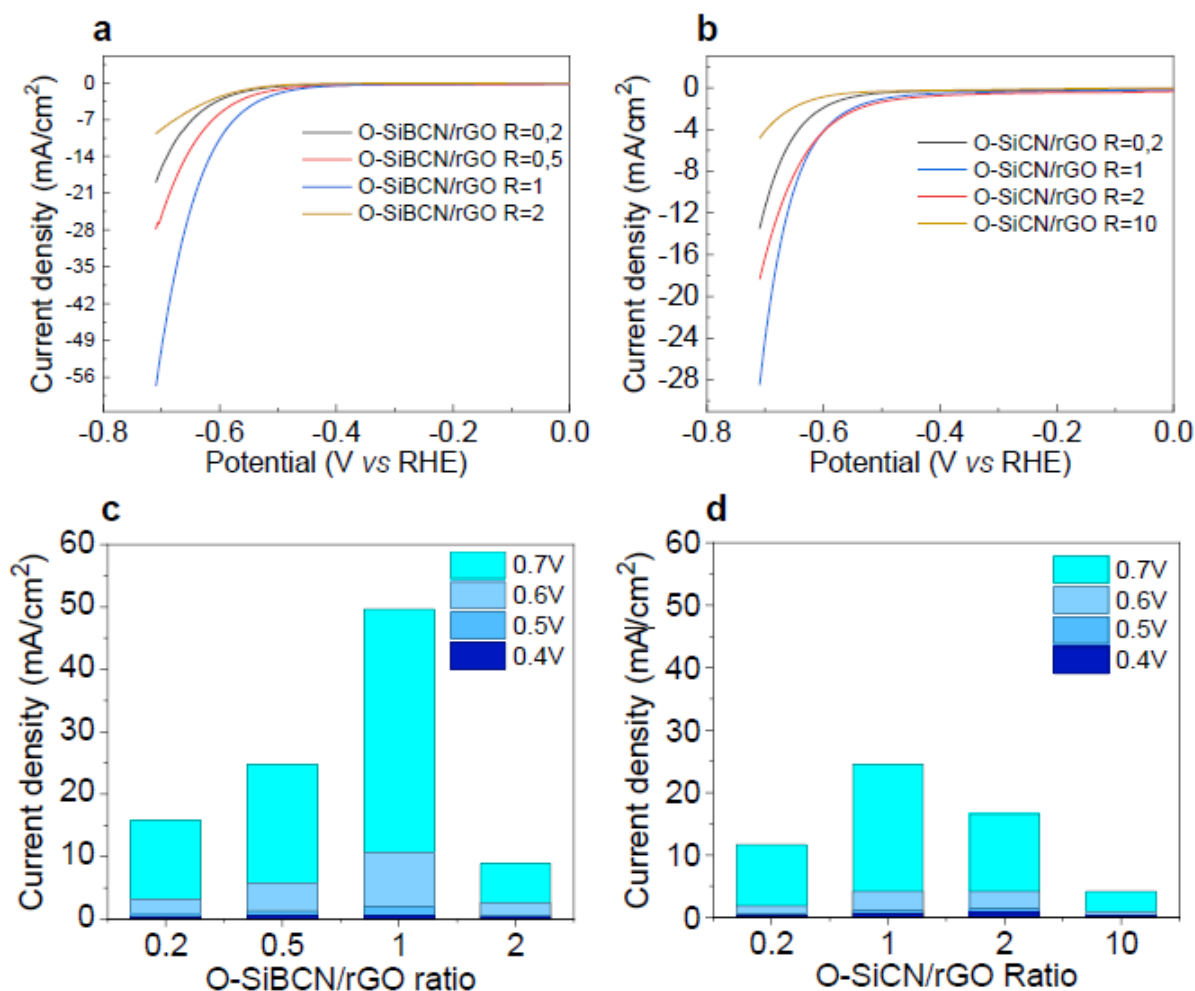


Figure 3-18: (a, b) Polarization curves of O-SiBCN/rGO and O-SiCN/rGO composites at different ratios, (c, d) Histograms representing the evolution of the current density at different potentials for the O-SiBCN/rGO and O-SiCN/rGO composites respectively.

For both PDC/rGO systems (O-SiBCN/rGO and O-SiCN/rGO), we found an optimum of the catalytic activity for a PDC/rGO 1:1 ratio. It seems that for ratio <1 the quantity of ceramic introduced in the foam is too low to transmit catalytic properties of the amorphous ceramic to the graphene supports. Increasing the ratio above 1 ($R >1$) tends to decrease the porosity, the active surface area and thus the electrocatalytic activity. This is relevant with the SEM observations of composite samples discussed in section 3.2.2.1.

3.3.4 Stability investigation

3.3.4.1 Stability curves

To further explore the potential of the O-SiBCN/rGO composites as electrocatalyst its stability in acidic medium with regard to HER activity has been studied. The electrode was continuously subjected to various current densities for a total of 168 h. During the stability test, the applied current density was set to 2.5 mA.cm^{-2} , 5 mA.cm^{-2} and 7.5 mA.cm^{-2} for 48, 24 and 96 h, respectively, to simulate the variation of the supply power mimicking the case of an electrolyser connected to a photovoltaic cell. Benchmark electrocatalyst Pt/C stability was also measured in the same conditions for a fair comparison with O-SiBCN/rGO sample (see Figure 3-19). As expected commercial Pt nanoparticles initially demonstrate high HER performance with a very low overpotential of 51 mV at 2.5 mA.cm^{-2} —clearly smaller than for O-SiBCN/rGO with initial overpotential of 454 mV. On the other hand, the overpotential for Pt rapidly increases by 493% during the first 12 h which demonstrates its poor stability towards HER activity. This is likely due to surface poisoning of the Pt surface by impurities from the electrolyte solution as well as possible leaching of the Pt nanoparticles in the acid electrolyte.

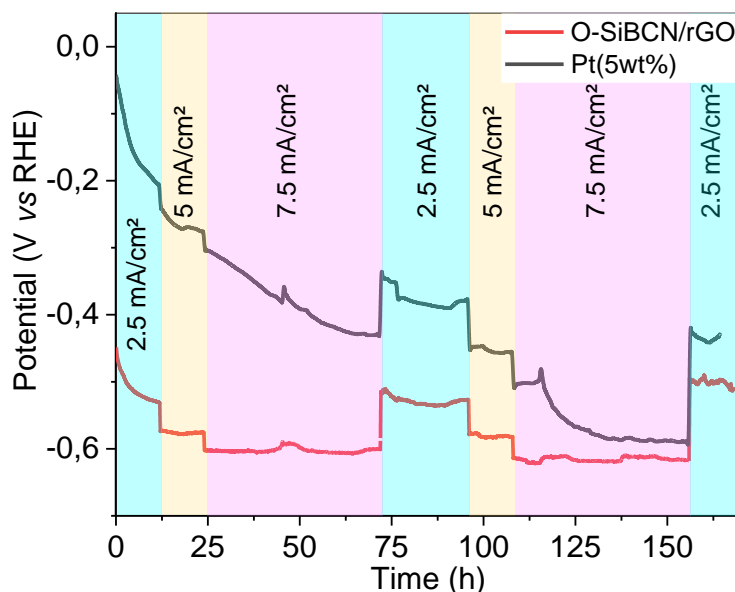


Figure 3-19: Chronopotentiometry measurements for supported Pt/C electrodes and O-SiBCN/rGO composite over 168 h.

O-SiBCN/rGO composite exhibits significantly better retention of the HER performance over ≈ 170 h with an increase of the overpotential of 18.4%, 0.3% and $\approx 0\%$ after 12, 24 and 48 h at $2.5 \text{ mA}\cdot\text{cm}^{-2}$, $5 \text{ mA}\cdot\text{cm}^{-2}$ and $7.5 \text{ mA}\cdot\text{cm}^{-2}$, respectively. After 168 h, the overpotential gap between O-SiBCN/rGO and 5%Pt/C sharply decreases from 424 mV to only 85 mV. Through these results, the interest of O-SiBCN/rGO through its ultra-stable behavior for HER in acidic medium is revealed.

3.3.4.2 Comparison with the literature

We also compared the stability of O-SiBCN/rGO electrode with that of several electrocatalysts previously reported in the literature in the same conditions. Our results clearly show outstanding stability of O-SiBCN/rGO over a long period demonstrating thus the potential of such materials for realistic operations (Figure 3-20).

The activity losses associated with benchmark Pt/C electrocatalysts was evaluated at $\sim 1200\%$ after 170h of uninterrupted utilization. On the other hand, the O-SiBCN/rGO electrocatalyst displayed a stability competing with the most stable catalysts such as nickel

based materials. For example, nickel phosphide embedded in carbon nanofibers exhibits approximately similar HER performances retention than our PDC based catalyst.

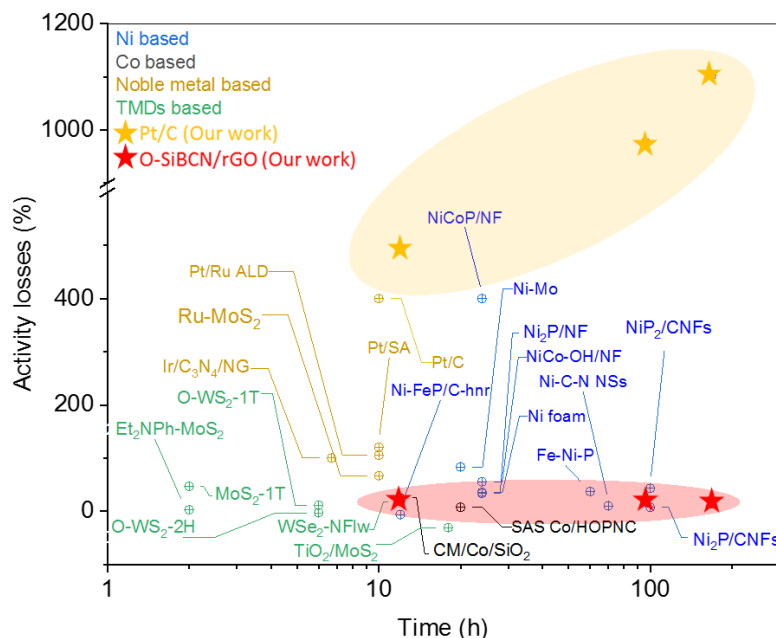


Figure 3-20: Change in overpotential (%) for O-SiBCN/rGO and other electrocatalysts in the literature: (Ni-FeP/C-hnr [26] (hnr = hollow nanorod), Ni₂P/CNFs [27] (CNFs = carbon nanofibers), NiP₂/CNFs [27], Ni foam [28], NiCo-OH/NF [28] (NF = nickel foam), Ni₂P/NF [28], NiCoP/NF [28], Ni-C-N NSs [29] (NSs = nanosheets), Ni-Mo [30], Fe-Ni-P [31], CM/Co/SiO₂ [32] (CM = carbon material), SAS/Co/HOPNC [33] (SAS = single-atomic Co sites, HOPNC = embedded in hierarchically ordered porous N-doped carbon), Ir/C₃N₄/NG [34], Pt/Ru ALD [35] (ALD = atomic layer deposition), Pt/SA [35] (SA = single atomic), Pt/C [35], Ru-MoS₂ [36], MoS₂ 1T [37], Et₂NPh fct MoS₂ [37], TiO₂/MoS₂ [38], O-WS₂-1T [39], O-WS₂-2H [39], WSe₂ NFlw [40] (NFlw = nano flowers).

3.3.5 Free standing electrodes

3.3.5.1 Polarization curves

The foam shape of the rGO foam was initially selected to support active material for HER reaction and bring porosity and electronic conductivity. Nevertheless, in the results previously discussed the foamy structure was crushed to prepare comparable samples for electrocatalytic measurements (See part 2.2.6 and inset in Figure 3-21.a.). To validate our initial concept, we fabricated a freestanding electrode based on O-SiBCN/rGO (inset in Figure 3-21.b.). Thanks to the mechanical properties of the ceramics reinforcement and the

electrical conductivity of the rGO scaffold, the electrode can directly be used without any conducting support. Such rational design of the composite electrode is associated with a high porosity thanks to the rGO nanosheets, while the HER activity originating from the O-SiBCN ceramic allows reaching a current of almost 130 mA (Polarization curves in Figure 3-21).

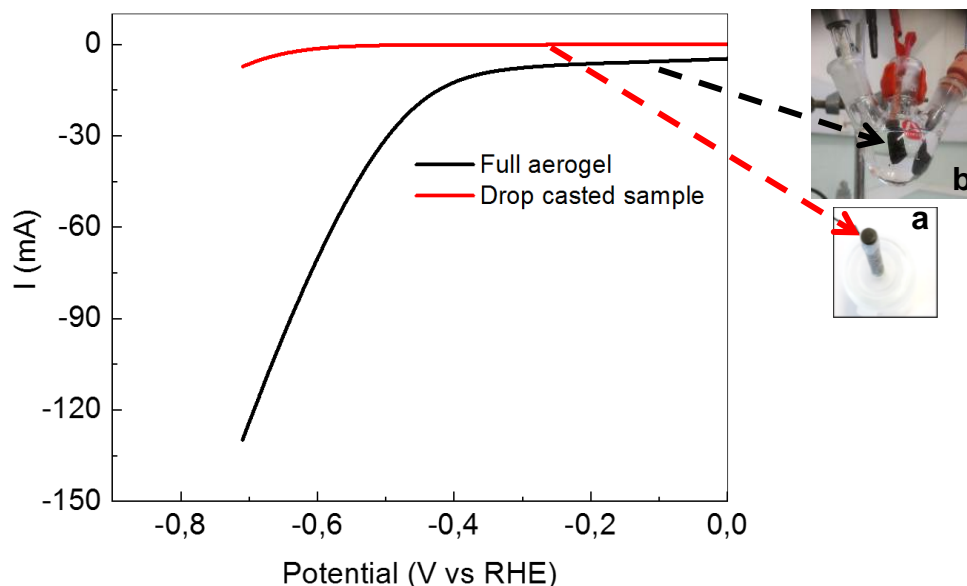


Figure 3-21: Comparison of the polarization curves from O-SiBCN/rGO composite catalyst deposited on the glassy carbon electrode and freestanding O-SiBCN/rGO. Note that the potentials of the free-standing electrode were not iR loss corrected.

3.3.5.2 Mechanical performances of composites

Free-standing electrodes applications can be considered in relation with the mechanical reinforcement provided by the foam impregnation by the ceramic. To demonstrate the enhancement of the mechanical behavior of the PDC/rGO composites compared to rGO, compression tests were carried out on both samples. The Young's moduli for both pristine rGO and O-SiBCN/rGO composites were deduced from the first linear part of stress-strain curves (Figure 3-22). Our results show that the O-SiBCN/rGO and rGO samples have a plastic behavior with a plasticity cross-over around 13% and 11% strain respectively. The Young's modulus of O-SiBCN/rGO is estimated to almost 50 kPa—approximately fourfold

larger than that of rGO. Clearly, this considerable improvement of the composites stiffness is attributed to the presence of the ceramic on the rGO nanosheets.

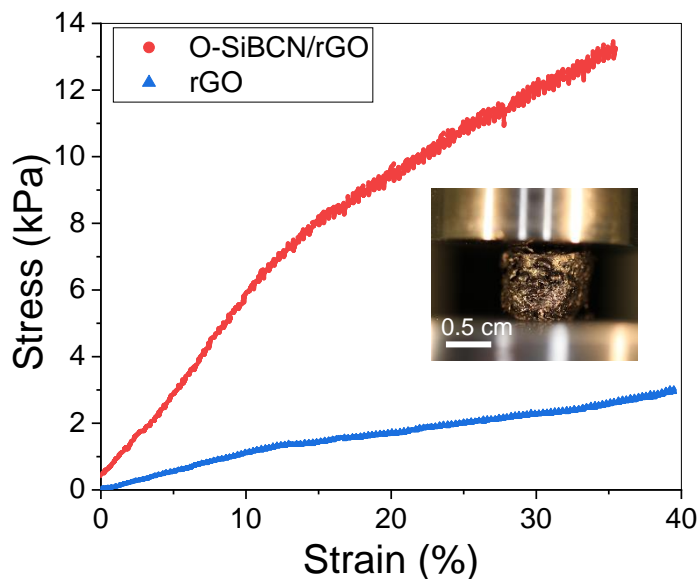


Figure 3-22: Compression curves of the rGO foam and the O-SiBCN/rGO composite. The inset shows that the composite remains stable after compression.

The plasticity modulus, extrapolated from the second linear part of the strain–stress curves, also decreases from 50 kPa for rGO to 25 kPa for O-SiBCN. The mechanical investigations reveal that the controlled coating of the rGO foam with the ceramic strongly benefits the mechanical properties of the composite thus allowing the preparation of mechanically-robust electrodes.

3.3.6 Conclusion/perspectives

Ceramics have been largely disregarded in electrocatalysis because of their insulating behavior. Here, we demonstrated an example of engineered PDC/rGO based composites as electrocatalytic active materials. Within the composite, rGO acts as a porous conductive network, with a high porosity of 93% and a high electrical conductivity allowing fast transport of the charge carriers and consequently activating the supported ceramic. In-depth investigations revealed that HER activity of the ceramics can be modulated by the presence of O, N and B in the Si–C systems. We also demonstrated that the performances of our catalyst were linked to the amorphous nature of the PDC. Our careful measurements

based on the ECSA and linear voltammetry allowed identifying O-SiBCN ceramic as stable HER catalyst. O-SiBCN/rGO exhibits the best performance with an onset potential of – 340 mV vs. RHE, while exhibiting an outstanding stability over almost 170 h with a minimal increase of the overpotential. Importantly, our results demonstrate the potential of ceramics for electrocatalysis when prepared in the form of an ultrathin film deposited on a conducting substrate. Considering the great stability of ceramics, we believe our work opens perspectives in the rational design of ceramic/graphene composites with controlled composition and rational structure and sheds light on novel applications of inorganic ceramics in electrocatalysis.

3.4 Bibliography

- [1] A. Viard *et al.*, « Molecular Chemistry and Engineering of Boron-Modified Polyorganosilazanes as New Processable and Functional SiBCN Precursors », *Chemistry – A European Journal*, vol. 23, n° 38, p. 9076-9090, 2017, doi: [10.1002/chem.201700623](https://doi.org/10.1002/chem.201700623).
- [2] J. Lücke, J. Hacker, D. Suttor, et G. Ziegler, « Synthesis and Characterization of Silazane-Based Polymers as Precursors for Ceramic Matrix Composites », *Applied Organometallic Chemistry*, vol. 11, n° 2, p. 181-194, 1997, doi: [10.1002/\(SICI\)1099-0739\(199702\)11:2<181::AID-AOC566>3.0.CO;2-Q](https://doi.org/10.1002/(SICI)1099-0739(199702)11:2<181::AID-AOC566>3.0.CO;2-Q).
- [3] M. Seifollahi Bazarjani *et al.*, « Nanoporous Silicon Oxycarbonitride Ceramics Derived from Polysilazanes In situ Modified with Nickel Nanoparticles », *Chem. Mater.*, vol. 23, n° 18, p. 4112-4123, sept. 2011, doi: [10.1021/cm200589n](https://doi.org/10.1021/cm200589n).
- [4] Y.-L. Li, E. Kroke, R. Riedel, C. Fasel, C. Gervais, et F. Babonneau, « Thermal cross-linking and pyrolytic conversion of poly(ureamethylvinyl)silazanes to silicon-based ceramics », *Applied Organometallic Chemistry*, vol. 15, n° 10, p. 820-832, 2001, doi: [10.1002/aoc.236](https://doi.org/10.1002/aoc.236).
- [5] R. Silva, D. Voiry, M. Chhowalla, et T. Asefa, « Efficient metal-free electrocatalysts for oxygen reduction: polyaniline-derived N- and O-doped mesoporous carbons », *J Am Chem Soc*, vol. 135, n° 21, p. 7823-7826, mai 2013, doi: [10.1021/ja402450a](https://doi.org/10.1021/ja402450a).
- [6] Z. Lu *et al.*, « High-efficiency oxygen reduction to hydrogen peroxide catalysed by oxidized carbon materials », *Nat Catal*, vol. 1, n° 2, p. 156-162, févr. 2018, doi: [10.1038/s41929-017-0017-x](https://doi.org/10.1038/s41929-017-0017-x).

- [7] S. H. Huh, *Thermal Reduction of Graphene Oxide*. IntechOpen, 2011. doi: [10.5772/14156](https://doi.org/10.5772/14156).
- [8] R. Riedel, G. Mera, R. Hauser, et A. Klonczynski, « Silicon-Based Polymer-Derived Ceramics: Synthesis Properties and Applications-A Review », *Journal of the Ceramic Society of Japan*, vol. 114, n° 1330, p. 425-444, 2006, doi: [10.2109/jcersj.114.425](https://doi.org/10.2109/jcersj.114.425).
- [9] A. C. Ferrari *et al.*, « Raman Spectrum of Graphene and Graphene Layers », *Phys. Rev. Lett.*, vol. 97, n° 18, p. 187401, oct. 2006, doi: [10.1103/PhysRevLett.97.187401](https://doi.org/10.1103/PhysRevLett.97.187401).
- [10] K. Dave, K. H. Park, et M. Dhayal, « Two-step process for programmable removal of oxygen functionalities of graphene oxide: functional, structural and electrical characteristics », *RSC Adv.*, vol. 5, n° 116, p. 95657-95665, nov. 2015, doi: [10.1039/C5RA18880F](https://doi.org/10.1039/C5RA18880F).
- [11] M. Idrees *et al.*, « Polyborosilazane derived ceramics - Nitrogen sulfur dual doped graphene nanocomposite anode for enhanced lithium ion batteries », *Electrochimica Acta*, vol. 296, p. 925-937, févr. 2019, doi: [10.1016/j.electacta.2018.11.088](https://doi.org/10.1016/j.electacta.2018.11.088).
- [12] Y. Feng, N. Feng, Y. Wei, et Y. Bai, « Preparation and improved electrochemical performance of SiCN-graphene composite derived from poly(silylcarbodiimide) as Li-ion battery anode », *J. Mater. Chem. A*, vol. 2, n° 12, p. 4168-4177, févr. 2014, doi: [10.1039/C3TA14441K](https://doi.org/10.1039/C3TA14441K).
- [13] H. Zhao, L. Chen, X. Luan, X. Zhang, J. Yun, et T. Xu, « Synthesis, pyrolysis of a novel liquid SiBCN ceramic precursor and its application in ceramic matrix composites », *Journal of the European Ceramic Society*, vol. 37, n° 4, p. 1321-1329, avr. 2017, doi: [10.1016/j.jeurceramsoc.2016.11.009](https://doi.org/10.1016/j.jeurceramsoc.2016.11.009).
- [14] X. Ji, S. Wang, C. Shao, et H. Wang, « High-Temperature Corrosion Behavior of SiBCN Fibers for Aerospace Applications », *ACS Appl. Mater. Interfaces*, vol. 10, n° 23, p. 19712-19720, juin 2018, doi: [10.1021/acsami.8b04497](https://doi.org/10.1021/acsami.8b04497).
- [15] K. Shimoda, J.-S. Park, T. Hinoki, et A. Kohyama, « Influence of surface structure of SiC nano-sized powder analyzed by X-ray photoelectron spectroscopy on basic powder characteristics », *Applied Surface Science*, vol. 253, n° 24, p. 9450-9456, oct. 2007, doi: [10.1016/j.apsusc.2007.06.023](https://doi.org/10.1016/j.apsusc.2007.06.023).

- [16] G. M. Ingo, N. Zacchetti, D. della Sala, et C. Coluzza, « X-ray photoelectron spectroscopy investigation on the chemical structure of amorphous silicon nitride ($a\text{-SiN}_x$) », *Journal of Vacuum Science & Technology A: Vacuum, Surfaces, and Films*, vol. 7, n° 5, p. 3048-3055, sept. 1989, doi: [10.1116/1.576314](https://doi.org/10.1116/1.576314).
- [17] M. Khalid et H. Varela, « A general potentiodynamic approach for red phosphorus and sulfur nanodot incorporation on reduced graphene oxide sheets: metal-free and binder-free electrodes for supercapacitor and hydrogen evolution activities », *J. Mater. Chem. A*, vol. 6, n° 7, p. 3141-3150, févr. 2018, doi: [10.1039/C7TA11342K](https://doi.org/10.1039/C7TA11342K).
- [18] Y.-C. Shi *et al.*, « One-step hydrothermal synthesis of three-dimensional nitrogen-doped reduced graphene oxide hydrogels anchored PtPd alloyed nanoparticles for ethylene glycol oxidation and hydrogen evolution reactions », *Electrochimica Acta*, vol. 293, p. 504-513, janv. 2019, doi: [10.1016/j.electacta.2018.10.068](https://doi.org/10.1016/j.electacta.2018.10.068).
- [19] H.-Y. Chen, H.-J. Niu, Z. Han, J.-J. Feng, H. Huang, et A.-J. Wang, « Simple fabrication of trimetallic platinum-nickel-cobalt hollow alloyed 3D multipods for highly boosted hydrogen evolution reaction », *J Colloid Interface Sci*, vol. 570, p. 205-211, juin 2020, doi: [10.1016/j.jcis.2020.02.090](https://doi.org/10.1016/j.jcis.2020.02.090).
- [20] E. J. Popczun *et al.*, « Nanostructured nickel phosphide as an electrocatalyst for the hydrogen evolution reaction », *J Am Chem Soc*, vol. 135, n° 25, p. 9267-9270, juin 2013, doi: [10.1021/ja403440e](https://doi.org/10.1021/ja403440e).
- [21] Y. Li, H. Wang, L. Xie, Y. Liang, G. Hong, et H. Dai, « MoS₂ nanoparticles grown on graphene: an advanced catalyst for the hydrogen evolution reaction », *J Am Chem Soc*, vol. 133, n° 19, p. 7296-7299, mai 2011, doi: [10.1021/ja201269b](https://doi.org/10.1021/ja201269b).
- [22] D. Voiry, H. S. Shin, K. P. Loh, et M. Chhowalla, « Low-dimensional catalysts for hydrogen evolution and CO₂ reduction », *Nat Rev Chem*, vol. 2, n° 1, p. 1-17, janv. 2018, doi: [10.1038/s41570-017-0105](https://doi.org/10.1038/s41570-017-0105).
- [23] K. Lian, S. J. Thorpe, et D. W. Kirk, « The electrocatalytic activity of amorphous and crystalline Ni-Co alloys on the oxygen evolution reaction », *Electrochimica Acta*, vol. 37, n° 1, p. 169-175, janv. 1992, doi: [10.1016/0013-4686\(92\)80026-I](https://doi.org/10.1016/0013-4686(92)80026-I).

- [24] C. G. Morales-Guio et X. Hu, « Amorphous molybdenum sulfides as hydrogen evolution catalysts », *Acc Chem Res*, vol. 47, n° 8, p. 2671-2681, août 2014, doi: [10.1021/ar5002022](https://doi.org/10.1021/ar5002022).
- [25] J. M. McEnaney *et al.*, « Electrocatalytic hydrogen evolution using amorphous tungsten phosphide nanoparticles », *Chem. Commun.*, vol. 50, n° 75, p. 11026-11028, août 2014, doi: [10.1039/C4CC04709E](https://doi.org/10.1039/C4CC04709E).
- [26] X. F. Lu, L. Yu, et X. W. D. Lou, « Highly crystalline Ni-doped FeP/carbon hollow nanorods as all-pH efficient and durable hydrogen evolving electrocatalysts », *Sci Adv*, vol. 5, n° 2, p. eaav6009, févr. 2019, doi: [10.1126/sciadv.aav6009](https://doi.org/10.1126/sciadv.aav6009).
- [27] J.-Y. Kim *et al.*, « Predictive fabrication of Ni phosphide embedded in carbon nanofibers as active and stable electrocatalysts », *J. Mater. Chem. A*, vol. 7, n° 13, p. 7451-7458, mars 2019, doi: [10.1039/C9TA00455F](https://doi.org/10.1039/C9TA00455F).
- [28] H. Liang, A. N. Gandi, D. H. Anjum, X. Wang, U. Schwingenschlögl, et H. N. Alshareef, « Plasma-Assisted Synthesis of NiCoP for Efficient Overall Water Splitting », *Nano Lett*, vol. 16, n° 12, p. 7718-7725, déc. 2016, doi: [10.1021/acs.nanolett.6b03803](https://doi.org/10.1021/acs.nanolett.6b03803).
- [29] J. Yin *et al.*, « Ni-C-N Nanosheets as Catalyst for Hydrogen Evolution Reaction », *J Am Chem Soc*, vol. 138, n° 44, p. 14546-14549, nov. 2016, doi: [10.1021/jacs.6b09351](https://doi.org/10.1021/jacs.6b09351).
- [30] M. Gong, D.-Y. Wang, C.-C. Chen, B.-J. Hwang, et H. Dai, « A mini review on nickel-based electrocatalysts for alkaline hydrogen evolution reaction », *Nano Res.*, vol. 9, n° 1, p. 28-46, janv. 2016, doi: [10.1007/s12274-015-0965-x](https://doi.org/10.1007/s12274-015-0965-x).
- [31] J. D. Costa *et al.*, « Electrocatalytic Performance and Stability of Nanostructured Fe-Ni Pyrite-Type Diphosphide Catalyst Supported on Carbon Paper », *J. Phys. Chem. C*, vol. 120, n° 30, p. 16537-16544, août 2016, doi: [10.1021/acs.jpcc.6b05783](https://doi.org/10.1021/acs.jpcc.6b05783).
- [32] Z.-Y. Wu *et al.*, « Transition metal-assisted carbonization of small organic molecules toward functional carbon materials », *Science Advances*, vol. 4, n° 7, p. eaat0788, doi: [10.1126/sciadv.aat0788](https://doi.org/10.1126/sciadv.aat0788).
- [33] T. Sun *et al.*, « Single-atomic cobalt sites embedded in hierarchically ordered porous nitrogen-doped carbon as a superior bifunctional electrocatalyst », *PNAS*, vol. 115, n° 50, p. 12692-12697, déc. 2018, doi: [10.1073/pnas.1813605115](https://doi.org/10.1073/pnas.1813605115).

- [34] B. Jiang, T. Wang, Y. Cheng, F. Liao, K. Wu, et M. Shao, « Ir/g-C₃N₄/Nitrogen-Doped Graphene Nanocomposites as Bifunctional Electrocatalysts for Overall Water Splitting in Acidic Electrolytes », *ACS Appl Mater Interfaces*, vol. 10, n° 45, p. 39161-39167, nov. 2018, doi: [10.1021/acsami.8b11970](https://doi.org/10.1021/acsami.8b11970).
- [35] L. Zhang *et al.*, « Atomic layer deposited Pt-Ru dual-metal dimers and identifying their active sites for hydrogen evolution reaction », *Nat Commun*, vol. 10, n° 1, p. 4936, oct. 2019, doi: [10.1038/s41467-019-12887-y](https://doi.org/10.1038/s41467-019-12887-y).
- [36] Z. Luo *et al.*, « Reactant friendly hydrogen evolution interface based on di-anionic MoS₂ surface », *Nat Commun*, vol. 11, n° 1, p. 1116, févr. 2020, doi: [10.1038/s41467-020-14980-z](https://doi.org/10.1038/s41467-020-14980-z).
- [37] E. E. Benson *et al.*, « Balancing the Hydrogen Evolution Reaction, Surface Energetics, and Stability of Metallic MoS₂ Nanosheets via Covalent Functionalization », *J Am Chem Soc*, vol. 140, n° 1, p. 441-450, janv. 2018, doi: [10.1021/jacs.7b11242](https://doi.org/10.1021/jacs.7b11242).
- [38] A. Tahira *et al.*, « Advanced Electrocatalysts for Hydrogen Evolution Reaction Based on Core-Shell MoS₂/TiO₂ Nanostructures in Acidic and Alkaline Media », *ACS Applied Energy Materials*, vol. 2, n° 3, p. 2053-2062, 2019.
- [39] P. V. Sarma, C. S. Tiwary, S. Radhakrishnan, P. M. Ajayan, et M. M. Shaijumon, « Oxygen incorporated WS₂ nanoclusters with superior electrocatalytic properties for hydrogen evolution reaction », *Nanoscale*, vol. 10, n° 20, p. 9516-9524, mai 2018, doi: [10.1039/C8NR00253C](https://doi.org/10.1039/C8NR00253C).
- [40] D. A. Henckel, O. M. Lenz, K. M. Krishnan, et B. M. Cossairt, « Improved HER Catalysis through Facile, Aqueous Electrochemical Activation of Nanoscale WSe₂ », *Nano Lett*, vol. 18, n° 4, p. 2329-2335, avr. 2018, doi: [10.1021/acs.nanolett.7b05213](https://doi.org/10.1021/acs.nanolett.7b05213).

***Chapter IV: Microfabrication of PDC
based materials via soft-lithography
for the purpose of micro-electrolyser
applications***

4	Microfabrication of PDC based materials <i>via</i> soft-lithography for the purpose of micro-electrolyser applications	153
4.1	Introduction and brief state-of-the-art review	153
4.2	Characterization of the synthesized photoresists.....	153
4.2.1	Brief recall on the preceramic polymers and their synthesis	154
4.2.2	Preceramic polymer characterization.....	154
4.2.2.1	FTIR spectroscopy.....	154
4.2.2.2	NMR spectroscopy	156
4.2.2.3	TGA measurements	160
4.2.3	Conclusion and interpretation.....	162
4.3	Micropattern fabrication from pure polymer	162
4.3.1	Mudcracks and Griffith criterion.....	162
4.3.2	Practical examples from literature.....	164
4.3.3	Microscopy observation	164
4.3.4	Conclusion.....	165
4.4	Introduction of fillers	166
4.4.1	Fillers description	166
4.4.2	Influence of fillers on shrinkage-microstructure.....	167
4.4.3	Investigation of <i>in-situ</i> phase formation	169
4.4.3.1	XRD Analysis	169
4.4.3.2	XPS analysis	173
4.4.4	Microscopy observation of microstructured patterns.....	179
4.4.4.1	Influence of filler's nature on cracking.....	179
4.4.4.2	Profilometry-topography	190
4.4.4.3	Mechanical properties.....	192
4.4.4.4	Electronic properties	193
4.5	Electrocatalytic performance	195

4.5.1	SiCN/MoS ₂ composites.....	197
4.5.1.1	Polarization curves	197
4.5.1.2	Tafel slopes.....	198
4.5.2	SiCN/MoS ₂ composites.....	199
4.5.3	SiCN/MoS ₂ /MoSi ₂ composites.....	200
4.5.4	Annealing temperature influence	203
4.5.5	Conclusion on HER activity	207
4.6	Chapter conclusion.....	208
4.7	Bibliography.....	209

4 Microfabrication of PDC based materials *via* soft-lithography for the purpose of micro-electrolyser applications

4.1 Introduction and brief state-of-the-art review

In chapter 1.2.3. we demonstrated the advantages of miniaturization on enhancing the performance of water-splitting devices. A direct consequence of miniaturization is the increase of efficiency and cost viability of electrolyser devices. The manufacturing techniques for such micro-devices have been mentioned in the state-of-the-art review of this manuscript in section 1.3.2, in particular the processes of soft-lithography. It is based on the replica molding thanks to micro-patterned elastomeric stamp.

The main objective of this section is to demonstrate the advantages of combining soft-lithography with the PDCs route to obtain defectless ceramic-based micro-patterns. In this chapter, the study and optimization of the micro-patterns manufacturing based on PDC materials will be detailed as a proof of concept to fabricate PDCs based microelectrodes for Hydrogen Evolution Reaction (HER).

This chapter has been divided into four sections. First, we describe the preceramic polymer employed and their chemical characterization with FTIR, NMR and TGA. Second, we reveal the limits of micro-molding of pure preceramic polymer and the origin of mud-cracks formation with such strategy. Third, we report how the introduction of passive and active fillers (Al_2O_3 , MoS_2 and MoSi_2) in the micromolding procedure affects the microstructure of the materials and conducts to the preparation of defectless micro-objects. Finally, in a fourth section we evaluate the electrocatalytic properties of PDC/filler composites conceived for this purpose.

4.2 Characterization of the synthesized photoresists

The preceramic polymers employed in this chapter consists in commercial polyvinylsilazane (PVZ) and boron modified polyvinylsilazane with Si/B ratio of 30 or 17, PBVZ30 and PBVZ17, respectively. The ratio of 17 corresponds to a complete hydroboration of vinyl groups (with almost no dehydrocoupling of N-H). Ratio was increased to 30 to decrease the crosslinking rate in PBVZ to obtain more fluid polymer.

4.2.1 Brief recall on the preceramic polymers and their synthesis

The description and synthesis of the preceramic polymers concerned in this chapter are presented in section 2.3.1 of Chapter II “materials & methods” of the manuscript. As mentioned before, PVZ purchased from Merck is a statistical copolymer composed of $\equiv\text{Si-NH-}$ backbone and grafted with methyl and/or vinyl groups. Its thermal treatment under nitrogen atmosphere at 1000°C conducts to a polymer-to-ceramic conversion resulting in an amorphous material composed of SiC, Si_3N_4 and free carbon nanodomains. The introduction of boron in PVZ was operated in laboratory through reaction between a borane complex (borane dimethyl sulfide, **BDMS**) and vinyl and/or N-H groups in PVZ. The synthesized polymer is denoted PBVZ and has a structure similar to PVZ excepting the partial conversion of vinyl and N-H groups to $=\text{B-C}\equiv$ and $=\text{B-N=}$, respectively. The microstructure of the ceramized polymer consists in an amorphous network of SiC, Si_3N_4 and free carbon plus BN and BN(C) nanodomains. A more precise description of these materials and their properties is developed in section 1.1.2.2.2.

4.2.2 Preceramic polymer characterization

To ensure the good progress of the synthesis and give a precise description of the chemical structure of the polymers used, a characterization campaign was carried out. FTIR and NMR spectroscopies were used to determine chemical groups present in the polymers and their environment. On the other hand, thermogravimetric analysis (TGA) was employed to investigate the polymer-to-ceramic transformation.

4.2.2.1 FTIR spectroscopy

FTIR spectra associated with PVZ, PBVZ30 and PBVZ17 samples are presented in Figure 4-1. The characteristics bands corresponding to PVZ polymer [1][2][3] as Si-N vibration, Si-H stretching and deformation of CH in Si-CH₃ bands at 1166, 2126 and 1253 cm⁻¹, respectively, confirm the presence of silicon and its bonds with nitrogen, carbon and hydrogen. The aliphatic CH_x band group detected at 2957, 2916, 2898 and 2849 cm⁻¹ (respectively corresponding to CH₃ asymmetric stretching, CH₂ stretching, CH stretching and CH₃ symmetric stretching) confirm the carbon content in PVZ. More specifically, the vinyl group presence is established thanks to the detection of C=C stretching band at 1593 cm⁻¹, CH_x deformation in the vinyl function at 1400 cm⁻¹ and the corresponding CH

stretching at 3047 and 3005 cm^{-1} . Si-C (850 cm^{-1}) and Si-N (700 cm^{-1}) bands can be distinguished below 1000 cm^{-1} despite of strong overlapping in this wavenumber range.

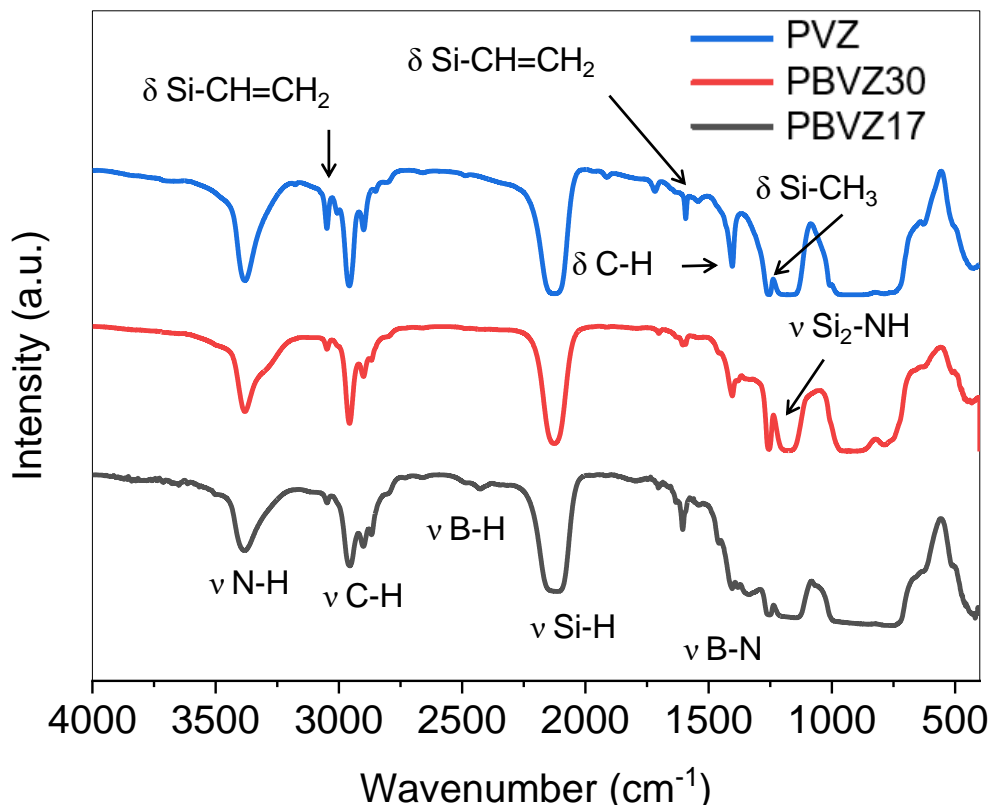


Figure 4-1 : FTIR spectroscopy of PVZ, PBVZ30 and PBVZ17 polymers; in KBr pellets (weight ratio polymer/KBr=1/50)

We notice a decrease in the intensity of aliphatic CH_x and Si-CH=CH_2 bands at 3047 and 1593 cm^{-1} associated with vinyl group, respectively after introducing boron. This is relevant with the consumption of vinyl groups by hydroboration with B-H groups occurring during the PBVZ synthesis. The decreasing of the vinyl bands is noticed for PBVZ30 and PBVZ17 suggesting that B-C bonds are created in both cases. Nevertheless, a small B-N band around 1300 cm^{-1} is detected for PBVZ30 polymer whereas this band is significantly more intense for PBVZ17 polymer. This result suggests that the dehydrocoupling of N-H by B-H groups happens for both Si/B ratio of 17 or 30 but it is more likely to occur in the case of PBVZ17. This is consistent with the work described in the literature [1] explaining the primary reactivity of B-H with vinyl towards N-H groups. The vinyl groups are the “first” to be

consumed by hydroboration reaction due its lower steric hindrance in comparison of N-H groups. It is also important to note that a small B-H band around 2400 cm^{-1} can be distinguished for the ration Si/B=17 suggesting that all the B-H groups from the BDMS are not integrally consumed and that the reactions mentioned above are not total in the case of PBVZ17.

Thanks to FTIR investigations we confirmed that the syntheses went smoothly occurred without oxidation of the polymer (no Si-O, B-O or OH bands detected) and with conservation of the characteristics polyvinylsilazane groups ensuring the precursors properties to the polymer. Nevertheless, those preliminary conclusions have to be confirmed with deeper analysis. Therefore NMR spectroscopy (discussed in the following section) were carried out on those preceramic polymers in order to confirm the results obtained *via* FTIR.

4.2.2.2 NMR spectroscopy

The experimental conditions associated with NMR characterization are mentioned in section 2.3.1. ^1H NMR spectroscopy was performed on PVZ, PBVZ30 and PBVZ17 polymers, the associated spectra are presented in Figure 4-2.

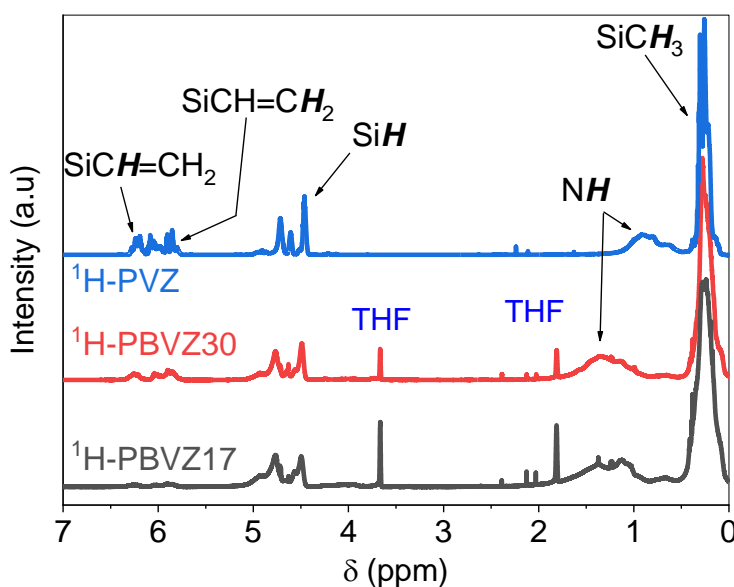


Figure 4-2: ^1H NMR spectroscopy of PVZ, PBVZ30 and PBVZ17 polymers; 50mg/ml in deuterated THF

Similarly to FTIR analysis, typical chemical groups of organosilazane are detected for PVZ [4]: SiCH_3 at $\delta=0.3$ ppm with a strong sharp peak, SiNH_2 between 0.9 and 1.6 ppm with small broad peak, a group of peaks between 4.4 and 5 ppm for SiH groups and another group of peaks at 6.3 and 5.8 ppm for $\text{SiCH}=\text{CH}_2$ and $\text{SiCH}=\text{CH}_2$, respectively. The small sharp peaks at 1.8 and 3.7 ppm are associated with $-\text{CH}_2-\text{CH}_2-$ and $-\text{CH}_2-\text{O}-$ of deuterated THF solvent [5].

Introduction of boron in PBVZ30 and PBVZ17 show clear differences in ^1H NMR spectra with regards to PVZ. The peak intensity of $\text{SiCH}=\text{CH}_2$ and $\text{SiCH}=\text{CH}_2$ at 6.3 and 5.8 ppm, respectively, decrease with the introduction of boron in the polymer. Again, this is relevant to the consumption of vinyl groups *via* hydroboration discussed previously in the FTIR investigation. The NH band is also affected after introduction of boron, especially in the case of PBVZ17 where its shape is modified and its intensity is a bit smaller than for PVZ and PBVZ30 [4][6][7]. The integrated intensity measured from ^1H NMR spectra of PVZ, PBVZ30 and PBVZ17 are given in Table 4-1. Two causes might be responsible for such phenomenon:

- Quartet peaks associated with BH_3 groups appears typically at 1.5 ppm [8]. The overlapping between BH_3 and NH bands could be responsible of the peak shape modification. This presence of residual BH species is consistent with the small BH band detected in PBVZ17 FTIR spectra discussed in the previous section.
- The decrease of NH peak intensity with increasing of boron content could also be explain by the dehydrocoupling reaction occurring between BH_3 and NH groups conducting to a consumption of these functions.

Moreover, a small peak is observable in the 0.6-0.8 ppm region for PBVZ30 and PBVZ17 spectra; it could be associated to $-\text{B}-\text{CH}_2$ groups formed during PBVZ synthesis. As mentioned in Table 4-1, the integrated intensity of the associated peak increases with the boron content. Detection of those groups confirms the formation of B-C bonds and thus the efficiency of the PBVZ synthesis method. [1]

Table 4-1: Integrated intensity of PVZ, PBVZ17 and PBVZ30 ^1H NMR peaks

Peak integrated intensity ► Polymer ▼	SiCH_3 ($\delta=0.3$ ppm)	SiNH ($\delta=0.9-1.6$ ppm)	SiH ($\delta=4.4-5.0$ ppm)	SiCH=CH_2 ($\delta=6.3-5.8$ ppm)	$-\text{B-CH}_2$ ($\delta=0.6-0.8$ ppm)
PVZ	1.0	0.36	0.23	0.26	0.0
PBVZ30	1.0	0.35	0.19	0.07	0.03
PBVZ17	1.0	0.31	0.19	0.01	0.05

^1H NMR investigations were completed with NMR spectroscopy around ^{13}C and ^{29}Si presented in Figure 4-3 and Figure 4-4, respectively. Small peaks in ^{13}C NMR spectra are detected between 127 and 143 ppm and are associated with Si-CH=CH_2 groups. Broad signals from -4.5 to 4.3 can be associated with Si-CH_3 groups [6][7]. Once again, intensity of the vinyl groups is attenuated with introduction of boron due to vinyl hydroboration.

The ^{29}Si NMR spectra (Figure 4-4) show 2 distinct signals: one intense and fine signal centered on -23 ppm (noted A) and a weaker and broader signal (noted B) between -20 and -14 ppm. Based on several references [4][9][10] and in particular the work of Viard et al. [1] we can attribute signals A and B to $(\text{CH}_3)_2\text{Si}(\text{CH=CH}_2)\text{N}_2$ and $\text{HSi}(\text{CH}_3)\text{N}_2$ units, respectively. Nevertheless, a closer look at the intensity of signals A and B reveals an inconsistency since the vinyl/methyl ratio in the initial polyvinylsilazane (Durazane 1800) is low while the ratio between the intensity of signals I_A/I_B is high. Moreover, the intensity of signal B seems to decrease with the increase of the boron content, which could correspond to a consumption of vinyls by hydroboration as observed in Figure 4-2 and Figure 4-3. Ultimately, we cannot give a clear attribution to these signals since our observations are at odds with the literature. A NMR 2D ^1H - ^{29}Si analysis would give additional information to decide on the attribution of the signals but this could not be done in this thesis.

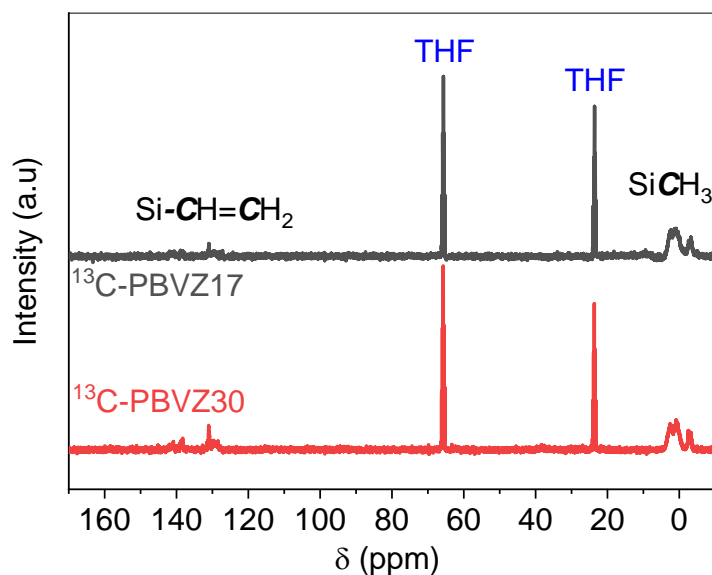


Figure 4-3: ^{13}C NMR spectroscopy of PBVZ30 and PBVZ17 polymers; 50mg/ml in deuterated THF

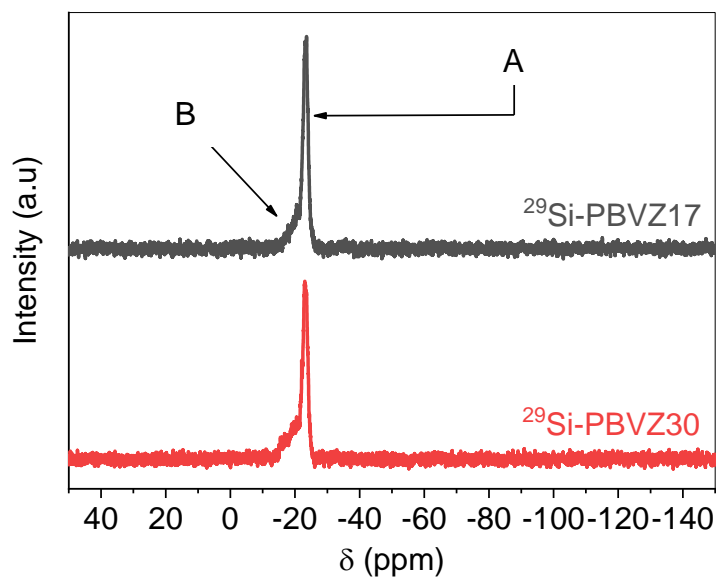


Figure 4-4: ^{29}Si NMR spectroscopy of PBVZ30 and PBVZ17 polymers; 50mg/ml in deuterated THF

The chemical investigation proceeded through FTIR and NMR spectroscopies was helpful to develop a precise description of the synthesized boron modified PVZ. Dehydrocoupling and hydroboration reactions conducting to B-N and B-C bonds formation was confirmed.

Thanks to the interpretation developed in this part a schematic representation of the PBVZ chemical structure is proposed in Figure 4-5.

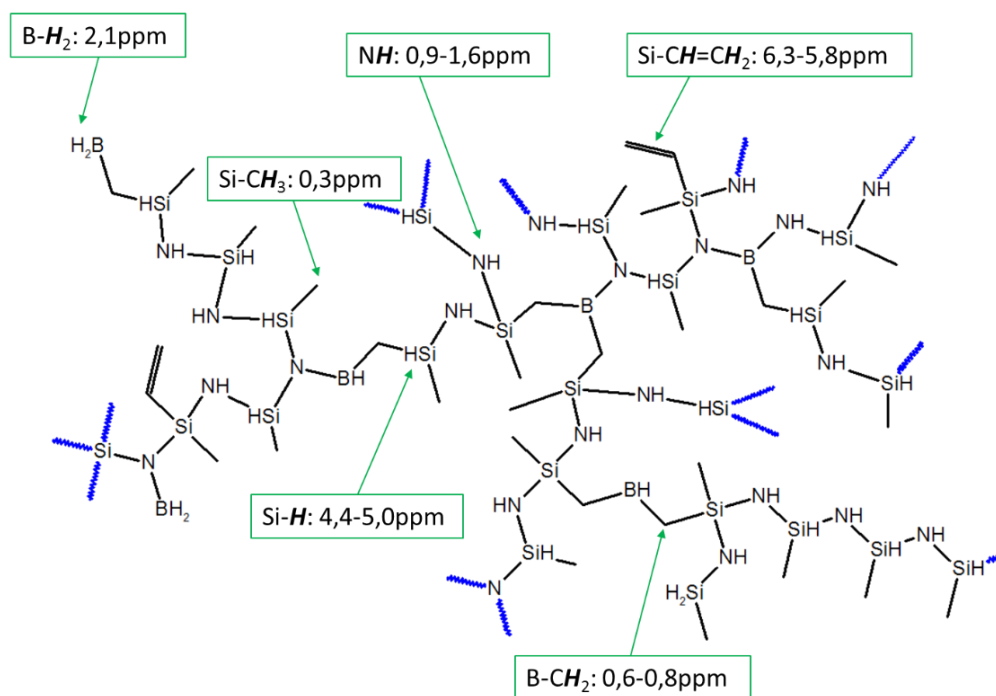


Figure 4-5: Representation of pre-SiBCN polymer synthesized in this work with associated ¹H NMR chemical shifts

The chemical structure of the PBVZ consists in -Si-N- backbone derived from initial PVZ structure with crosslinking nodes formed by the addition of boron. The network structure is designed thanks to the triple reactivity of BH₃ species conducting to N-BN-C, C-BC-N, N-BH-C... nodes connecting polymer chains together. To evaluate the influence of the preceramic polymer's composition as well as the network structure on the ceramization process thermal gravimetric analysis are developed in the next part.

4.2.2.3 TGA measurements

TGA curves of PVZ, PBVZ30, PBVZ17, performed under nitrogen from 25 to 1000°C are presented in Figure 4-6. For the three polymers studied, three distinct weight losses occur during thermal cycle. In the case of PVZ, a first major loss (≈21%) happens between 100 and 250°C. It mainly corresponds to NH₃ gaseous release caused by transamination reaction. In this temperature range, the polymer is cross-linked *via* polymerization of vinyl groups, hydrosilylation and transamination conducting to formation of new C-C, Si-C and Si-

N bonds, respectively. In the second weight loss ($\approx 8\%$), between 300 and 500°C, CH_4 , C_2H_6 , and H_2 species are released through dehydrocoupling (of Si-H, N-H, and C-H groups) and Si-C, C-C bond breaking reactions. The final step between 600 and 1000°C correspond to ceramization of the polymer through complex mechanism reaction releasing methane, ethane and propene species. The three cumulative weight losses conduct to a total weight loss of 40%. The ceramization of PVZ and PBVZ is complex and probably consists of a superposition of numerous mechanisms, separation of the different steps is not as clear as suggested above. [1][11]

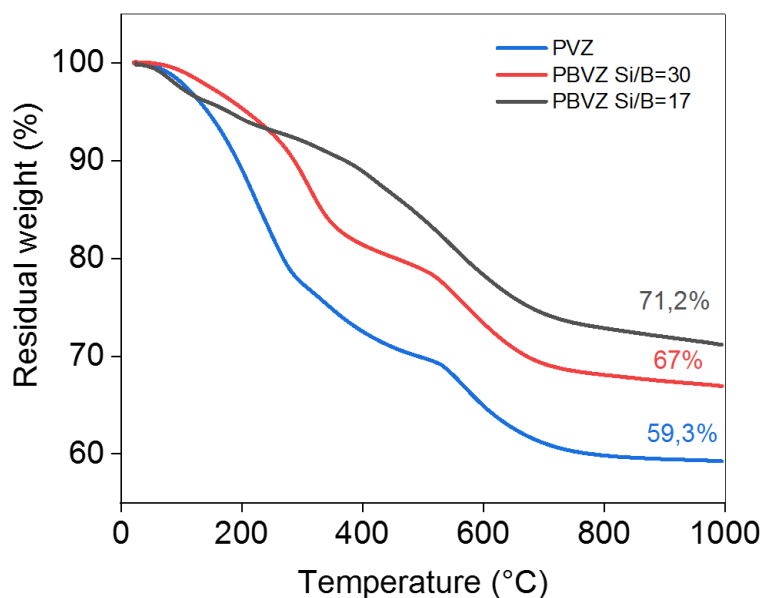


Figure 4-6: TGA curves of PVZ, PBVZ30 and PBVZ17 preceramic polymers; Nitrogen atmosphere, 5°C/min

Addition of boron clearly increase the final ceramic yield of the polymer to 67% for Si/B=30 and 71.2% for Si/B=17. For Si/B=17 the weight loss during step I (from 150 to 300°C) is reduced in comparison to PVZ polymer. It can be explained by the fact that a certain amount of the vinyl and N-H group has been consumed during the synthesis of PBVZ17. In these conditions, the hydrosylation and transamination reactions are less likely to occur and the release of gaseous species such as NH_3 and H_2 is lower than that of PVZ. In the case of PBVZ30 the quantity of N-H group consumed during its synthesis is lower than that of PBVZ17, as suggested by FTIR and NMR analysis. For PBVZ30, the weight loss reduction

during step I is less intense than that of PBVZ17. Furthermore, the global role of boron on the decrease of segment and chain mobility is known [1]. It may explain the global increase of the ceramic yield with the rate of boron in the polymer's composition.

4.2.3 Conclusion and interpretation

According to the chemical characterization developed in this part, we are able to conclude on the mechanism involved during the introduction of boron in polyvinylsilazane backbone. As it was demonstrated through FTIR and NMR spectroscopies, the synthesis of PBVZ consists in formation of B-C and B-N bonds through hydroboration and dehydrocoupling, respectively. According to these investigations, a structure of PBVZ was thus proposed and presented in Figure 4-5, that shows a cross-linked network with N-Si-N backbone and N-B-C, N-B-N or C-B-C crosslinking nodes. Such chemical structure conducts to an increase of ceramic yield as it is observed in TGA study.

In a context of soft-lithography process combined with the PDCs route, the increase of ceramic yield is of great interest. A high ceramic yield is usually associated with a low shrinkage after pyrolysis and can thus preserve the micropattern from strong deformation and delamination. The next part focuses on one of the great challenge encountered with the microfabrication of PDCs *via* soft lithography namely mudcracking of micropattern during heat treatment. More globally, the preparation of micropatterns based on PVZ and PBVZ polymers and additives fillers is explored below.

4.3 Micropattern fabrication from pure polymer

The soft-lithography method employed here is described in section 2.3.2.2. Briefly, it consists in molding the preceramic polymer with PDMS mold previously prepared from photolithographed SU-8 master. After crosslinking of the polymer, the micropattern is demolded and pyrolysed at 1000°C under N₂.

4.3.1 Mudcracks and Griffith criterion

As mentioned previously, one major challenge faced in this study was to understand and control the “mud-cracks” and substrate/ceramic adhesion problem occurring during the thermal treatment. The significant shrinkage associated to the PDCs process and substrate dilatation during heat treatment are two phenomena that can cause important constraints

on the materials.. The mud-cracks formation following a large volume decrease depend on the Griffith criterion [12][13][14]. Its principle is described in equation (1) and Figure 4-7: Cracks are likely to form if the thickness t of a coating exceeds a certain critical thickness t_c dependent on ω , E and ν associated with specific energy, elastic modulus and passion ratio of the thin film, respectively. With c a dimensionless geometrical factor, and σ the biaxial stress applied to the film.

$$t \geq t_c = \frac{4\omega E}{c(1-\nu)\sigma^2} \quad (1)$$

Thanks to the analysis of (1) different strategies were envisaged to manage problems of micro-cracks and peeling off:

- Decrease the thickness t of the coating below t_c
- Act on the intrinsic material properties by increasing it elastic modulus, specific energy and Poisson ratio to increase t_c
- Decrease the biaxial stress occurring during the pyrolysis or in other words decrease the shrinkage

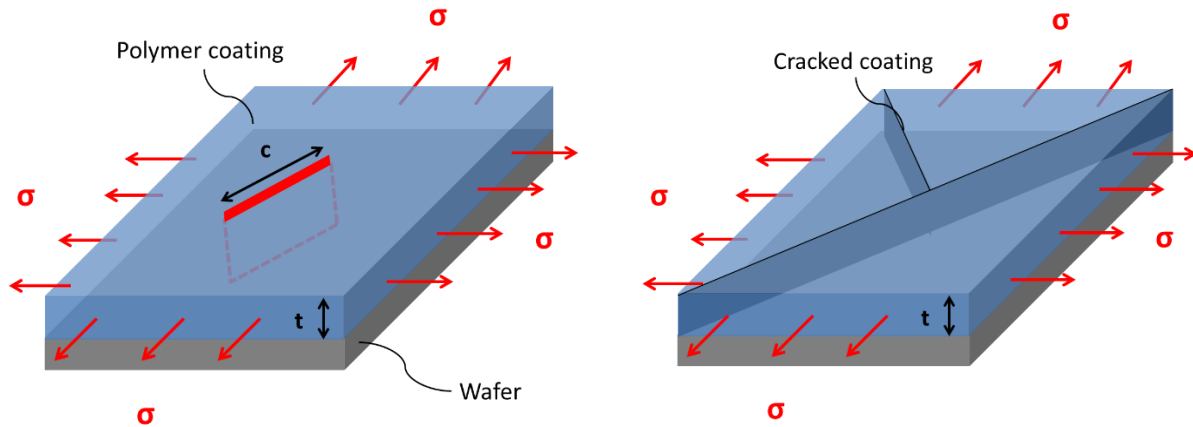


Figure 4-7: Griffith criterion description [13]

In the literature, the preparation of PDCs thin films or micropatterns has been explored and report critical thickness t_c between 1 and 5 μm (see next section). To avoid these mud-cracks formation the solution is to increase t_c according to undermentioned strategies.

- Act on mechanical properties (ω , E and ν) wasn't envisaged because it leads to changing the preceramic polymer nature previously developed
- Decrease shrinkage occurring during the pyrolysis of the precursor was thus selected as a privileged strategy and was explored through two different routes:
 - Increasing ceramic yield of the preceramic polymer *via* introduction of boron
 - Utilization of passive and active fillers

The following parts 4.3.3 and 4.4.4 gather the results and discussion associated with those strategies.

4.3.2 Practical examples from literature

According to literature, Table 4-2 regroups, for different materials, the maximum thickness of thin films and micropatterns prepared without cracking.

Table 4-2: Maximum thickness of ceramic coating derived from preceramic polymer

<i>Material</i>	<i>Technique</i>	<i>Maximum thickness</i>	<i>Reference</i>
ZrO_2	Sol-gel	2 μ m	[15] Beh <i>et al.</i>
PZT	Sol-gel	1.85 μ m	[16] Martin and Aksay <i>et al.</i>
PCS/SiC	PDCs	1 μ m	[14] Colombo <i>et al.</i>
PHPS/SiCN	PDCs	1.5 μ m	[17] Günther <i>et al.</i>
Polysiloxane/SiOC	PDCs	3 μ m	[18] Goerke <i>et al.</i>

For higher thickness, the film cracks because of the shrinkage occurring during the thermal treatment. It is possible to enhance the critical thickness by introducing fillers in order to reduce shrinkage and thus intern constraints. According to Barroso *et al.*, the addition of filler in a preceramic polymer matrix can conduct to ceramic/filler coating with thickness reaching 25 μ m.[19]

4.3.3 Microscopy observation

The procedure for the preparation of the micropatterns observed in this section is described in 2.3.2. We performed the PDMS mold preparation thanks to SU-8 masters made of microchannels with 50 to 200 μ m width.

With regards to Griffith criterion developed in the previous part, the reduced weight loss (and thus reduced shrinkage) observed for PBVZ by TGA analysis (see Figure 4-6) represent a great advantage in soft-lithography context. HRNM and SEM pictures of PVZ, PBVZ30 and 17 before and after pyrolysis are presented in Figure 4-8. In comparison with SiCN micropatterns, the quantity of cracks and delamination is much lower for SiBCN30 and especially SiBCN17. It is relevant to TGA analysis previously discussed which shows an improvement of the ceramic yield with the increase of Si/B ratio. Nevertheless, cracks are still distinguished in the SiBCN30 and SiBCN17 microstructure. Synthesis of PBVZ preceramic polymers with higher Si/B ratio were carried out in order to further increase the ceramic yield but the obtained products were gels or solids. Their shaping in the context of soft-lithography was more difficult or impossible considering their low solubility in toluene (or other solvents).

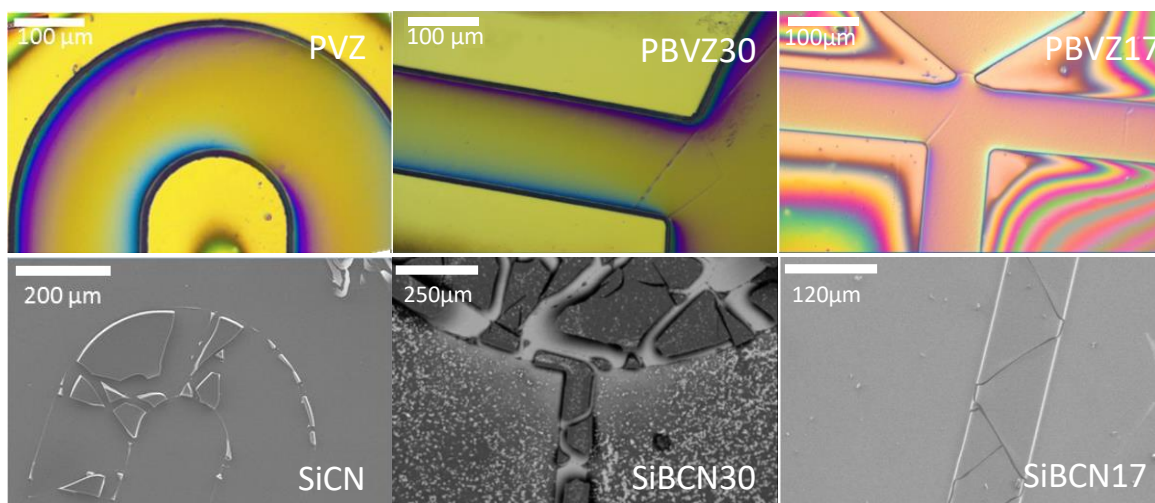


Figure 4-8: Optical microscopy pictures of PVZ, PBVZ30 and PBVZ17 micropatterns before and after pyrolysis (1000°C/2h, nitrogen atmosphere, heat and cooling rate of 1°C/min and 2°C/min, respectively)

4.3.4 Conclusion

Despite the increasing of ceramic yield and thus the lower shrinkage in the case of boron based preceramic polymers, it was not possible to prepare SiCN or SiBCN micropatterns free from cracks. The improvement of ceramic yield *via* introduction of higher boron quantity isn't the ideal route since it leads to too strong cross-linking of the polymer. Such gelled or solidified polymers were not compatible with the soft-lithography process since

they are almost insoluble in the different tested solvents (THF, toluene and acetone). According to these results, another strategy was envisaged to avoid the cracks formation. The next section introduces the “filler strategy” investigated and develops the influence of the filler nature, quantity and properties on the final micropattern based on Si(B)CN/filler composites.

4.4 Introduction of fillers

The filler strategy combined with the PDCs process has been previously explored in literature with the “near-net-shape” objective [20][21][22]. Section 1.1.2.3. in the state-of-the-art gathers the results of literature studies explaining the “near-net-shape” strategy and the use of fillers with preceramic polymers. In summary, it consists in adding powder with liquid polymer to reduce or eliminate shrinkage occurring during thermal treatment. Passive fillers consist in inert particles reducing global shrinkage of the filler/polymer composite, nevertheless, the shrinkage is never totally eliminated. On the other hand, active fillers react at high temperature with the preceramic polymer and the gas in the furnace to produce new phases. Expansion occurring by the newly formed phase can counterbalance the shrinkage caused by the preceramic polymer pyrolysis.

4.4.1 Fillers description

In this study, alumina (Al_2O_3), molybdenum disulfide (MoS_2) and molybdenum disilicide (MoSi_2) were used as fillers to produce composite micropatterns based on Si(B)CN. Al_2O_3 is a cheap, stable and abundant material. MoSi_2 is a conductive material with a high resistance to high temperatures and was previously reported as active filler in PDCs by Greil *et al.* [21]. Based on these properties, we believe mixing MoSi_2 with PDCs can induce conductive properties –non existant in filler-free PDCs- which can be of great interest for MEMS and electronic applications. MoS_2 is a transition metal dichalcogenide (TMD) with semi-conduction properties; it is a well-known electrocatalyst for Hydrogen Evolution Reaction (HER). The properties of each filler described above are presented in Table 4-3.

Table 4-3: Properties of Al_2O_3 , MoS_2 and $MoSi_2$ fillers; ICSD database;

	Grain size	Crystalline phase	Density (g/cm^3)	Specific properties
Al_2O_3	30-50 nm	Corindon	3,91	Cheap, stable, inert, abundant
$MoSi_2$	1-3 μm	Molybdenum disilicide	6,26	Conductive, refractory
MoS_2	1-3 μm	Molybdenite (2H-polytype)	4,92	Semi-conductive, electrocatalytic properties

4.4.2 Influence of fillers on shrinkage-microstructure

Composites based on PBVZ17 were not studied in this part. Indeed due to the high viscosity of PBVZ17 caused by early crosslinking, the preparation of moldable suspension was not successful. The obtained mixture consisted of a viscous paste rather than a liquid that cannot be easily injected in small channels of PDMS mold. The results discussed below concern fillers suspension based on PVZ and PBVZ30.

The influence of the filler's nature on the ceramic yield of polymer/filler suspensions was investigated *via* TGA, results are presented in Figure 4-9. As a reminder, the ceramic yields measured for pure PVZ or PBVZ30 were of 59,2 and 67 %, respectively. According to Figure 4-9, the presence of fillers clearly increases the ceramic yield independently from filler's nature.

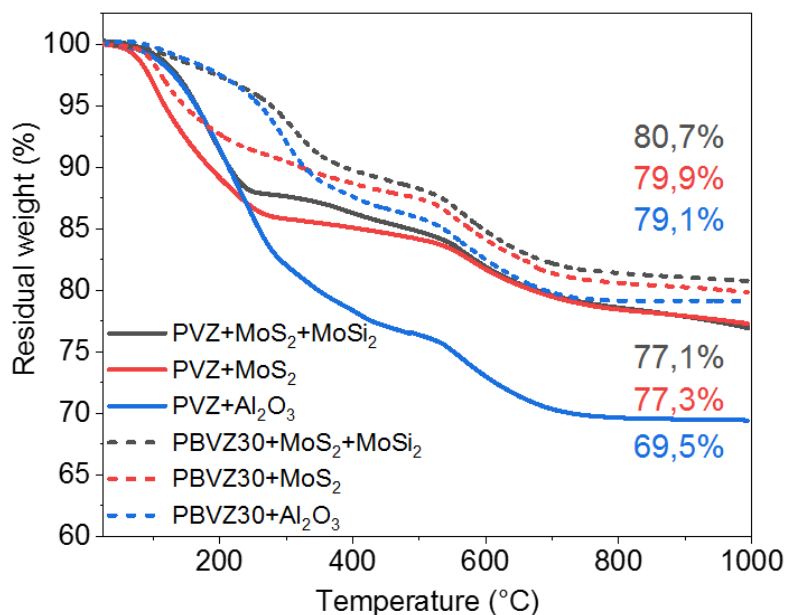


Figure 4-9: TGA curves of PVZ and PBVZ30 suspensions with MoS₂, MoSi₂ and Al₂O₃ fillers (Nitrogen atmosphere, 5°C/min, filler content 40wt%)

For the TGA of polymer/filler suspensions presented, each sample was loaded with 40wt% of filler (20-20wt% in the case of SiCN/MoS₂/MoSi₂). As for pure preceramic polymer, thermal decomposition is divided in three distinct weight loss steps (step I: 150-250°C; step II: 300-500°C; step: 600-1000°C) (see Figure 4-6). The introduction of 40wt% of filler in PVZ conducts to a reduction of weight loss of 10.2%, 17.8% and 18.4% in comparison with pure PVZ for Al₂O₃, MoS₂ and MoS₂/MoSi₂ fillers, respectively. The influence of fillers on the weight loss is crucial for reducing the “mud cracking” occurring during the pyrolysis (if we suppose that shrinkage and global residual weight are linked). The gap of weight loss between PVZ/Al₂O₃ and PVZ/MoS₂/MoSi₂ is important and may be explained by the formation of new phases (investigation on *in-situ* phase formation is discussed in next part 4.4.3). As expected, PBVZ30/filler samples follow the same pattern of thermal degradation but with a lower global weight loss.

To confirm the formation of new phases for suspensions containing MoS₂ and/or MoSi₂ XRD and XPS analysis were carried out. The investigation of phase formation is developed in the following section.

4.4.3 Investigation of *in-situ* phase formation

4.4.3.1 XRD Analysis

We believe that mixing the preceramic polymer with active fillers i.e. MoS_2 and MoSi_2 leads to the formation of a new phase. To confirm that, XRD analysis was carried out on SiCN/MoS_2 ; $\text{SiCN}/\text{MoSi}_2$ and $\text{SiCN}/\text{MoS}_2/\text{MoSi}_2$ composites obtained from pyrolysis (at 1000°C) and subsequent annealing (at different higher temperatures) of polymer/filler suspension. Diffractograms in Figure 4-10 are associated with PVZ/ MoS_2 (40wt% loaded) suspension heated between 800 and 1400°C under nitrogen atmosphere. The only crystalline phase detected in samples treated at 800°C is molybdenite 2H (MoS_2) which correspond to the initial filler introduced in the PVZ/ MoS_2 suspension. According to this result, no reaction seems to occur for treatment below 800°C . After a thermal treatment at 1000°C the initial molybdenite 2H (MoS_2) is still present but small “new peaks” can be distinguished at 35.5 , 48.6 and 63.7° (black arrow). The emergence of these new peaks suggest the formation of a new crystalline phase during the thermal treatment, unfortunately due to the small size, the low number of peaks and the presence of SiCN amorphous phase, the identification of this new phase wasn’t possible at this stage. In order, to further crystallize and grow this “unknown” phase, PVZ/ MoS_2 sample was treated at higher temperature (1200 and 1400°C) under nitrogen. At 1200°C , the initial MoS_2 is not detected anymore in the material and seems replaced by a Mo_2C phase exclusively. Formation of Mo_2C suggests a reaction between the free carbon of the SiCN phase and the molybdenum present in the initial MoS_2 . Disappearance of MoS_2 suggests the gaseous evacuation of sulfur which is confirmed by the strong sulfur odor emanating from the furnace when opened. After treatment at 1400°C , Mo_2C phase is still present but other small peaks associated with $\text{Mo}_{4,8}\text{Si}_3\text{C}_{0,6}$ phase can be distinguished. Nowotny *et al.* identified in 1954 the only ternary compound in the Mo-Si-C system [23]. Its composition is $\text{Mo}_{3+2x}\text{Si}_3\text{C}_y$ ($x \leq 1$, $y \leq 1$) with fluctuating occupancies of C and Mo2 sites, the crystal structure was precisely determined for $\text{Mo}_{4,8}\text{Si}_3\text{C}_{0,6}$ composition [24][25]. The “unknown” phase detected at 1000°C is not detected neither at 1200 nor 1400°C and seems to correspond to a transition phase between the initial MoS_2 and the formed Mo_2C .

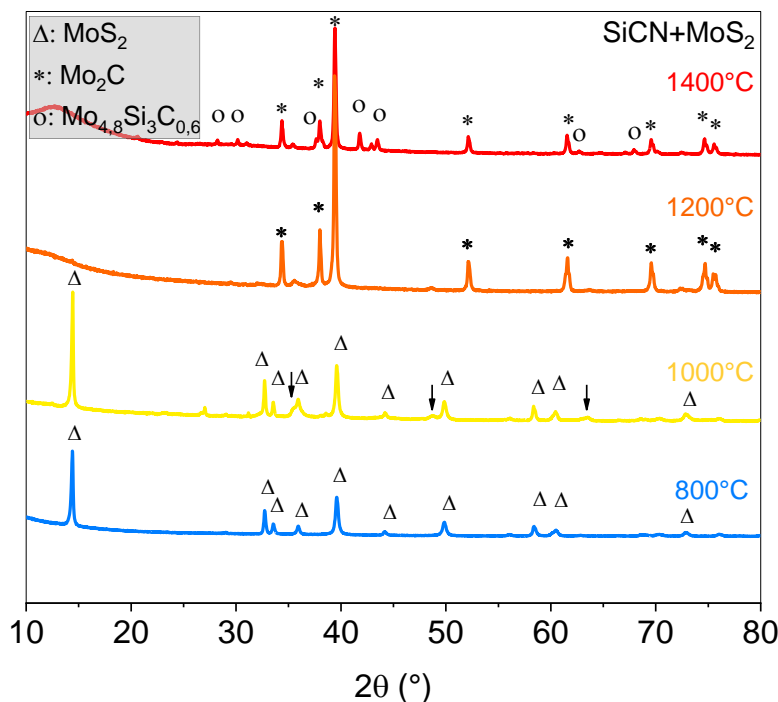


Figure 4-10: XRD diffractograms associated with SiCN/MoS₂ composites heat treated between 800 and 1400°C (40wt% MoS₂ content in initial PVZ/MoS₂ suspension; 2h, nitrogen atmosphere, heat and cooling rate of 1°C/min and 2°C/min, respectively)

A similar XRD analysis, presented in Figure 4-11, was performed on a PVZ/MoSi₂ 40wt% sample. Below 1000°C no other peaks than the one associated with the initial MoSi₂ filler are distinguished, this suggests that no reaction occurs between PVZ and MoSi₂ below such a temperature. New peaks are detected for higher temperatures and confirm the presence of the Nowotny Mo_{4,8}Si₃C_{0,6} phase. The “unknown” phase is not detected for PVZ/MoSi₂ system which confirms the hypothesis that it is generated from reaction involving MoS₂ filler.

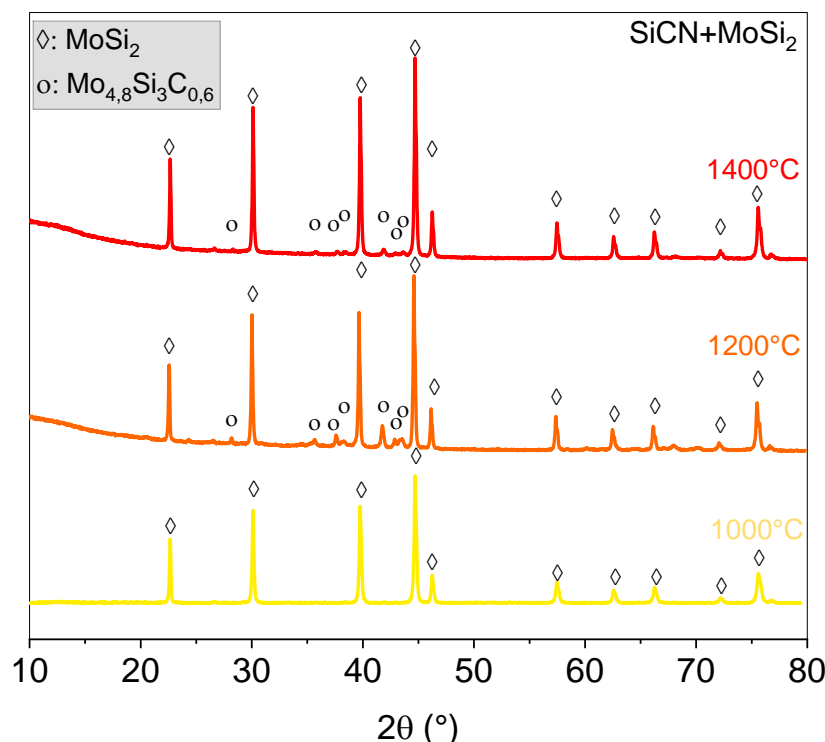


Figure 4-11: XRD diffractograms associated with SiCN/MoSi₂ composites and heat treated between 800 and 1400°C (40wt% MoSi₂ content in initial PVZ/MoSi₂ suspension; 1000°C/2h, nitrogen atmosphere, heat and cooling rate of 1°C/min and 2°C/min, respectively)

In the case of the diffractogram associated with PVZ/MoS₂/MoSi₂ system in Figure 4-12 no reaction seems to take place below 800°C given that the associated diffractograms contain exclusively peaks corresponding to initial MoS₂ and MoSi₂ fillers. On the contrary, with SiCN/MoS₂ and SiCN/MoSi₂ systems, the Nowotny Mo_{4.8}Si₃C_{0.6} phase is detected at lower temperature (1000°C *versus* 1200°C for SiCN/MoS₂ and SiCN/MoSi₂), the combined presence of MoS₂ and MoSi₂ seems to favor its formation. With temperature rising, the number of phases increases dramatically with the appearance of 5 different types of crystallites detected at 1200°C: Mo₂C, Mo₅Si₃ and Mo_{4.8}Si₃C_{0.6} present strong and small peaks associated with Si₃N₄ and MoSi₂. When temperature reaches 1400°C, Mo₅Si₃, Mo_{4.8}Si₃C_{0.6}, Si₃N₄ and MoSi₂ are still present but Mo₂C phase is no longer in the sample. Si₃N₄ peaks are stronger than for 1200°C suggesting a higher quantity of this phase at 1400°C.

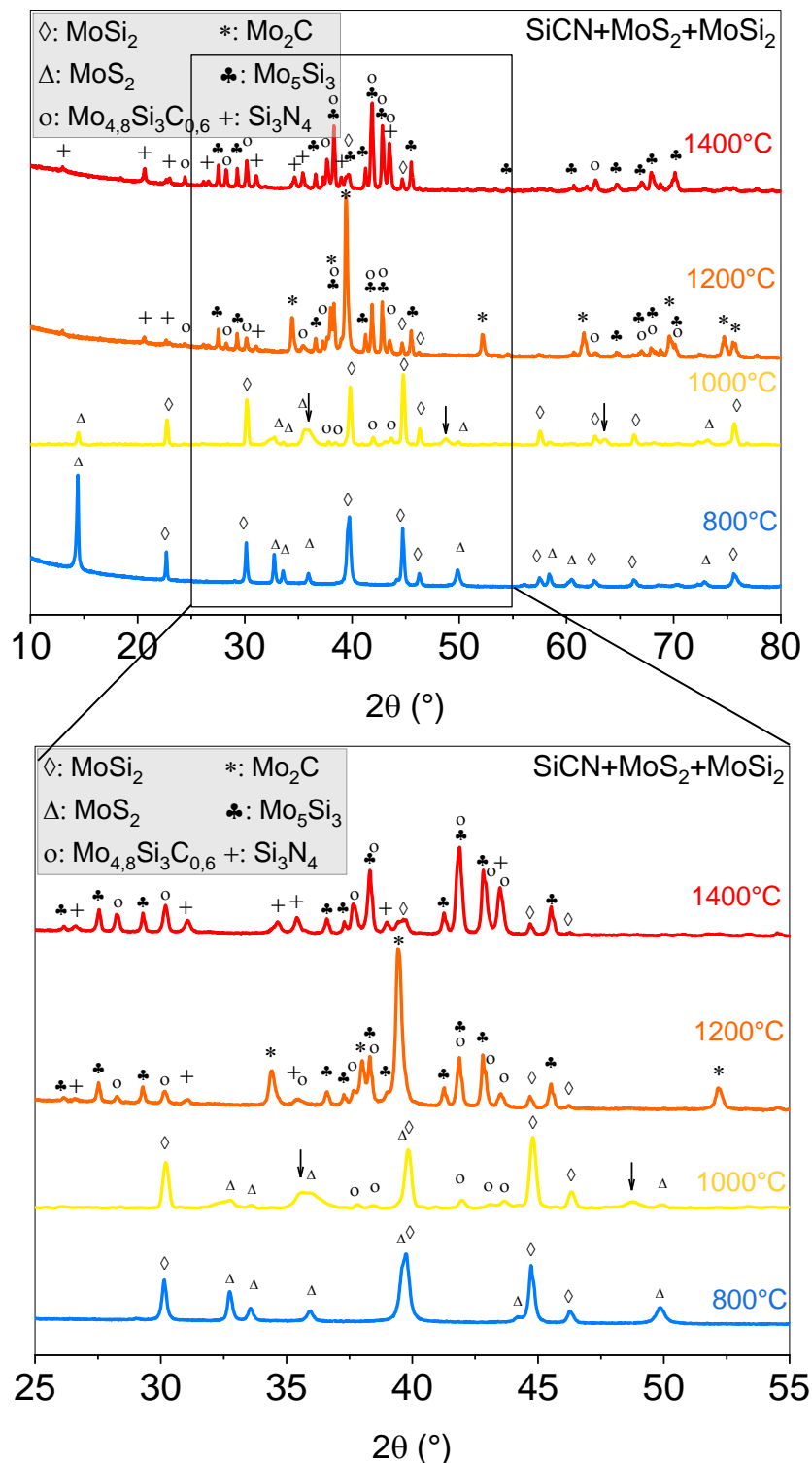


Figure 4-12 XRD diffractograms associated with $\text{SiCN}/\text{MoSi}_2/\text{MoS}_2$ composites and heat treated between 800 and 1400°C with inset on 25-55° 2θ range (20/20wt% $\text{MoSi}_2/\text{MoS}_2$ content in initial PVZ/ $\text{MoSi}_2/\text{MoS}_2$ suspension; 1000°C/2h, nitrogen atmosphere, heat and cooling rate of 1°C/min and 2°C/min, respectively)

According to this XRD study, the formation of new phases at 1000°C for PVZ/MoS₂ and PVZ/MoS₂/MoSi₂ systems could justify the weight loss gap in comparison to PVZ/Al₂O₃ (see Figure 4-9). In regard with the diffractograms obtained at higher temperatures the reactions to form new phase seems to consume a part of the free carbon present in the amorphous SiCN phase to form phase like Mo₂C or Mo_{4,8}Si₃C_{0,6}. This consumption of free carbon conduct to a lower production of gaseous species like CH₄ or C_xH_y conventionally released in the pyrolysis of preceramic polymers and could explain the low weight loss measured for PVZ/MoS₂ and PVZ/MoS₂/MoSi₂ samples. All the properties and description of the crystalline phases mentioned above are gathered in Table 4-4 below.

Table 4-4: Description of the crystalline phase discussed in this part

	Crystal system	Space group	Cell parameters	Code ICSD
<i>MoS₂-2H</i>	Hexagonal	P 63/m m c	3.15(2) 3.15(2) 12.30(7) 90. 90. 120.	24000
<i>MoSi₂</i>	Tetragonal	I 4/m m m (139)	3.2112(1) 3.2112 7.8249(3) 90. 90. 90.	73598
<i>Mo₂C</i>	Hexagonal	P 63/m m c (194)	4.732(2) 6.037(3) 5.204(2) 90. 90. 90.	1326
<i>Mo₅Si₃</i>	Tetragonal	I 4/m c m (140)	9.650(2) 9.650(2) 4.911(1) 90. 90. 90.	35756
<i>Mo_{4,8}Si₃C_{0,6}</i>	Hexagonal	P 63/m c m (193)	7.286(1) 7.286(1) 5.046(2) 90. 90. 120.	23858
<i>Si₃N₄</i>	Hexagonal	P 63/m (176)	7.60182(7) 7.60182(7) 2.90713(3) 90. 90. 120.	74740

XRD technique gives information about the crystalline phase in the materials but is not efficient for investigating the amorphous nature of the materials. It is thus not very helpful for the study of amorphous SiCN. To gather more information about reactions occurring and new phases formed at 1000°C with eventual amorphous microstructures, XPS investigations were performed on SiCN/MoS₂, SiCN/MoSi₂, SiCN/MoS₂/MoSi₂ and SiCN materials. The results are presented below.

4.4.3.2 XPS analysis

To complete the characterization of the composites, XPS was carried out on SiCN/MoS₂ and SiCN/MoS₂/MoSi₂ heat treated at 1000°C in order to investigate about the unidentified phase discussed before and about the amorphous phase in the composite. Figure 4-13 to

Figure 4-16 present the C1s, Mo3d, Si2p and S2s XPS signal, respectively, of PVZ/MoS₂, PVZ/MoS₂/MoSi₂, SiCN, MoS₂ and MoSi₂ materials.

The deconvolution of C1s peak of SiCN material (Figure 4-13) reveals different oxidation degrees of the carbon. Peak at 284.4 eV is associated with C-C bond and is characteristic of the free carbon nanodomains in the SiCN amorphous phase. C-Si, C-O and C=O bonds are also detected in the pure ceramic with signals at 283.1eV, 285.8 and 286.4 eV, respectively [3][26][27][28][29][30].

Similar bonds are detected in SiCN/MoS₂ and SiCN/MoS₂/MoSi₂ systems, which confirms the presence of SiCN amorphous phase in the composites. Nevertheless, an additional deconvoluted peak at 283.9 eV could be attributed to C-Mo bonds [31][32][33][34][35]. Those observations on the C1s XPS signal are consistent with the Mo3d signal of such sample (see Figure 4-14). Deconvolution of the pure MoS₂ filler signal reveals a couple of Mo3d_{5/2} and Mo3d_{3/2} bands associated with Mo⁴⁺ oxidation degree (Mo3d_{5/2} at 230.5 eV). S2s signal strongly overlaps the Mo3d region and confirm the presence of S-Mo bonds with peak at 227.4 eV [36][37][38][39] .

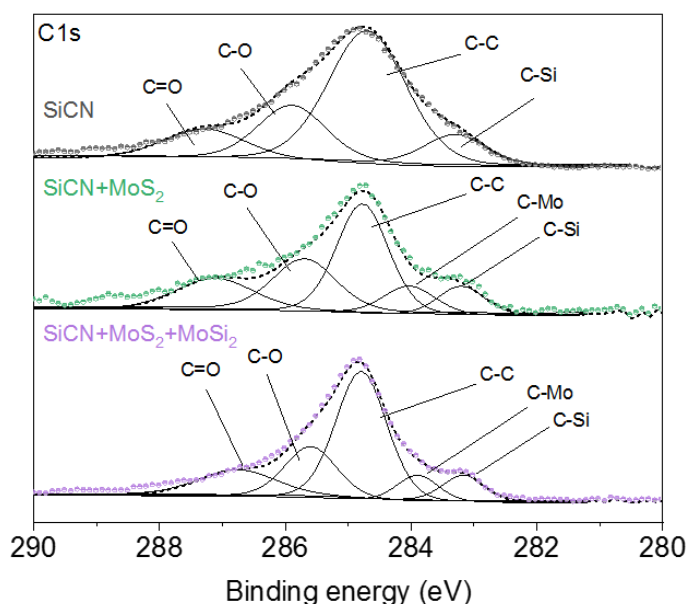


Figure 4-13: C1s XPS spectra for SiCN, SiCN/MoS₂ (40wt% of MoS₂ content) and SiCN/MoS₂/MoSi₂ (20/20wt% MoSi₂/MoS₂ content); powder deposited on Si wafer gold coated

Considering the XPS signals of SiCN/MoS₂ and SiCN/MoS₂/MoSi₂, Mo⁴⁺ signal is still present in the sample but other oxidation degrees seems to co-exist. Mo³⁺ and Mo²⁺ peaks at 229.6 and 228.8 eV, respectively, suggest the formation of S-Mo=C and C=Mo=C environments [33][34][35]. These observations are coherent with the presence of the transitory “unknown phase” discussed before in the XRD analysis. Regarding the information gathered thanks to this chemical investigation, we can suppose that the unidentified phase is a transitory phase between MoS₂ and Mo₂C, containing Mo-S, Mo=C and Mo-C bonds. From now on, this “unknown phase” will be named Mo_xS_yC_z.

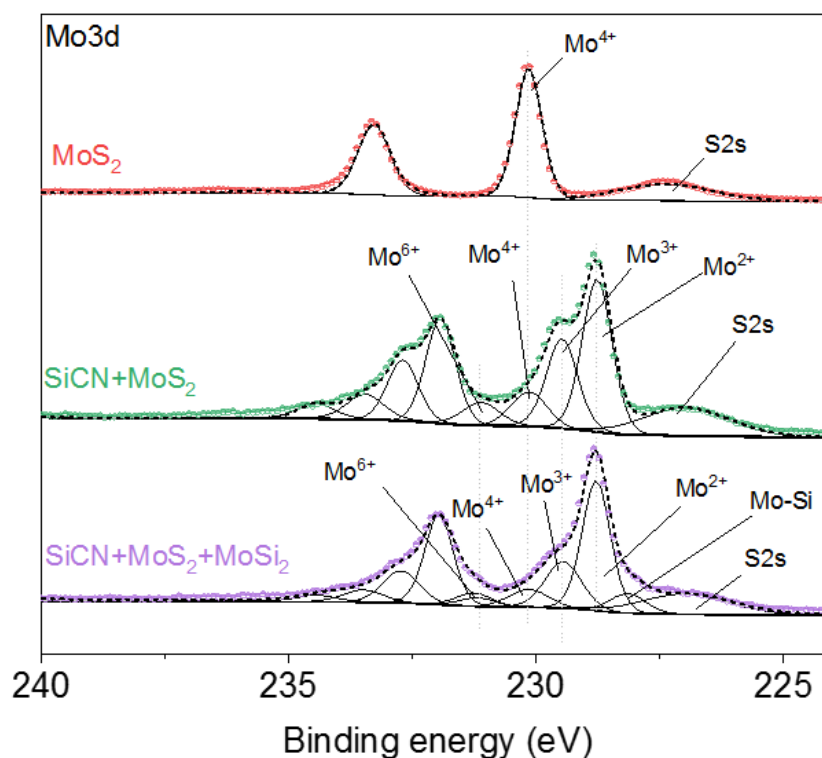


Figure 4-14: Mo3d XPS spectra for MoS₂, SiCN/MoS₂ (40wt% of MoS₂ content) and SiCN/MoS₂/MoSi₂ (20/20wt% MoSi₂/MoS₂ content); powder deposited on Si wafer gold coated

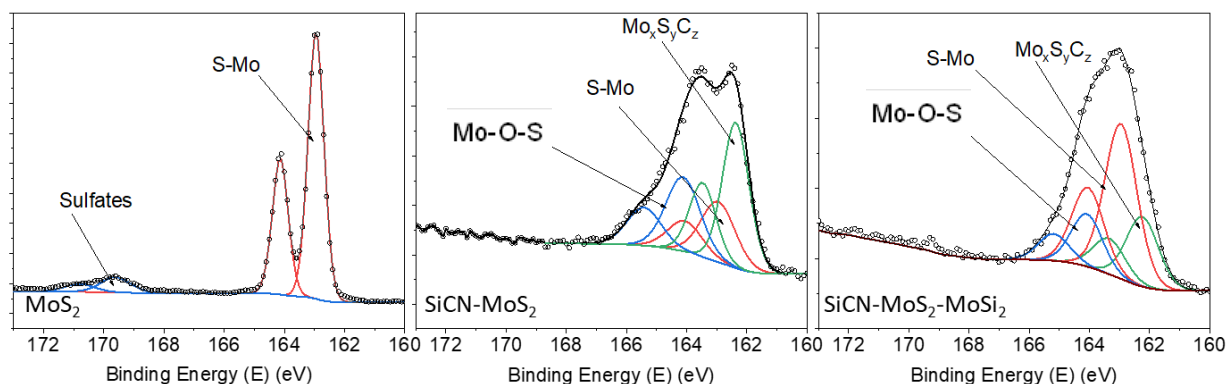


Figure 4-15: S2p XPS spectra for MoS₂, SiCN/MoS₂ (40wt% of MoS₂ content) and SiCN/MoS₂/MoSi₂ (20/20wt% MoSi₂/MoS₂ content); powder deposited on Si wafer gold coated

The existence of Mo_xS_yC_z phase seems to be also confirmed by the analysis of S2p XPS peaks discussed in Figure 4-15. The couple of peak with S2p_{3/2} peak at 162.96 eV associated with S-Mo bond is detected in pure MoS₂, SiCN/MoS₂ and SiCN/MoS₂/MoSi₂ systems (Sulfate peaks at 169.63 eV are considered as pollution initially present in the commercial powder). In the case of SiCN/MoS₂ and SiCN/MoS₂/MoSi₂, other signals are detected: couple of peaks with S2p_{3/2} signals at 162.37 eV corresponds to a lower oxidation degree of sulfur, with regards to Mo3d XPS signals, this peak was associated with the Mo_xS_yC_z phase. The peak at higher binding energy (S2p_{3/2} 164.13 eV) was associated with Mo-O-S bonds formed after side reaction of oxidation.

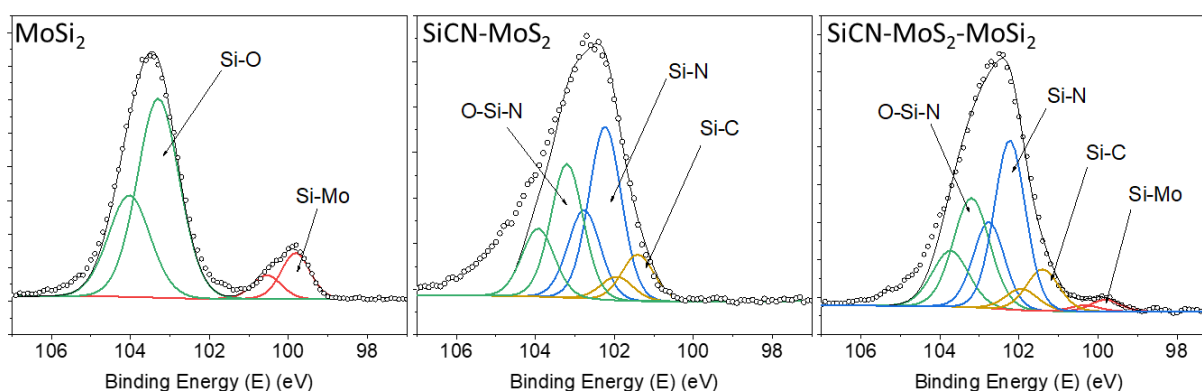


Figure 4-16: Si2p XPS spectra for MoSi₂, SiCN/MoS₂ (40wt% of MoS₂ content) and SiCN/MoS₂/MoSi₂ (20/20wt% MoSi₂/MoS₂ content); powder deposited on Si wafer gold coated

Finally, Si2p XPS signals presented in Figure 4-16 confirm the presence of SiCN ceramic in SiCN/MoS₂ and SiCN/MoS₂/MoSi₂ systems by Si2p_{3/2} signals at 102.24 and 101.41 eV

associated with Si-N and Si-C bonds. Si-Mo bonds at 99.82 eV in MoSi₂ and SiCN/MoS₂/MoSi₂ systems come from initial MoSi₂ filler and Mo_{4,8}Si₃C_{0,6} *in situ* formed phase [40][41][42].

A final remark concerning the presence of oxygen in the samples is necessary before concluding on the XPS analyzes. According to the elemental composition of each sample detailed in Table 4-5, oxygen content is very high in the sample (reaching 59,2 % for pure MoSi₂). Several XPS signals associated with oxygen-based groups have been detected and explained in Figure 4-13 to Figure 4-16. However, the experimentation and manipulation of those materials were carried out under inert atmosphere to avoid oxidation of pre-SiCN polymer. Several hypothesis and explanation could justify this strong content of oxygen:

- The elemental composition determined on commercial MoS₂ and MoSi₂ fillers reveal a strong oxygen level. It is probably due to the presence of oxidized species at the filler's surface such as sulfates in the case of MoS₂ and MoO₂ and/or SiO₂ for MoSi₂. The same observation can be made for the pure SiCN sample with C-O bonds detected in the C1s XPS signal. The commercial PVZ (Durazane 1800) was received in air packaging, in this condition, formation of Si-O bonds and presence of dissolved oxygen in the preceramic polymer is conceivable.
- XPS is above all a surface analysis technique, specific surface phenomenon such as surface oxidation or oxygen adsorption are overrepresented against the phenomenon happening in the core of the material.
- The hypothesis of slight oxidation during experimentation and/or thermal treatment can also be considered even though all precautions were taken (use of glove box and Schlenk lines)..

Table 4-5: Elemental composition of MoS₂, MoSi₂, SiCN, SiCN/MoS₂, SiCN/MoSi₂ and SiCN/MoS₂/MoSi₂ samples determined thanks to XPS analysis

Sample	Si2p (at%)	C1s (at%)	O1s (at%)	N1s (at%)	Mo3d (at%)	S2p (at%)
<i>MoS₂</i>	0.0	21.5	19.0	0.0	17.5	42.0
<i>MoSi₂</i>	22.3	11.4	59.2	0.0	7.1	0.0
<i>SiCN</i>	27.0	29.3	25.5	18.2	0.0	0.0
<i>SiCN/MoS₂</i>	27.7	36.3	20.5	0.0	5.2	10.2
<i>SiCN/MoS₂/MoSi₂</i>	29.0	34.8	24.6	0.0	4.0	7.6

To conclude on the microstructure investigations of SiCN/filler composites, it is confirmed that reaction occurs in PVZ/MoS₂ and PVZ/MoS₂/MoSi₂ suspensions during the pyrolysis. Molybdenum environment tends to be reduced with increasing of the temperature and conducts to formation of Mo₂C, Mo₅Si₃, Mo_{4.8}Si₃C_{0.6} phases. The Mo_xS_yC_z phase detected at 1000°C in the SiCN/MoS₂ and SiCN/MoS₂/MoSi₂ samples wasn't clearly identified but it is highly probable that it is composed of Mo-C and/or Mo=C bonds. Such phase formation during the thermal treatment represents a great advantage in the preparation of PDCs based micro-patterns by decreasing shrinkage and tends to reduce cracks formation. Moreover, regarding the water splitting application, some studies have demonstrated the interesting electrocatalytic performance of MoS₂, Mo₂C and Nowotny phases [25][43]. The link with the electrocatalysis study developed in Chapter III is now clearer and the interest of MoS₂ and/or MoSi₂ - as fillers and electrocatalysts- is relevant to our objective.

The aim of this study is to prove the feasibility of soft-lithography process with preceramic polymer based suspension for the fabrication of microstructured electrocatalyst device. The next section focuses on the influence of filler nature on the shape reproduction, cracking and shrinkage of the micropattern. The ceramic/filler based micropatterns are studied there with microscopy, topography, EDX and profilometric investigations.

4.4.4 Microscopy observation of microstructured patterns

4.4.4.1 Influence of filler's nature on cracking

With regards to the results discussed in the previous parts, passive and active fillers have great potential for reducing or eliminating mud-cracks. The “*in-situ*” Nowotny-like phase formation observed in the case of SiCN/MoS₂ and SiCN/MoS₂/MoSi₂ systems is compatible with the “near-net-shape” strategy developed in section 1.1.2.3. In the following sections, the microcopy, topographic and EDX observations of micropatterns prepared from PVZ/fillers and PBVZ30/fillers suspensions are presented and discussed. The influence of the filler's nature on cracking and faithful shape reproduction will be investigated also. As a reminder, the preparation method of ceramic/filler micropattern is explained in section 2.3.2.2.

4.4.4.1.1 PVZ/Al₂O₃

Figure 4-17 gathers microscopic observations of SiCN/Al₂O₃ 40wt% micro-pattern reproduced thanks to the “embossing route” (see part 2.3.2.2). Figure 4-17.a shows large scale SEM picture of SiCN/Al₂O₃ samples. The global shape of the micro-device seems conserved and no big cracks are observed. Considering high magnification SEM picture presented in Figure 4-17.b, small cracks can be distinguished suggesting that shrinkage is still too high to conserve the net shape of the original molded polymer.

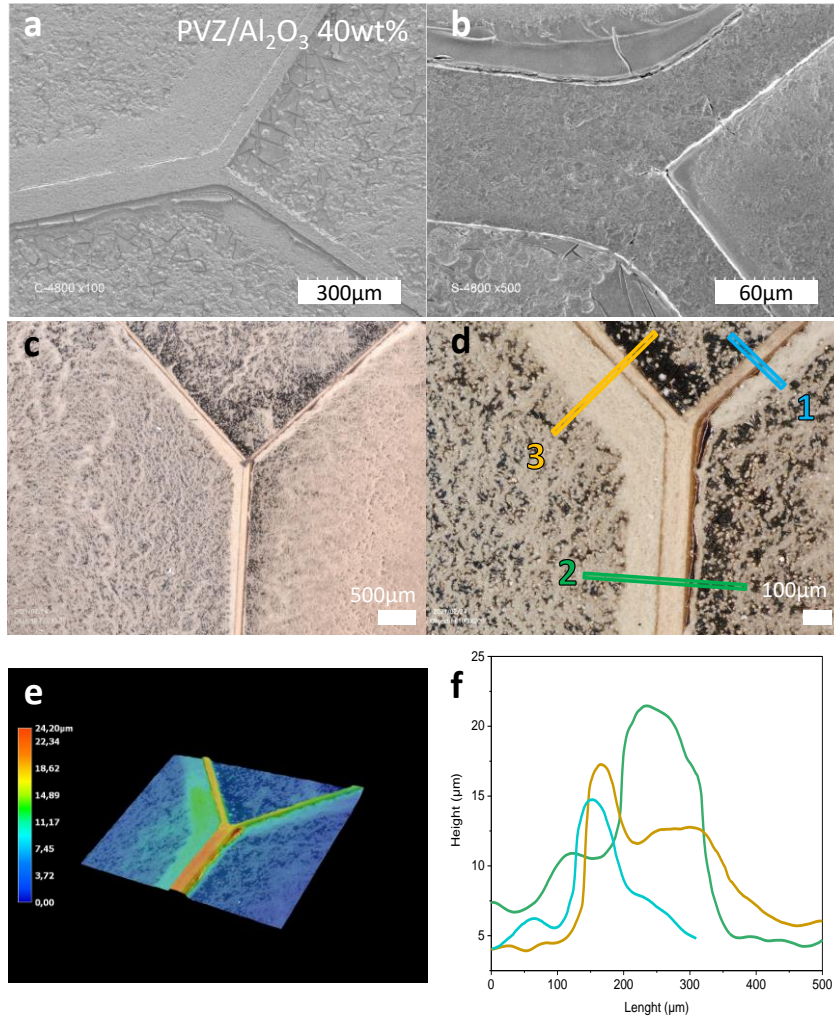


Figure 4-17: Microscopy and topography observations of SiCN/Al₂O₃ 40wt% sample with a) and b) SEM pictures obtained at low and high magnification, respectively; c) and d) HRNM pictures obtained with low and high magnification, respectively; e) 3D reproduction of the micropattern via DFD technology; f) Cross-section reproduction of the micropattern obtained via DFD technology

Thanks to numerical microscopy and DFD (Depth from defocus), technology the topography of SiCN/Al₂O₃ micro-patterns was reproduced in Figure 4-17.e from high-resolution pictures presented in Figure 4-17.c-d. The shape and the thickness of the sample were analyzed by profilometry (Figure 4-17.f) that shows its poor homogeneity and a remarkable deformation of the initial rectangular shape of the channels of the PDMS mold.

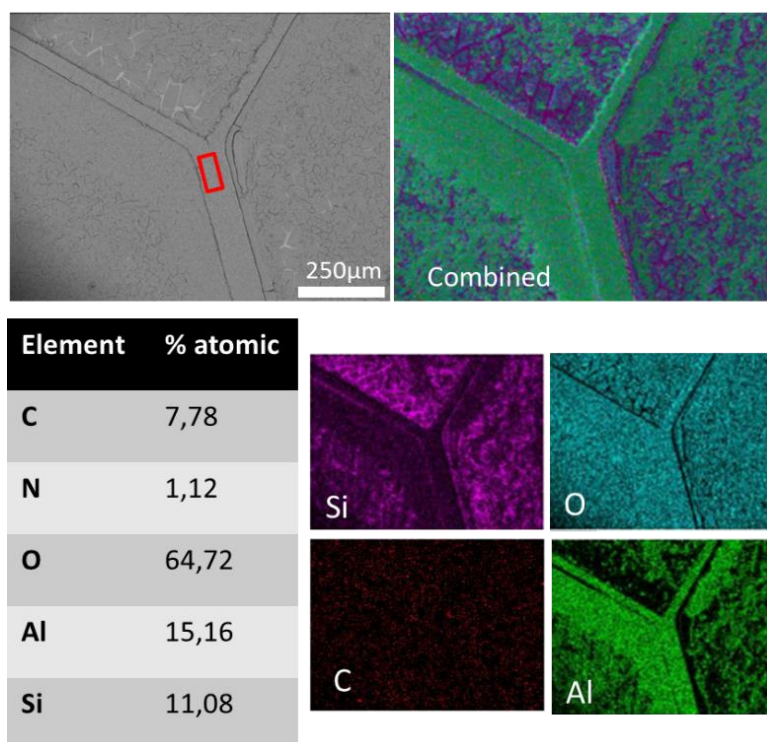


Figure 4-18 : EDX mapping and elemental analysis of SiCN/Al₂O₃ 40wt% sample

EDX mapping of SiCN/Al₂O₃ presented in Figure 4-18 shows the cartography sample C, O, Al and Si atoms and confirm the presence of Al₂O₃ filler and SiCN ceramic in a homogeneous distribution. Nevertheless, the low Al/O ratio of 0,28 detected in red square suggest that alumina filler is not the only source of oxygen in the microstructure. PVZ has probably been oxidized during optical microscope observation proceeded outside of the glove box.

Globally, those observations confirm the great interest of the filler strategy for the preparation of free from cracks PDCs based microdevices. Utilization of Al₂O₃ passive fillers conduct to lower shrinkage and deformation during the pyrolysis and prevent the structure from big cracking in comparison with pure polymer (see Figure 4-17).

4.4.4.1.2 PVZ/MoS₂

Microscopy observations of PVZ/MoS₂ 40wt% are presented in Figure 4-19. Large scale SEM, numerical high-resolution picture and associated topography of the micropattern in Figure 4-19.a-f revealed net-shaped channels with homogeneous thickness reaching almost 20μm according to profilometry analysis. Smaller scaled SEM picture in Figure 4-19.b reveals channels free from microcracks unlike SiCN/Al₂O₃ discussed in Figure 4-17.

Moreover, this net-shaped microstructure was obtained with a lower volumetric filler content in comparison with SiCN/Al₂O₃ sample considering the higher density of MoS₂ filler. This observation tends to confirm the advantageous “active filler” properties of MoS₂ for PDCs never reported in the literature before.

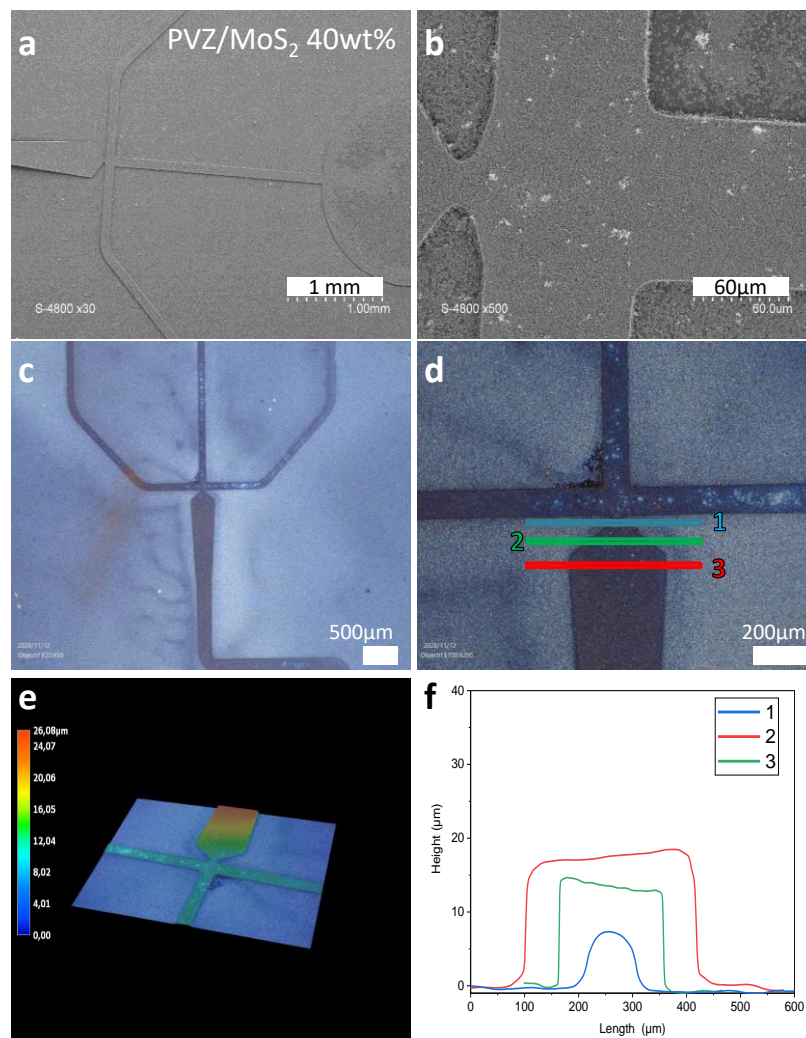


Figure 4-19: Microscopy and topography observations of SiCN/MoS₂ 40wt% sample with a) and b) SEM pictures obtained at low and high magnification, respectively; c) and d) HRNM pictures obtained with low and high magnification, respectively; e) 3D reproduction of the micropattern via DFD technology; f) Cross-section reproduction of the micropattern obtained via DFD technology

The composition in the red square in SiCN/MoS₂ microchannel has been determined by EDX technique (Figure 4-20). The detection of Si, C and N atom confirms the presence of the SiCN ceramic in the micro-pattern. The Mo and S atoms detection with Mo/S ratio lower than 2 suggests that a part of the sulfur escaped from the material during the pyrolysis. It is

confirmed by the intense odor of sulfur emanating from the furnace when opened. This result suggests reactions implying S and Mo occur during this thermal treatment. This interpretation is coherent with the XRD analysis on the powder (Figure 4-20) obtained from SiCN/MoS₂ suspension pyrolysis revealing formation of new phase Mo_xS_yC_z.

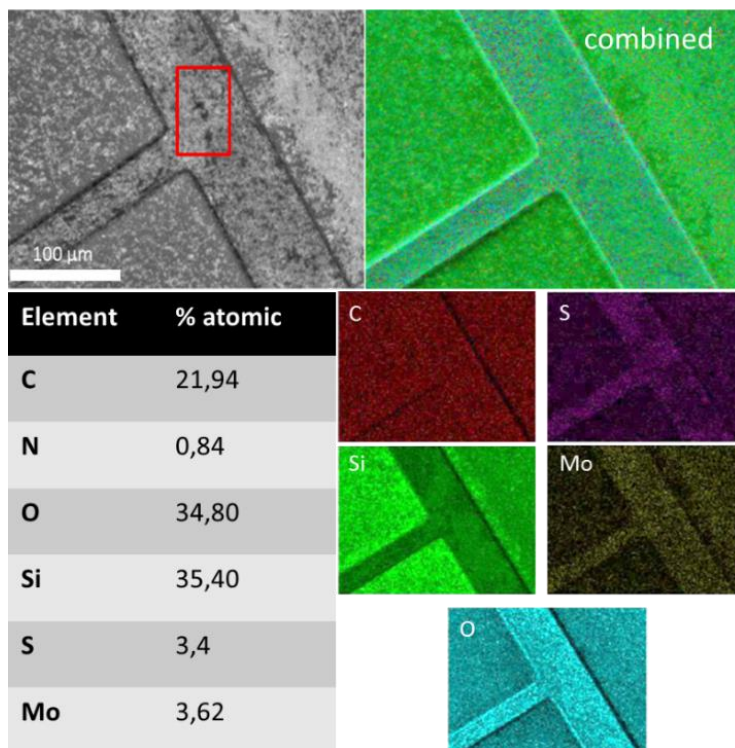


Figure 4-20: EDX mapping and elemental analysis of SiCN/MoS₂ 40wt% sample

4.4.4.1.3 PVZ/MoS₂/MoSi₂

SEM and optical microscopy carried out on SiCN/MoS₂/MoSi₂ samples are presented in Figure 4-21. According to low magnification observations (a and c) the PDMS mold shape is well reproduced, without formation of big cracks or peeling off. High magnification (b and d) observations do not reveal presence of major defects but small initiations of microcracks are distinguishable. The derivation from the initial PDMS mold shape seems also higher with this system in comparison to SiCN/MoS₂. The double “peak shape” observable with profilometry in Figure 4-21. f is characteristic of a strong shrinkage, such a profilometric shape is not visible on SiCN/MoS₂ sample. It suggests stronger deformation and a lower efficiency of the MoS₂/MoSi₂ filler mix *versus* MoS₂ alone. According to XRD and XPS studies developed in section 4.4.3, thermal treatment at 1000°C of PVZ/MoS₂/MoSi₂ system leads

to formation of two new phases: Nowotny phase $\text{Mo}_{4.8}\text{Si}_3\text{C}_{0.6}$ and intermediate phase $\text{Mo}_x\text{S}_y\text{C}_z$ between MoS_2 and Mo_2C . On the other hand, in the case of PVZ/ MoS_2 , $\text{Mo}_x\text{S}_y\text{C}_z$ is the only *in-situ* formed phase. Regarding those considerations, it seems that the reactions conducting to $\text{Mo}_x\text{S}_y\text{C}_z$ formation are more favorable for reducing shrinkage and suitable with the “net-shape” strategy. The stronger shrinkage could also be caused by the lower volumetric filler content in PVZ/ MoS_2 / MoSi_2 system in comparison to PVZ/ MoS_2 caused by higher density of MoSi_2 filler.

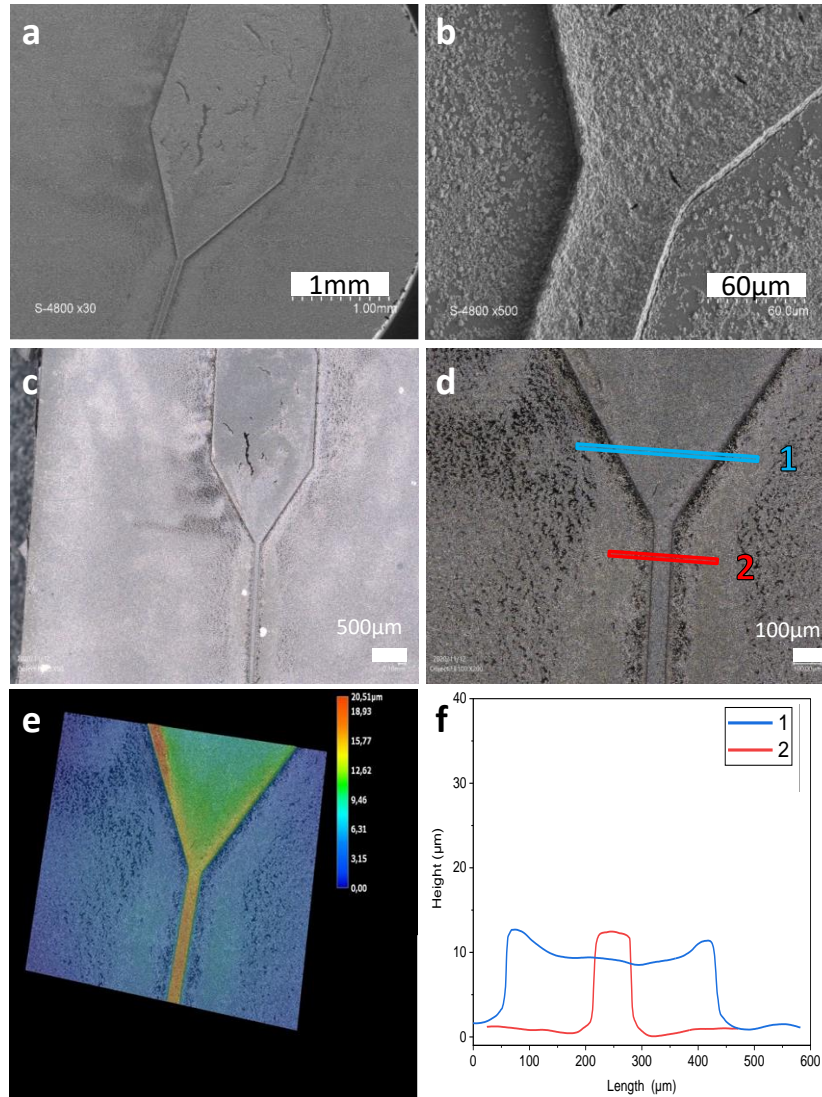


Figure 4-21: Microscopy and topography observations of $\text{SiCN}/\text{MoS}_2/\text{MoSi}_2$ 20/20wt% sample with a) and b) SEM pictures obtained at low and high magnification, respectively; c) and d) HRNM pictures obtained with low and high magnification, respectively; e) 3D reproduction of the micropattern via DFD technology; f) Cross-section reproduction of the micropattern obtained via DFD technology

The composition of the micropattern prepared from PVZ/MoS₂/MoSi₂ suspension was measured on the area represented by the red square in Figure 4-22. All the expected elements are detected and the cartography represented fits well with the drawn pattern.

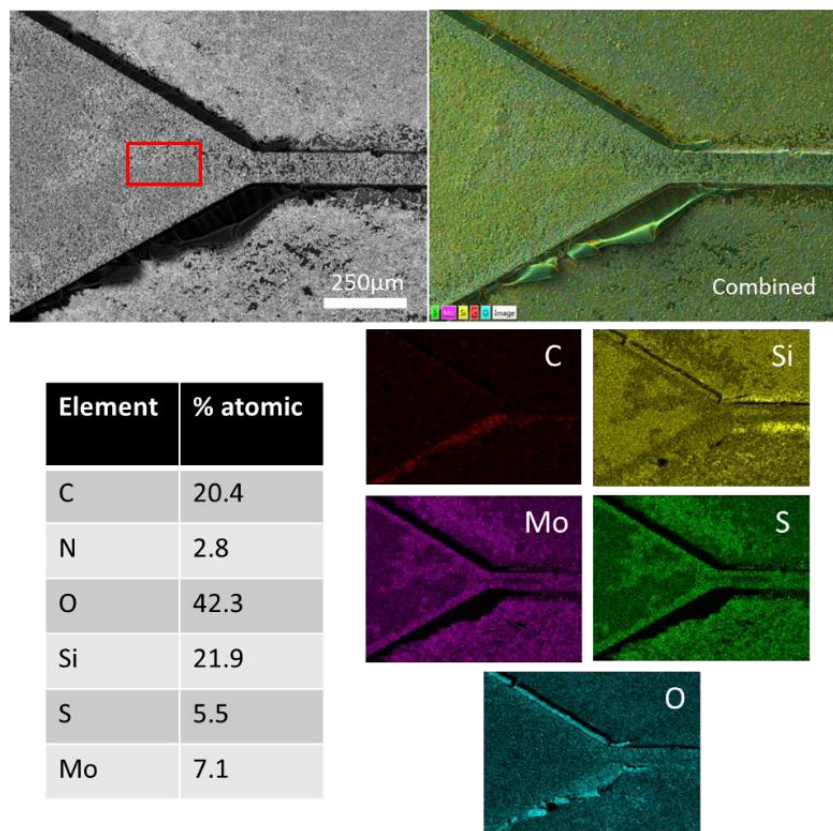


Figure 4-22: EDX mapping and elemental analysis of SiCN/MoS₂/MoSi₂ 20/20wt% sample

The discussion on Figure 4-21 and Figure 4-22 clearly demonstrate the feasibility of SiCN/MoS₂/MoSi₂ microdevice. Nevertheless, the SiCN/MoS₂ system has shown a higher efficiency for faithful reproduction of initial PDMS mold shape by embossing in comparison with SiCN/MoS₂/MoSi₂ and more specifically with SiCN/Al₂O₃. The efficiency of MoS₂ as active filler seems confirmed according to the results discussed in this section and was never reported in the literature before.

4.4.4.1.4 PBVZ30/Al₂O₃

According to TGA results gathered on the different polymer/filler suspensions and presented in Figure 4-9, the systems based on PBVZ30 have a higher yield than that containing a PVZ polymer. This higher yield involves a lower shrinkage during the thermal treatment and suggests a better efficiency of PBVZ30 based suspension in the context of the

near-net-shape strategy. These expectations have been nuanced by the practice and are discussed thanks to the next figures.

As for SiBCN/ Al_2O_3 sample, the quantity of cracks in SiBCN30/ Al_2O_3 pattern is strongly reduced in comparison with micropatterns prepared from pure polymer. Nevertheless, due to the high viscosity of PBVZ30, dispersion of filler particle is harder and conducts to paste-like suspension. In these conditions, the molding of the suspension in PDMS mold is more difficult and it conducts to a less homogeneous dispersion of the filler in the preceramic polymer matrix.

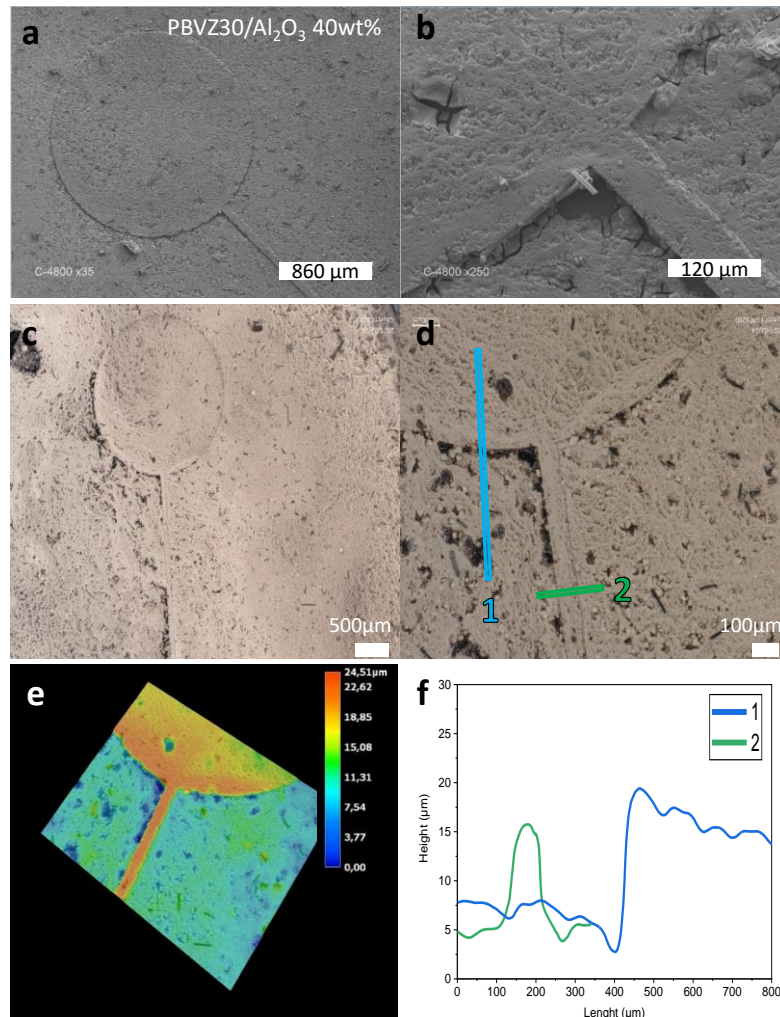


Figure 4-23: Microscopy and topography observations of SiBCN30/ Al_2O_3 40wt% sample with a) and b) SEM pictures obtained at low and high magnification, respectively; c) and d) HRNM pictures obtained with low and high magnification, respectively; e) 3D reproduction of the micropattern via DFD technology; f) Cross-section reproduction of the micropattern obtained via DFD technology

The microscopic observations of SiBCN30/Al₂O₃ presented in Figure 4-23 reveal a micropattern free from major cracks. Contrary to our expectations, numerous small defects are nevertheless visible on the top and at the edge of the pattern. As discussed before, passive filler weren't able to eliminate all the micro-cracks and defects appearing after the shrinkage. The observations delivered in Figure 4-23 does not allow to differentiate the results with pattern obtained with SiCN/Al₂O₃ system. The EDX mapping and elemental composition presented in Figure 4-24 confirm the detection of alumina and SiCN.

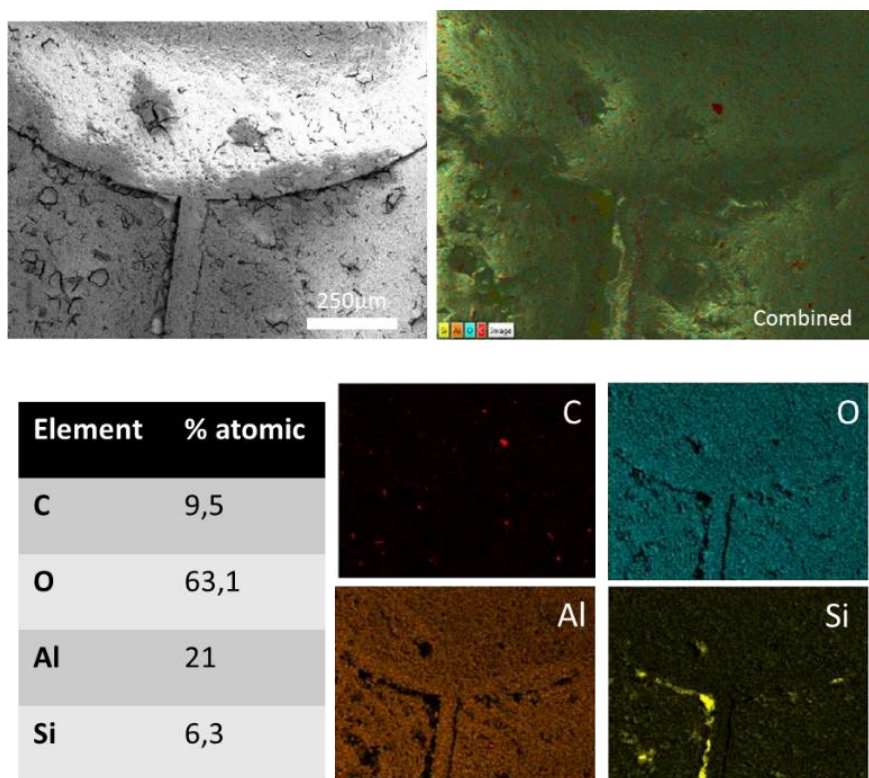


Figure 4-24: EDX mapping and elemental analysis of SiBCN30/Al₂O₃ 40wt% sample

4.4.4.1.5 PBVZ30/MoS₂

The microstructured pattern prepared from PBVZ30/MoS₂ suspension has been observed with microscopy and topography techniques, the associated pictures and graphics are presented in Figure 4-25. On the contrary of SiCN/MoS₂ sample (Figure 4-21), the micropattern presents cracks and peeling off problems. Despite this, the micro-channels are not totally break and conserved a relative integrity. The edges conserve a good definition and smoothness and the shape is globally well reproduced. This suggests again the active nature of MoS₂ filler. As discussed above, the poor dispersion of fillers in PBVZ30 polymer

caused by its high viscosity may have conducted to small areas with lower filler concentration. Such local inhomogeneities are likely to undergo higher constraints caused by localized strong shrinkage.

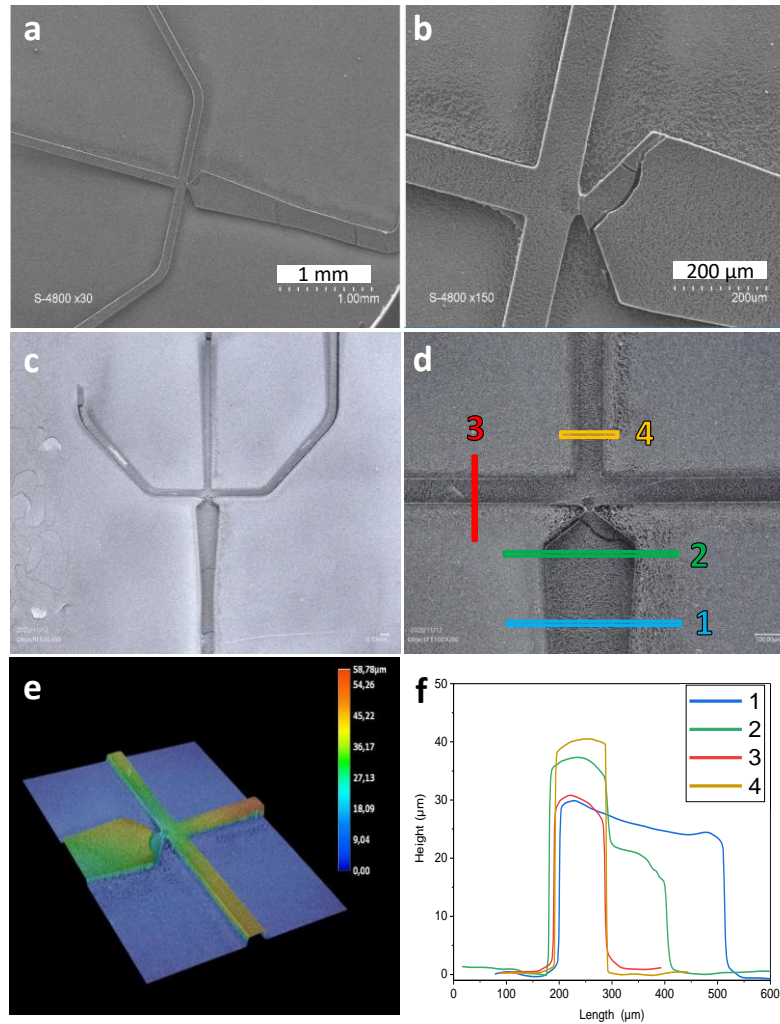


Figure 4-25: Microscopy and topography observations of SiBCN30/ MoS₂ 40wt% sample with a) and b) SEM pictures obtained at low and high magnification, respectively; c) and d) HRNM pictures obtained with low and high magnification, respectively; e) 3D reproduction of the micropattern via DFD technology; f) Cross-section reproduction of the micropattern obtained via DFD technology

The topographical and profilometry investigation reveal a well-defined patterns but with height around twice as big as patterns studied in the previous pages. In reality, it is due to peeling off of the object from the wafer. The EDX mapping and elemental composition presented in Figure 4-25 confirm the detection of alumina and SiCN. Boron, being a light element, could not be detected by EDX.

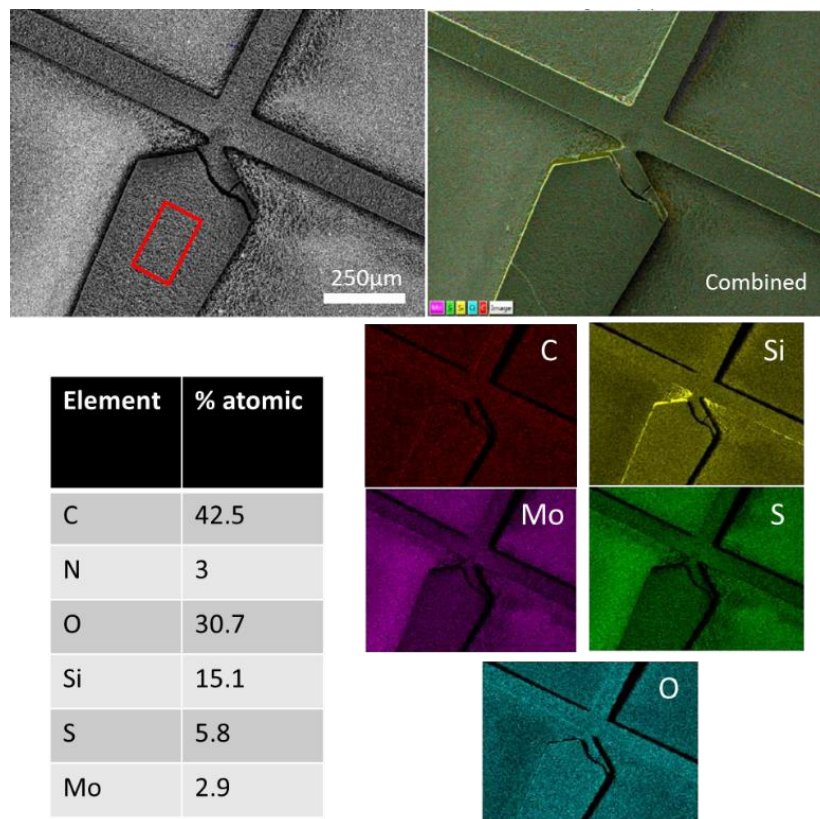


Figure 4-26: EDX mapping and elemental analysis of SiBCN30/ MoS₂ 40wt% sample

According to the observations and the discussions developed in this part, the influence of fillers and/or preceramic polymer nature on the micropattern's aspect and cracking has been identified. MoS₂ and MoS₂/MoSi₂ fillers have shown active filler properties conducting to “near-net-shape” objects on the contrary of Al₂O₃ passive fillers leading to more damaged patterns. Counter intuitively, the micro-patterns prepared from PBVZ30/fillers suspensions were subjects to more important and numerous defects (peeling off, cracking) than PVZ/fillers patterns. According to TGA developed in Figure 4-9, PBVZ30 based suspensions have higher ceramic yield and thus lower shrinkage than suspensions prepared with PVZ. Utilization of PBVZ30 should then enhance quality of micro-patterns but unexpectedly conduct to opposite results. This unexpected result was attributed to a poorer dispersion or stabilization of filler in suspension caused by the higher viscosity of PBVZ30 against PVZ.

The next part focuses on the shrinkage behavior associated with the different polymer/filler molded suspensions. Profilometric representations of the micropatterns after pyrolysis are compared with the initial SU-8 master shape.

4.4.4.2 Profilometry-topography

One challenge in soft-lithography techniques consists in evaluating and anticipating the geometrical shift operating between the initial masters and the final pattern. Thanks to profilometry measurements exhibited in Figure 4-27, SU8 master shape is compared with the final SiCN/filler profile. SU-8 masters reach about 25 μm in height. At first look, it seems clear that the micro-pattern shrinkage occurring during heat treatment is mainly radial against Si wafer.

Figure 4-27 a. associated with SiCN/ Al_2O_3 pattern shows the bad reproduction of the SU-8 master geometry with important radial and lateral shrinkage of 47,7% and 20,6% measured, respectively. The unfaithful reproduction noted in SiCN/ Al_2O_3 can be caused by a poor molding. For SiCN/ MoS_2 and SiCN/ $\text{MoS}_2/\text{MoSi}_2$ systems presented in Figure 4-27 b and c, the master geometry reproduction is more accurate than for SiCN/ Al_2O_3 pattern. Radial shrinkage is evaluated at 32,4% and 53% for SiCN/ MoS_2 and SiCN/ $\text{MoS}_2/\text{MoSi}_2$, respectively and associated lateral shrinkage reaches 7,6% and 32%, respectively. Those results are consistent with the microscopy observations developed in the previous part designating SiCN/ $\text{MoS}_2/\text{MoSi}_2$ and more specially SiCN/ MoS_2 as the most efficient systems for the near-net-shape strategy. The rectangular profile is rather preserved for the systems based on MoS_2 and MoSi_2 filler unlike Al_2O_3 based systems conducting to a rounded profile.

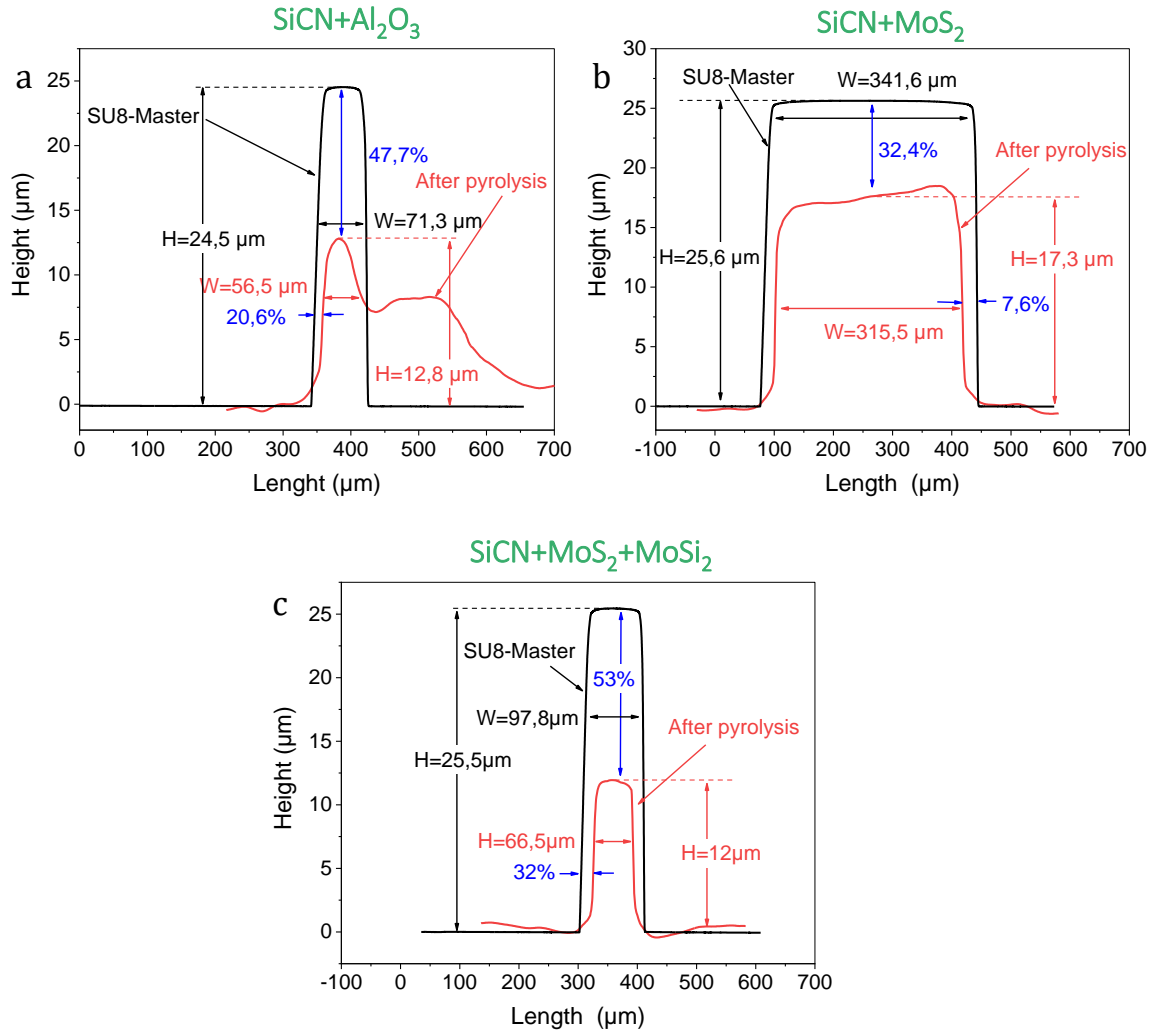


Figure 4-27: Evaluation of the shrinkage occurring during pyrolysis for SiCN/filler systems (a) Al₂O₃; b) MoS₂; c) MoS₂/ MoSi₂); profilometry curves measured on SU-8 masters and prepared micropattern; filler loading of 40wt%

The profilometric measures carried out on PBVZ30 based systems are reported in Figure 4-28. The rounded profile of SiBCN30/Al₂O₃, characteristic of this passive filler, is measured again (Figure 4-28 a). The corresponding radial and lateral shrinkage are of 52,8% and 35,5%, respectively. Regarding SiBCN/MoS₂ system profile, the micro-pattern height after pyrolysis is higher than the initial master. It is not associated with an expansion of the material but with it peeling from the silicon wafer as it is observable in Figure 4-25. In these conditions, the evaluation of a precise radial shrinkage is not possible. The interpretation of the results presented in Figure 4-28 confirms that PBVZ30 used caused defects such as peeling off, strong deformation and cracking.

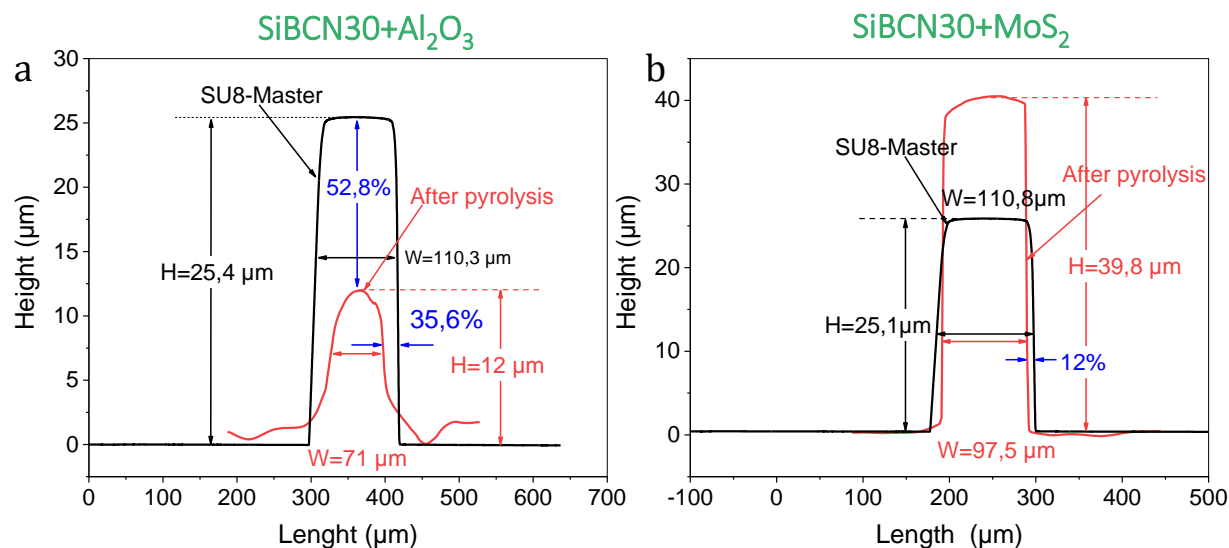


Figure 4-28: Evaluation of the shrinkage occurring during pyrolysis for SiBCN30/filler systems (a) Al₂O₃; b) MoS₂); profilometry curves measured on SU-8 masters and prepared micropattern; filler loading of 40wt%

According to the results discussed in section 4.4 we are able to give an evaluation of the fillers and preceramic polymer efficiency for the preparation, *via* soft lithography, of pattern free from defects. The fabrication of micro-objects with pure pre-Si(B)CN polymers led to micro-cracked channels even if the introduction of boron in the system has been shown beneficial for the reduction of microcracks. By introducing fillers such as Al₂O₃, MoS₂ and MoSi₂, the major defects caused by pyrolysis were eliminated. The influence of the filler's nature on the master reproduction fidelity was evaluated and MoS₂ and MoS₂/MoSi₂ fillers mixed with PVZ were designated as suitable systems for the near-net-shape strategy.

4.4.4.3 Mechanical properties

We evaluated the mechanical properties of a micropattern prepared by embossing technique thanks to microindentation (see section 2.4.4 for method description). The Figure 4-29 shows indentation area and load-displacement curve associated to SiCN/MoS₂/MoSi₂ sample. A Young modulus reaching 63 GPa was measured after a depth penetration of 383 nm.

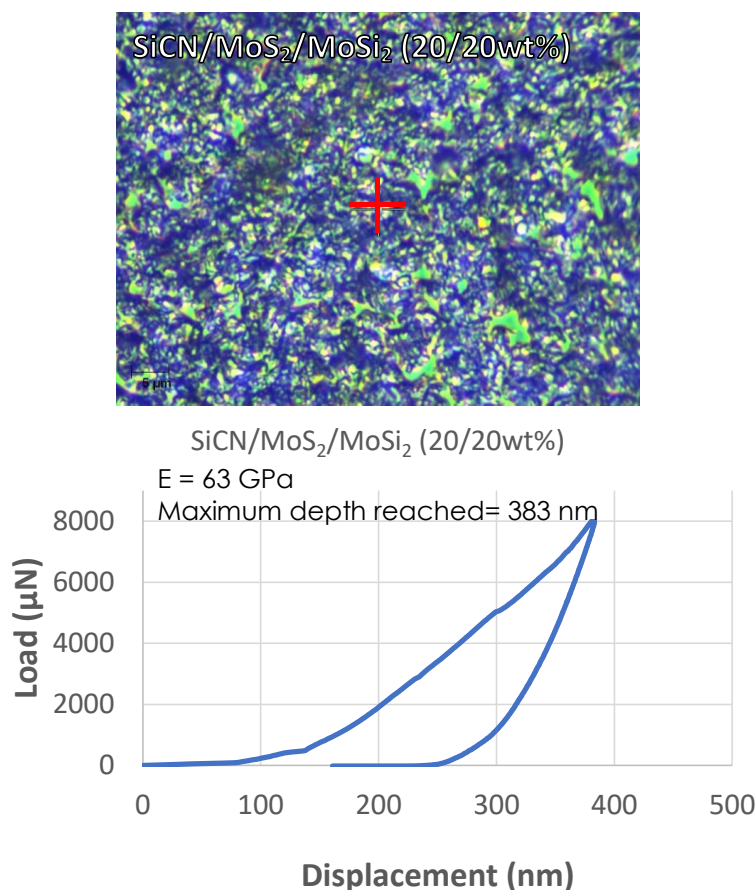


Figure 4-29: Load-displacement curve collected thanks to microindentation performed on SiCN/MoS₂/MoSi₂ micropattern

Such modulus value is relevant with the studies reported in the literature for PDC based materials. Mirkhalaf *et al.* [42] study has estimated young modulus values for PDC modified with filler between ~40 and 200 GPa. The microindentation measurement performed on this SiCN/MoS₂/MoSi₂ sample is thus a proof of the “ceramic behavior” of the imprinted micropatterns.

4.4.4.4 Electronic properties

In addition to the microcopy, geometrical and chemical characterization developed in the previous sections, we assessed the electrical properties of the synthesized materials. The resistivity of SiCN/MoS₂, SiCN/MoSi₂ and SiCN/MoS₂/MoSi₂ materials was evaluated on pellets shaped by warm pressing. The curves associated with those investigations are presented in Figure 4-30 and Figure 4-31 illustrating the resistivity of the samples and their

permittivity and capacitance, respectively. The resistivity values were calculated according to the following equations (2) and (3):

$$tg\delta = \frac{\varepsilon_{im}}{\varepsilon_{Re}} \quad (2)$$

Where $tg\delta$ is the dielectric loss factor and ε_{im} and ε_{Re} are the imaginary and real part of the relative permittivity.

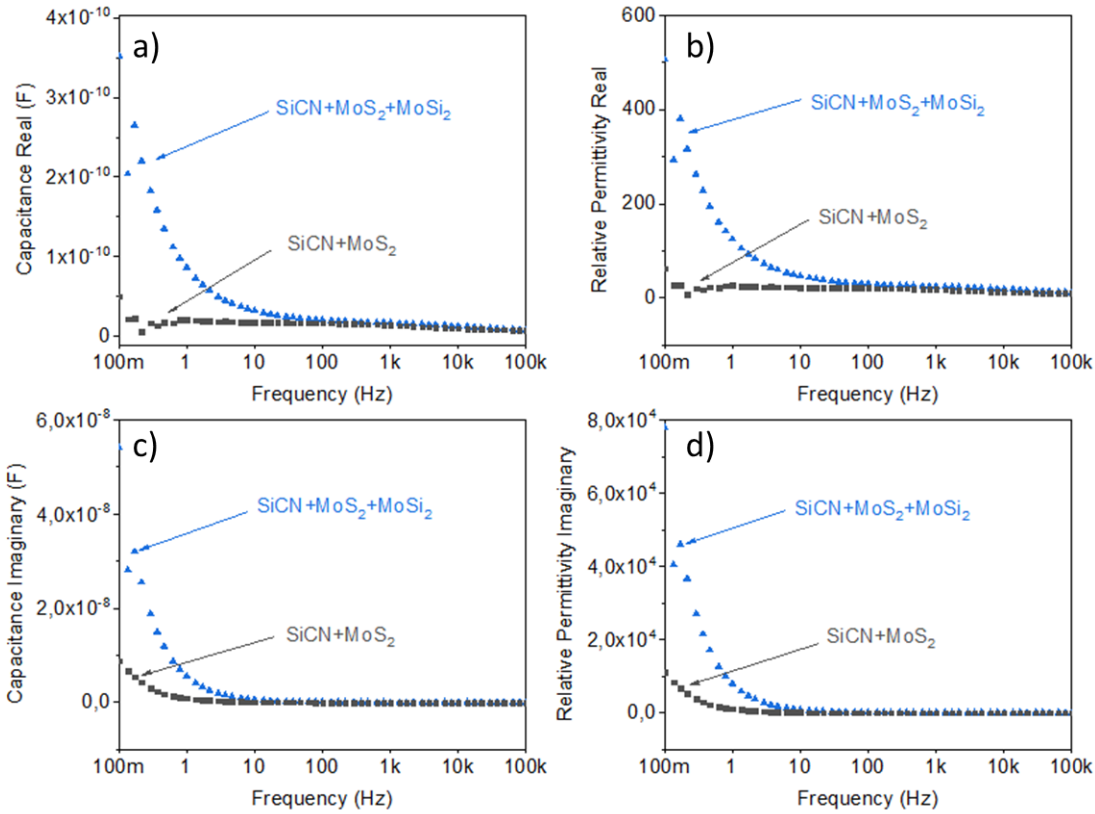


Figure 4-30: Real part of a) capacitance and b) relative permittivity and imaginary part of c) capacitance and d) relative permittivity associated with SiCN+MoS₂ and SiCN/MoSi₂/MoS₂ samples

$$\rho = \frac{1}{tg\delta \omega C} \quad (3)$$

With ρ as the resistivity, ω as the frequency and C as the real part of the capacitance. The resistivity value was then obtained from the capacitance and permittivity data presented in Figure 4-30.

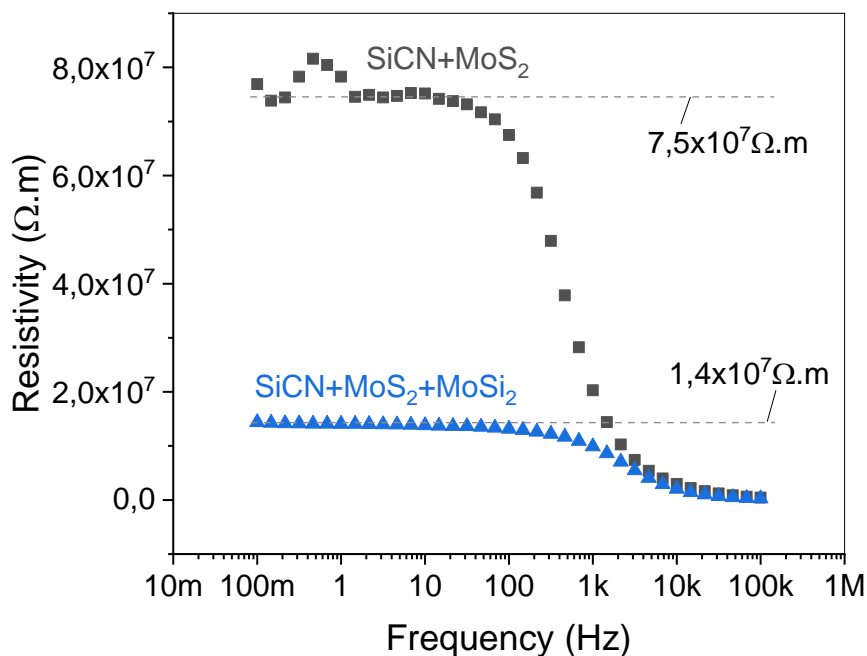


Figure 4-31: Resistivity values against frequency associated with SiCN/MoS₂ and SiCN/MoS₂/MoSi₂ samples

The values of resistivity at low frequency for both SiCN/MoS₂ and SiCN/MoS₂/MoSi₂ samples were evaluated at 7.5×10^7 and 1.4×10^7 Ω.m, respectively. It corresponds to high resistivity materials but we can clearly notice that the introduction of MoSi₂ increases the electronic conductivity in the sample. Nevertheless, such resistivity values are too high to hope for applications requiring electronic conduction such as electrocatalysis. Moreover, increasing the quantity of MoSi₂ in the materials seems to be a technical challenge in the context of soft-lithography since it quickly decreases the fluidity of the suspension.

4.5 Electrocatalytic performance

Suspensions of PVZ mixed with bulk MoS₂ powder were prepared in glove box and pyrolysed under nitrogen atmosphere at 1000°C. The procedure for the sample preparation discussed in this section is detailed in chapter 2 part 2.3.4. From now on, the indicated additive loading mentioned in the text or figures denotes the rate in the initial PVZ/MoS₂ suspensions and not the rate after thermolysis. For example, the SiCN/MoS₂ 30 wt% sample was prepared from a PVZ suspension loaded with 30 wt% of MoS₂ filler and subsequently pyrolysed. Figure 4-32 shows the C_{dl} slopes associated with the samples discussed in this

section. The first global overview of those slopes shows that the C_{dl} associated with PDC/filler samples is significantly lower than for PDC/rGO composites discussed in the chapter III. Secondly, the C_{dl} values are not constant over the samples and vary from ~ 6 to $141 \mu\text{F}/\text{cm}^2$ which corresponds to very different electrochemical active surface area (ECSA).

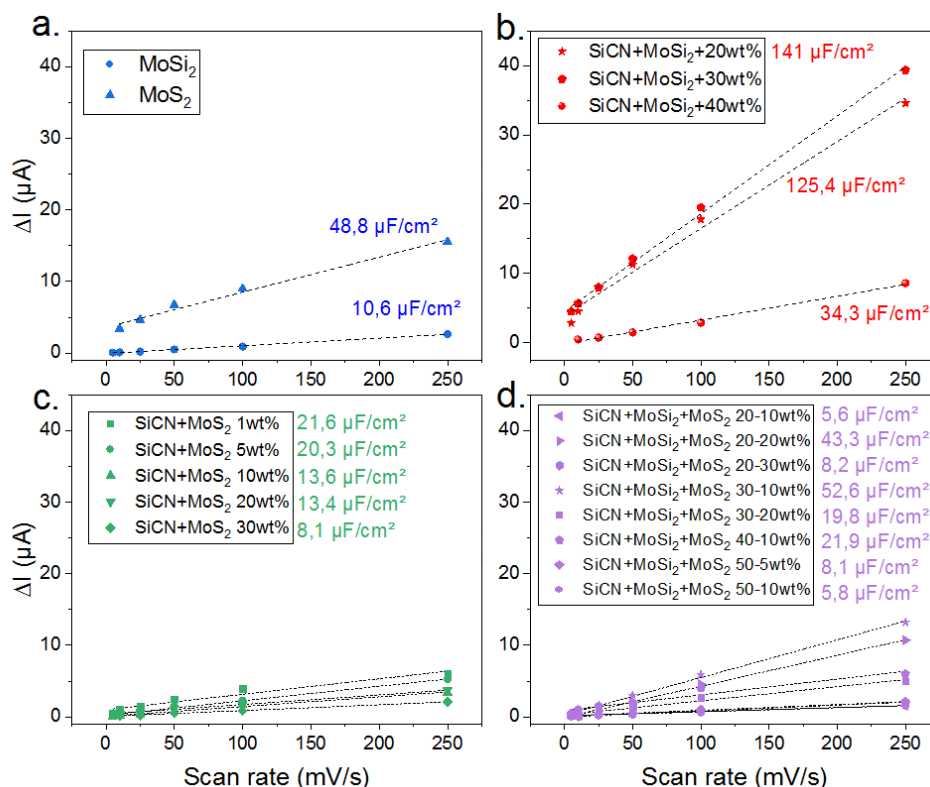


Figure 4-32: C_{dl} slopes of PDC/fillers composites a) Fillers alone b) SiCN/MoSi₂ c) SiCN/MoS₂ and d) SiCN/MoS₂/MoSi₂

Figure 4-32.a. is associated with C_{dl} slopes of MoSi₂ and MoS₂ fillers alone with values of 48.8 and 10.6 $\mu\text{F}/\text{cm}^2$, respectively. For SiCN/MoSi₂ samples, the C_{dl} is significantly higher with values of C_{dl} reaching 125.4 and 141 $\mu\text{F}/\text{cm}^2$ (see Figure 4-32.b), it contrasts with the C_{dl} values of SiCN/MoS₂ samples below 22 $\mu\text{F}/\text{cm}^2$. Moreover, the C_{dl} of SiCN/MoS₂ decreases with the increase of MoS₂ content in the composite. Finally, SiCN/MoS₂/MoSi₂ composite has C_{dl} values varying from ~ 5 to 52.6 $\mu\text{F}/\text{cm}^2$.

4.5.1 SiCN/MoS₂ composites

4.5.1.1 Polarization curves

Figure 4-33 provides the polarization curves (a) and current density histograms (b) associated with Si(B)CN/MoS₂ systems. HER activity of pristine MoS₂ was also evaluated since it is considered as one of the best electrocatalysts among noble-metal-free materials. MoS₂ tested here does not have “tremendous” activity since it is 2H phase and bulk material in comparison to HER active 1T MoS₂ nanosheets (see part 1.2.2.4 and 4.4.3).

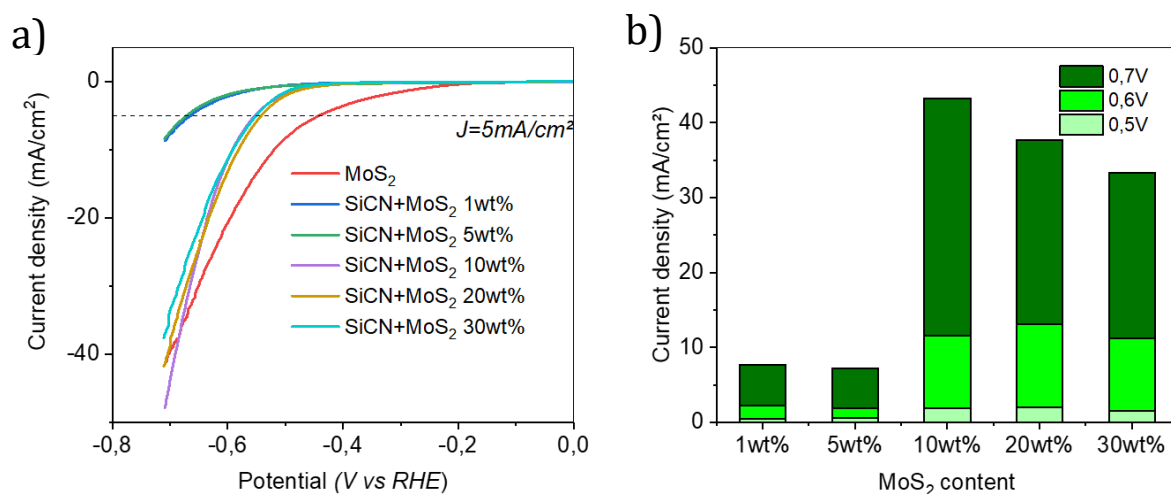


Figure 4-33: Polarization curves (a) and current density histogram (b) associated with SiCN/MoS₂ systems; MoS₂ loading varies from 1wt% to 30wt%, 50μg of material drop casted on glassy carbon electrodes, 0.5M H₂SO₄ electrolyte

For MoS₂ loading below 5wt%, HER activity is poor with an overpotential of 665 and 672 mV @5mA/cm² for 1wt% and 5wt%, respectively. For higher MoS₂ ratios, electrocatalytic performances strongly increase with a current density $\sim 44 \text{ mA/cm}^2$ @0.7V and overpotential of 554mV @5mA/cm² for 10wt% MoS₂ content. With this composition, the current density at 0.7V of pristine MoS₂ is exceeded ($\sim 39 \text{ mA/cm}^2$). Counter-intuitively, superior to 10wt% ratio, HER activity slowly decreases with current density of ~ 39 and $\sim 34 \text{ mA/cm}^2$ @0.7V for MoS₂ contents of 20 and 30wt%, respectively. The optimal MoS₂ loading in SiCN matrix seems then to be around 10wt% as suggests the histograms displayed in Figure 4-33 (b).

4.5.1.2 Tafel slopes

For further details, Tafel slopes have been plotted and displayed in Figure 4-34. As observed, with polarization curves analysis Tafel slopes of 1 and 5wt% samples are very high (171 and 178 mV/dec, respectively) which translates low electrocatalysts performances. The pristine MoS_2 sample shows a slope of 124 mV but in the case of 10, 20 and 30 wt% MoS_2 samples it is systematically lower with values at 123, 113 and 89 mV/dec. In summary, the prepared SiCN/MoS_2 were not able to surpass pristine MoS_2 in terms of overpotential but lower values of Tafel slope and higher current density can be measured for optimized MoS_2 contents.

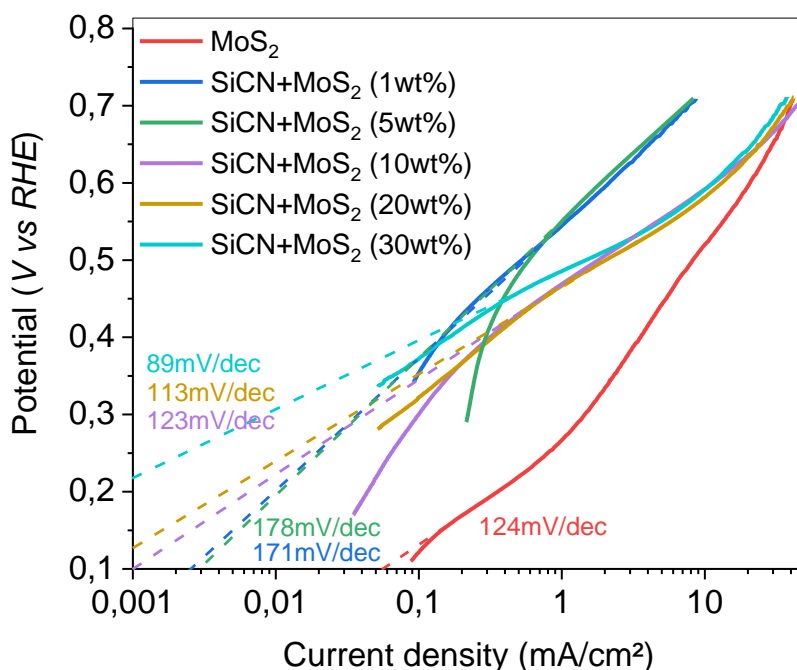


Figure 4-34: Tafel slopes associated with SiCN/MoS_2 systems

Since the electrochemical reactions involved are based on electron exchange, electrocatalytic performances of our composites might be degraded by the poor electronic conductivity of PDCs. SiCN and MoS_2 are respectively an insulating ceramic and a semi-conducting additive, introducing additives with metallic conduction properties might be a promising strategy to boost the composite's HER activity. The next section is dedicated to PDC/MoSi_2 systems (MoSi_2 has significant electronic conduction [45][46][47] and has been

reported in the literature as an effective additive to reduce insulating nature of PDCs materials [48]).

4.5.2 SiCN/MoSi₂ composites

Similarly to SiCN/MoS₂ composites, SiCN/MoSi₂ samples were prepared *via* pyrolysis of PVZ/MoSi₂ suspension at 1000°C under N₂ atmosphere (see section 2.3.4). The evaluation of SiCN/MoSi₂ samples is displayed in the Figure 4-35.a. showing polarization curves and associated histograms for several MoSi₂ content. Pure MoSi₂ HER activity was measured revealing poor performances with overpotential 648 mV @5mA/cm². On the other hand, once MoSi₂ is introduced in a SiCN matrix the HER activity is remarkably improved which is in line with the results discussed in section 3.3 revealing the intrinsic electrocatalytic properties of Si(B)CN when combined with a conductive material.

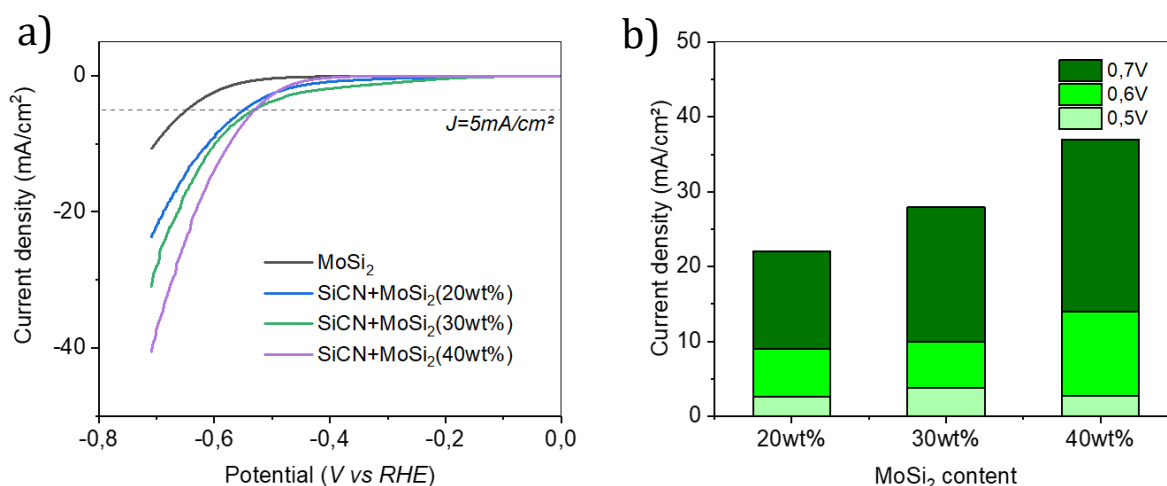


Figure 4-35: Polarization curves (a) and current density histogram (b) associated with SiCN/MoSi₂ systems; MoSi₂ loading varies from 20wt% to 40wt% , 50µg of material drop casted on glassy carbon electrodes , 0.5M H₂SO₄ electrolyte

According to our results, the overpotential @5mA/cm² of 20, 30, and 40 wt% samples is of 550, 532 and 530 mV. In the same way the current density @0.7V is of 22.4, 28.7, 38.6 mA/cm². It suggests the improvement of the catalysts with increasing of the MoSi₂ content as it is illustrated by the histogram in Figure 4-35.b.

Corresponding Tafel slopes are presented in Figure 4-36. We can deduce that SiCN/MoSi₂ 40wt% shows the highest HER activity among the tested samples. Nevertheless, performances are far from the benchmark catalysts such as Pt or 1T-MoS₂.

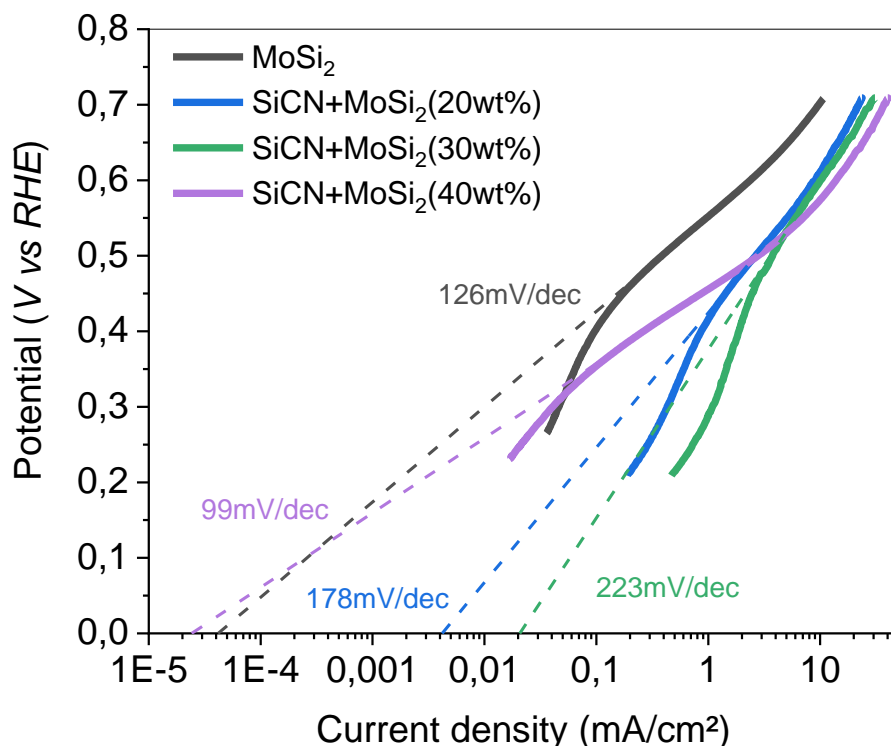


Figure 4-36: Tafel slopes corresponding to SiCN/MoSi₂ systems

The final strategy has then consisted in combining both MoS₂ and MoSi₂ additives in SiCN matrix in order to benefit from electrocatalytic performances and electronic conductivity, respectively. The following section will deal with results related to SiCN/MoSi₂/MoS₂ system.

4.5.3 SiCN/MoS₂/MoSi₂ composites

Various compositions have been experimented in order to explore the combined influence of the two additives introduced in SiCN matrix. MoSi₂ content ranged from 20 to 50wt% while MoS₂ from 5 to 30 wt%. Polarization curves associated to these samples are displayed in Figure 4-37.a. Due to the numerous displayed curves reading the graphic is difficult. At

first sight, we can notice that all the tested composites have better performances than pure MoSi₂ but never exceed the performances of pristine MoS₂ in term of overpotential.

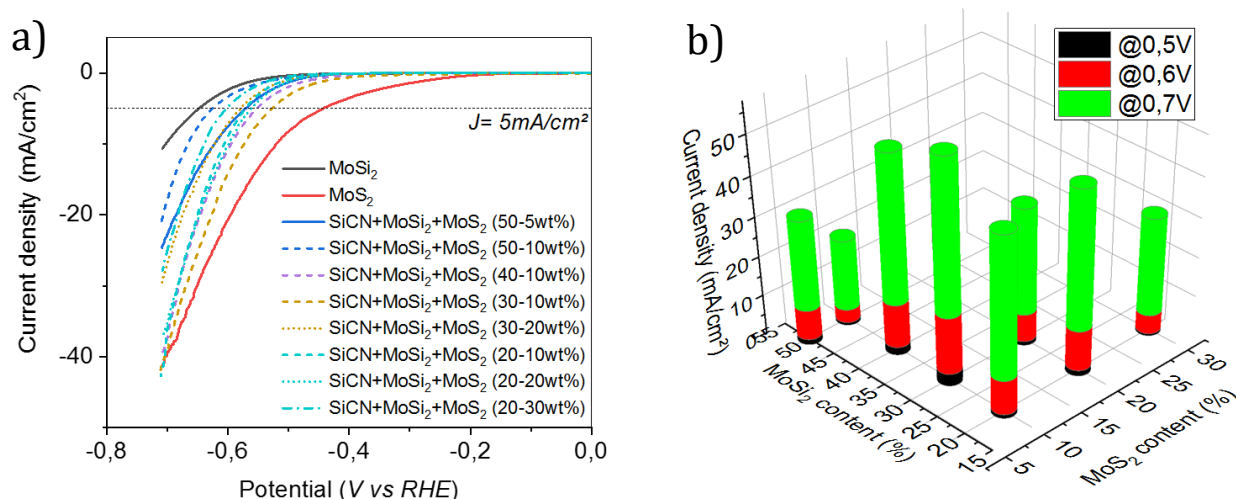


Figure 4-37: Polarization curves (a) and current density histogram (b) associated with SiCN/MoS₂/MoS₂ systems; MoSi₂ and MoS₂ loading varies from 20wt% to 50wt% and from 50 to 30wt%, respectively; 50μg of materials drop casted on glassy carbon electrode, 0.5M H₂SO₄ electrolyte

The histogram in Figure 4-37.b. provides an illustration of the current density measured at 0.5, 0.6 and 0.7 V depending on MoS₂ and MoSi₂ contents. In term of current density, the most performant composite is obtained for 10wt% of MoS₂ and 30wt% of MoSi₂ with a $J@0.7\text{mV}$ of 38.8 mA/cm² and an overpotential of 528 mV @5mA/cm². On the other hand, the Tafel slopes plotted in Figure 4-38 show the lowest values for a fixed MoSi₂ content of 20wt% and 10, 20 and 30wt% of MoS₂.

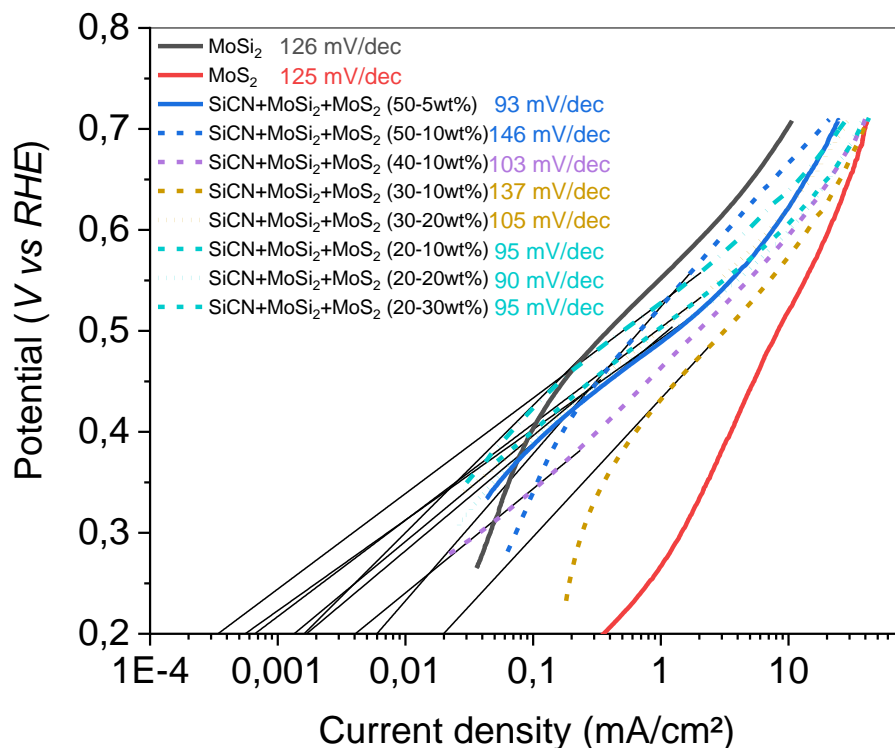


Figure 4-38: Tafel slopes corresponding to SiCN/MoSi₂/MoS₂ systems

Except for the 50-10% and 30-10% samples, Tafel slope values of the samples based on MoS₂ and MoSi₂ are all below 120 mV/dec. This suggests a change in the mechanism leading to the production of hydrogen. When the Volmer step determines the reaction rate, Tafel slope value is close to 120 mV/dec [50][51]. This corresponds to too weak adsorption of the protons at the surface of the catalyst (catalyst is then placed on the right side of the volcano plot (see section 1.2.2.1)). The lowest values are measured for the other samples are below 120 mV/dec *i.e.* between 105 and 90 mV/dec. This suggests a modification in the mechanism step determining the reaction rate associated with these samples. For Tafel slopes values of 30 or 40 mV/dec, it is the Volmer-Tafel or Volmer-Heyrosky which governs the kinetic in the water-splitting mechanism. It is therefore not possible to make a clear decision about the real mechanisms involved and associated with values between 105 and 90 mV/dec. Figure 4-39 is an histogram visualizing the value of Tafel slopes as a function of the composition of the samples. However, it is not possible to determine a clear trend to predict an optimal composition leading to the lowest possible value.

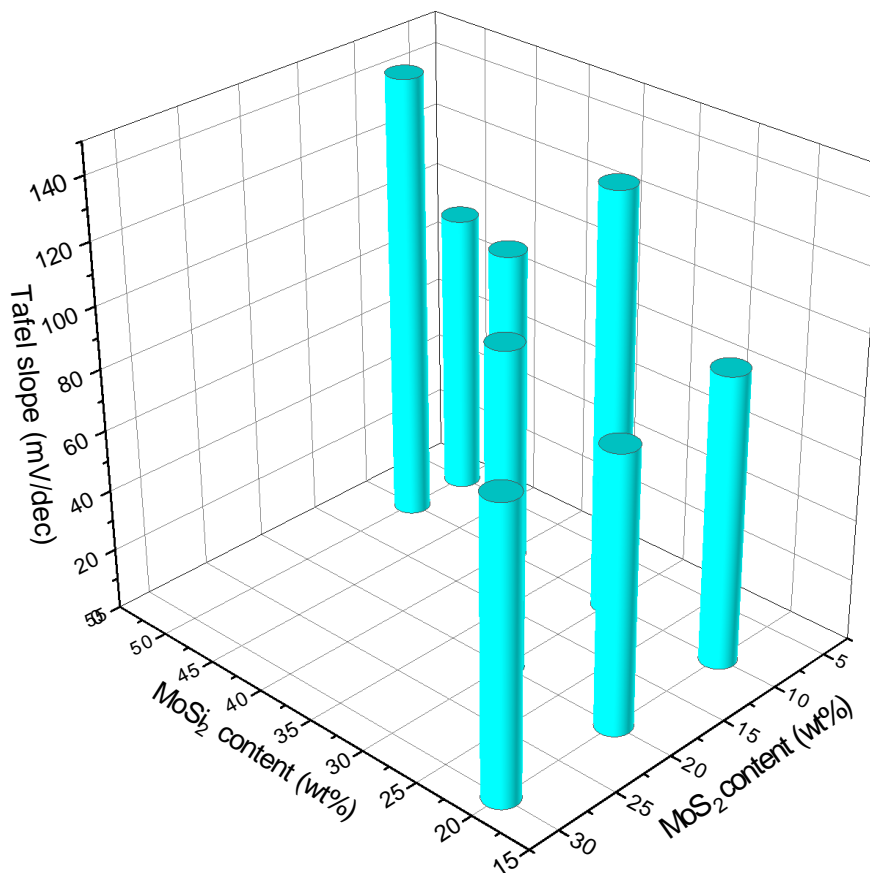


Figure 4-39: Tafel slope histogram corresponding to SiCN/MoSi₂/MoS₂

4.5.4 Annealing temperature influence

XRD and XPS studies performed in section 4.4.3 (see Figure 4-10) show that the samples based on PVZ and MoS₂ fillers lead, after pyrolysis, to a SiCN/MoS₂ composite. It is composed of an amorphous SiCN phase, a residual MoS₂ crystalline phase and a new phase formed *in situ via* reaction between the PVZ and MoS₂. The Mo_xS_yC_z formed phase could not be clearly identified since the XRD peaks that appear in the diffractogram after pyrolysis are too weak and could not be associated with a phase listed in the XRD databases (PDF2 - COD). Numerical computation *i.e.* DFT could be interesting to identify this phase, however it was not in the scope of this work. The presence of this phase can potentially influence the performance in electrocatalysis. In addition, as the annealing temperature (under nitrogen) increases, new phases are formed *in situ* while others disappear. After annealing at 1200°C, MoS₂ and Mo_xS_yC_z phases are no longer detected in the composite while the Mo₂C phase is

identified. At 1400°C, in addition to the Mo_2C formed at 1200°C, $\text{Mo}_{4,8}\text{Si}_3\text{C}_{0,6}$ phase (Nowotny-like [25]) appears.

According to the literature, Mo_2C and $\text{Mo}_{4,8}\text{Si}_3\text{C}_{0,6}$ phases can be HER active [25]. Figure 4-40 displays the polarization curves collected on SiCN/MoS_2 samples annealed at different temperatures. Unexpectedly, the values of over-potential @5mA/cm² increase

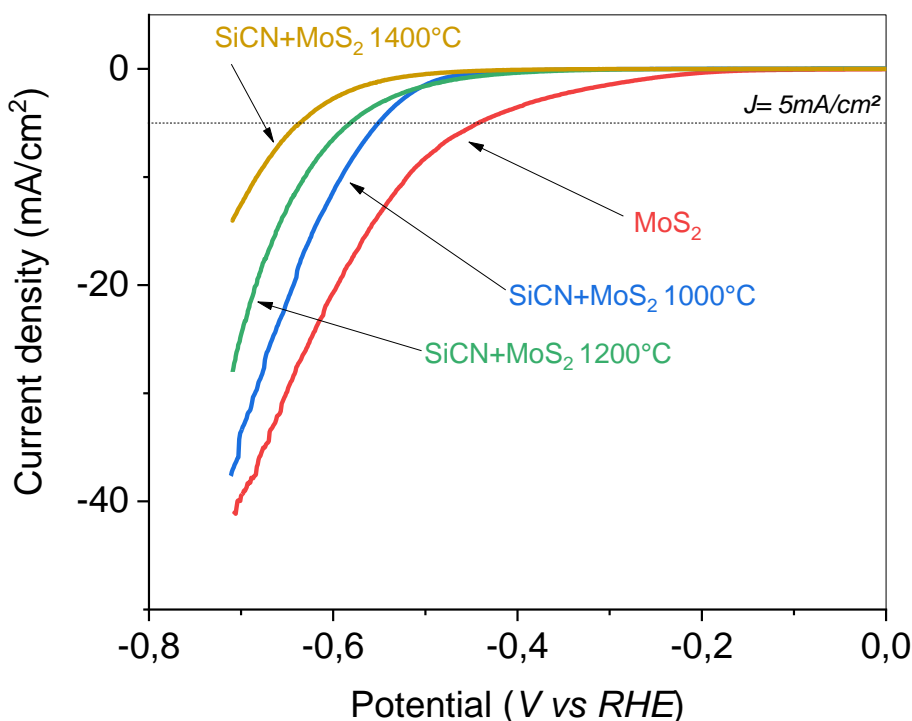


Figure 4-40: Polarization curves corresponding to SiCN/MoS_2 sample annealed at 1000, 1200 and 1400°C under nitrogen atmosphere; Sample PVZ/ MoS_2 30wt%

Despite the formation of the active HER phase, the efficiency of the annealed electrocatalysts decreases with the temperature treatment. This is also shown by the Tafel curves plotted in Figure 4-41 since the value of their slopes increases with the annealing temperature. It goes from 89 mV/dec for a sample pyrolysed at 1000°C to 127 and 133 mV/dec for samples treated at 1200 and 1400°C, respectively. Based on the diffractograms available in Figure 4-10 it seems clear that the formation of Mo_2C and $\text{Mo}_x\text{S}_y\text{C}_z$ phases is done to the detriment of the decomposition of MoS_2 . The HER activity of the phases formed therefore does not compensate for the activity lost with the disappearance of the MoS_2

phase. In addition, the studies discussed in section 3.3.2 have shown that the intrinsic activity of SiCN ceramics arises from the amorphous nature of its microstructure. As suggested by the diffractograms shown in section 4.4.3.1 when the annealing temperature increases, the amorphous phase crystallizes and HER activity drops.

It seems that increasing the annealing temperature to form Mo_2C and $\text{Mo}_{4,8}\text{Si}_3\text{C}_{0,6}$ phases to the detriment of MoS_2 is not the optimal strategy to obtain more efficient catalysts in the case of SiCN/ MoS_2 samples.

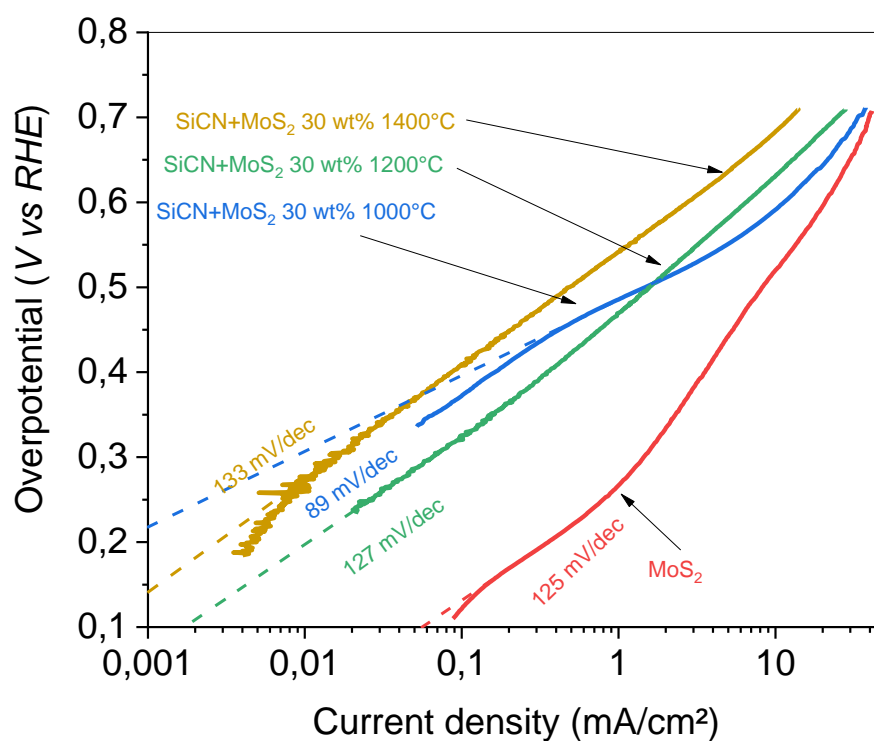


Figure 4-41: Tafel slopes corresponding to SiCN/ MoS_2 sample annealed at 1000, 1200 and 1400°C under nitrogen atmosphere; Sample PVZ/ MoS_2 30wt%

In the case of SiCN/ MoSi_2 / MoS_2 samples, the evolution of the crystalline phases is different from the SiCN/ MoS_2 case and much more complex as the number of phases formed is high. From 1000°C, in addition to the initial MoSi_2 and MoS_2 phases, the $\text{Mo}_x\text{C}_y\text{S}_z$ and $\text{Mo}_{4,8}\text{Si}_3\text{C}_{0,6}$ phase is formed while it is only detected at 1200 and 1400°C for samples SiCN/ MoSi_2 and SiCN/ MoS_2 , respectively. The rather correct performance of the 1000°C SiCN/ MoS_2 / MoSi_2 samples could therefore come from the simultaneous presence of the MoS_2 , MoSi_2 ,

$\text{Mo}_{4,8}\text{Si}_3\text{C}_{0,6}$, $\text{Mo}_x\text{C}_y\text{S}_z$ and amorphous SiCN phases, but this remains a still unverified hypothesis. By heating to 1200°C , the MoS_2 and MoSi_2 phases are consumed and the $\text{Mo}_{4,8}\text{Si}_3\text{C}_{0,6}$, $\text{Mo}_x\text{C}_y\text{S}_z$, Mo_5Si_3 , Mo_2C and Si_3N_4 phases are detected. This results in a net drop in HER performance as shown in Figure 4-42. The performance degrades even more when the sample is treated at 1400°C , which leads to a disappearance of an active phase such as Mo_2C to the detriment of the growth of Si_3N_4 , inert to HER.

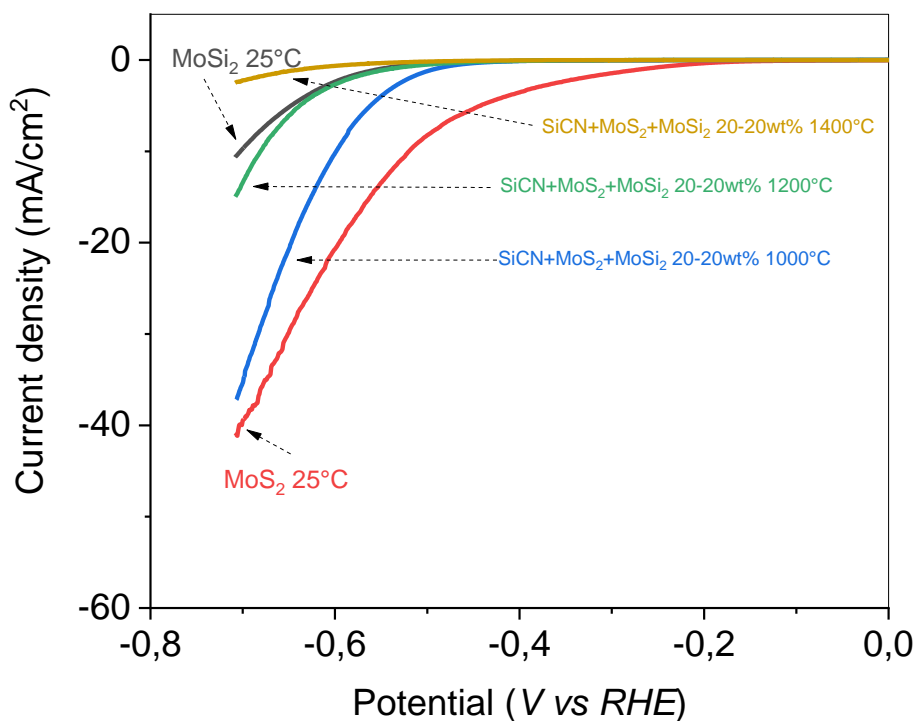


Figure 4-42: Polarization curve associated to $\text{SiCN}/\text{MoSi}_2/\text{MoS}_2$ sample annealed at 1000, 1200 and 1400°C under nitrogen atmosphere; Sample PVZ/ $\text{MoSi}_2/\text{MoS}_2$ 20-20wt%

This trend is confirmed when we observe the Tafel curves in Figure 4-43. The initial value of 90 mV/dec measured for the sample treated at 1000°C increases to 140 and 176 mV/dec after treatment at 1200 and 1400°C . Based on these studies, treating samples at higher temperatures to form new active phases does not appear to be an effective strategy.

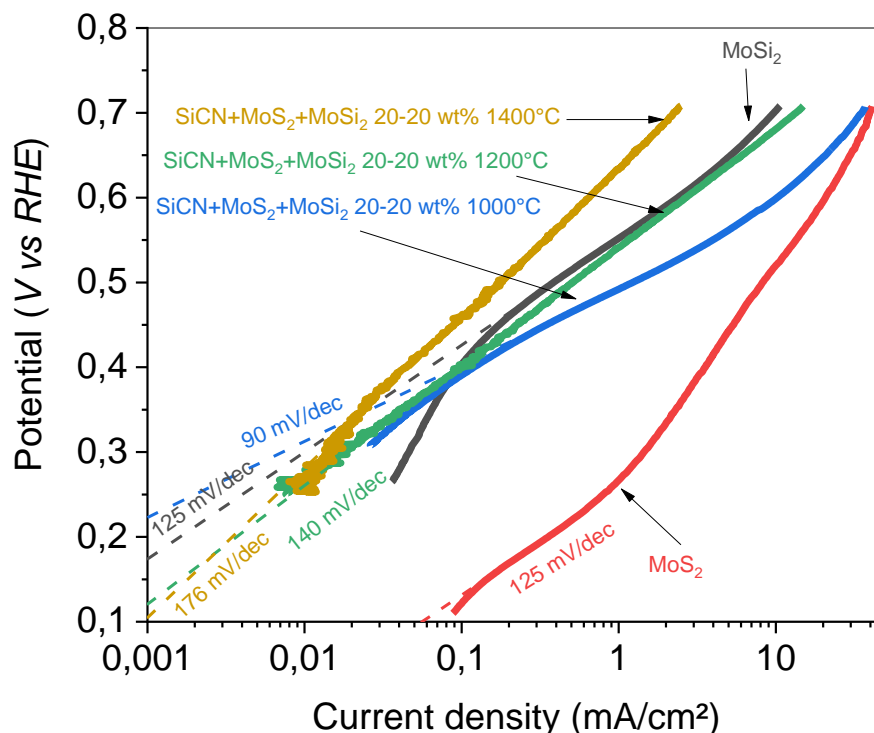


Figure 4-43: Tafel slope associated to SiCN/MoSi₂/MoS₂ sample annealed at 1000, 1200 and 1400°C under nitrogen atmosphere; Sample PVZ/MoSi₂/MoS₂ 20-20wt%

4.5.5 Conclusion on HER activity

According to the results gathered in this section 4.5 the introduction of MoSi₂ and/or MoS₂ filler in an amorphous SiCN matrix conducts to improvement of HER activity against SiCN alone. Furthermore, according to the results associated to SiCN/MoS₂ samples the intrinsic HER activity of SiCN was proved since those samples have shown better electrocatalyst properties than MoSi₂ alone. It is relevant with the conclusion stated in chapter 3 on PDC/rGO composite which show an activation of catalysts properties of the Si(B)CN materials when combined with conductive but HER inert material. Nevertheless, in spite of several tested composition and annealing temperature the performances of SiCN/MoS₂, SiCN/MoSi₂ or SiCN/MoSi₂/MoS₂ never surpassed that of pristine MoS₂. The interest of those PDC/TMD's composites therefore remains limited since they are not able, in those conditions, to replace benchmark noble-metal-free MoS₂ catalyst.

There are still some avenues to explore in order to enhance the HER activity of PDC/TMD's composites. First, the 2H MoS₂ phase tested as filler material is the less HER active phase against 1T or 1T' phases recognized for their superior activity. Two possibilities are conceivable :

- Replace the initial 2H-MoS₂ filler by 1T-MoS₂ or 1T'-MoS₂. It may be an unproductive move since 1T(') MoS₂ phase are metastable and could re-crystallized to 2H form during the heat treatment necessary for PDC/TMD's preparation
- Form 1T phase during or after the thermal treatment and from the initial 2H phase. According to Shi's review on 1T-MoS₂ synthesis [52], it is possible to form 1T phases from bulk 2H MoS₂ *via* several routes. Inducing S vacancies thanks to a low temperature gas treatment is a method compatible with the work developed in this section.

According to the C_{dl} values discussed in this section (see Figure 4-32), the surface area of the samples is very low and could explain the poor current density measured. They were measured ~3 to 6 fold smaller than for PDC/rGO composites discussed in part 3.3. Here again, two possibilities co-exist to enhance surface area of the sample:

- As discussed in part 1.2.2.4 the exfoliation of bulk MoS₂ conduct to 2D nanosheets of MoS₂ rich in HER active sites. Replace bulk MoS₂ powder with 2D nanosheet MoS₂ powder. This combined with 2H to 1T conversion could potentially conduct to high performance catalyst.
- The surface area of the electrocatalyst may be increase by microstructuration or miniaturization of the material. The foamy structure of PDC/rGO previously discussed in the part 3.2.2 is an example of highly porous structure conducting to high current density. Other strategies exist such as microfabrication of miniaturized electrolyzers mentioned in this chapter 4 and in part 1.3.2 of Chapter I.

4.6 Chapter conclusion

In this chapter, IV the molding of PDCs based materials *via* soft-lithography in the perspective of miniaturization of water-splitting device has been explored. Indeed,

according to the results discussed in the chapter III it is possible to employ PDCs as an electrocatalyst for HER reaction.

The first attempts of PDCs micropatterning discussed in this chapter have been performed with pure polymer. With this strategy, the resulting patterns have shown a dramatic mud-cracking making such microstructure useless for any application. Thanks to the addition of boron atoms in the polymer structure, the ceramic yield can be enhanced and the shrinkage reduced. With a lower shrinkage, the intern constraints occurring in the shaped polymer during the heat treatment are reduced as the mud-cracking intensity. Polymer modified with boron was then implemented in the soft-lithography process conducting to reduction of the cracks quantity and intensity. However, the total suppression of cracks in the micropattern derived from pure polymer was not possible in this study.

The introduction of passive (Al_2O_3) and active (MoS_2 and MoS_2) fillers to reduce shrinkage and maintain the integrity of the imprinted profiles was achieved. This strategy has conducted to PDC/filler composites and with, in the case of active fillers, generation of expansive phases balancing the shrinkage. Thanks to XRD and XPS analysis, we were able to identify this expansive phase (*i.e.* $\text{Mo}_{4.8}\text{Si}_3\text{C}_{0.6}$ or Mo_2C) which were favorable for the elimination of cracks formation. We have therefore established an efficient procedure for the preparation Si-(B)-CN/fillers micropatterns. A minimized lateral shrinkage between 7.6% and 32% was measured on the micropatterns elaborated *via* this procedure, which explain the elimination of cracks. Finally, we evaluate the impact of these new phases on the HER activity and report Tafel slope of 89 mV/dec and onset over-potential of 530 mV@5 mA/cm² for SiCN/ MoS_2 composite.

4.7 Bibliography

- [1] A. Viard *et al.*, « Molecular Chemistry and Engineering of Boron-Modified Polyorganosilazanes as New Processable and Functional SiBCN Precursors », *Chemistry – A European Journal*, vol. 23, n° 38, p. 9076-9090, 2017, doi: [10.1002/chem.201700623](https://doi.org/10.1002/chem.201700623).
- [2] S. Sarkar, Z. Gan, L. An, et L. Zhai, « Structural Evolution of Polymer-Derived Amorphous SiBCN Ceramics at High Temperature », *J. Phys. Chem. C*, vol. 115, n° 50, p. 24993-25000, déc. 2011, doi: [10.1021/jp203287h](https://doi.org/10.1021/jp203287h).

- [3] Q. Zhang, Z. Yang, D. Jia, Q. Chen, et Y. Zhou, « Synthesis and structural evolution of dual-boron-source-modified polysilazane derived SiBCN ceramics », *New J. Chem.*, vol. 40, n° 8, p. 7034-7042, août 2016, doi: [10.1039/C5NJ03723A](https://doi.org/10.1039/C5NJ03723A).
- [4] C. Gerardin, F. Taulelle, et J. Livage, « Pyrolysis of a polyvinylsilazane, polymeric precursor for silicon carbonitride : structural investigation by ^1H , ^{13}C , ^{29}Si , ^{15}N and ^{14}N nuclear magnetic resonance », *J. Chim. Phys.*, vol. 89, p. 461-467, 1992, doi: [10.1051/jcp/1992890461](https://doi.org/10.1051/jcp/1992890461).
- [5] THF: https://www.chemicalbook.com/SpectrumEN_109-99-9_1HNMR.htm
- [6] J. Kong, M. Wang, J. Zou, et L. An, « Soluble and Meltable Hyperbranched Polyborosilazanes toward High-Temperature Stable SiBCN Ceramics », *ACS Appl. Mater. Interfaces*, vol. 7, n° 12, p. 6733-6744, avr. 2015, doi: [10.1021/am509129a](https://doi.org/10.1021/am509129a).
- [7] X. Wang, H. Wang, et J. Shi, « Synthesis, characterization, and ceramic conversion of a liquid polymeric precursor to SiBCN ceramic via borazine-modified polymethylsilane », *Journal of Materials Science*, vol. 53, août 2018, doi: [10.1007/s10853-018-2452-8](https://doi.org/10.1007/s10853-018-2452-8).
- [8] BDMS: https://www.chemicalbook.com/SpectrumEN_13292-87-0_1HNMR.htm
- [9] J. Lücke, J. Hacker, D. Suttor, et G. Ziegler, « Synthesis and Characterization of Silazane-Based Polymers as Precursors for Ceramic Matrix Composites », *Applied Organometallic Chemistry*, vol. 11, no 2, p. 181-194, 1997, doi: [10.1002/\(SICI\)1099-0739\(199702\)11:2<181::AID-AOC566>3.0.CO;2-Q](https://doi.org/10.1002/(SICI)1099-0739(199702)11:2<181::AID-AOC566>3.0.CO;2-Q).
- [10] Y.-L. Li, E. Kroke, R. Riedel, C. Fasel, C. Gervais, et F. Babonneau, « Thermal cross-linking and pyrolytic conversion of poly(ureamethylvinyl)silazanes to silicon-based ceramics », *Applied Organometallic Chemistry*, vol. 15, n° 10, p. 820-832, 2001, doi: [10.1002/aoc.236](https://doi.org/10.1002/aoc.236)
- [11] C. García-Garrido, P. E. Sánchez-Jiménez, L. A. Pérez-Maqueda, A. Perejón, et J. M. Criado, « Combined TGA-MS kinetic analysis of multistep processes. Thermal

decomposition and ceramification of polysilazane and polysiloxane preceramic polymers », *Phys. Chem. Chem. Phys.*, vol. 18, n° 42, p. 29348-29360, oct. 2016, doi: [10.1039/C6CP03677E](https://doi.org/10.1039/C6CP03677E).

[12] C. R. Martin et I. A. Aksay, « Submicrometer-Scale Patterning of Ceramic Thin Films », *Journal of Electroceramics*, vol. 12, n° 1, p. 53-68, janv. 2004, doi: [10.1023/B:JECR.0000034001.15359.98](https://doi.org/10.1023/B:JECR.0000034001.15359.98).

[13] F. F. Lange, « Chemical Solution Routes to Single-Crystal Thin Films », *Science*, vol. 273, n° 5277, p. 903-909, août 1996, doi: [10.1126/science.273.5277.903](https://doi.org/10.1126/science.273.5277.903).

[14] P. Colombo, T. E. Paulson, et C. G. Pantano, « Synthesis of Silicon Carbide Thin Films with Polycarbosilane (PCS) », *Journal of the American Ceramic Society*, vol. 80, n° 9, p. 2333-2340, 1997, doi: [10.1111/j.1151-2916.1997.tb03124.x](https://doi.org/10.1111/j.1151-2916.1997.tb03124.x).

[15] W. S. Beh, Y. Xia, et D. Qin, « Formation of patterned microstructures of polycrystalline ceramics from precursor polymers using micromolding in capillaries », *J. Mater. Res.*, vol. 14, n° 10, p. 3995-4003, oct. 1999, doi: [10.1557/JMR.1999.0540](https://doi.org/10.1557/JMR.1999.0540).

[16] C. R. Martin et I. A. Aksay, « Topographical Evolution of Lead Zirconate Titanate (PZT) Thin Films Patterned by Micromolding in Capillaries », *J. Phys. Chem. B*, vol. 107, n° 18, p. 4261-4268, mai 2003, doi: [10.1021/jp034055+](https://doi.org/10.1021/jp034055+).

[17] M. Günthner, T. Kraus, W. Krenkel, G. Motz, A. Dierdorf, et D. Decker, « Particle-Filled PHPS Silazane-Based Coatings on Steel », *International Journal of Applied Ceramic Technology*, vol. 6, n° 3, p. 373-380, 2009, doi: [10.1111/j.1744-7402.2008.02346.x](https://doi.org/10.1111/j.1744-7402.2008.02346.x).

[18] O. Goerke, E. Feike, T. Heine, A. Trampert, et H. Schubert, « Ceramic coatings processed by spraying of siloxane precursors (polymer-spraying) », *Journal of the European Ceramic Society*, vol. 24, n° 7, p. 2141-2147, juin 2004, doi: [10.1016/S0955-2219\(03\)00362-5](https://doi.org/10.1016/S0955-2219(03)00362-5).

[19] G. S. Barroso, W. Krenkel, et G. Motz, « Low thermal conductivity coating system for application up to 1000°C by simple PDC processing with active and passive fillers », *Journal of the European Ceramic Society*, vol. 35, n° 12, p. 3339-3348, oct. 2015, doi: [10.1016/j.jeurceramsoc.2015.02.006](https://doi.org/10.1016/j.jeurceramsoc.2015.02.006).

- [20] P. Greil, « Polymer Derived Engineering Ceramics », *Advanced Engineering Materials*, vol. 2, n° 6, p. 339-348, juin 2000, doi: [10.1002/1527-2648\(200006\)2:6<339::AID-ADEM339>3.0.CO;2-K](https://doi.org/10.1002/1527-2648(200006)2:6<339::AID-ADEM339>3.0.CO;2-K).
- [21] P. Greil, « Active-Filler-Controlled Pyrolysis of Preceramic Polymers », *Journal of the American Ceramic Society*, vol. 78, n° 4, p. 835-848, avr. 1995, doi: [10.1111/j.1151-2916.1995.tb08404.x](https://doi.org/10.1111/j.1151-2916.1995.tb08404.x).
- [22] P. Greil, « Near Net Shape Manufacturing of Polymer Derived Ceramics », *Journal of the European Ceramic Society*, vol. 18, n° 13, p. 1905-1914, nov. 1998, doi: [10.1016/S0955-2219\(98\)00129-0](https://doi.org/10.1016/S0955-2219(98)00129-0).
- [23] H. Nowotny, E. Parthé, R. Kieffer, et F. Benesovsky, « Das Dreistoffsystem: Molybden?Silizium?Kohlenstoff », *Monatshefte für Chemie*, vol. 85, n° 1, p. 255-272, 1954, doi: [10.1007/BF00900444](https://doi.org/10.1007/BF00900444).
- [24] E. Parthé, W. Jeitschko, et V. Sadagopan, « A neutron diffraction study of the Nowotny phase $\text{Mo}_{45}\text{Si}_3\text{C}_{41}$ », *Acta Cryst*, vol. 19, n° 6, p. 1031-1037, déc. 1965, doi: [10.1107/S0365110X6500484X](https://doi.org/10.1107/S0365110X6500484X).
- [25] Y. Feng *et al.*, « Nowotny phase $\text{Mo}_{3+2x}\text{Si}_3\text{C}_{0.6}$ dispersed in a porous SiC/C matrix: A novel catalyst for hydrogen evolution reaction », *Journal of the American Ceramic Society*, vol. 103, n° 1, p. 508-519, 2020, doi: [10.1111/jace.16731](https://doi.org/10.1111/jace.16731).
- [26] X. Ji, S. Wang, C. Shao, et H. Wang, « High-Temperature Corrosion Behavior of SiBCN Fibers for Aerospace Applications », *ACS Appl. Mater. Interfaces*, vol. 10, n° 23, p. 19712-19720, juin 2018, doi: [10.1021/acsami.8b04497](https://doi.org/10.1021/acsami.8b04497).
- [27] K. Shimoda, J.-S. Park, T. Hinoki, et A. Kohyama, « Influence of surface structure of SiC nano-sized powder analyzed by X-ray photoelectron spectroscopy on basic powder characteristics », *Applied Surface Science*, vol. 253, n° 24, p. 9450-9456, oct. 2007, doi: [10.1016/j.apsusc.2007.06.023](https://doi.org/10.1016/j.apsusc.2007.06.023).

[28] J. Li *et al.*, « Microstructure and Dielectric Properties of LPCVD/CVI-SiBCN Ceramics Annealed at Different Temperatures », *Materials*, vol. 10, n° 6, p. 655, juin 2017, doi: [10.3390/ma10060655](https://doi.org/10.3390/ma10060655).

[29] H. Zhao, L. Chen, X. Luan, X. Zhang, J. Yun, et T. Xu, « Synthesis, pyrolysis of a novel liquid SiBCN ceramic precursor and its application in ceramic matrix composites », *Journal of the European Ceramic Society*, vol. 37, n° 4, p. 1321-1329, avr. 2017, doi: [10.1016/j.jeurceramsoc.2016.11.009](https://doi.org/10.1016/j.jeurceramsoc.2016.11.009).

[30] G. M. Ingo, N. Zacchetti, D. della Sala, et C. Coluzza, « X-ray photoelectron spectroscopy investigation on the chemical structure of amorphous silicon nitride ($a\text{-SiN}_x$) », *Journal of Vacuum Science & Technology A: Vacuum, Surfaces, and Films*, vol. 7, n° 5, p. 3048-3055, sept. 1989, doi: [10.1116/1.576314](https://doi.org/10.1116/1.576314).

[31] Y. Luo *et al.*, « A high-performance oxygen electrode for Li-O₂ batteries: Mo₂C nanoparticles grown on carbon fibers », *J. Mater. Chem. A*, vol. 5, n° 12, p. 5690-5695, mars 2017, doi: [10.1039/C7TA01249G](https://doi.org/10.1039/C7TA01249G).

[32] D. Wang, J. Wang, X. Luo, Z. Wu, et L. Ye, « In Situ Preparation of Mo₂C Nanoparticles Embedded in Ketjenblack Carbon as Highly Efficient Electrocatalysts for Hydrogen Evolution », *ACS Sustainable Chem. Eng.*, vol. 6, n° 1, p. 983-990, janv. 2018, doi: [10.1021/acssuschemeng.7b03317](https://doi.org/10.1021/acssuschemeng.7b03317).

[33] L. Lin *et al.*, « Low-temperature hydrogen production from water and methanol using Pt/ α -MoC catalysts », *Nature*, vol. 544, n° 7648, p. 80-83, avr. 2017, doi: [10.1038/nature21672](https://doi.org/10.1038/nature21672).

[34] C. Wan, Y. N. Regmi, et B. M. Leonard, « Multiple Phases of Molybdenum Carbide as Electrocatalysts for the Hydrogen Evolution Reaction », *Angewandte Chemie*, vol. 126, n° 25, p. 6525-6528, 2014, doi: <https://doi.org/10.1002/ange.201402998>.

[35] Q. Cao *et al.*, « Tailored synthesis of Zn-N co-doped porous MoC nanosheets towards efficient hydrogen evolution », *Nanoscale*, vol. 11, n° 4, p. 1700-1709, janv. 2019, doi: [10.1039/C8NR07463A](https://doi.org/10.1039/C8NR07463A).

- [36] Y. Huang *et al.*, « Atomically engineering activation sites onto metallic 1T-MoS₂ catalysts for enhanced electrochemical hydrogen evolution », *Nat Commun*, vol. 10, n° 1, p. 1-11, févr. 2019, doi: [10.1038/s41467-019-08877-9](https://doi.org/10.1038/s41467-019-08877-9).
- [37] Y.-X. Chen, C.-W. Wu, T.-Y. Kuo, Y.-L. Chang, M.-H. Jen, et I.-W. P. Chen, « Large-Scale Production of Large-Size Atomically Thin Semiconducting Molybdenum Dichalcogenide Sheets in Water and Its Application for Supercapacitor », *Sci Rep*, vol. 6, n° 1, p. 1-8, mai 2016, doi: [10.1038/srep26660](https://doi.org/10.1038/srep26660).
- [38] L. Liu *et al.*, « Phase-selective synthesis of 1T' MoS₂ monolayers and heterophase bilayers », *Nature Mater*, vol. 17, n° 12, p. 1108-1114, déc. 2018, doi: [10.1038/s41563-018-0187-1](https://doi.org/10.1038/s41563-018-0187-1).
- [39] S. K. Kim *et al.*, « Synergetic effect at the interfaces of solution processed MoS₂-WS₂ composite for hydrogen evolution reaction », *Applied Surface Science*, vol. 425, p. 241-245, déc. 2017, doi: [10.1016/j.apsusc.2017.06.211](https://doi.org/10.1016/j.apsusc.2017.06.211).
- [40] Z. Yang, C. Xu, Y. Xia, et Z. Xiong, « C,N-codoped MoSi₂ ceramic with excellent heat resistance for microwaves absorption application », *Royal Society Open Science*, vol. 7, n° 7, p. 200740, doi: [10.1098/rsos.200740](https://doi.org/10.1098/rsos.200740).
- [41] L. Guo, X. Hu, X. Tao, H. Du, A. Guo, et J. Liu, « Low-temperature oxidation resistance of the silica-coated MoSi₂ powders prepared by sol-gel preoxidation method », *Ceramics International*, vol. 46, n° 15, p. 23471-23478, oct. 2020, doi: [10.1016/j.ceramint.2020.06.117](https://doi.org/10.1016/j.ceramint.2020.06.117).
- [42] C. Dang *et al.*, « Novel MoSi₂ catalysts featuring surface activation as highly efficient cathode materials for long-life Li-O₂ batteries », *J. Mater. Chem. A*, vol. 8, n° 1, p. 259-267, déc. 2019, doi: [10.1039/C9TA10713D](https://doi.org/10.1039/C9TA10713D).
- [43] X. Zou et Y. Zhang, « Noble metal-free hydrogen evolution catalysts for water splitting », *Chem. Soc. Rev.*, vol. 44, n° 15, p. 5148-5180, 2015, doi: [10.1039/C4CS00448E](https://doi.org/10.1039/C4CS00448E).

- [44] M. Mirkhalaf, H. Yazdani Sarvestani, Q. Yang, M. B. Jakubinek, et B. Ashrafi, « A comparative study of nano-fillers to improve toughness and modulus of polymer-derived ceramics », *Sci Rep*, vol. 11, n° 1, p. 6951, déc. 2021, doi: [10.1038/s41598-021-82365-3](https://doi.org/10.1038/s41598-021-82365-3).
- [45] J. Cordelair et P. Greil, « Electrical Characterization of Polymethylsiloxane/MoSi₂-Derived Composite Ceramics », *Journal of the American Ceramic Society*, vol. 84, n° 10, p. 2256-2259, 2001, doi: [10.1111/j.1151-2916.2001.tb00998.x](https://doi.org/10.1111/j.1151-2916.2001.tb00998.x).
- [46] Data from ASM Metals Reference Book, Third Edition, Michael Baucchio, Ed., ASM International,
- [47] Materials Park, OH, p157-158, (1993).
- [48] X. Guo, Y. Feng, X. Lin, Y. Liu, H. Gong, et Y. Zhang, « The dielectric and microwave absorption properties of polymer-derived SiCN ceramics », *Journal of the European Ceramic Society*, vol. 38, n° 4, p. 1327-1333, avr. 2018, doi: [10.1016/j.jeurceramsoc.2017.10.031](https://doi.org/10.1016/j.jeurceramsoc.2017.10.031).
- [49] T. Shinagawa, A. T. Garcia-Esparza, et K. Takanabe, « Insight on Tafel slopes from a microkinetic analysis of aqueous electrocatalysis for energy conversion », *Sci Rep*, vol. 5, n° 1, p. 13801, sept. 2015, doi: [10.1038/srep13801](https://doi.org/10.1038/srep13801).
- [50] Y.-H. Fang et Z.-P. Liu, « Tafel Kinetics of Electrocatalytic Reactions: From Experiment to First-Principles », *ACS Catal.*, vol. 4, n° 12, p. 4364-4376, déc. 2014, doi: [10.1021/cs501312v](https://doi.org/10.1021/cs501312v).
- [51] B. A. Gnesin et I. B. Gnesin, « Synthesis of the Nowotny phase Mo_{4.8}Si₃C_{0.6} from Mo₅Si₃ + carbon mixtures », *Inorg Mater*, vol. 51, n° 10, p. 991-998, oct. 2015, doi: [10.1134/S0020168515090071](https://doi.org/10.1134/S0020168515090071).
- [52] S. Shi, Z. Sun, et Y. H. Hu, « Synthesis, stabilization and applications of 2-dimensional 1T metallic MoS₂ », *J. Mater. Chem. A*, vol. 6, n° 47, p. 23932-23977, déc. 2018, doi: [10.1039/C8TA08152B](https://doi.org/10.1039/C8TA08152B).

***Chapter V: Synthesis and
characterization of novel preceramic
photoresists implemented in
photolithography process***

5	Synthesis and characterization of novel preceramic photoresists for photolithography	218
5.1	Introduction and reminder of state of the art.....	218
5.2	Original photoresist synthesis	218
5.2.1	Chemical characterization	219
5.2.1.1	FTIR investigations.....	220
5.2.1.2	NMR investigations.....	226
5.2.2	Photoresist properties	231
5.2.2.1	Polymer-to-ceramic conversion (TGA)	231
5.2.2.2	Photosensitivity (UV-vis spectroscopy)	233
5.3	Photolithographic preparation of ceramic micropatterns.....	235
5.3.1	Spin-coating of photoresists	236
5.3.2	UV exposure and development.....	238
5.3.2.1	UV Dose estimation.....	240
5.3.2.2	Profilometry investigations	246
5.3.3	Polymer-to-ceramic conversion	248
5.3.3.1	SEM observations - shrinkage estimation	249
5.3.3.2	Profilometry characterization	251
5.3.3.3	Mechanical properties - nanoindentation.....	252
5.4	Chapter conclusions.....	255
5.5	Bibliography.....	256

5 Synthesis and characterization of novel preceramic photoresists for photolithography

5.1 Introduction and reminder of state of the art

The previous chapter was dedicated to the development of a soft-lithography fabrication procedure for PDC based micro-patterns. In the present chapter, we were interested in the photolithography strategy for direct patterning of SiCN and SiBCN micro-objects that can be used as potential micro-electrodes for micro-devices or MEMS. Such photolithography process is technically complex to implement in comparison with soft-lithography route since photosensitive preceramic polymers are required. In the state of the art review (chapter I), we mentioned several studies dealing with micro-patterning of PDCs *via* UV-lithography. Those works are limited to photolithography of pre-SiCN and pre-SiC polymers.

The main objectives of this chapter are the following: (i) Synthesize and characterize pre-SiCN and pre-SiBCN photoresists compatible with UV-lithography *via* grafting of acrylate and methacrylate species (ii) Incorporate the as-synthesized photoresists in a photolithographic procedure for Si(B)CN micro-pattern preparation (iii) Optimize both resists (UV-curable PVZ and PBVZ) and process parameters to obtain the most faithful negative reproduction of the photomask geometry.

This chapter is divided in two main sections. First, we will discuss the results associated with the chemical characterization of the range of preceramic photoresists synthesized for this work. Second, we will describe the optimization of UV-lithography parameters and the influence of photoresists composition on the process feasibility.

5.2 Original photoresist synthesis

The description of the preceramic photoresist synthesis is available in section 2.3.1.1. It consists in grafting photosensitive functions on the backbone of the preceramic polymer based on the work of Kim's group [1][2][3][4][5]. The sample notation employed in this chapter is described in Table 5-1.

Table 5-1: Sample notation for synthesized preceramic photoresists discussed in chapter5

Notation	Boron content	Nature of the photosensitive group	Content of photosensitive function
<i>aPVZ10</i>	0	acrylate	10 wt% of IEA
<i>aPVZ20</i>	0	acrylate	10 wt% of IEA
<i>mPVZ5</i>	0	methacrylate	5 wt% of IEM
<i>mPVZ10</i>	0	methacrylate	10 wt% of IEM
<i>mPVZ20</i>	0	methacrylate	20 wt% of IEM
<i>aPBVZ30-10</i>	Si/B=30	acrylate	10 wt% of IEA
<i>mPBVZ30-10</i>	Si/B=30	methacrylate	10 wt% of IEM
<i>aPBVZ17-10</i>	Si/B=17	acrylate	10 wt% of IEA
<i>mPBVZ17-10</i>	Si/B=17	methacrylate	10 wt% of IEM

5.2.1 Chemical characterization

The grafting of acrylate or methacrylate photosensitive functions consists in a conversion of isocyanate in urea group *via* an addition reaction. The mechanism of such reaction is described in Figure 5-1 for grafting either acrylate or methacrylate groups on PVZ backbone.

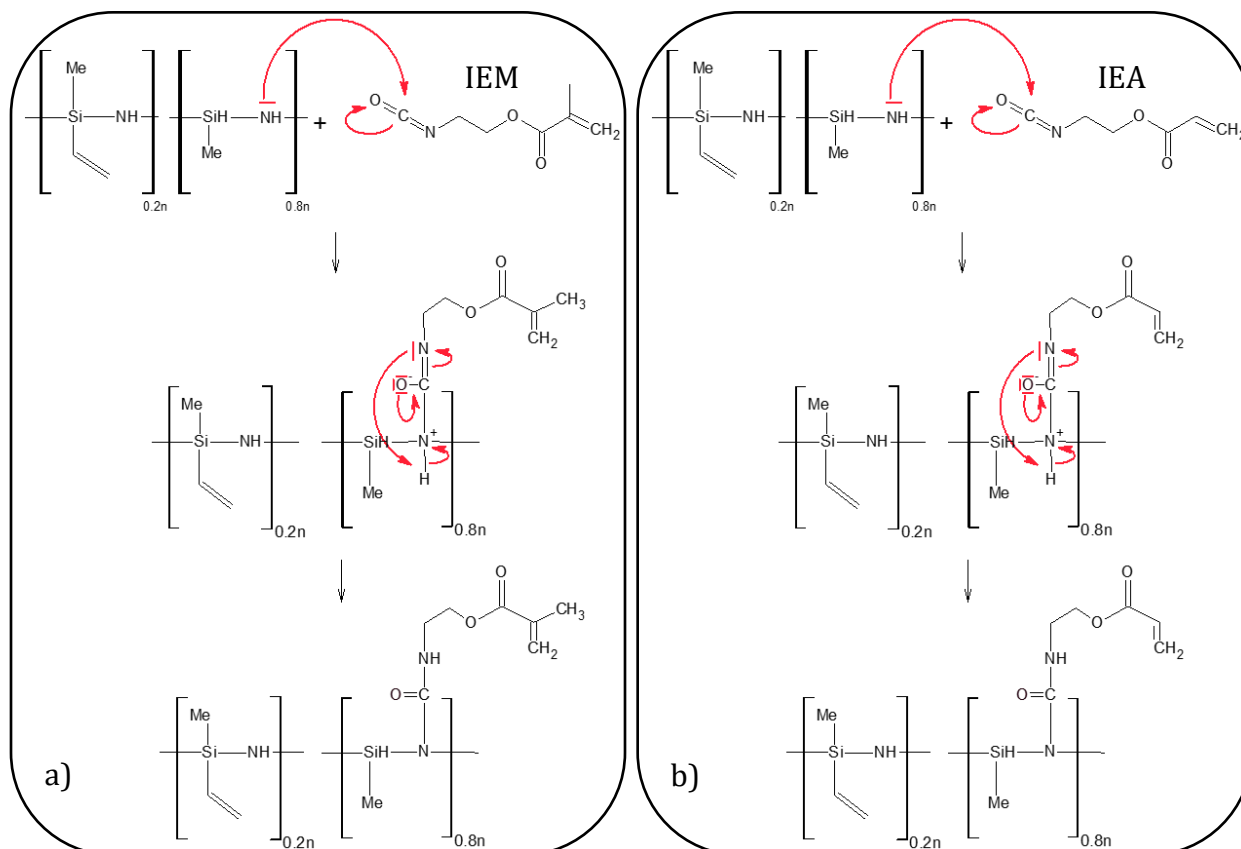


Figure 5-1: Reaction mechanism of photosensitive groups on polyvinylsilazane backbone a) IEM b) IEA

To monitor the functionalization, a complete chemical characterization of the sample was carried out. Chemical and structural investigation were carried out through FTIR and NMR spectroscopy and evaluation of the preceramic photoresists properties *via* TGA and UV-vis studies.

5.2.1.1 FTIR investigations

The grafting of acrylate and methacrylate functions on PVZ were investigated by FTIR. Results are presented in Figure 5-2.a for acrylate and Figure 5-2.b for methacrylate grafting. The conversion of isocyanate ($-NCO$) in IEM or IEA to urea ($CO-NH$) in the synthesized product is confirmed by the IR absorption peaks associated with urea group at 1545 cm^{-1} [1][2]. The extinction of the isocyanate peaks ($-NCO$) at 2272 and 1363 cm^{-1} in modified PVZ confirms the consumption of isocyanate to form urea group. Further, introduced methacrylate or acrylate appeared at 1714 cm^{-1} ($C=O$) and 1639 cm^{-1} ($C=C$) [3][4][5]. According to FTIR chemical analysis, the grafting of acrylate or methacrylate on PVZ is confirmed. Moreover, the introduction of IEM or IEA does not seem to affect the

characteristic peaks associated with the PVZ backbone such as N-H at 3400 cm^{-1} , Si₂-NH at 1166 cm^{-1} and Si-H at 2126 cm^{-1} . The influence of the acrylate or methacrylate contents in the polymer was also investigated. In Figure 5-2.a, aPVZ10 and aPVZ20 curves contain the same IR bands but some differences are notable:

- The NCO band at 2272 cm^{-1} is still distinguishable in the aPVZ20 final product but not in aPVZ10, which suggests that the added quantity of IEA on PVZ in aPVZ20 is too high and conduct to a non-total reaction.
- The intensity of -C=O ; -CO-NH and -C-N bonds at 1714 cm^{-1} , 1545 cm^{-1} and 1455 cm^{-1} , respectively, is higher in aPVZ20 than in aPVZ10 confirming a higher acrylate content.

A similar approach is presented for methacrylate addition in Figure 5-2.b with mPVZ5, mPVZ10 and mPVZ20 curves. As for aPVZ, FTIR spectra contain the same bands regardless of the methacrylate content and the same observation can be made:

- -NCO band at 2272 cm^{-1} is observable in the mPVZ20 final product but not in mPVZ10 or mPVZ5, the added quantity of IEM on PVZ in mPVZ20 is too high, the grafting reaction is not total.
- As expected, the intensity of the methacrylate bands (-C=O ; -CO-NH and -C-N) increase with the quantity of introduced IEM

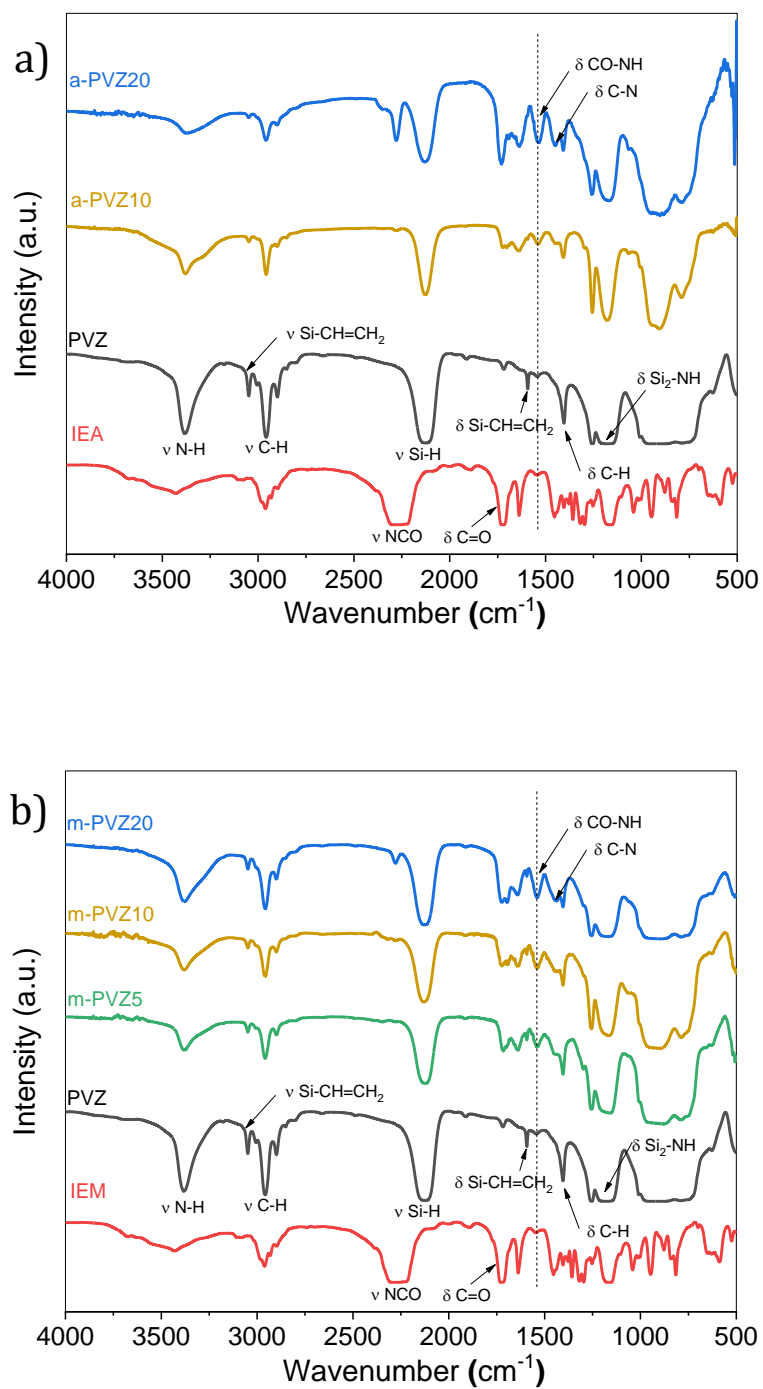


Figure 5-2: FTIR spectra of modified polysilazane with (a) acrylate or (b) methacrylate grafting

Based on our results, we conclude that for a 10 wt% amount of IEM or IEM the grafting reaction is considered total. This amount of photosensitive function was considered as optimal and fixed for the continuation of the study.

The grafting of photosensitive functions was also applied for boron modified polyvinylsilazane (PBVZ) synthesis as it is described in section 2.2.1.2. Such mechanism is described in Figure 5-3, it consists in the same conversion reaction of isocyanate group into urea function described in Figure 5-1. Nevertheless, some N-H and vinyl groups have already reacted with B-H group during the PBVZ synthesis as it is suggested by the represented N-B-N, C-B-N and C-B-C units displayed on the figure.

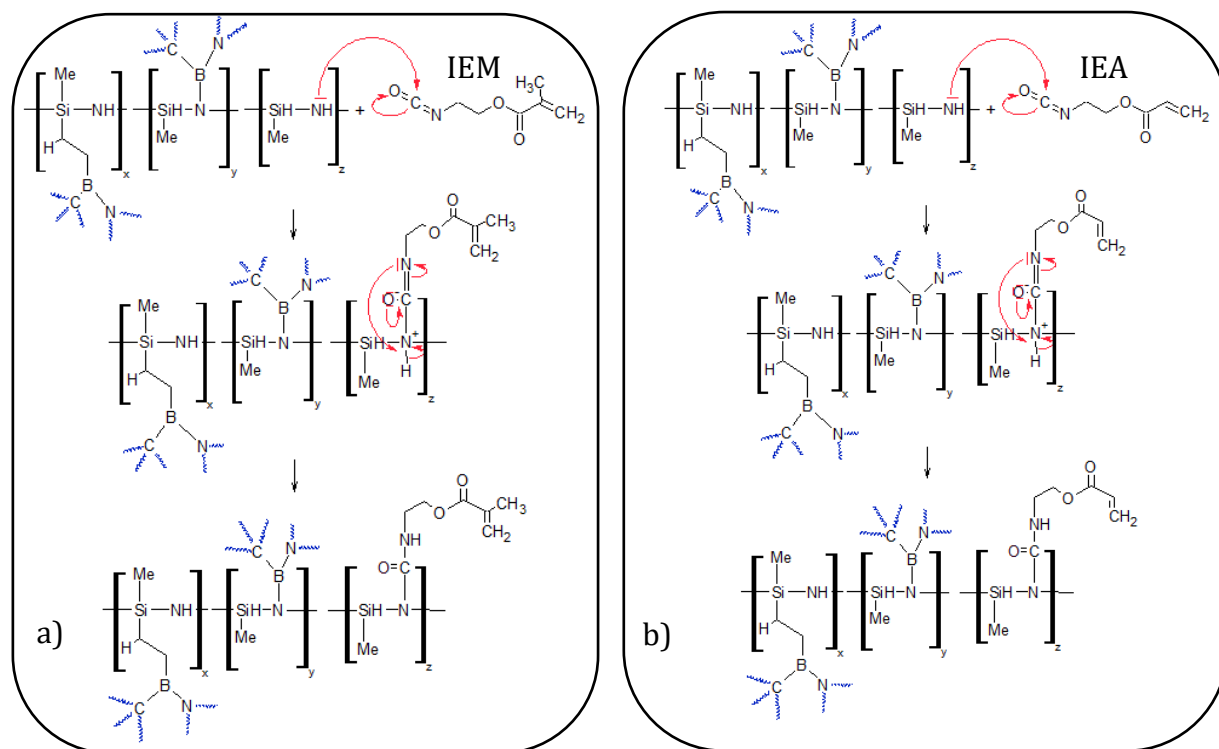


Figure 5-3: Reaction mechanism of photosensitive groups on polyvinylsilazane modified with boron backbone a) IEM b) IEA

FTIR spectra presented in Figure 5-4 show the signals of boron-modified polysilazane grafted with acrylate or methacrylate functions, Si/B ratio being fixed at 30 for a partial hydroboration of the vinyl. The -CO-NH band characteristic of the grafting reaction is distinguishable at 1545 cm^{-1} , nevertheless, -NCO band at 2270 cm^{-1} is detected in the final product suggesting that unreacted IEM or IEA is still present in the final product. The consumption of a part of the available -NH group by the previous addition of boron in the

initial PVZ could be an explanation of the poorer reactivity of isocyanate (fewer N-H group available). On the other hand, the crosslinking is higher in PBVZ polymer than in PVZ given the N-B-N; C-B-N and C-B-C bonds created during PBVZ synthesis (see Figure 5-3). This higher rate of crosslinking is a source of steric hindrance and could be a hypothesis justifying the unreacted -NCO groups in the final resin. The intensity decrease of vinyl group in boron containing polymers compared with PVZ is supported by the hydroboration reaction occurring during PBVZ30 synthesis.

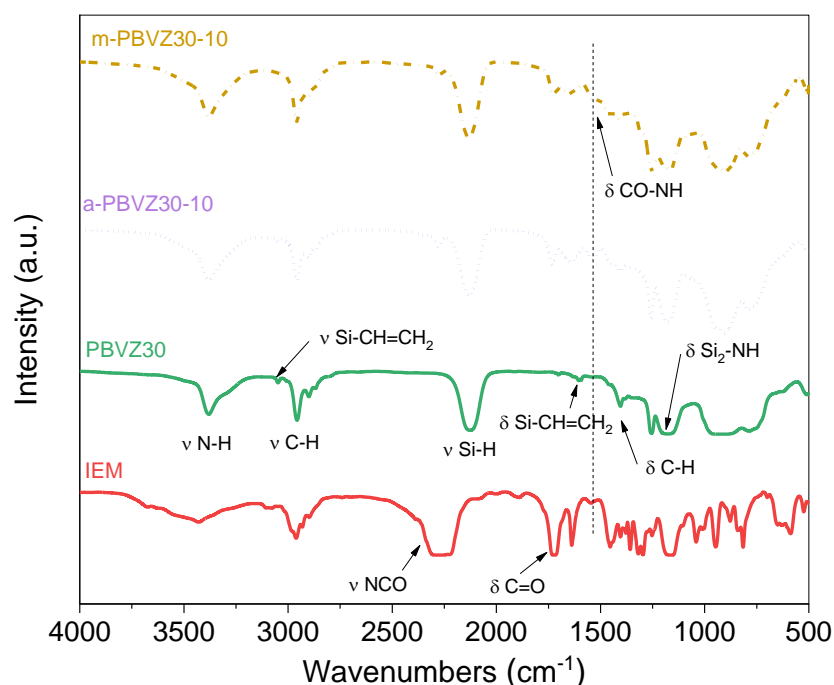


Figure 5-4: FTIR spectra of boron-modified polysilazane (Si/B=30) with acrylate or methacrylate grafting

Finally, a last FTIR study was carried out on boron modified polyvinylsilazane with ratio Si/B fixed at 17 (for a total hydroboration of the vinyl in PVZ) and grafted with acrylate or methacrylate. Figure 5-5 shows FTIR spectra for these samples. The higher content in boron in PBVZ17 *versus* PBVZ30 is suggested by the hardly distinguishable -B-H band and -B-N at 2427 and at 1336 cm^{-1} revealing respectively the presence of unreacted BDMS in the final product and the formation of B-N bonds by dehydrocoupling. After the grafting of acrylate

or methacrylate through IEM or IEA addition, CO-NH band at 1540 cm^{-1} is detected again confirming the grafting of photosensitive groups on polymer backbone [6].

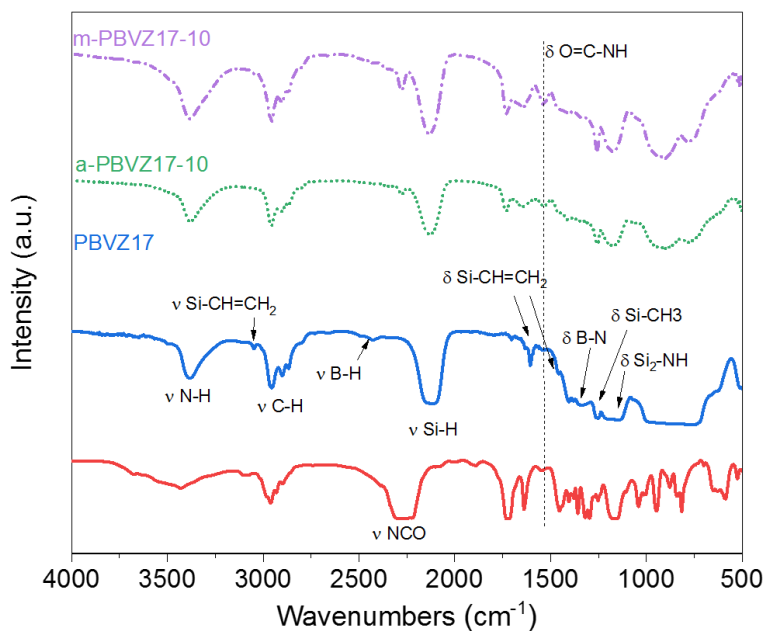


Figure 5-5: FTIR spectra of modified boron containing polysilazane (Si/B=17) with acrylate or methacrylate grafting

Thanks to FTIR analysis previously developed, the grafting of photosensitive functions as acrylate or methacrylate on polymer backbone is confirmed by the detection of the urea function (CO-NH at 1540 cm^{-1}). The introduction of those photosensitive functions does not affect the characteristic groups of the organosilicon preceramic polymer. The addition of IEA or IEM at a ratio superior to 10 wt% leads to a non-total reaction. A 10 wt% content was considered as the optimal ratio and thus was fixed for the rest of the study. Nevertheless, in the boron containing preceramic polymers, the grafting reaction is not total and seems hampered by the low availability of -NH groups because of their lower content and a higher steric hindrance in PBVZ polymers. According to this study, the synthesis method employed here seems effective for the preparation of suitable photoresists for photolithography. However, FTIR analysis is not efficient enough to determine the precise structure of these photosensitive preceramic polymers. Solid and liquid state NMR spectroscopies were therefore performed to determine the atomic and molecular arrangement of the samples.

5.2.1.2 NMR investigations

5.2.1.2.1 Solid-state NMR

We first performed solid-state NMR spectroscopy on aPBVZ30-10 and mPBVZ17-10 polymers as described in section 2.2.1. Spectra are presented in Figure 5-6 and Figure 5-7 for ^1H NMR and ^{13}C NMR, respectively. For ^1H NMR, signals at 0.3 ; 1-1.2 ; 4.4-4.9 and 6.0-6.5 ppm demonstrate the presence of Si-CH₃ ; NH ; SiH and Si-CH=CH₂ units in both aPBVZ30-10 and mPBVZ10-10. Nevertheless, peaks observable on these spectra have poor resolution and low intensity. It is caused by the low mobility of the units composing the polymers. Clear identification of chemical units is thus difficult in the case of solid aPBVZ30-10 and mPBVZ17-10.

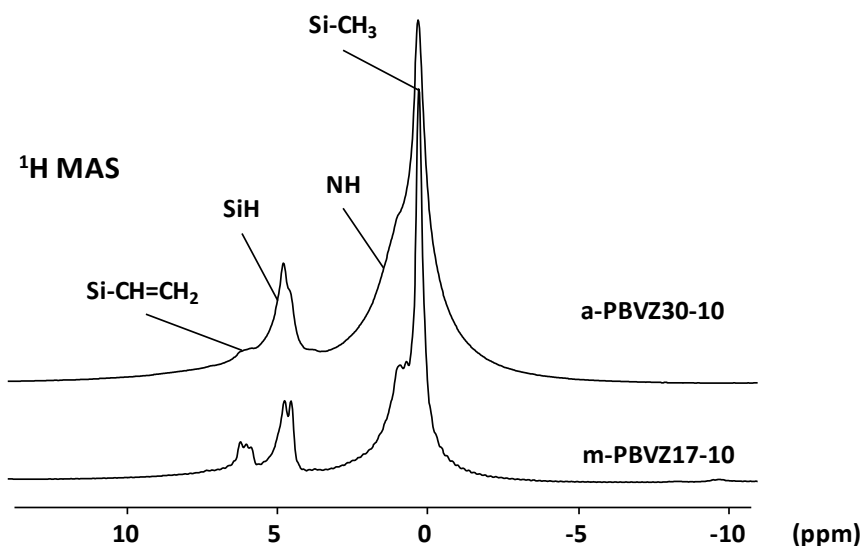


Figure 5-6: Solid state ^1H NMR spectra of aPBVZ30-10 and mPBVZ30-10

For the ^{13}C NMR spectroscopy presented in Figure 5-7, spectra were collected with cross-polarization activated (CP MAS) and disabled (MAS) in order to increase intensity of units with low and high mobility, respectively. Characteristics units of acrylate and methacrylate i.e. -N-CH₂- ; -O-CH₂- and -C=O are detected at 46 ; 62 and 167 ppm, respectively. The presence of those peaks in the spectra are an other proof of the photosensitive units on the polymer backbone.

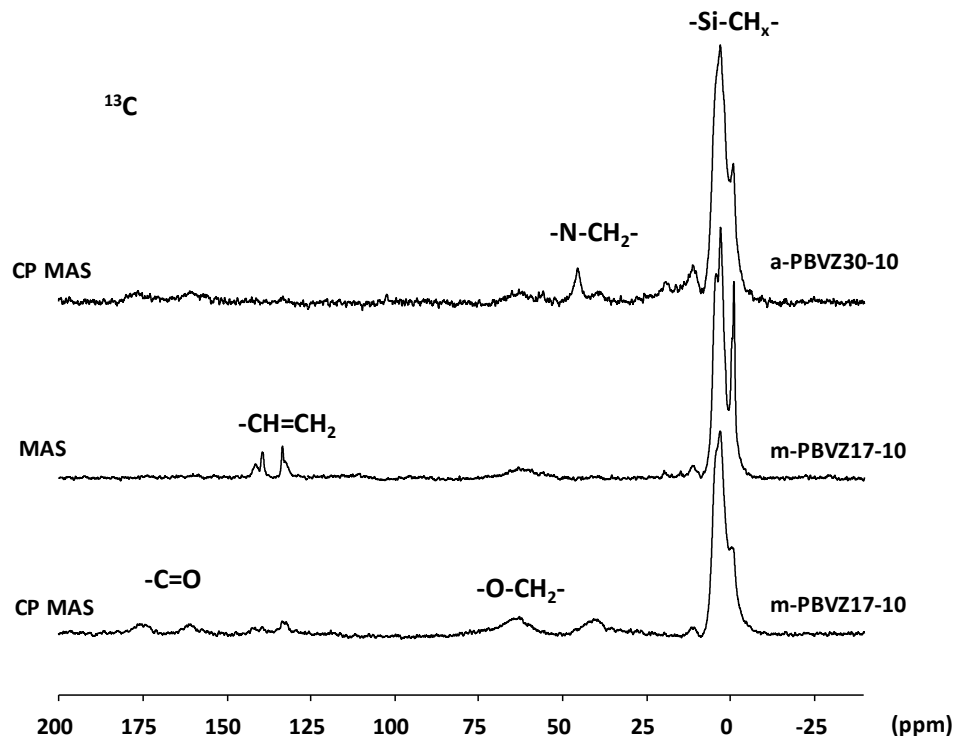


Figure 5-7: Solid state ^{13}C NMR spectra of aPBVZ30-10 and mPBVZ30-10

For both ^{13}C and ^1H solid-state NMR, the peaks intensity and resolution are too low to perform precise identification of the chemical functions composing the polymers. To overcome this problem, we carried out NMR analysis at liquid-state (before crosslinking) in order to obtain spectra with better resolution. These results are developed in the next section.

5.2.1.2.2 Liquid-state NMR

^1H NMR spectra associated with the PVZ and the photosensitive resins mPVZ10 and aPVZ10 are shown in Figure 5-8. As in the case of the previously mentioned FTIR analyzes the characteristic groups of PVZ, namely, Si-CH_3 , NH , Si-H , SiCH=CH_2 and SiCH=CH_2 appear in the NMR spectrum at 0.3 ppm, 0.9-1.4 ppm, 4.5-5 ppm, 5.9 and 6.3 ppm. The introduction of photosensitive functions in aPVZ10 and mPVZ10 samples is confirmed by the detection of $\text{CH}_2\text{-NH}$; $\text{CH}_2\text{-O}$, C-C=CH_2 and C-CH=CH_2 groups at 3.5 ppm, 4.3 ppm, 5.5 ppm and 6.2 ppm. The aPVZ10 and mPVZ10 spectra are very similar but can be differentiated thanks to the peak at 2.0 ppm attributed to C=C-CH_3 group characteristic of methacrylate species but absent from acrylates molecules. According to these results, the organosilicon groups are

not affected by the introduction of photosensitive functions that are detected in the photoresists [7][8] .

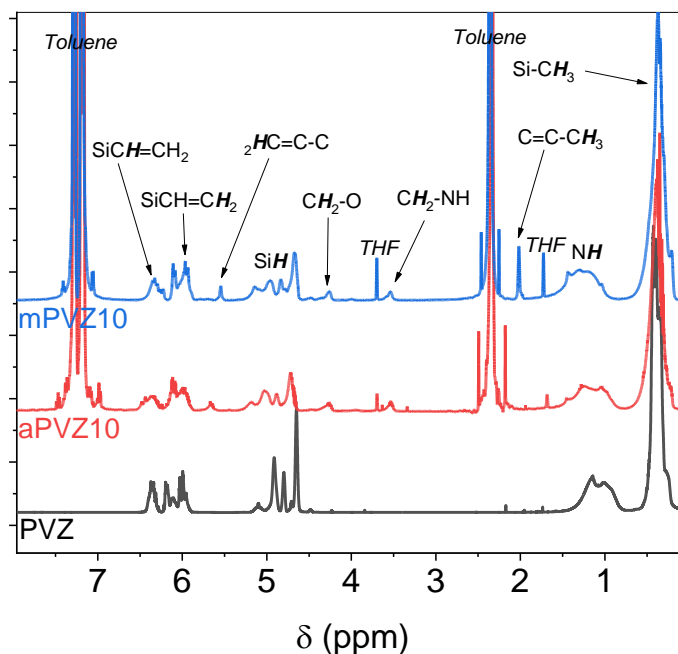


Figure 5-8: ^1H NMR spectra of PVZ, aPVZ10 and mPVZ10 photoresist; 50mg/ml in deuterated THF for aPVZ10 and mPVZ10

Grafting of the photosensitive groups onto the PVZ polymer is confirmed by the DOSY (Diffusion Ordered Spectroscopy NMR) analysis (Figure 5-9) which reveals two distinct Brownian motion modes. One being associated with all the chemical groups of photosensitive resins (diffusion coefficient between 10^{-9} and $10^{-9.5}$ m^2/s) and the other associated with THF and toluene solvent residues (centered diffusion coefficient 10^{-8} m^2/s) [7][8].

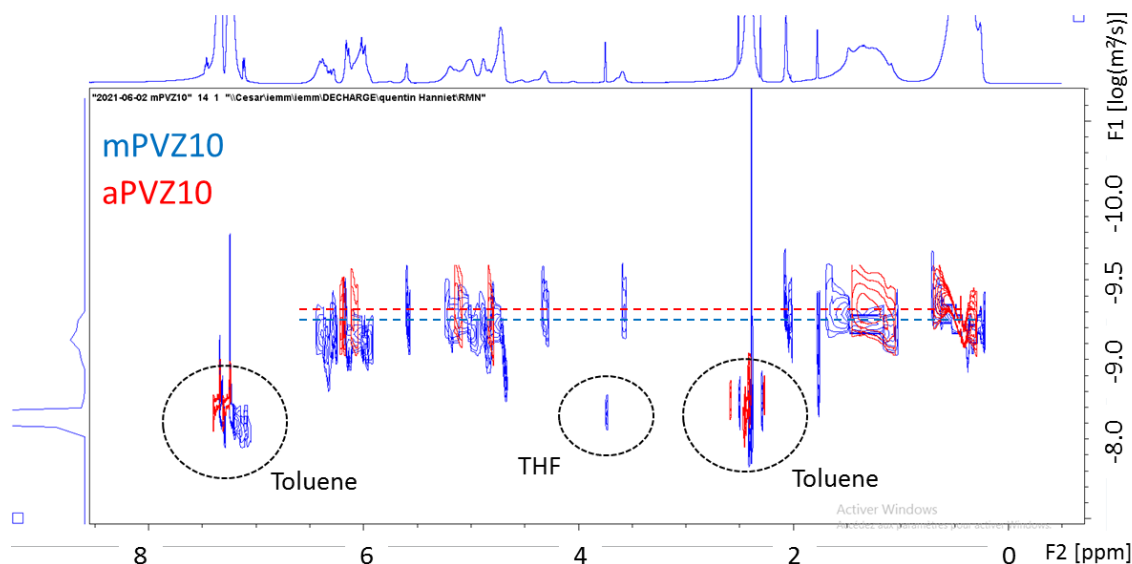


Figure 5-9: 2D DOSY analysis of mPVZ10 and aPVZ10 photoresists; 50mg/ml in deuterated THF

¹H NMR analyzes concerning boron based photosensitive resists are presented in Figure 5-10. The chemical functions present in PVZ are found in PBVZ30 with nevertheless a decrease in the signal intensity associated with SiCH=CH₂ (5.9-6.3 ppm) caused by hydroboration *via* BDMS (see Figure 5-3). After the addition of IEA or IEM, CH₂-NH and CH₂-O groups are visible but with a much lower intensity than in the case of non-borated resins. This suggests that the grafting of the photosensitive groups is less favorable in the presence of boron which is in agreement with the FTIR analyzes presented in Figure 5-4 and Figure 5-5. The effects of steric hindrance and the consumption of a part of the NH groups caused by dehydrocoupling reactions taking place during the introduction of boron seems to cause a decrease in the availability of NH sites for the grafting of the (meth)acrylate groups.

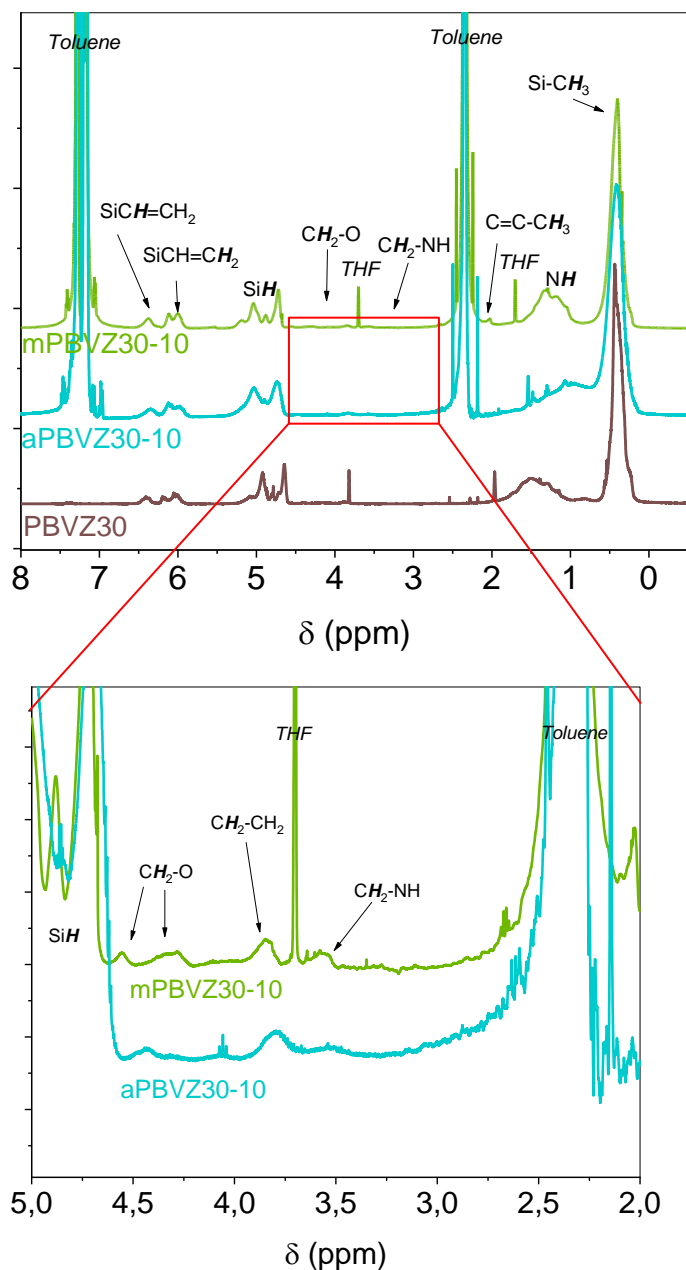


Figure 5-10: ^1H NMR spectra of PBVZ30 , aPBVZ30-10 and mPBVZ30-10 photoresist; 50mg/ml in deuterated THF for PBVZ30 and mPBVZ30-10

Despite the low intensity of the signals associated with the photosensitive groups, DOSY analysis (Figure 5-11.b) confirms the proper grafting of the photosensitive sites on the PVZ polymer chain with a Brownian motion mode around $10^{-9.5} \text{ m}^2/\text{s}$.

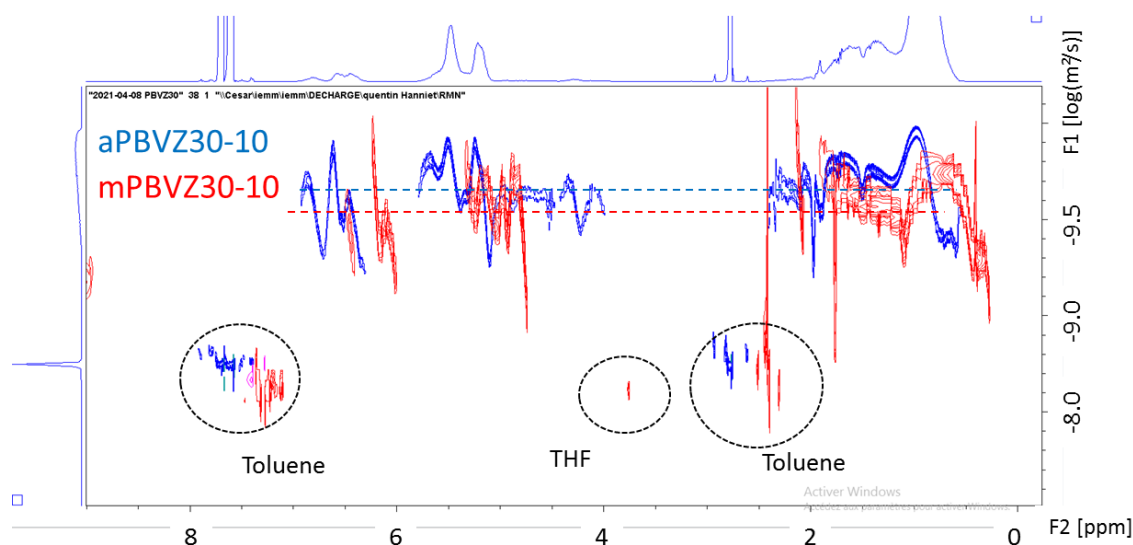


Figure 5-11: 2D DOSY analysis of mPBVZ30-10 and aPBVZ30-10 photoresist; 50mg in Deuterated THF

5.2.2 Photoresist properties

In this part, the polymer-to-ceramic conversion and the photosensitivity of the synthesized pre-ceramic photoresists are investigated *via* TGA and UV-vis spectroscopy, respectively.

5.2.2.1 Polymer-to-ceramic conversion (TGA)

Figure 5-12 present the TGA curves of grafted polyvinylsilazane under nitrogen. As previously discussed in chapter IV, PVZ conversion into SiCN ceramic occurs in 3 steps (**1**: 100°C-250°C NH₃ evacuation; **2**: 300-500°C releases of CH₄, C₂H₆ and H₂; **3**: 600-1000°C ceramization of the preceramic polymer). The grafting of (meth)acrylate groups on polymer backbone conducts to an increase of the ceramic yield compared to PVZ (upon 67% for aPVZ20 against 59,2% for PVZ). This yield increase could be explained by the early crosslinking induced after the grafting reaction, indeed an increase of the viscosity and even solidification is observed on the prepared photoresists. Moreover, the grafting of acrylate or methacrylate groups can possibly participate in the ceramization process by feeding the carbon free nanodomains and thus increasing the ceramic yield.

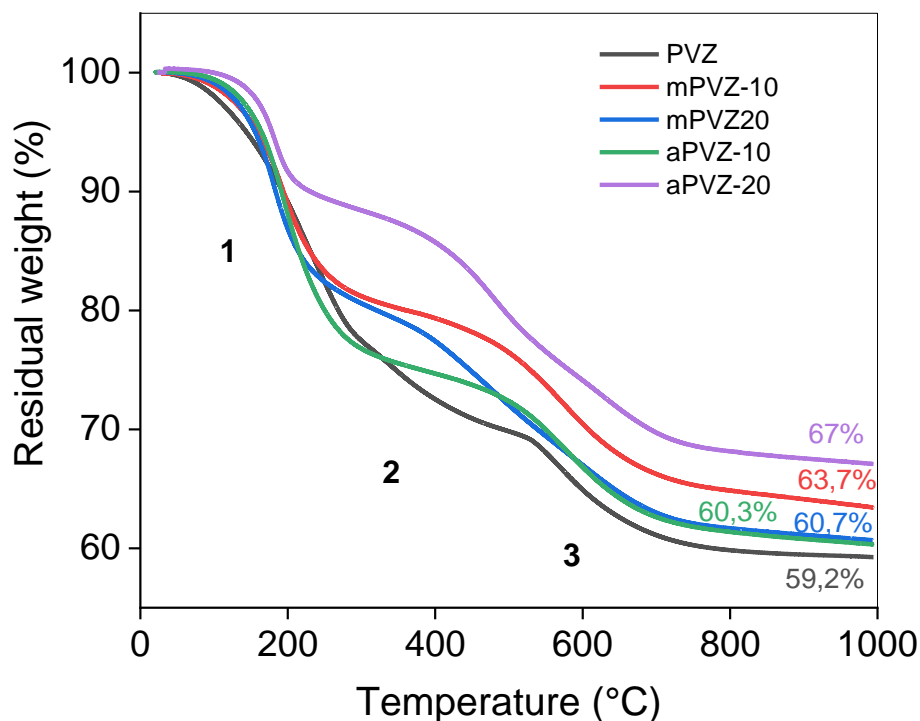


Figure 5-12: TGA curves of pre-SiCN photoresist grafted with acrylate or methacrylate groups. Under nitrogen atmosphere; heating and cooling rate 5°C/min

As observed on TGA curves in Figure 5-13, the introduction of boron increases the ceramic yield up to 67% for Si/B=30 and 68% for Si/B=17 in comparison with boron free polysilazane. For PBVZ17 and PBVZ30 the weight loss of the 1st step (from 150 to 250°C) is reduced in comparison with PVZ. Indeed, a certain amount of vinyl and N-H groups is consumed during the synthesis of PBVZ through B-N and B-C bonds formation (described in section 5.2.1). In these conditions, the transamination reactions conducting to NH₃ releasing are less likely to occur. Furthermore, the role of boron in decreasing segments and chain mobility is known [6]. It explains the increasing of the ceramic yield with the boron content in the preceramic polymer. Finally, the higher ceramic yield of the photoresists aPBVZ and mPBVZ present the highest ceramic yield thanks to the effect of acrylate/methacrylate grafted functions and the presence of B-C and B-N bonds (Ceramic yield reaches 73.5% for aPBVZ17-10).

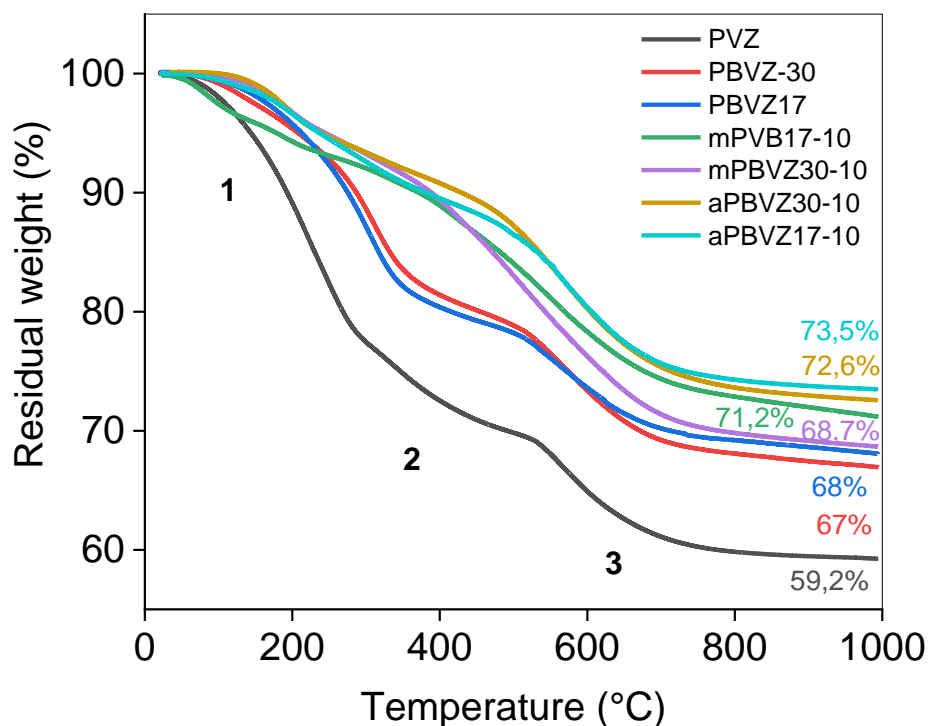


Figure 5-13: TGA curves of pre-SiBCN30 and pre-SiBCN17 photoresists grafted with acrylate or methacrylate groups. Under nitrogen atmosphere; heat rate 5°C/min

The high ceramic yield of boron containing photoresists has great interest in the optic of micro-pattern preparation. A too low ceramic yield is synonym of high shrinkage during the pyrolysis step, it can conduct to “mud-cracks” formation or peeling off of the ceramic from the silicon wafer [9][10] as discussed in section 4.3.1 of chapter IV. The grafting of acrylate and methacrylate groups have, in conclusion, a double role: (i) it gives photosensitive properties to the preceramic polymer (ii) it tends to increase the ceramic yield of the polymer.

5.2.2.2 Photosensitivity (UV-vis spectroscopy)

The influence of the introduced photosensitive functions on the UV-light/polymer interaction was evaluated *via* UV-vis spectroscopy. Figure 5-14 presents UV absorption curves of pre-SiCN photoresists, the nature and the quantity of grafted groups was investigated. The different absorption spectra show a unique peak between 225 and 275 nm. It is clear that the presence of acrylate or methacrylate groups increases the intensity of

such an absorption peak. Moreover the intensity of this peak increases with the content in photosensitive function (if $I_{225-275}$ is the intensity of the absorption peak: $I_{225-275}(\text{mPVZ5}) < I_{225-275}(\text{mPVZ10}) < I_{225-275}(\text{mPVZ20})$ and $I_{225-275}(\text{aPVZ10}) < I_{225-275}(\text{aPVZ20})$).

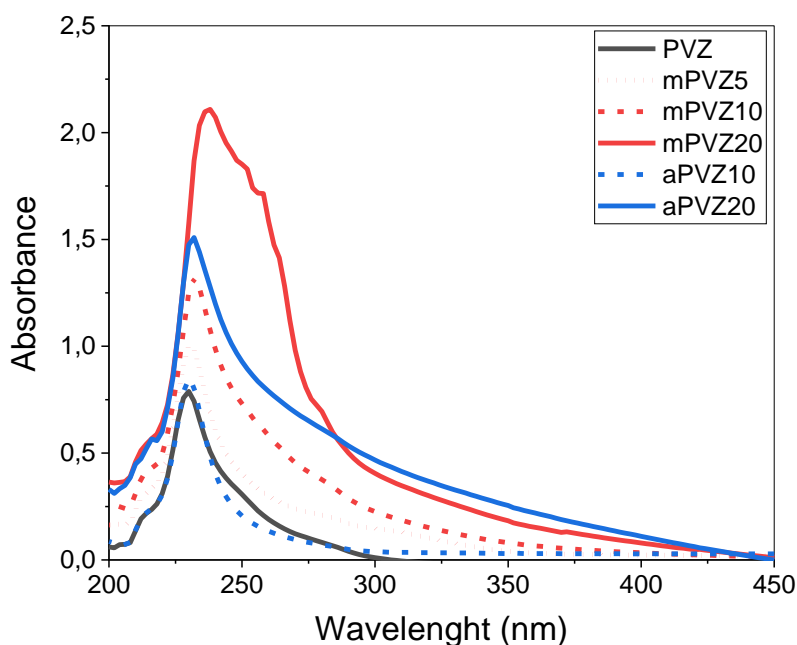


Figure 5-14: UV-vis spectra of pre-SiCN photoresists (0.5mg/ml in THF; Quartz cell)

The previously described trend is reproduced for boron-based photoresists (pre-SiBCN), in comparison with PBVZ17 and PBVZ30 the addition of the photosensitive functions increases the absorption peak intensity.

The UV-vis spectroscopy investigations on the synthesized preceramic photoresists confirms the presence of acrylated or methacrylated units. In comparison with non-acrylated preceramic polymers, the preceramic photoresists show a higher absorption of UV light which confirms the higher photosensitivity of the grafted polymers [1][2][11].

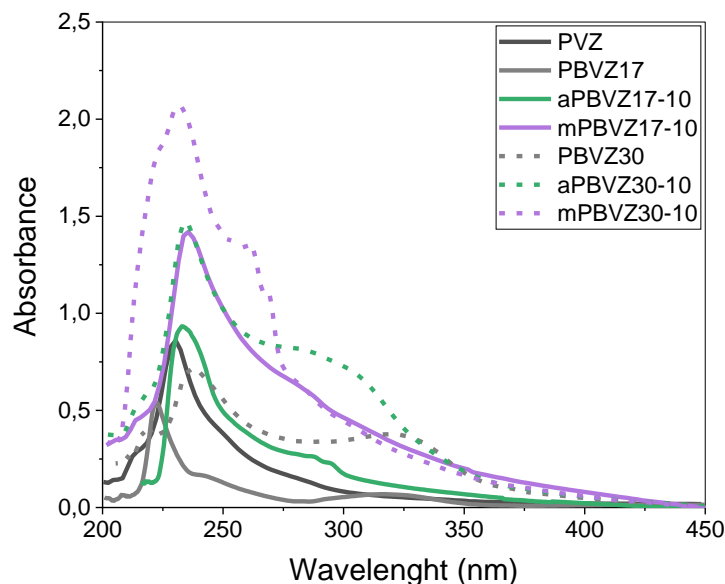


Figure 5-15: UV-vis spectra of pre-SiBCN30 and pre-SiBCN17 photoresists (0.5mg/ml in THF; Quartz cell)

The global chemical characterization of photosensitive preceramic polymers has been developed in section 5.2.1. FTIR and NMR investigation have confirmed the grafting of acrylate and methacrylate groups in the inorganic polymer backbone. The initial polyvinylsilazane units (Si-H, C-H_x, Si-C, etc.) were not affected by the grafting of such photosensitive functions, the preceramic polymers properties were thus conserved. TGA curves have shown that the (meth)acrylation conducts to an improvement of the ceramic yield either by crosslinking before pyrolysis and/or carbon feeding during pyrolysis.

5.3 Photolithographic preparation of ceramic micropatterns

The photosensitive properties of mPVZ, aPVZ, mPBVZ and aPBVZ photoresists were illustrated by microfabrication of micropatterns thanks to the method described in chapter II (section 2.4.2).

In this part, we present the investigation, results and problems encountered with the preparation of ceramic microstructures *via* photolithography. The following subjects will be mentioned: (i) Results on dissolution of the solid photoresist (ii) Compatibility of synthesized photoresists with the spin coating technique (iii) Reactivity of the photoresist towards UV light (iv) Development step of the micropatterns after light exposition

(removing the unexposed photoresist by solvent dissolution) (v) Estimation of the accurate energy dose (namely, dose-to-size E_s) for crosslinking and faithful reproduction of photomask geometry.

5.3.1 Spin-coating of photoresists

The first step in the photolithography process is the spin coating of the photoresist on silicon wafer. Spin-coating requires a liquid solution of preceramic photoresist deposited on a substrate to form a film thanks to the centrifuge force. After drying step of the preceramic photoresist synthesis (see section 2.4.2 of Chapter II) the obtained products consist in a viscous liquid or a solid polymer depending on the quantity of boron added and/or photosensitive groups. Two strategies were then considered:

- Strategy A: Dissolve the solid photoresist in a solvent to get a solution compatible with spin-coating
- Strategy B: Stop the drying step of the synthesis at an earlier stage to avoid the crosslinking of the polymer

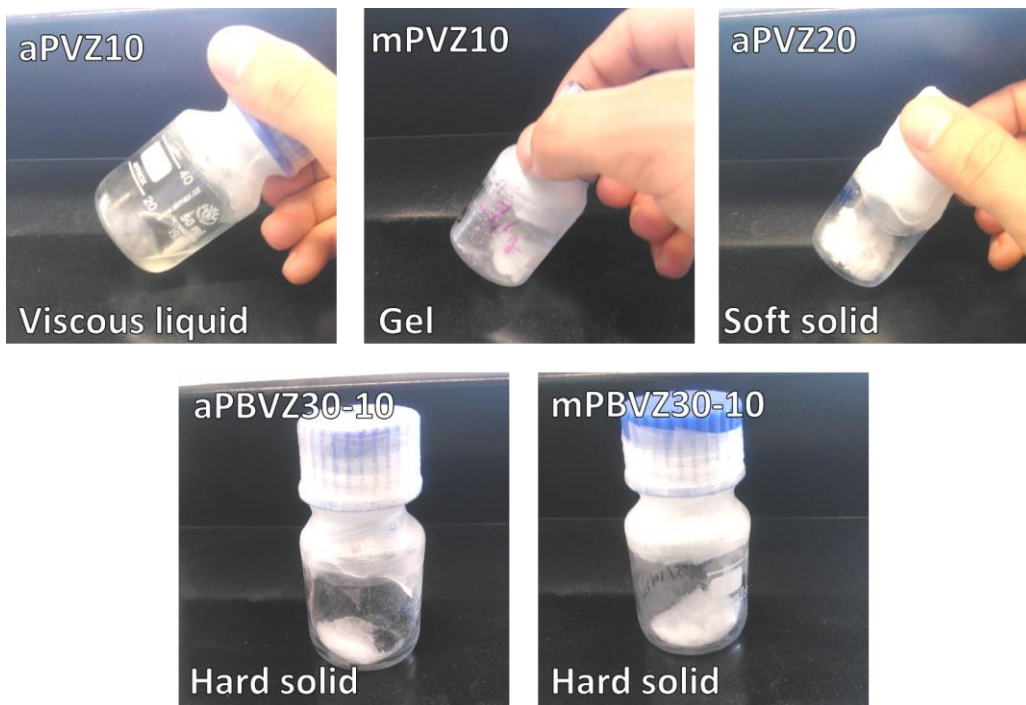


Figure 5-16: Pictures of synthesized preceramic photoresists after a complete drying

Figure 5-16 presents pictures of the synthesized preceramic photoresists after a complete drying. For aPVZ10 and mPVZ10, the obtained products are a viscous liquid and a gelled solid, respectively. The increase of the acrylate or methacrylate contents in preceramic polymers leads to a greater solidification of the product. Considering, aPBVZ30-10, mPBVZ30-10, aPBVZ17-10 and mPBVZ17-10 the polymer consists in a hard white solid.

To prepare a solution compatible with spin-coating, the solid polymers were dissolved in toluene or THF (strategy A). Nevertheless, due to their high rate of crosslinking, the dissolution is very difficult or even impossible in most of the cases. Figure 5-17 presents microscopy observation of spin coated films of dissolved photoresists in THF (25 wt.% concentration; see section 2.4.2 of chapter II for spin-coating method). The dissolution problems are visible on the resulting film with numerous distinguishable micro-pieces of undissolved resist. Films of such poor quality are not compatible with an efficient photolithography process. The undissolved resist is a source of defect in the envisaged final microstructure. Strategy A mentioned above was thus abandoned.

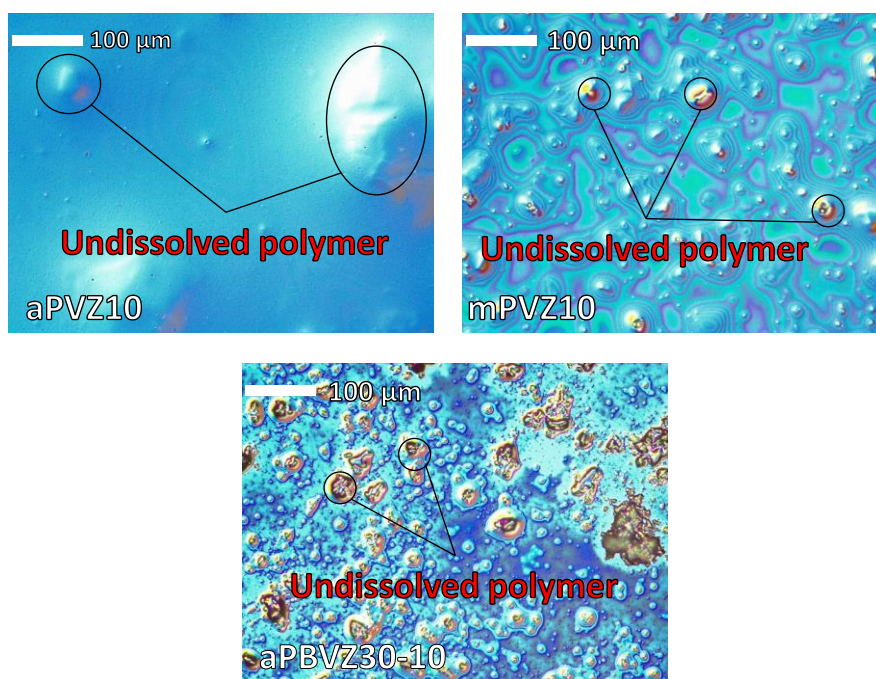


Figure 5-17: Spin coated film of 25wt% a) aPVZ10 b) mPVZ10 and c) aPBVZ30-10 solution dissolved in THF; undissolved parts of the solid preceramic polymer are distinguishable; spin coating cycle 1000rpm-30s and 2000rpm-10s

In the rest of this study, the presented results are obtained thanks to strategy B mentioned above. The drying step during the photoresist synthesis has not been integrally completed to avoid the crosslinking of the polymer. The photoresist solution resulting of such a synthesis method consists in a photosensitive polymer dissolved in toluene with a concentration of approximately 50 mg/ml.

5.3.2 UV exposure and development

The photolithography process consists in selectively exposing photoresist film to UV light. The exposed pattern is determined thanks to a photolithographic mask, a microscopy observation of the photomask employed for this study is given in Chapter 2.4.2. As a reminder, the employed UV mask contains 4 different patterns named as follow:

- Pattern **A**: small dots with a radius $R_s \approx 20\mu\text{m}$
- Pattern **B**: big dots with radius $R_b \approx 100\mu\text{m}$
- Pattern **C**: big channels with width $W_b \approx 1\text{mm}$
- Pattern **D**: small channels-dots with width $W_c \approx 50\mu\text{m}$ and $R_c \approx 200\mu\text{m}$

Development stage following the UV exposure consists in dissolving the unexposed photoresist to “reveal the printed” micro-pattern. The selection of the adequate developer and time of development was carried out thanks to several tests. THF, acetone, toluene and ethanol were considered as potential solvents developer. Figure 5-18 presents microscopy observation of micropatterns developed with different solvents and duration.

In Figure 5-18.a, the micropatterns were developed using toluene. After 30s of development, some of the unexposed photoresist was not integrally removed. Moreover, the resolution of the patterns seems very poor. Shards defects are visible at the edge of the exposed resin. After 120s, a part of the UV-exposed film begins to dissolve and dissociate from the substrate, it is a sign of poor development. After 300s, polymer is integrally dissolved and all the micropatterns dissociate from the silicon wafer.

Figure 5-18.b and c correspond to development with THF and acetone, respectively. It seems clear that regardless of the time of development these solvents are not able to dissolve the unexposed resist. Furthermore, development with THF causes the apparition of

small defects either on exposed and unexposed polymers. In the case of acetone development, no defects are observable but it seems to have no dissolving power.

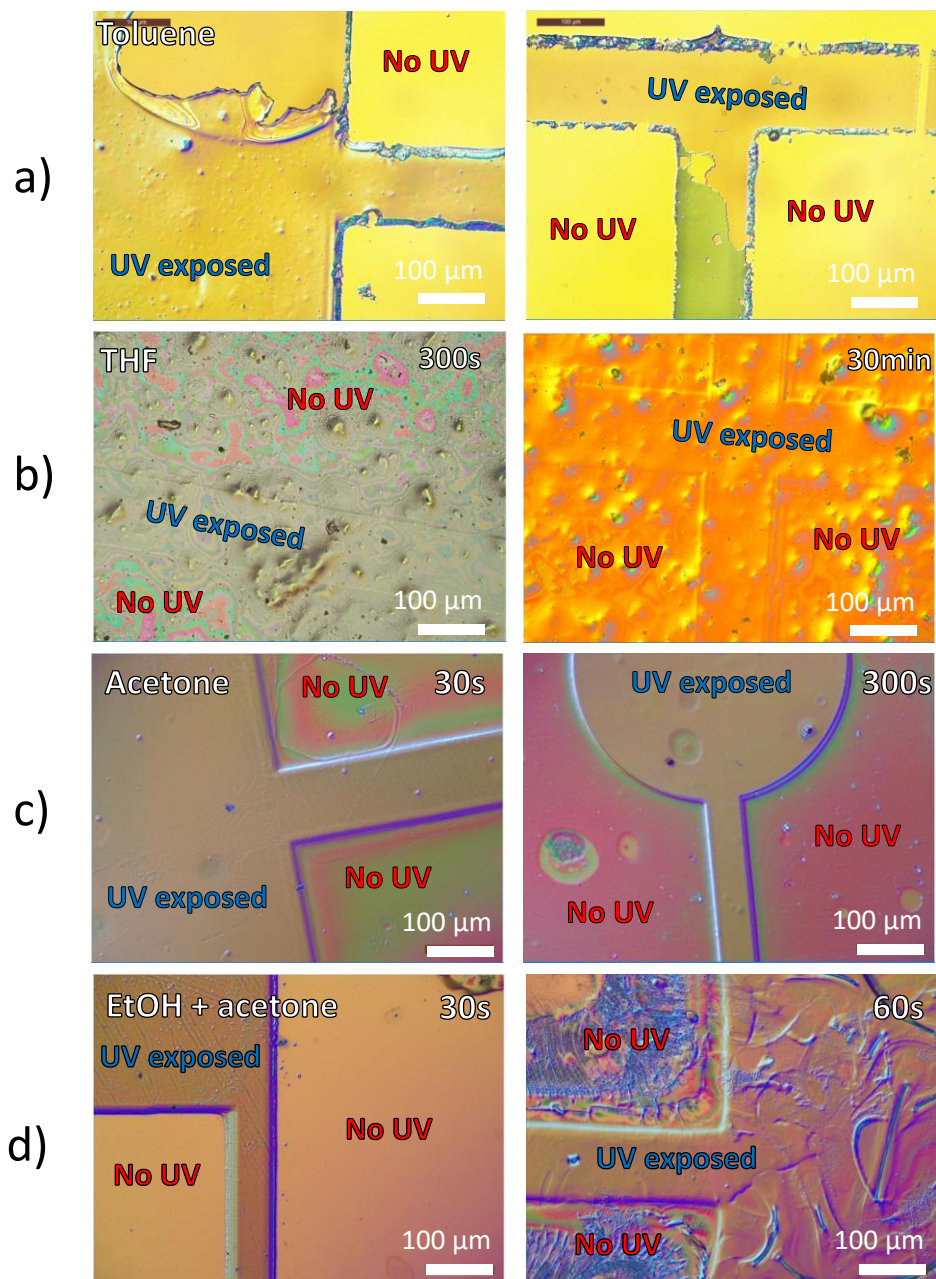


Figure 5-18: Microscopy observation of aPBVZ30-10 micropattern after development with a) Acetone and b) Ethanol then acetone (UV exposure 90s; 3wt% of PI369)

Finally, in Figure 5-18.d., the development of micropatterns with ethanol for 30s seems clean and efficient. All the exposed resist is removed and the UV-exposed resist is preserved

from defects. On the other hand, for higher time of development, the exposed resist start to dissolve and is deformed by the action of the developer.

Thanks to these investigations on the development of preceramic photoresist, we were able to choose ethanol as an efficient developer unlike toluene, THF and acetone. The development duration for ethanol was fixed at 30s. This method of development was employed for all the samples discussed in the next parts.

5.3.2.1 UV Dose estimation

The crosslinking of polymers *via* UV irradiation takes place under several conditions. The activation of the photoinitiator and the conversion of (metha)crylate monomers are possible if energy of irradiation exceeds a certain critical threshold E_c [12][13]. Furthermore, the quantity of irradiating energy must be optimized since it can affect the reproduced patterns dimension. The dose-to-size energy value (E_s) corresponds to the adequate amount of energy exposure required for a proper reproduction of the resist feature dimensions. To evaluate E_s and E_c associated with the preceramic photoresists synthesized in this study, several UV dose estimation tests were carried out. Those tests consist in exposing the spin-coated photoresist film with UV for different duration. After development, the obtained developed micropatterns were observed with high resolution numerical microscopy, Figure 5-19, Figure 5-20, Figure 5-21 and Figure 5-22 show those optical micrographs. Four areas are visible on the presented micropatterns, they are associated with UV exposition of 10, 30, 60 and 90s with a 365nm UV lamp. The intensity delivered by the UV lamp is 20 mW/cm², the density of energy irradiating the 4 areas is 200, 600, 1200 and 1800 mJ/cm², respectively. The influence of the irradiating density of energy on the dimensions of the photoresist micropatterns was evaluated to estimate the UV-dose providing the best resolution. The measured dimensions of the pattern are described on the microscopic observations in 2.4.2. Patterns A, B, C and D are associated in small dots with radius R_s , big dots with radius R_b , Big channels with W_b width and small channels with radius R_c and width W_c .

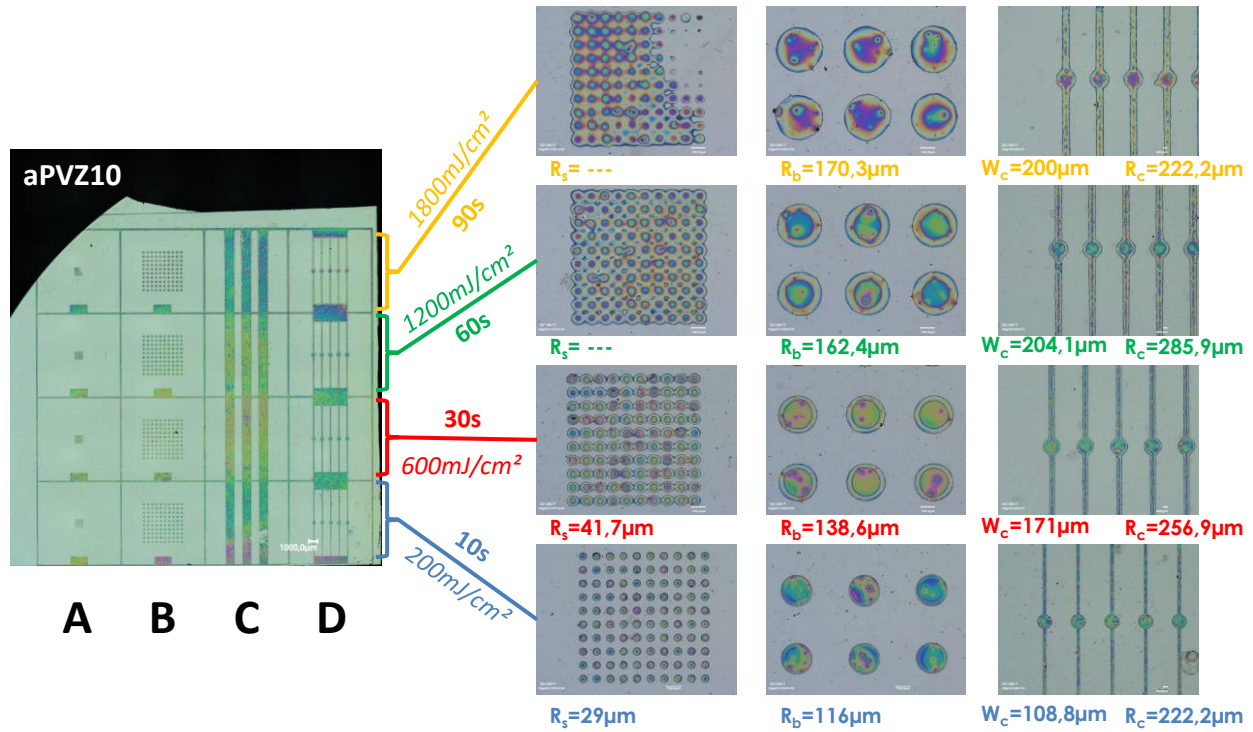


Figure 5-19: Test of UV dose for aPVZ10 photoresist ; before pyrolysis

In Figure 5-19, optical micrographs of the UV-dose sample prepared with aPVZ10 resist are presented. The negative mask pattern is reproduced on the wafer, regardless of the density of energy meaning that E_c associated with aPVZ10 is below $200\text{mJ}/\text{cm}^2$. Globally, the dots and channels dimensions are increasing with the quantity of energy irradiating the photoresist, suggesting a surpolymerization phenomenon due to high reactivity of acrylate groups. The surpolymerization conducts to a decrease of the pattern fidelity, the most faithful reproduction of the mask pattern is thus obtain for a 10s irradiation in the case of aPVZ10 photoresist, it suggest that E_s value is close to $200\text{mJ}/\text{cm}^2$.

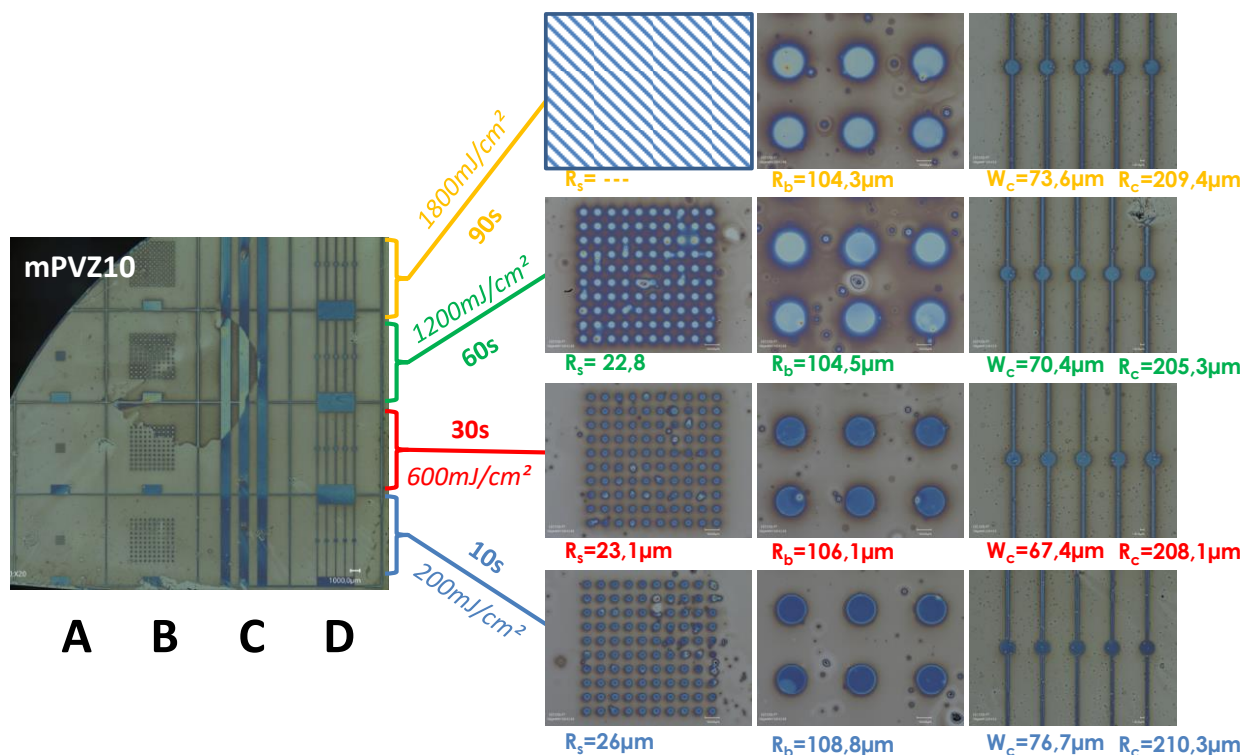


Figure 5-20: Test of UV dose for mPVZ10 photoresist ; before pyrolysis

Similarly to aPVZ10, the UV dose tests on mPVZ10 photoresist (Figure 5-20) show a reproduction of the mask pattern regardless of the irradiating density of energy. E_s associated to mPVZ10 resist is also below 200mJ/cm². The objects dimensions are increasing with the exposition time suggesting the same surpolymerization phenomenon. Nevertheless, the surpolymerization is less intense in the case of mPVZ10 than in aPVZ10 case. For example, the surpolymerization on pattern B for an exposition of 60s can be evaluated at 25,6μm for mPVZ10 against 62,4μm for aPVZ10. This can be explained by the higher reactivity of acrylate groups towards UV crosslinking in comparison to methacrylate. The control of the dimensions and resolution is thus easier in the case of mPVZ10 resist than in aPVZ10 case. E_s value seems once again close to 200mJ/cm².

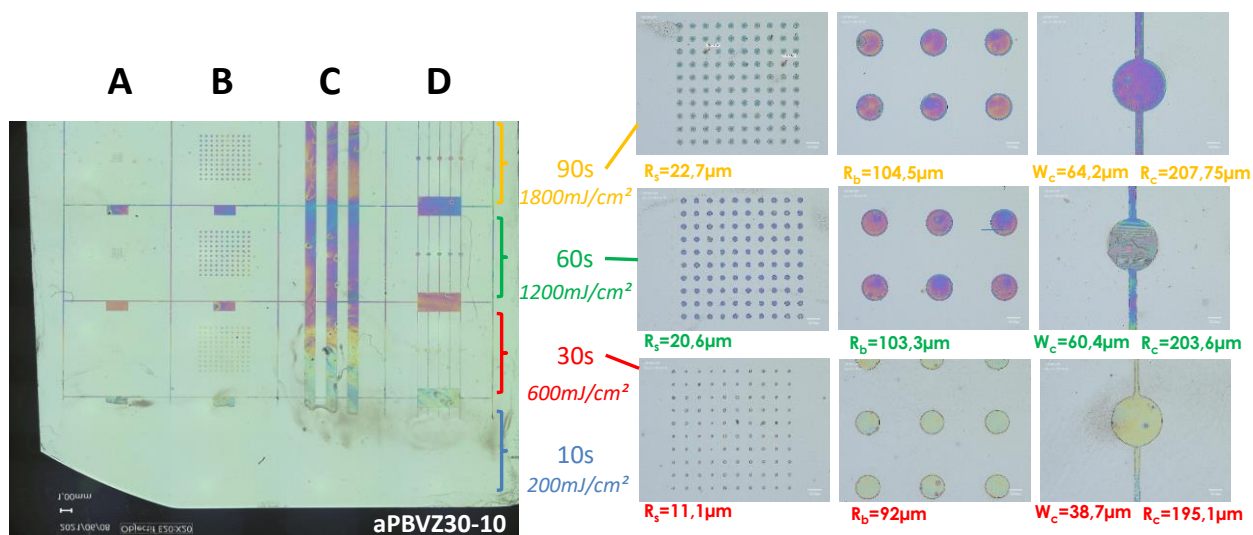


Figure 5-21: Test of UV dose for aPBVZ30-10 photoresist ; before pyrolysis

The UV dose sample presented in Figure 5-21 is associated with aPBVZ30-10 photoresist. For an exposition of 10s (200 mJ/cm²) the exposed polymer does not resist to the development, no microstructure is visible on this area. For 30 and 60s (600 and 1200 mJ/cm²) exposition, some micropatterns are visible but the reproduction of the mask pattern is not satisfying. E_s seems then placed between 200 and 600 mJ/cm². For 30s exposition, the small dots (pattern A), big dots (pattern B) and the small channels (pattern D) are smaller than expected (radius and channel shift between 5 and 9 μ m). The reproduction of the mask pattern is of better quality for 60s but the channels of column D seem damaged by the development step. Finally, the most faithful reproduction of the mask shape is obtained for an irradiating density of energy of 1800 mJ/cm² with non-damaged patterns and surpolymerization below 8 μ m. In summary, aPBVZ30-10 photoresist seems ideally crosslinked by an irradiating density of energy between 1200 and 1800 mJ/cm². On the contrary of non-boron containing photoresists (mPVZ0 and aPVZ10) the E_s associated with aPBVZ30-10 is between 1200 and 1800 mJ/cm² suggesting a lower reactivity of the resist towards UV crosslinking. This is relevant with the NMR analysis detailed in 5.2.1.2 showing that the grafting of photosensitive groups is more difficult in the case of boron presence in the polymer. The lower content of (meth)acrylate groups leads to a lower photosensitivity of the boron containing photoresists.

This analysis is confirmed by the UV-dose test associated with mPBVZ30-10 polymer in Figure 5-22. In the global view, the defects due to a too low density of irradiating energy are visible, the mask pattern being unfaithfully reproduced for exposition times of 10, 30 and 60s. For all energy dose tested the small dots in column **A** are not reproduced with the mPBVZ30-10 photoresists. Moreover, the observations on the micropatterns in column **B** show degraded dots for exposition of 30 and 60s. The most faithful reproduction is associated with an exposition time of 90s even then the **A** column microstructure are not reproduced. As for aPBVZ30-10, E_s dose to size value seems close to 1800 mJ/cm².

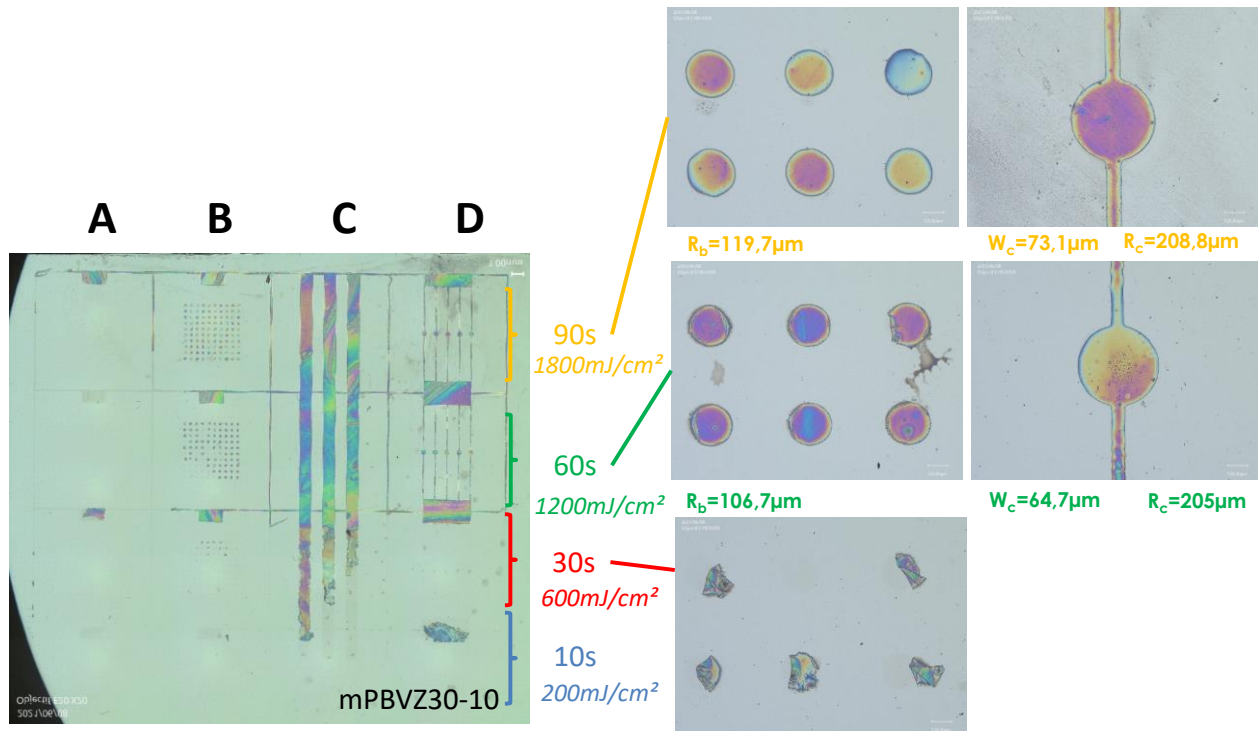


Figure 5-22: Test of UV dose for mPBVZ30-10 photoresist ; before pyrolysis

In summary, the observations and discussions carried out from Figure 5-19 to Figure 5-22 conducts to two main conclusions:

- The methacrylate groups seem to have lower reactivity towards UV-radical crosslinking than acrylate as it is mentioned in the literature [12][13][14][15][16].

- The introduction of boron in the initial polymer decreases the availability of N-H groups. IEM or IEA additives are less likely to graft on the polymer, which leads to lower reactivity towards UV light of the aPBVZ30-10 and mPBVZ30-10 photoresists.

Those two observations are illustrated thanks to the graphic in Figure 5-23 showing the dimensional shift of R_c , W_c , R_b and R_s values compared to the UV-mask dimensions and against the irradiating density of energy. On this graphic, the surpolymerization phenomenon is clearly visible in the case of aPVZ10 and mPVZ10 resists. On the other hand, this phenomenon is clearly less intense for the boron containing photoresists aPBVZ30-10 and mPBVZ30-10.

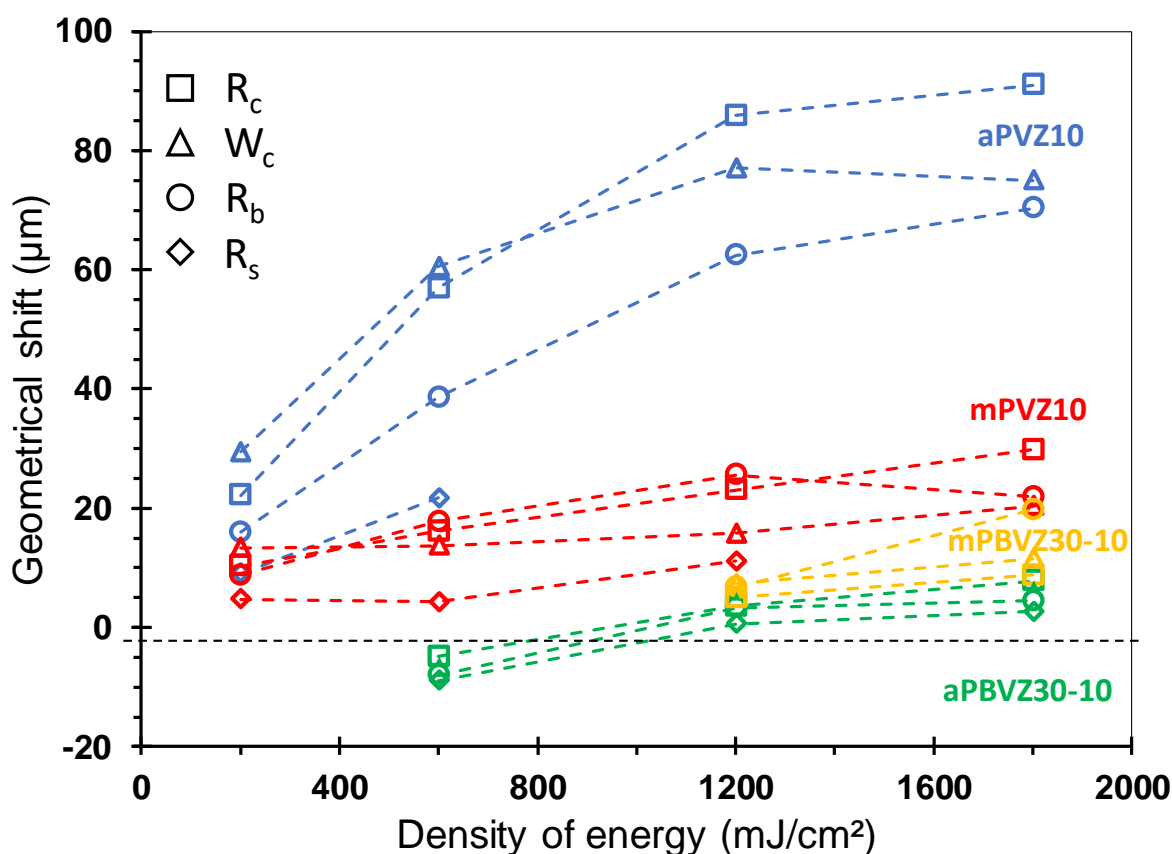


Figure 5-23: Geometrical shift on R_c , W_c , R_b and R_s the UV cross-linked photoresist against the irradiating density of energy ; before pyrolysis

In case of boron containing photoresists an irradiation of 90s (1800 mJ/cm²) is necessary to obtain faithful reproduction of the photolithographic mask negative pattern.

Furthermore, the free from boron photoresists are cross-linked with the proper dimensions for fewer energy density ($\sim 200 \text{ mJ/cm}^2$).

In addition to the microscopic observation, profilometry analysis was carried out to investigate the influence of exposition time on micropattern shape. These results are developed in the next part.

5.3.2.2 Profilometry investigations

Thanks to the microscopy observations discussed in the previous part, surpolymerization phenomenon was highlighted and an evaluation of E_s was revealed for each photoresist. To complete those observations, the exposition time influence on micropattern topography was evaluated by profilometry (see Figure 5-24). Globally, the profilometric representation of the samples confirmed the observations made in the previous part: the micropattern width increases with the exposition time and their values measured *via* profilometry are in the same order of magnitude than for microscopic observations.

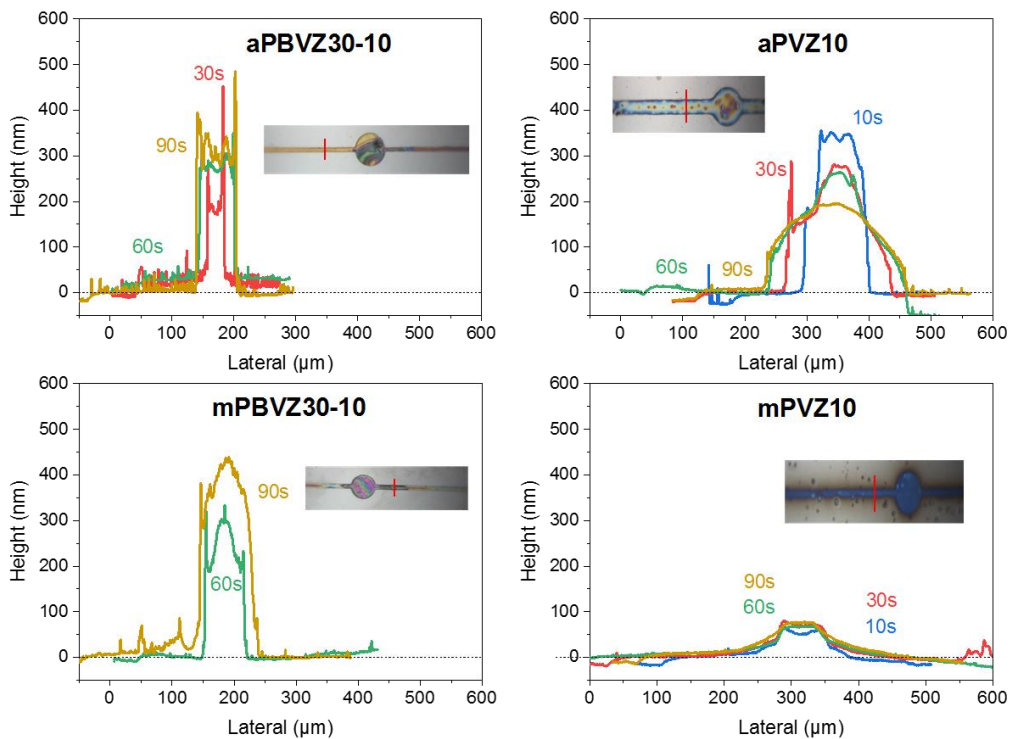


Figure 5-24: Profiles of aPBVZ30-10, mPBVZ30-10, aPVZ10 and mPVZ10 micropatterns after UV exposition of 10, 30, 60 or 90s ; before pyrolysis

The measured reliefs presented in Figure 5-24 confirm the presence of micropatterned photoresists on the silicon wafer. By comparing the micropatterns profiles obtained, it is clear that the exposition time greatly influences the shape and the measured height. Concerning, aPBVZ30-10 and mPBVZ30-10 profiles their “wall shape” with vertical edges is quite similar and their height and width increases with exposition time. On the contrary, for aPVZ10 photoresists as the channel width is increasing its height is decreasing with irradiation density of energy. Moreover, the aPVZ10 shape observed for higher exposition shape changes from “wall” to “dome” shape. This shape and height evolution is explainable by two causes:

- The width increase was previously attributed to surpolymerization (see previous section).
- The height decrease could be associated to the shrinkage occurring during the photo-crosslinking of the resist.

The combination of the two phenomenon described above conducts to the “dome” shape observed *via* profilometry. Finally, for mPVZ10 micropatterns the shape does not seem to be affected by the evolution of exposition time. This result is probably more related to the significantly lower height measured in the case of mPVZ10 in comparison with other samples. This low height of mPVZ10 is linked with the low concentration of photoresists in the spin-coating solution used for their preparation (see section 5.3.1.).

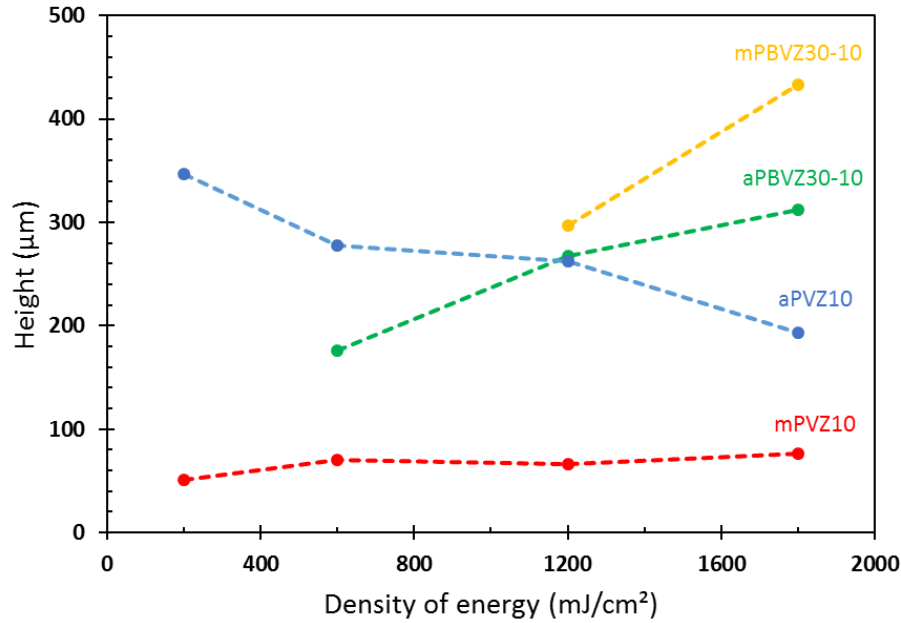


Figure 5-25: Height of aPBVZ30-10, mPBVZ30-10, aPVZ10 and mPVZ10 micropatterns samples against the irradiating density of energy; before pyrolysis

In summary, Figure 5-25 gathers the evolution of aPBVZ30-10, mPBVZ30-10, aPVZ10 and mPVZ10 height micropatterns against density of energy. Increasing of height with density of energy is clearly observable for aPBVZ30-10 and mPBVZ30-10 as for its decreasing in aPVZ10 case.

According to the investigations developed in section 5.3.2.1, the optimal amount of energy exposure for aPVZ and mPVZ10 was fixed at 200 mJ/cm² and at 1800 mJ/cm² for mPBVZ30-10 and aPBVZ30-10 in the next parts. Those density of energy were selected because they are the most efficient to give a faithful reproduction of the initial UV mask geometry. The next section develops the observations of micro-patterns obtained after ceramic conversion of the photolithographed preceramic photoresist. The geometrical and profilometry characterization are discussed through SEM, profilometry and high-resolution numerical microscopy. Nanoindentation characterization was finally performed.

5.3.3 Polymer-to-ceramic conversion

The ceramization of the photolithographed photoresist was carried out by pyrolysis under nitrogen atmosphere at 1000°C. Such a thermal treatment causes shrinkage and defects formation which are discussed in this part.

5.3.3.1 SEM observations - shrinkage estimation

The Figure 5-26 gather SEM pictures of SiCN micropatterns derived from aPVZ10 and mPVZ10 photoresists. According to these observation no cracks, microcracks, pore formation or important deformation are noticed. The ceramic conversion seems to occur without conducting to critical defect formation. An evaluation of the lateral shrinkage occurring during ceramization is carried out by comparing the width of channel and radius of dots before and after pyrolysis. A lateral shrinkage of 4,2 % and 4,7 % was measured for aPVZ10 and mPVZ10 derived SiCN micropattern (based on the measurement of radius R_c before and after pyrolysis). Nevertheless, the evaluation of lateral shrinkage is more difficult for the mPVZ10 micro-pattern because of the poorer edges definition than for aPVZ10.

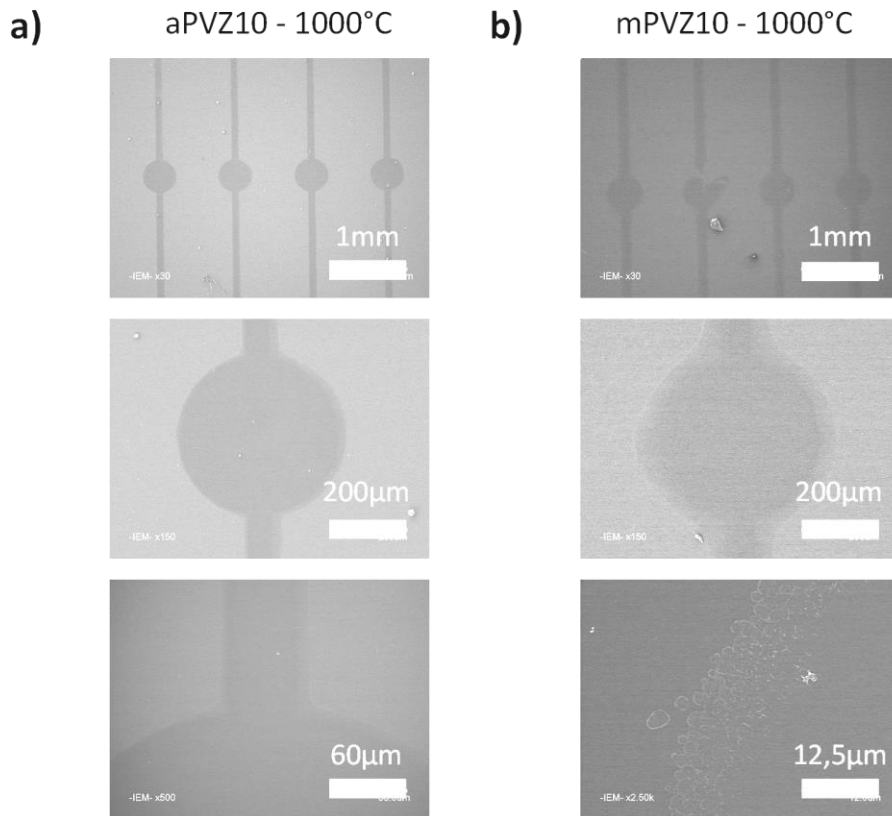


Figure 5-26: SEM pictures of SiCN photolithographed and pyrolysed pattern derived from a) aPVZ10 and b) mPVZ10

In the Figure 5-27, SEM pictures of SiBCN photolithographed patterns derived from aPBVZ and mPBVZ are presented. As for SiCN (see Figure 5-26), the SiBCN micropatterns are free

from massive defects such as cracks, deformation or pores formations. At first sight, the behavior of the pre-SiCN photoresists during ceramization process seems similar to pre-SiCN photoresists. By comparing patterns dimensions before and after thermal treatment, the lateral shrinkage of aPBVZ30-10 and mPBVZ30-10 photolithography was estimated at 3,6 and 3,9 %, respectively. A slightly lower value than for aPVZ10 and mPVZ10, it is consistent with the higher ceramic yield measured for boron based resists (see TGA curves in Figure 5-12 and Figure 5-13 in part 5.2.2.1).

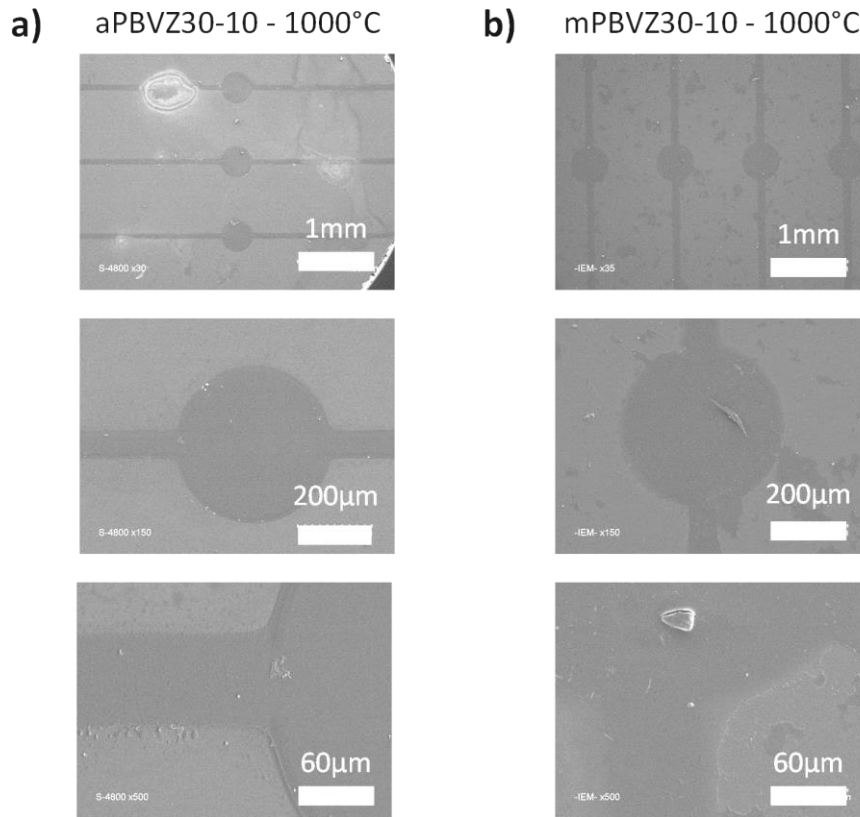


Figure 5-27: SEM pictures of SiBCN photolithographed and pyrolysed pattern derived from a) aPBVZ30-10 and b) mPBVZ30-10

Either for pre-SiCN and pre-SiBCN photoresist the photolithography and ceramization of reproduced micropattern was successful. No critical defects were observed on ceramic pattern even if resolution problems were noticed, especially for methacrylate-based photoresists. This phenomenon could be explained by the lower reactivity of methacrylate against acrylate, conducting to less intense adhesion of the resist on the substrate. This low

adhesion force can caused delamination of the polymer from the substrate especially in the areas where the crosslinking rate is the lowest, namely at the edges of the pattern.

This microscopy study allows the estimation of lateral shrinkage and the detection of eventual defects. Nevertheless, radial deformations are not appreciable with SEM observations. The evaluation of radial shrinkage and roughness was carried out by profilometry and AFM characterization and will be is discussed in next part.

5.3.3.2 Profilometry characterization

The profilometric shape of micro-pattern before and after ceramization is discussed in Figure 5-28 to evaluate the radial shrinkage and deformation occurring during the thermal treatment. Usually, in the case of channel shaped microstructure, the shrinkage occurring during drying or after thermal treatment leads to double peaks profile [9]. This shape is observable on the profiles presented in Figure 5-28, especially for aPBVZ30-10, mPBVZ30-10 and mPVZ10.

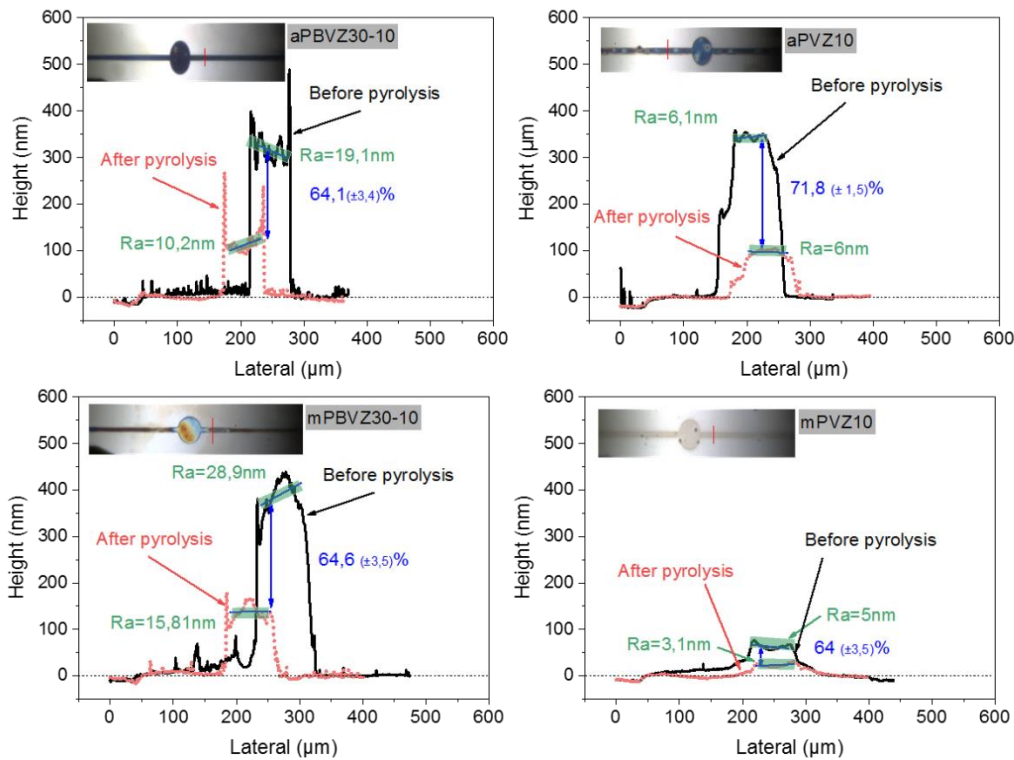


Figure 5-28: Profilometry analysis of pyrolysed micro-patterns derived from pre-SiCN and pre-SiBCN photoresists

First, it seems clear that the lateral shrinkage occurring during the thermal treatment is very low regardless of the concerned photoresist. On the other hand, radial shrinkage is very important. It is convenient with the Griffith criterion discussed in chapter IV (part 4.3.1.) and in the literature [10], due to the small thickness of micropatterns, the shrinkage direction is almost fully radial. A detailed report of radial and lateral shrinkage associated with each photoresists is gathered in Table 5-2. Due to roughness, and double peak shape the dimensions measure are not easily reproducible, this is why strong standard deviation are reported on the Table 5-2 dataset.

Table 5-2: Lateral and shrinkage of micropattern during thermal treatment; measured on microchannels with W_c width and height H ; W_c measured on the middle of the profile

Sample	Before pyrolysis		After pyrolysis		Shrinkage	
	Height H (nm)	Width W_c (μ m)	Height H (nm)	Width W_c (μ m)	Radial (%)	Lateral (%)
<i>aPVZ10</i>	344,1 ($\pm 5,6$)	97,1	97,1 ($\pm 4,0$)	93,5	71,8 ($\pm 1,5$)	2,5
<i>mPVZ10</i>	63,1 ($\pm 8,4$)	77,3	22,7 ($\pm 3,6$)	75,1	64,0 ($\pm 10,5$)	2,8
<i>aPBVZ30-10</i>	314,1 ($\pm 25,3$)	64,1	112,76($\pm 22,8$)	62,7	64,1 ($\pm 10,6$)	3,2
<i>mPBVZ30-10</i>	390,2 ($\pm 50,7$)	83,5	138,0 ($\pm 2,5$)	77,1	64,6 ($\pm 3,5$)	7,7

The small micropattern thickness ($<1\mu\text{m}$) preserves the micropatterns from microcracks and peeling off from the wafer. According to literature [9][17][18][19][20], a ceramic coating prepared from PDCs process is prone to cracks for a thickness above $2\mu\text{m}$. Such “coating behavior” represents a limit for the photolithographic PDCs process, indeed preparing a micropattern with high thickness is a technical challenge.

5.3.3.3 Mechanical properties - nanoindentation

We evaluate the mechanical properties of the micro-patterns observed in the previous section thanks to nano-indentation (see section 2.4.4 for method). It was important to demonstrate that SiCN and SiBCN patterns derived from photoresists pyrolysis exhibit Young modulus values consistent with PDCs materials. Figure 5-29 explicits the

measurements condition on aPVZ10 sample after pyrolysis at 1000°C. Irregularity phenomenon is observable on the sample and illustrates the inhomogeneity of the coating thickness, therefore indentation was performed on distinct areas. Film stiffness was evaluated between 55 and 65 GPa, it is similar to the Young modulus value reported for analogous studies [1][2]. The load-displacement curve associated with one of the nanoindented area is displayed on the Figure 5-29, it confirms the brittle behavior of the PDC material.

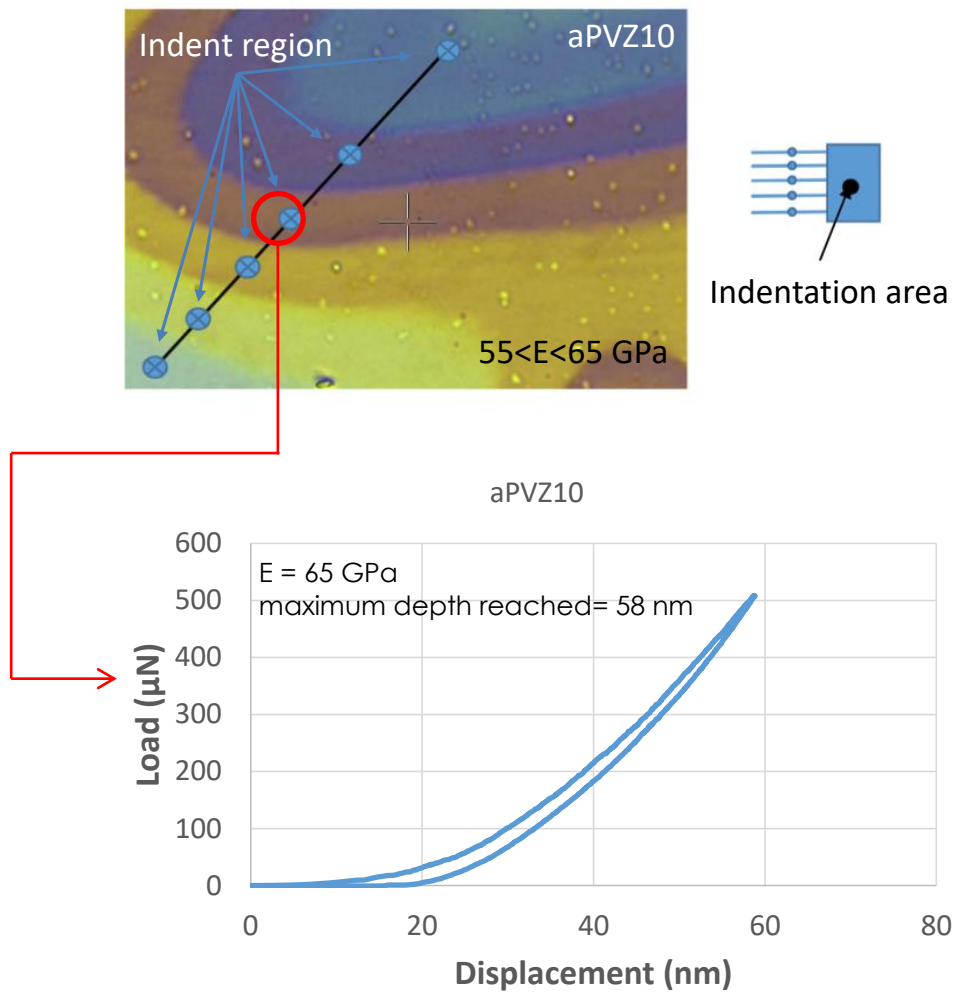


Figure 5-29: Nano-indentation test on aPVZ10 sample after pyrolysis

Comparative study was performed on aPBVZ30-10 micropattern. A greater thickness homogeneity was noticed for this sample which allowed a more precise measurement. According to this result (Figure 5-30), the introduction of boron in the Si-C-N matrix seems

to decrease the mechanical properties of the film with a Young modulus of ~ 39 GPa. This is relevant with literature as suggested in Colombo's review [21].

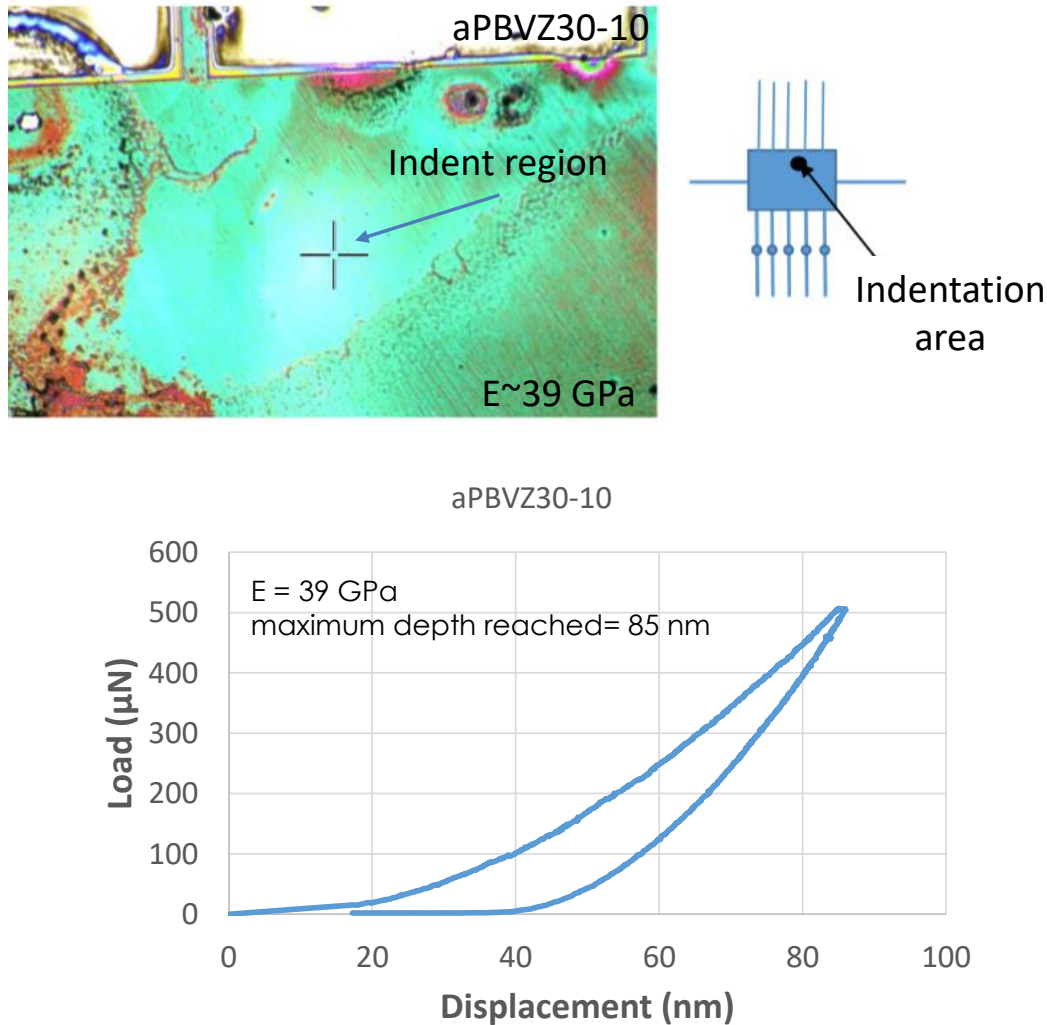


Figure 5-30: Nano-indentation test on aPBVZ30-10 sample after pyrolysis

With this final examination of mechanical properties, we believe that we proved the feasibility of a photolithographic process for the preparation of SiBCN and SiCN patterns. Furthermore, the procedure described in this chapter seems compatible for achieving micro-objects with strength close to bulk PDCs.

5.4 Chapter conclusions

The description of the synthesis of preceramic photoresists based on organosilicon preceramic polymers grafted with photosensitive groups has been discussed in this chapter. For the first time, pre-SiBCN photoresists were designed and employed in a photolithographic process to prepare SiBCN micro-patterns. The grafting of (meth)acrylate on pre-SiCN and pre-SiBCN polymers and their photosensitivity and preceramic polymer properties were proved thanks to FTIR, NMR, TGA and UV-vis spectroscopy, respectively. Moreover, the introduction of boron and (meth)acrylate in polyvinylsilazane conduct to an increasing of ceramic yield reaching 13,4% when comparing PVZ and aPBVZ30-10 systems. Nevertheless, it has been shown that the grafting of (meth)acrylate groups on a boron-modified polyvinylsilazane is more difficult than in the case of boron free polymer. It conducts thus to a lower rate of photosensitive groups in the boron free resist, it tends to increase the critical density of energy E_s required to initiate polymerization and thus UV curing for boron containing polymers : $1200 < E_s < 1800 \text{ mJ/cm}^2$ for aPBVZ30-10 and mPBVZ30-10 photoresists against $E_s < 200 \text{ mJ/cm}^2$ for aPVZ10 and mPVZ10. Because of their higher reactivity towards UV light the resolution of micropatterns prepared from aPVZ10 and mPVZ10 was poorly controlled on the contrary of aPBVZ30-10 and mPBVZ30-10 samples with surpolymerization kept below 8 and 15 μm , respectively. The ceramization treatment operated on such micropatterned photoresists conducts to ceramic micropatterns free from cracks, micro-cracks and major deformation. Ceramization of the photoresists has been proven thanks to the observed lateral and radial shrinkage occurring during the thermal treatment (between 3 % and 7 % for lateral shrinkage, 64 % and 72 % for radial shrinkage) but also the increasing of Young modulus (or Hardness) reaching $\sim 60 \text{ GPa}$ for aPVZ10 sample.

Of course, numerous unresolved problems and ways of improvement have been noted during the progress of this study.

The efficiency of IEM and IEA species in the synthesis of preceramic photoresists has been demonstrated in this chapter. Nevertheless, those species present several disadvantages as their high toxicity and air sensitivity that could interfere with a potential industrialization

of the process. Eventual alternatives have been investigated and several leads are described below:

- 2-Aminoethyl methacrylate hydrochloride
- Methyl 2-(bromomethyl)acrylate
- Methyl 2-(chloromethyl)acrylate
- 2-Chloroethyl acrylate

Surpolymerization phenomenon was noticed on the samples discussed in this chapter. This phenomenon can conduct to a deterioration of resolution and faithful reproduction of micropatterns shape. The surpolymerization consists in the resist crosslinking beyond the UV irradiated area. It is caused by either the propagation of free radical species and/or the diffusion of light in the polymer film. One solution could be the introduction of free radical scavengers (ex: quinone) and/or UV-light absorber (ex: Sudan orange) in the preceramic photoresist solution. Nevertheless, the introduction of too many additives in a solution can lead to a complexification of the reactional mechanism.

5.5 Bibliography

- [1] T. Anh Pham, P. Kim, M. Kwak, K. Y Suh, et D. Kim, « Inorganic Polymer Photoresist for Direct Ceramic Patterning by Photolithography », Chemical communications (Cambridge, England), vol. 39, p. 4021-3, nov. 2007, doi: [10.1039/b708480c](https://doi.org/10.1039/b708480c).
- [2] T. A. Pham, D.-P. Kim, T.-W. Lim, S.-H. Park, D.-Y. Yang, et K.-S. Lee, « Three-Dimensional SiCN Ceramic Microstructures via Nano-Stereolithography of Inorganic Polymer Photoresists », Advanced Functional Materials, vol. 16, no 9, p. 1235-1241, juin 2006, doi: [10.1002/adfm.200600009](https://doi.org/10.1002/adfm.200600009).
- [3] J. Kong, X. Fan, G. Zhang, X. Xie, Q. Si, et S. Wang, « Synthesis and UV-curing behaviors of novel rapid UV-curable polyorganosilazanes », Polymer, vol. 47, no 5, p. 1519-1525, févr. 2006, doi: [10.1016/j.polymer.2006.01.007](https://doi.org/10.1016/j.polymer.2006.01.007).
- [4] Y.-H. Li, X.-D. Li, et D.-P. Kim, « Acrylation of polyvinylsilazane with allyl bromide for an UV photosensitive inorganic polymer », Journal of Organometallic Chemistry, vol. 692, no 23, p. 5303-5306, nov. 2007, doi: [10.1016/j.jorganchem.2007.08.016](https://doi.org/10.1016/j.jorganchem.2007.08.016).

- [5] Y.-H. Li, X.-D. Li, et D.-P. Kim, « Chemical development of preceramic polyvinylsilazane photoresist for ceramic patterning », *J Electroceram*, vol. 23, no 2, p. 133, sept. 2007, doi: [10.1007/s10832-007-9331-z](https://doi.org/10.1007/s10832-007-9331-z).
- [6] A. Viard et al., « Molecular Chemistry and Engineering of Boron-Modified Polyorganosilazanes as New Processable and Functional SiBCN Precursors », *Chemistry – A European Journal*, vol. 23, no 38, p. 9076-9090, 2017, doi: [10.1002/chem.201700623](https://doi.org/10.1002/chem.201700623).
- [7] K.-W. Gyak et al., « Magnetically Actuated SiCN-Based Ceramic Microrobot for Guided Cell Delivery », *Advanced Healthcare Materials*, vol. 8, no 21, p. 1900739, nov. 2019, doi: [10.1002/adhm.201900739](https://doi.org/10.1002/adhm.201900739).
- [8] K.-W. Gyak, N. K. Vishwakarma, Y.-H. Hwang, J. Kim, H. Yun, et D.-P. Kim, « 3D-printed monolithic SiCN ceramic microreactors from a photocurable preceramic resin for the high temperature ammonia cracking process », *Reaction Chemistry & Engineering*, vol. 4, no 8, p. 1393-1399, 2019, doi: [10.1039/C9RE00201D](https://doi.org/10.1039/C9RE00201D).
- [9] C. R. Martin et I. A. Aksay, « Topographical Evolution of Lead Zirconate Titanate (PZT) Thin Films Patterned by Micromolding in Capillaries », *J. Phys. Chem. B*, vol. 107, n° 18, p. 4261-4268, mai 2003, doi: [10.1021/jp034055+](https://doi.org/10.1021/jp034055+).
- [10] F. F. Lange, « Chemical Solution Routes to Single-Crystal Thin Films », *Science*, vol. 273, n° 5277, p. 903-909, août 1996, doi: [10.1126/science.273.5277.903](https://doi.org/10.1126/science.273.5277.903).
- [11] C. Thanh Nguyen, P. Huy Hoang, J. Perumal, et D.-P. Kim, « An inorganic-organic diblock copolymer photoresist for direct mesoporous SiCN ceramic patterns via photolithography », *Chemical Communications*, vol. 47, no 12, p. 3484-3486, 2011, doi: [10.1039/C0CC05836J](https://doi.org/10.1039/C0CC05836J).
- [12] J. Bennett, « Measuring UV Curing Parameters of Commercial Photopolymers used in Additive Manufacturing », *Addit Manuf*, vol. 18, p. 203-212, déc. 2017, doi: [10.1016/j.addma.2017.10.009](https://doi.org/10.1016/j.addma.2017.10.009).

- [13] C. Decker, « The use of UV irradiation in polymerization », *Polymer International*, vol. 45, no 2, p. 133-141, 1998, doi: [10.1002/\(SICI\)1097-0126\(199802\)45:2<133::AID-PI969>3.0.CO;2-F](https://doi.org/10.1002/(SICI)1097-0126(199802)45:2<133::AID-PI969>3.0.CO;2-F).
- [14] M. Kaur et A. K. Srivastava, « PHOTOPOLYMERIZATION: A REVIEW », *Journal of Macromolecular Science, Part C: Polymer Reviews*, vol. 42, n° 4, p. 481-512, janv. 2002, doi: [10.1081/MC-120015988](https://doi.org/10.1081/MC-120015988).
- [15] C. E. Hoyle, « Photocurable Coatings », in *Radiation Curing of Polymeric Materials*, vol. 417, 0 vol., American Chemical Society, 1990, p. 1-16. doi: [10.1021/bk-1990-0417.ch001](https://doi.org/10.1021/bk-1990-0417.ch001).
- [16] P. T. Weissman, « COMPARISON of PERFORMANCE of ACRYLATE and METHACRYLATE ALIPHATIC URETHANES », 2004. <https://www.semanticscholar.org/paper/COMPARISON-of-PERFORMANCE-of-ACRYLATE-and-ALIPHATIC-Weissman/23ee454dfd6745853adebc21b94a002e5747a5c4>
- [17] W. S. Beh, Y. Xia, et D. Qin, « Formation of patterned microstructures of polycrystalline ceramics from precursor polymers using micromolding in capillaries », *J. Mater. Res.*, vol. 14, no 10, p. 3995-4003, oct. 1999, doi: [10.1557/JMR.1999.0540](https://doi.org/10.1557/JMR.1999.0540).
- [18] P. Colombo, T. E. Paulson, et C. G. Pantano, « Synthesis of Silicon Carbide Thin Films with Polycarbosilane (PCS) », *Journal of the American Ceramic Society*, vol. 80, n° 9, p. 2333-2340, 1997, doi: [10.1111/j.1151-2916.1997.tb03124.x](https://doi.org/10.1111/j.1151-2916.1997.tb03124.x).
- [19] M. Günthner, T. Kraus, W. Krenkel, G. Motz, A. Dierdorf, et D. Decker, « Particle-Filled PHPS Silazane-Based Coatings on Steel », *International Journal of Applied Ceramic Technology*, vol. 6, n° 3, p. 373-380, 2009, doi: [10.1111/j.1744-7402.2008.02346.x](https://doi.org/10.1111/j.1744-7402.2008.02346.x).
- [20] O. Goerke, E. Feike, T. Heine, A. Trampert, H. Schubert, Ceramic coatings processed by spraying of siloxane precursors (polymer-spraying), *Journal of the European Ceramic Society*, Volume 24, Issue 7, 2004, Pages 2141-2147, ISSN 0955-2219, doi:[10.1016/S0955-2219\(03\)00362-5](https://doi.org/10.1016/S0955-2219(03)00362-5).

[21] P. Colombo, G. Mera, R. Riedel, et G. D. Sorarù, « Polymer-Derived Ceramics: 40 Years of Research and Innovation in Advanced Ceramics », *Journal of the American Ceramic Society*, vol. 93, no 7, p. 1805-1837, juill. 2010, doi: [10.1111/j.1551-2916.2010.03876.x](https://doi.org/10.1111/j.1551-2916.2010.03876.x).

General conclusion and perspectives

6 Conclusions and perspectives

6.1 Results summary

This PhD work is in line with the CNRS exploratory project “CeraMicroPac” that started in 2018. It consists in a contribution to the hydrogen energy vector development in micro-fabrication field. The main purpose associated with “CeraMicroPac” project is to demonstrate the feasibility of elaborating new materials at molecular scale for electrodes based on ceramics. The strategy to achieve this objective is built on combination of the PDCs route with lithography techniques. The thesis work presented in this manuscript addressed different research questions that ran through this exploratory project:

- How to develop an electrocatalyst for HER based on low-cost stable and efficient PDC materials with optimized microstructure?
- Which strategy to adopt in order to miniaturize a water electrolysis microdevice designed with PDCs-based electrodes?
- How to prepare Si(B)CN ceramic-based micropatterns *via* "soft-lithography" in a perspective of microelectrode development?
- How to combine the PDCs route and the photolithography process in order to shape Si(B)CN ceramic-based micro-objects?

These questions allowed us to set up research objectives that were used to draw up a guideline and to frame the research work carried out during these three years. The research objectives are presented below:

- Set a protocol for the preparation of PDC/rGO composites with an optimized microstructure for the electrocatalysis of water
- Tune a soft-lithography method for the fabrication of PDC-based micro-objects functionalized for HER reaction purpose
- Design preceramic photoresists and introduce them in a photolithography process for the manufacture of SiCN and SiBCN micropatterns

The first chapter is dedicated to a state-of-the-art review to introduce the diverse disciplines involved in this research study. In particular, we first detailed the history, the

principles and the advantages of the PDC materials. Discussions concerned non-oxide and silicon-based PDCs mainly employed in this PhD (SiCN and SiBCN). Then we analyzed the stakes associated with the hydrogen vector and in particular the questions concerning its production. Our review focused on the water-splitting method as a solution to generate a decarbonized or low carbon dihydrogen and we questioned how PDCs could play a role in this field. Finally, a description of the lithography process used in micro-fabrication was performed. Its benefits for water-splitting were exposed as the transition to a micrometric scale generates specific consequences (on ionic or fluidic resistance, fluid flux control and surface-to-volume ratio). The recent literature studies on combinations of PDCs route and soft-lithography or photolithography techniques have been discussed and are considered as a solid basis for this PhD.

In the second chapter, we report the characterization, synthesis and sample preparation methods for this work. We have set-up procedures to limit the oxidation of the precursors thanks to Schlenk glassware, vacuum/Ar lines, furnaces and glove box operating under inert atmosphere. The chemical investigations of the synthesized precursors were carried out thanks to FTIR, NMR, UV-vis spectroscopies and TGA. The microstructure of the ceramic materials and composites was explored *via* XRD, Raman, SEM, EDX and XPS techniques. Electrocatalytic performances of our materials were reported thanks to the standard three-electrodes set up combined with a potentiostat.

In the third chapter, our explorations on (O)-Si-(B)-C-(N)/rGO composites as stable and robust electrocatalyst for HER were reported. We demonstrate for the first time the intrinsic catalytic activity of PDC based material when its insulating nature is counteract by a combination with conductive rGO foam. The investigations on the microstructure composites has shown that the HER activity was favored by the amorphous nature of PDCs and the presence of O, N and B in Si-C matrix. Thanks to such optimization of O-SiBCN/rGO catalyst microstructure, we have shown its great stability with an activity loss of only 18% over an operating cycle of more than 170h. At the same time, a commercial Pt/C catalyst is subject to a loss of 1700% under the similar conditions.

General conclusion

In chapters four and five, our objective was to build different approaches to miniaturize PDC based electrodes in order to incorporate them in a water-splitting microdevice. Both soft-lithography and photolithography were envisaged to manufacture such microelectrodes.

The soft-lithography strategy was investigated in the fourth chapter and consisted in shaping SiCN and SiBCN precursors thanks to micro-patterned PDMS molds. Nevertheless, the conversion of the micro-patterned polymeric precursor has led to cracks formation because of the shrinkage inherent to PDCs. We used passive (Al_2O_3) and active (MoS_2 and MoS_2) fillers to reduce shrinkage and maintain the integrity of the imprinted profiles. More specifically, with active fillers, new phases tend to appear by reaction with the pyrolysis atmosphere or the precursor itself. Thanks to a detailed investigation of the microstructure, we report the formation of Mo_2C or $\text{Mo}_{4.8}\text{Si}_3\text{C}_{0.6}$ among other phases. We finally evaluate the impact of these new phases on the HER activity and report Tafel slope of 89mV/dec and onset over potential of 530mV@5 mA/cm² for SiCN/ MoS_2 composite.

In the fifth chapter, the direct patterning of SiCN and SiBCN microelectrodes was carried out by photolithography. To set up such procedure we had to develop preceramic photoresists by grafting acrylate or methacrylate units on polyvinylsilazane and boron-modified polysilazane backbones. The Si(B)CN micropatterns produced after photolithography and subsequent pyrolysis display good mechanical properties (Young's modulus ~ 60 GPa) and low roughness ($R_a < 20\text{nm}$). Concisely, chapters four and five illustrate the feasibility of lithographic methods for manufacturing crack-free non-oxide micro-patterns.

The work developed in these successive chapters raised several scientific questions that could not all be solved during these 3 years of thesis. These have been mentioned in the heart of this manuscript but we can propose a quick list in this conclusion:

- We report the formation of an unknown phase denoted $\text{Mo}_x\text{S}_y\text{C}_z$ in chapter four. It would be very interesting to continue the investigations through computational studies on the identification of this crystalline phase for a better understanding of the reactions between Si(B)CN precursors and MoS_2 fillers

- The precursor/filler suspensions employed for the preparation of PDC based micro-patterns could not be stabilized. Indeed, sedimentation phenomena could be noticed on those suspensions. A precise study of the stabilization of the suspensions (with selection of proper dispersant and deflocculant) must be carried out in order to obtain micro-shaped patterns with correct homogeneity, better reproducibility and higher filler loading.

6.2 Perspectives

Preliminary work has been carried out in order to imagine perspectives to pursue the objectives specified in the project. Our ultimate goal is to conceive an operational micro-electrolyser supplied with PDC based microelectrodes.

6.2.1 *In-situ* tests

The electrocatalytic measurements conducted on SiCN/MoSi₂/MoS₂ composites and presented in chapter 4 were not performed directly on the micro-patterns but on a powder specifically prepared for HER tests. An intermediate step between those powder tests and an operational micro-electrolyser would be to test HER activity directly on the micro-patterns. We propose a procedure depicted in Figure 6-1.a-c. describing the preparation of the micropattern for electrocatalytic measurements. An electrical contact made of a thin film of silver lacquer is deposited on the SiCN/MoSi₂/MoS₂ micropattern and is connected to the working electrode (*i.e.* SiCN/MoSi₂/MoS₂ micropattern). Thanks to an epoxy resin, the Ag contact is sealed to avoid short-circuiting. With an as prepared sample, electrocatalytic tests may be carried out with a probe station and micro-positionners connected to a potentiostat as depicted in Figure 6-1.d. H₂SO₄ 0,5M electrolyte solution is dropped on the micropattern surrounded by epoxy, working electrode contact is ensured thanks to Ag lacquer, a Pt counter electrode and an Ag pseudo-reference electrode are immersed in the electrolyte drop. In such configuration, a three-electrode set-up connected to a potentiostat is reproduced as displayed in Figure 6-1.e.

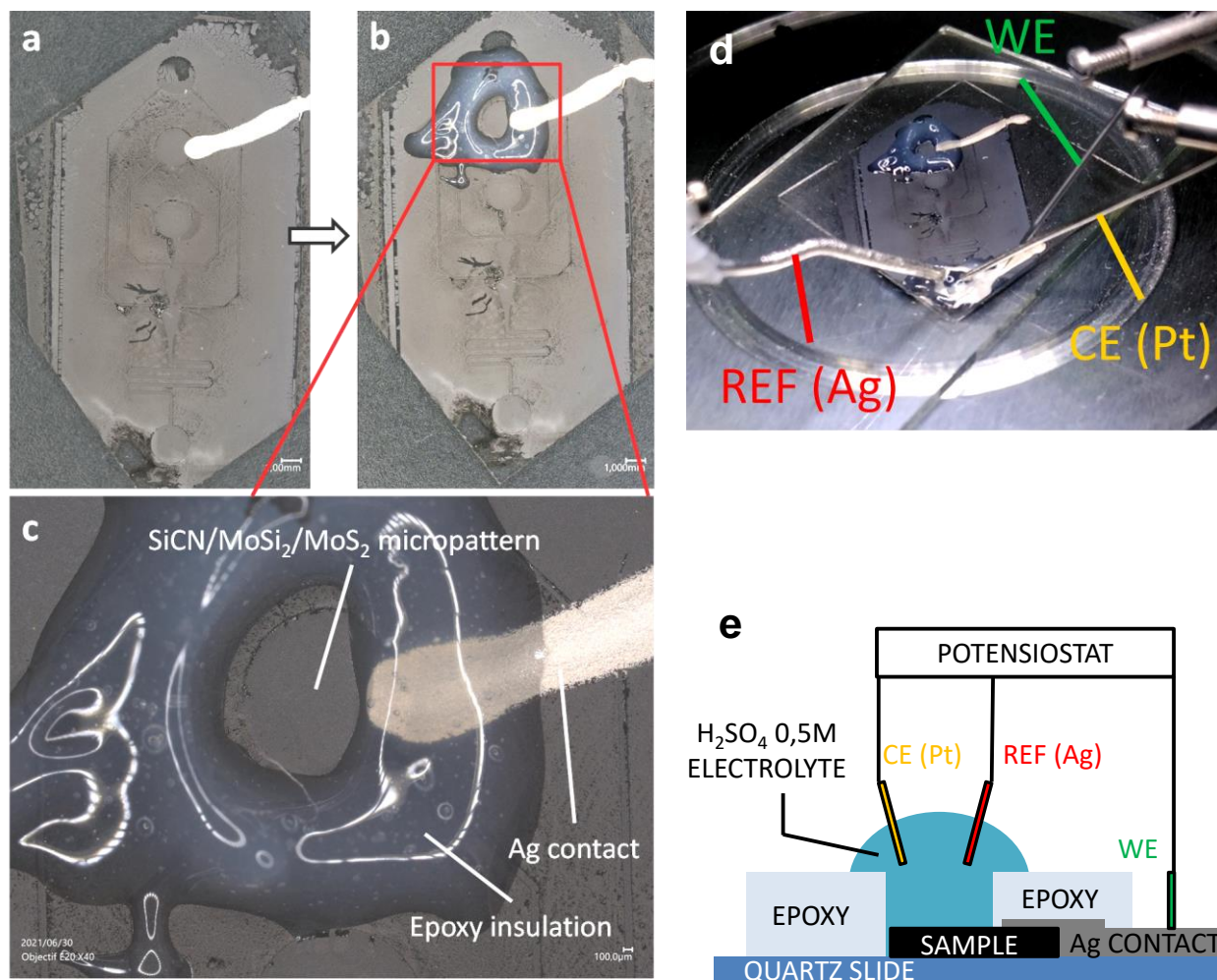


Figure 6-1: Preparation of SiCN/MoSi₂/MoS₂ micropattern for in-situ HER test

Unfortunately, the preliminary *in-situ* tests carried out were unsuccessful as no HER activity was measured with such setup on the contrary of powder test described in chapter 2 (part 2.2.6). This failure was attributed to a poor electronic conductivity in the SiCN/MoSi₂/MoS₂ sample as discussed in chapter 4 (part 2.3.4). MoSi₂ has been introduced in the sample in order to enhance its electronic conductivity but due to a poor colloidal dispersion, the amount of conductive fillers added in the sample was limited. Electronic conductivity may be increased by raising MoSi₂ content.

6.2.2 Operational microdevices for Water-Splitting

The last task of this work was to imagine, design and conceive a micro-electrolyser device based on PDC micro-electrodes. Figure 6-2 represents a CAD visualization of our design based on Modestino *et al* works already discussed in this manuscript. It consists in a

microfluidic chip spiral shaped with two microchannels as shown in Figure 6-2.a. One of the channels is provided for water flow circulation whereas in the second channel a flow of hydrogen produced *via* water-splitting is recovered. The microfluidic channels are shaped thanks to photolithography and made of SU-8 photoresists. One the other hand, PDC micro-electrodes consists in the negative spiral pattern design for SU-8 channels. According to the results discussed in chapters 4 and 5 of this manuscript, they may be fabricated either *via* soft-lithography or *via* photolithography.

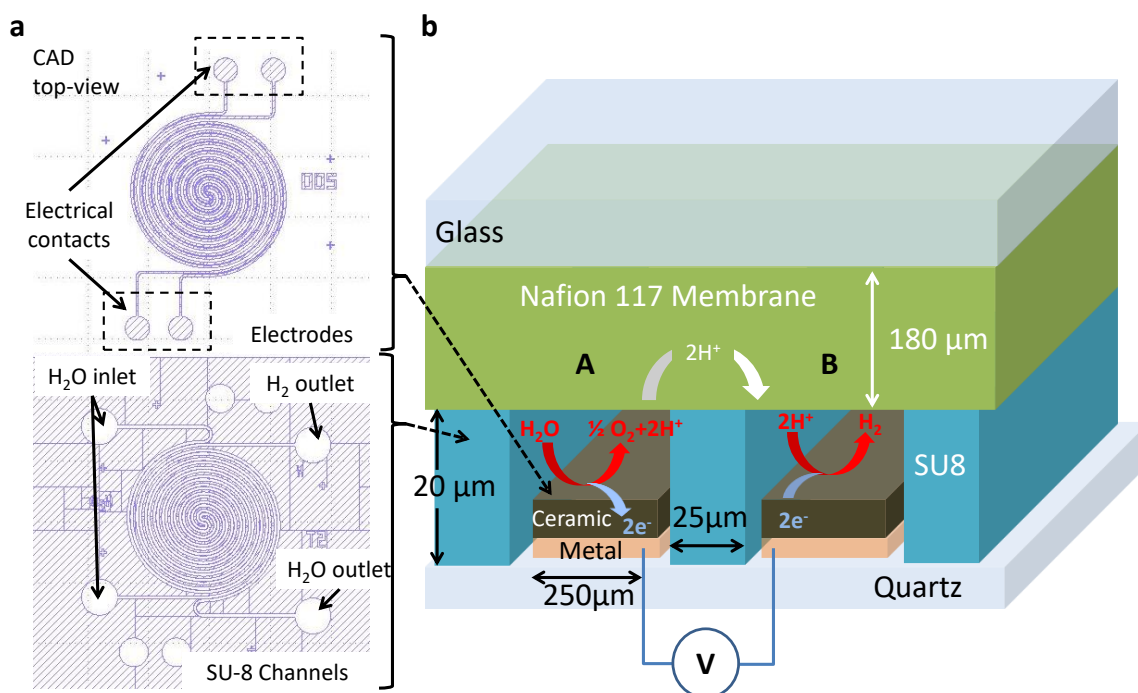


Figure 6-2: CAD visualization of micro-electrolyser supplied with PDCs based micro-electrodes; a) CAD top-view of the PDCs electrodes and SU-8 microchannels and b) 3D view of micro-device transection

In anticipation of the low conductivity of PDCs, we planned to prepare these electrodes on a layer of metal previously deposited (for example titanium). The expected functioning of this micro-electrolyser is described in Figure 6-2.b. The spiral shaped PDC electrodes are contained in the SU-8 microchannels, the assembly is closed by a nafion membrane with proton conduction properties. The application of a potential V between anode and cathode conducts to dihydrogen production. In details, in the micro-channel A H_2O is oxidized and leads to O_2 , H^+ and one electron formation. Thanks to the nafion membrane, the protons are conducted to channel B and reduced in dihydrogen. At the outlet of both channels A and B, O_2 and H_2 in a H_2O in excess flow may be recovered, respectively.

Figure 6-3 exhibits the fabrication steps envisaged for the elaboration of this micro-electrolyser. The first part of this procedure consists in the preparation of the micro-patterned PDC electrodes and has been widely discussed in previous chapters. In Figure 6-3, we choose to suggest the example of soft-lithography method explained in chapter 4 of the manuscript but the photolithographic process developed in chapter 5 may be envisaged. On a quartz slide coated with metallic thin film, a preceramic polymer based solution is micro-molded thanks to a micro-patterned PDMS mold. After crosslinking step, the patterned precursor is converted to ceramic *via* pyrolysis treatment. The un-covered metallic coating is removed thanks to a metal etching treatment. It remains spiral-patterned micro-electrodes with a bottom layer made of metal ensuring electronic conductivity and a top layer in PDCs acting as active catalyst for HER.

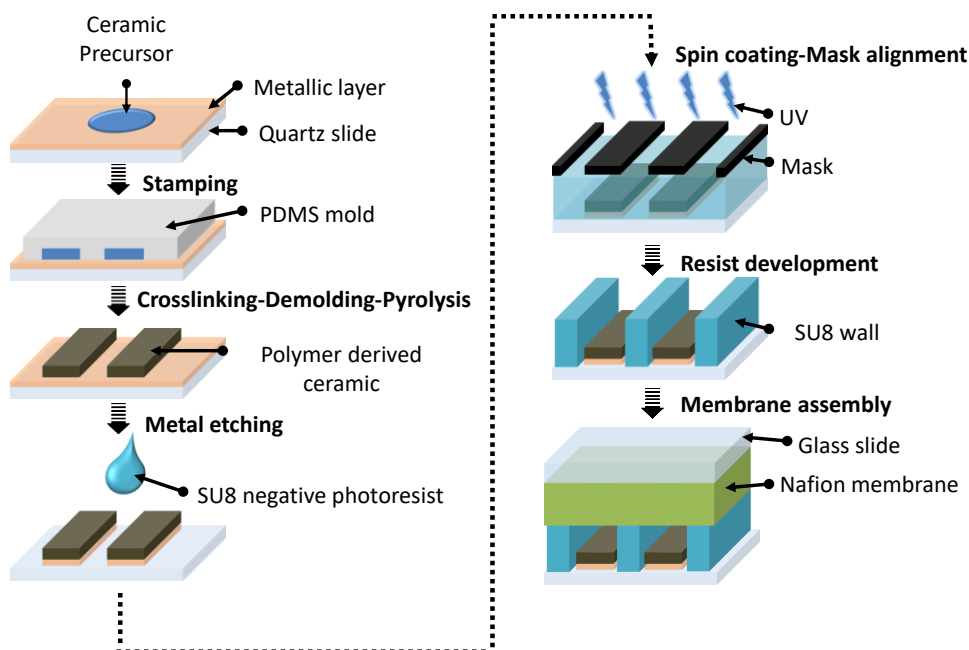


Figure 6-3: Fabrication procedure suggestion for a micro-electrolyser supplied with PDCs based electrodes

Such micro-electrodes are then covered with spin-coated SU-8 photoresist and selectively crosslinked thanks to a properly designed photomask and UV-light. The development step dissolved the un-irradiated resist leaving spiral shaped SU-8 channels. Final stage consists of enclosing the micro-channels with the nafion membranes and a glass slide.

6.2.3 Boron nitride based micropatterns

On another note, we were interested in microfabricating BN patterns. Indeed boron nitride is a ceramic material with particularly impressive refractory and mechanical properties. In fact, its cubic phase (c-BN) is considered as the second hardest known material beyond diamond. In its hexagonal form (h-BN), boron nitride crystallizes in a layered anisotropic microstructure close to graphite. Its low density, high stiffness, non-wettability against metallic melts, high oxidative resistance and thermal conductivity and low dilatation coefficients are desired properties in many application fields. More specifically, its semiconductor properties may be of interest for development of MEMS.

A PDCs pathway exists to synthesize BN material from pyrolysis of polyborazylene precursor. We therefore performed preliminary work on the micromoulding of pre-BN polymer *via* soft-lithography route developed in chapter 4 of this manuscript. Our investigations consisted in synthesizing borazine molecule from reaction between sodium borohydride and ammonium sulfate as already reported in our group. The borazine monomer was then polymerized by poly-condensation thanks to a 10 days treatment in autoclave. The resulting polyborazylene BN precursor consists in a white powder with a ceramic yield close to 90% for pyrolysis at 1000°C under N₂.

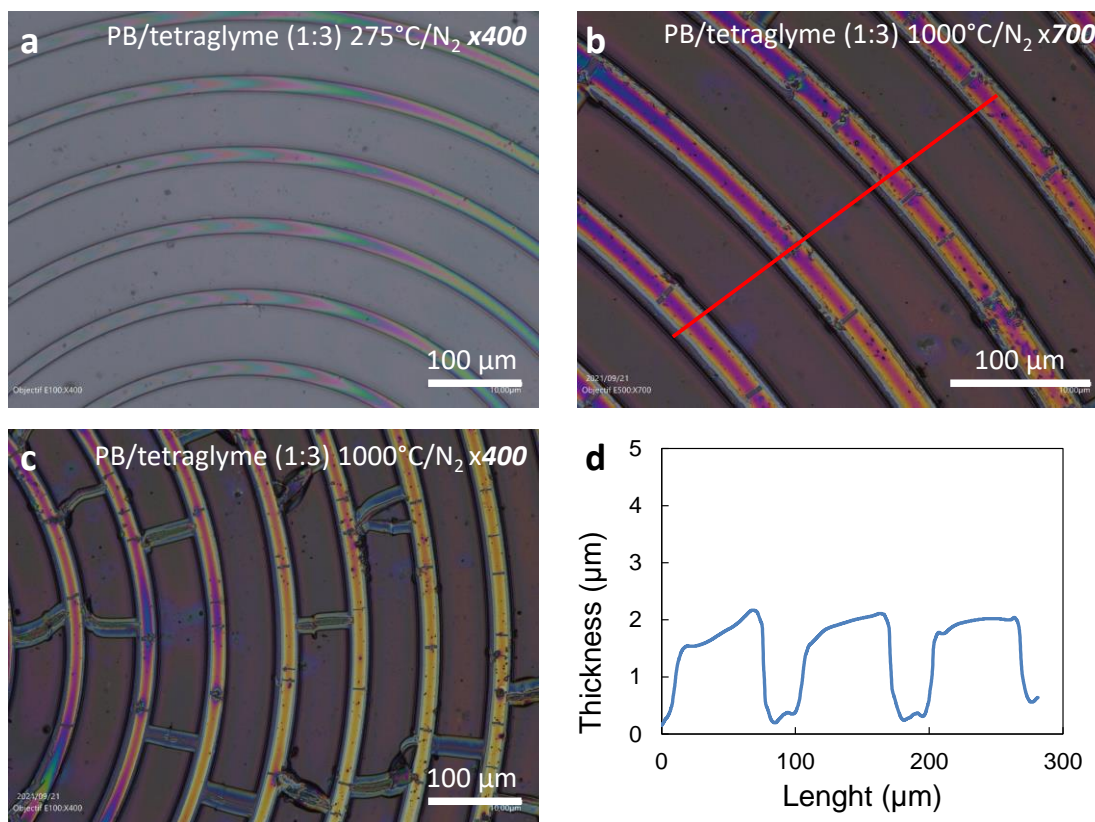


Figure 6-4: Micro-patterning of BN via soft-lithography of polyborazylene; a) Optical micrographs of Polyborazylene micro-pattern before pyrolysis; BN channels observed with b) high magnification and c) low magnification; d) BN channels profilometry

Polyborazylene (PB) was then implemented in the soft-lithography process by dissolving the white powder in tetraglyme and micro-molded with patterned PDMS. After crosslinking and tetraglyme evacuation *via* a thermal treatment at 275°C the micro-patterns displayed in Figure 6-4.a were obtained. After pyrolysis treatment BN channels observed in Figure 6-4.b, d and c reveals relief patterns with thickness close to 2 μm but strewn with micro-cracks.

Obviously, the outlooks presented in this final section of this manuscript would deserve further exploration. We hope that they will motivate the initiation of studies that continue to explore these research opportunities.